UNIVERSITY OF CALIFORNIA
RIVERSIDE

# Star Clusters:
# Constraining Gas Clearing Timescales With HST H$\alpha$ Imaging and Classifying Cluster Morphology With Machine Learning

A Dissertation submitted in partial satisfaction
of the requirements for the degree of

Doctor of Philosophy

in

Physics

by

Stephen Hannon

December 2022

Dissertation Committee:

Dr. Bahram Mobasher, Chairperson
Dr. Janice C. Lee
Dr. Brian Siana
Dr. George Becker

The Dissertation of Stephen Hannon is approved:

_____

_____

_____

_____

Committee Chairperson

University of California, Riverside

## Acknowledgments

This work would not be possible without the support of such a wonderful community of astronomers, to whom I cannot express enough gratitude.

First, I would like to thank my advisor Bahram Mobasher for all his guidance throughout graduate school, and for always pushing me to be the best astronomer I can be. Bahram has shown considerable care and provided sage advice in my development not only as a scientist, but also as a person, and I am very grateful for the opportunity to have been a part of his group.

I would also like to offer special thanks to Janice Lee who, throughout our work & many enlightening conversations, has been an invaluable teacher to me personally, academically, and professionally. Janice's ability to lead our research team week in and week out while managing a multitude of other scientific and organizational pursuits is nothing short of impressive, and her clear passion for the field and its community will continue to inspire myself and those who are fortunate enough to work with her.

Thank you also to Brad Whitmore for all of our encouraging discussions, whether they were scientific- or career-oriented, while also being an absolutely superb model for the love of scientific research. Additional thanks to close collaborators Dave Thilker, Sinan Deger, Rupali Chandar, Aida Wofford, Danny Dale, and the rest of the LEGUS & PHANGS collaborations for their support throughout the publishing of the works presented in this dissertation, and for exemplifying the beauty of studying the stars as a team. Lastly, I would like to sincerely thank all of my peers at UCR for providing me with such a fun and understanding community over the years.

I could not have been surrounded with a more intelligent and encouraging group of people, and again, this work would not be possible without all of their individual efforts.

This dissertation is dedicated to all those whom I love.

To name a few amongst countless other friends and family,

Patricia, Gregory, William, Emily, Christopher, Jennifer, Ian, Ryan, Joshua, Bryson, you all have fundamentally shaped, supported, & continued to inspire my values, and our unconditional relationships keep me endlessly grateful.

ABSTRACT OF THE DISSERTATION

Star Clusters:
Constraining Gas Clearing Timescales With HST H$\alpha$ Imaging and
Classifying Cluster Morphology With Machine Learning

by

Stephen Hannon

Doctor of Philosophy, Graduate Program in Physics
University of California, Riverside, December 2022
Dr. Bahram Mobasher, Chairperson

This dissertation focuses on two topics related to the properties of star clusters as resolved by *HST* imaging taken by the Legacy ExtraGalactic UV Survey (LEGUS) and Physics at High Angular Resolution in Nearby GalaxieS (PHANGS) surveys:

First, the analysis of star cluster ages in tandem with the detailed morphology of any associated HII regions can provide insight into the processes that clear a cluster's natal gas, as well as the accuracy of cluster ages and dust extinction derived from Spectral Energy Distribution (SED) fitting. We classify 3757 star clusters in 16 nearby galaxies according to their H$\alpha$ morphology (concentrated, partially exposed, no emission), using HST imaging from LEGUS. We find: 1) The mean SED ages of clusters with concentrated (1-2 Myr) and partially exposed HII region morphologies (2-3 Myr) indicate a relatively early onset of gas clearing and a short (1-2 Myr) clearing timescale. 2) The extinction of clusters can be overestimated due to the presence of red supergiants, which is a result of stochastic sampling of the IMF in low mass clusters. 3) The age-reddening degeneracy impacts the results of the SED fitting - out of 169 clusters with $M_* \geq 5000$

solar masses, 46 have SED ages which appear significantly underestimated or overestimated based on their environment, and the presence or absence of H$\alpha$. 4) Lastly, for galaxies at 3-10 Mpc, we find that uncertainties in morphological classification due to distance-dependent resolution effects do not affect overall conclusions on gas clearing timescales when using HST H$\alpha$ images, whereas ground-based images do not provide sufficient resolution for the analysis.

Secondly, the time required to visually inspect star cluster candidates identified in HST imaging of nearby galaxies has limited the availability of star cluster catalogs. To greatly expand upon these samples, deep transfer learning has recently been proven capable of creating models to accurately classify star cluster morphologies at production-scale for nearby spiral galaxies (D < 20 Mpc). In order to optimize the reliability of such models, we use HST UV-optical imaging of over 20,000 cluster candidates from PHANGS to create & evaluate two new sets of models: i) distance-independent, which uses the candidates from 18 galaxies regardless of galactic distance, and ii) distance-dependent, which splits the sample into three distance bins (9-12 Mpc, 14-18 Mpc, 18-23 Mpc). From our experiments, we find: 1) our new models outperform the current pipeline models [137] in the classification of PHANGS-HST clusters (~2x the accuracy for class 2 & 3 objects), 2) the overall accuracy of our models are comparable to previous star cluster classification studies (~60-80%), 3) while we observe, at best, a weak negative correlation between model accuracy and galactic distance, we find that training separate models for the three distance bins does not significantly improve model accuracy. Lastly, 4) we identify dependencies between model accuracy and the properties of clusters such as brightness, color, and SED age.

# Contents

# List of Figures

# List of Tables

# Chapter 1

# Introduction

Anyone who has gone outside for a walk on a calm, clear night has beheld the alluring nature of stars. These celestial objects have captured the imagination of humans throughout our history, with questions ranging from their philosophical place in our universe down to their subatomic structure & function. It has become evident that as our understanding of stars has evolved over generations of study, so too have our inquiries about them. In astronomy today, this evolution has directed us toward establishing a complete understanding of how stars form, evolve throughout their lifetime, and eventually disperse back into the field, known altogether as the star formation cycle.

One of the key observations of the last few decades regarding this cycle is how *inefficient* the formation of stars in galaxies is. This formation process begins with molecular gas clouds, which serve as stellar nurseries. These clouds of cold gas gravitationally coalesce to form stars, most of which are thought to form in clusters within giant molecular clouds (GMCs; [92]). If gravity were the sole acting force, then a cloud would collapse to form stars within what is called the dynamical time of the cloud. However, the actual time for a cloud to convert all of their gas into stars (i.e. depletion

time) has been observed to be much longer than this dynamical time [78]. In fact, only a few percent of the mass of GMCs is converted into stars before the clouds are disrupted [152, 146, 54, 91, 55]. To understand these observations, we first must answer the following question:

*I. What is halting the formation of stars within GMCs?*

Despite the fact that [152] first made their observations nearly fifty years ago, the exact processes governing the dynamics of these GMCs are still debated. As discussed in [90], stellar feedback is found at the forefront of the discussion. This feedback, which includes processes such as supernovae (SNe) explosions, stellar winds, photoionization, and radiation pressure, have been shown in several studies to be capable of disrupting the parent molecular cloud, thus halting star formation and adequately limiting star formation efficiency to the observed degree [6, 39, 74, 86]. When simulations of star formation specifically exclude stellar feedback, the resulting star formation rate and efficiency are far greater than the aforementioned observations [22, 131, 73, 45, 89]. Further, these feedback mechanisms affect the larger scale properties of galaxies as well. Through the transfer of energy and momentum, they contribute to the observed dynamical equilibrium in the interstellar medium (ISM; [129]) among other galactic-scale properties (e.g., [105, 63, 114, 88]).

Critically, these feedback processes occur on different timescales. Thus constraining the timescale for a star cluster to clear its natal gas will inform us as to which of these processes are responsible for the clearing, represented by our second primary question:

*II. Given stellar feedback occurs on different timescales, how can we constrain the timescale for gas clearing?*

One of the methods to constrain such timescales is through the study of nebular H$\alpha$ emission in conjunction with inferred properties of parent star clusters (e.g. [139, 72, 68]). As

mentioned above, most of the star formation in the universe occurs in a clustered fashion within GMCs [92]. The resultant star clusters contain numerous individual stars, the most massive of which (OB-type stars) produce radiation which is strong enough to ionize their surrounding gas, known as an HII region. The hot, ionized gas of an HII region produces emission lines, and the strongest amongst them occurs at 656.3nm, known as H$\alpha$. A large diversity in the morphology (i.e. size, shape, extent, etc.) of HII regions has been observed via imaging of H$\alpha$ emission (e.g. [77, 37, 139, 9, 68]), and this variety has been attributed to factors including gas density distributions and the aforementioned stellar feedback mechanisms [90].

Together with these wide-ranging states of cloud dispersal are an array of properties derived from the host star cluster. In addition to representing a significant percentage of all stars in galaxies, star clusters are uniquely useful because the individual stars form at roughly the same time and can thus be effectively characterized by a single-aged stellar population, which can be derived by the fitting of their spectral energy distributions (SEDs; e.g. [4]). We can then leverage the knowledge of their ages to use them as "clocks" to age-date the dispersal states of their surrounding HII regions, the gas from which they formed. Comparison between the morphologies of HII regions and the properties of their parent star clusters can therefore inform us about a potential HII region evolutionary sequence and its timescale, thus helping us better understand the gas clearing process.

Previous studies have examined such correlations between H$\alpha$ morphology and star cluster properties derived from SED-fitting using photometry from the Hubble Space Telescope (*HST*; e.g. [139, 72]), however one of the main drawbacks of studies such as these is their limitation to young (SED ages $\leq$ 10 Myr), massive ($\geq$ 5000 $M_\odot$) clusters. Observed star cluster mass functions appear to be well-fit by power laws of the form $dN/dM \propto M^{-2}$ (e.g., [146, 151, 97, 18, 56, 59]), implying

that clusters in the mass range $10^{2.5}$-$10^{3.5}$ $M_\odot$ are nearly ten times as numerous as those in the range $10^{3.5}$-$10^{5.5}$ $M_\odot$. Thus by utilizing a mass cutoff, these prior studies are removing a significant portion of the overall star cluster population. A primary reason for the cutoff is that analyses of lower-mass clusters have been shown to be affected by the stochastic sampling of the upper part of the stellar mass function (e.g. [13, 61, 94, 25, 31, 44]), making it challenging to study their physical properties. In this low-mass regime, the predicted luminosity and color distributions can be far from Gaussian even when the total cluster mass exceeds $10^5$ $M_\odot$, as they depend strongly on the mass distribution of stars in the cluster [58, 59]. Additionally, these analyses often ignore all star clusters with SED ages > 10 Myr under the assumption that H$\alpha$ will only be present when the clusters have ages < 10 Myr (e.g. [49, 139, 138, 72]). However, such an assumption ignores the impact of the age-reddening degeneracy, which occurs because the light from young star clusters can be absorbed and scattered by surrounding dust resulting in redder observed light, while stars also naturally become redder as they age. Thus SED-fitting can result in poorly estimated ages for star clusters (e.g. age is overestimated while reddening is underestimated and vice versa), as has been observed in [140] & [135]. Thus the use of age cutoffs can eliminate clusters from the sample which are in fact young while including truly older clusters with significantly underestimated ages.

In this dissertation, we seek to establish these gas clearing timescales using one of the largest sample of star clusters and HII regions, while also addressing these issues related to star cluster mass and SED age. Our sample comes from the Legacy ExtraGalactic UV Survey (LEGUS; [28]), which has collected *HST* imaging with the Wide Field Camera 3 (WFC3; F275W, F336W, F438W, F555W, and F814W) for 50 nearby galaxies spanning a range of galactic properties, paired

with data from the LEGUS-H$\alpha$ follow-up survey (GO-13773; PI R. Chandar) with imaging for 25 of the LEGUS galaxies with the highest star formation rates.

Chapter 2 of this work examines gas clearing timescales in three of the nearest spiral galaxies from LEGUS while also focusing on effects related to the use of a low-mass cluster sample. Namely, we examine the evidence for stochastic sampling effects in the properties of clusters (e.g. color, age, mass, reddening), and also explore potential methods which could be employed to mitigate against stochastic sampling effects and provide better constraints on cluster properties. Chapter 3 expands the study of gas clearing timescales to the full available star cluster sample from LEGUS, which includes a more robust sample of massive clusters while also including clusters of all SED ages. By examining all clusters regardless of SED age, we are able to examine the reliability of SED-fit ages. In these chapters, we not only contribute constraints on the timescales for gas clearing, but also provide important insight into the nature of star clusters and their study in tandem with their SED-fit properties regardless of predicted age and mass.

Lastly, while star clusters are a natural basis for the study of gas clearing timescales [139, 72, 67, 64, 68, 69], they represent a fundamental unit for star formation in general, and as such have also served as the basis for a wide-range of other studies in the field. For example, such studies inform us about the formation of globular cluster systems [143, 142, 99], the characterization of the star cluster luminosity function [145, 97] and initial cluster mass function [96, 33, 35, 108, 109], the spatial distribution of clusters and their hierarchical formation [19, 66, 52], correlations with various galactic parameters such as surface brightness, morphological type [95, 98], and star formation history [20], among many others.

As these star cluster studies continue to advance, so too have their sample sizes, with two recent examples in LEGUS and PHANGS-HST each containing tens of thousands of cluster candidates. In these surveys, star clusters are categorized according to a four-class system based on morphology [2], which not only crucially differentiates clusters from artifacts, but has also shown correlations with the physical properties of clusters including age and mass (e.g. [65, 66, 140, 141]). The classification of these objects has conventionally been performed by one or more human(s), which is becoming increasingly time-consuming and can thus limit sample size, which leads us to our final primary question:

*III. How can our classification of star clusters keep pace with the growth of sample sizes?*

Recently, there has been some success in the use of machine learning techniques for the rapid classification of production-scale star cluster candidates. [67] created a generally successful classification model (∼70% agreement with human classifications) using a bagged decision tree algorithm with star clusters from LEGUS [2], however it did not perform as well for more distant objects or for compact associations of stars (Class 3 objects). [137] and [117] then improved upon these models by utilizing deep learning with even larger samples of LEGUS galaxies, resulting in ∼10x greater recovery rates for the compact associations. The accuracy of the deep learning models in particular (∼70% overall) rival the consistency found between human classifiers, and thus highlight the viability of machine learning in producing star cluster catalogs much more efficiently than with human classification.

While the aforementioned models perform well for samples of clusters from LEGUS, on which they were trained, they do not perform as well for the more recent cluster sample from PHANGS-HST [137, 141]. One explanation for this is that in PHANGS-HST, the definition of Class

3 objects is more explicitly specified in order to avoid stellar pairs or triplets, which are sometimes categorized as Class 2 or 3 objects by LEGUS [141]. Another is that the PHANGS-HST cluster sample occupies a different distance range (4–23 Mpc) than the LEGUS sample (3–16 Mpc), as more distant samples have shown to be correlated with lower model accuracy (e.g., [117]).

Chapter 4 of this dissertation is complementary to Chapters 2 & 3, and seeks to address the above issues by developing two experiments to produce more accurate star cluster classifications. First, we train a new set of deep learning models based on the full, available PHANGS-HST sample of star clusters, which will allow us to compare our model performance with previous models and a variety of galactic properties. Secondly, we introduce a novel distance-dependent model system in which multiple models are trained based on the galactic distance of the star clusters. Overall, these experiments aim to provide a more reliable machine learning-based classification for the PHANGS-HST program and potentially future star cluster studies as well.

# Chapter 2

# H$\alpha$ Morphologies of Star Clusters: A LEGUS study of HII region evolution timescales and stochasticity in low mass clusters

## 2.1 Introduction

The study of young star clusters is crucial for understanding the formation and evolution of stars in general, as most of the star formation in our universe occurs in a clustered fashion [92]. Star clusters are born in clouds of cold gas which are subsequently ionized by massive OB-type stars formed within the clusters, resulting in nebular H$\alpha$ emission.

Stellar feedback within these star-forming regions significantly affects the size, shape and extent of this H$\alpha$ emission (e.g. [77, 37, 139, 9]). By examining the morphology of these HII regions across a large cluster sample, we can investigate questions such as: 1) Is there an evolutionary pattern found amongst different morphological types? 2) If so, what is the timescale associated with the evolution? 3) What physical processes drive the evolution? 4) What other properties are correlated with HII region morphology and why?

Previous studies have examined correlations between H$\alpha$ morphology and star cluster properties, derived from the fitting of Spectral Energy Distributions (SEDs) to *HST* photometry. For example, [139] investigated the use of H$\alpha$ morphologies of the star cluster population in M83 to constrain cluster ages. This led to a classification scheme for H$\alpha$ morphologies representing different stages in a cluster's evolution (from concentrated H$\alpha$ to a gradually more blown-out region). Whitmore et al. argue that this classification scheme provides a viable method for dating young ($\sim$1-10Myr) clusters. [72] also examined the young ($\leq$ 10Myr), massive ($\geq$5000$M_{\odot}$) clusters of M83 by including data from 6 additional *HST* fields. From the H$\alpha$ morphologies, they inferred how much time clusters spent in an "embedded" state, thereby providing insight into the timescales associated with gas clearing for their sample. In addition to finding an evolutionary pattern generally consistent with the results of [139], they concluded that the gas removal process began in most clusters at ages of 2-3 Myr, implying that supernovae (SNe) could not be the sole driver. Using a different approach by comparing ALMA CO detections of giant molecular clouds (GMCs) with the positions of star clusters in NGC 7793, [67] found that the timescale for star clusters to dissociate from their natal clouds is similarly very short, between 2-3Myr, roughly consistent with the timescales found based on ALMA CO data for the Antennae galaxies [107].

Here, we study the H$\alpha$ morphologies of the ionized gas surrounding star clusters in a sample of three nearby spiral galaxies (NGC 1313, NGC 4395, NGC 7793) and retain the more common low-mass clusters in our analysis. Observed star cluster mass functions appear to be well-fit by power laws of the form dN/dM $\propto$ M$^{-2}$ (e.g. [146, 151, 97, 18, 56, 59]), implying that clusters in the mass range $10^{2.5}$-$10^{3.5}$ $M_{\odot}$ are nearly ten times as numerous as those in the range $10^{3.5}$-$10^{5.5}$ $M_{\odot}$. However, analyses of lower-mass clusters have been shown to be affected by the stochastic sampling of the upper part of the stellar mass function (e.g. [13, 61, 94, 25, 31, 44]), making it challenging to study their physical properties. In this low-mass regime, the predicted luminosity and color distributions can be far from Gaussian even when the total cluster mass exceeds $10^5$ $M_{\odot}$, as they depend strongly on the mass distribution of stars in the cluster [58, 59].

This paper examines these stochastic sampling effects observationally, and aims to address the following questions: 1) Is there evidence for stochastic effects in the properties of clusters (color, age, mass, reddening)? 2) What potential methods could be employed to mitigate against stochastic effects and provide better constraints on cluster properties? Addressing these questions will provide important insight into the nature of star clusters, and possible strategies for future studies of low-mass star clusters, which constitute the bulk of the population.

In Section 3.2 we summarize the observations and the star cluster catalogs used in the study. Section 3.3 describes the visual classification scheme used for H$\alpha$ morphologies. Section 3.4 examines the cluster age and reddening distributions as a function of H$\alpha$ morphological class. In Section 3.7, we investigate the effects of stochastic sampling of the stellar IMF and examine methods to mitigate against its impact. In Section 2.6, we discuss the implications of our results for H$\alpha$

morphology evolution and compare our study with previous works. Section 2.7 provides an overall summary of the work as well as potential future studies.

## 2.2 Data

### 2.2.1 Observations

We use data from the Legacy ExtraGalactic UV Survey (LEGUS; [28]), which has collected *HST* imaging with the Wide Field Camera 3 (F275W, F336W, F438W, F555W, and F814W) for 50 nearby (within ∼12 Mpc) galaxies spanning a range of properties. WFC3 observations taken specifically for the LEGUS program in Cycle 21 (GO-13364) are combined with ACS data taken in previous cycles by other programs to provide full 5-band coverage for the LEGUS sample. We also use data from the LEGUS-H$\alpha$ follow-up survey (GO-13773; PI R. Chandar), where a narrow-band filter covering the H$\alpha$ emission-line (F657N) and a medium-band filter sampling the line-free continuum (F547M) were used to image the 25 LEGUS galaxies with the highest star formation rates. To produce H$\alpha$ emission-line images[1], the drizzled and aligned F657N images are continuum subtracted using an image formed from a combination of F814W and F547M, appropriately scaled using their AB zeropoints.

For this study, we have selected the three nearest (d $\approx$ 4Mpc) spiral galaxies (six *HST* pointings) from the LEGUS survey: NGC 1313 (E and W pointings), NGC 4395 (N and S pointings), and NGC 7793 (E and W pointings), all of which have *HST* H$\alpha$ emission-line and continuum imaging. We choose the three nearest galaxies to maximize resolution for H$\alpha$ morphological classification. Fig. 2.1 shows the *HST* footprints for each of the pointings for the three galaxies in this study.

[1]Note that the emission-line images also contain flux from the adjacent [NII] 6548,83 line.

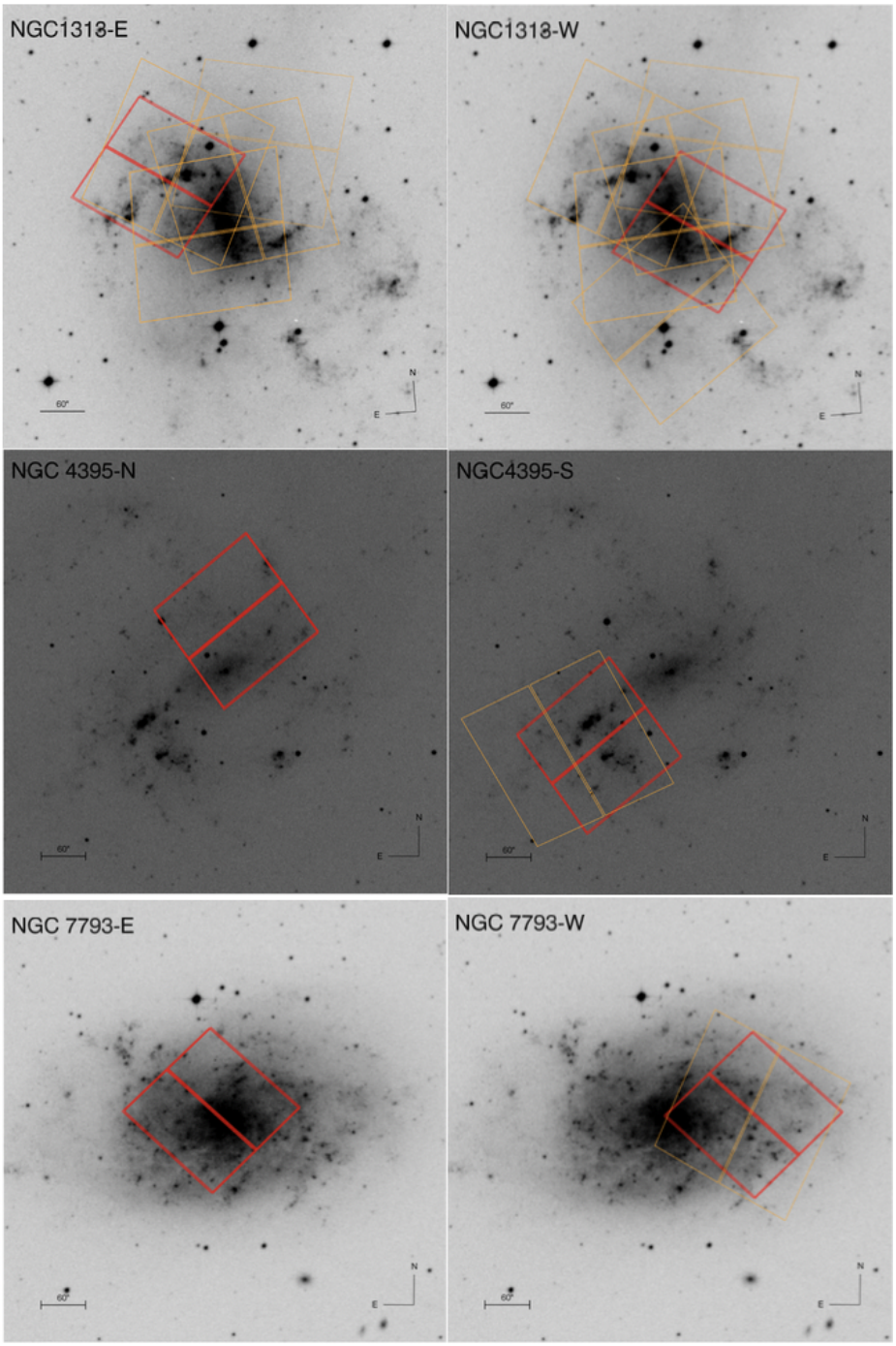


Figure 2.1: *HST* footprints on digitized sky survey (DSS) images for each of the 6 fields used in this study: NGC 1313-E, NGC 1313-W, NGC 4395-N, NGC 4395-S, NGC 7793-W, and NGC 7793-E. Red outlines represent WFC3 images and orange outlines, where available, represent previously available ACS images. The field of view of WFC3 is 162" x 162".

Details on filters, exposure times, and other pertinent information on selection techniques and properties of these galaxies can be found in [28].

### 2.2.2 Star Cluster Catalogs

Catalogs of the photometric and physical properties of star clusters for the majority of LEGUS galaxies have been developed and publicly released by the LEGUS team (https://legus.stsci.edu)[2]. Here, we provide a short overview of the selection criteria, as we use these catalogs to select young star clusters for our analysis. A full description of the selection methods, photometry, and derivation of cluster masses, ages, and reddening via SED fitting are given in [2] and [38].

The star clusters in LEGUS were selected using the following criteria:

1. detection in at least 4 filters (UBVI, UV-BVI, or UV-UBVI) with photometric error less than 0.3 mag.

2. $M_V \leq$ -6.0 (using the F555W filter)

3. a concentration index (CI) threshold, where CI = mag(1pix) - mag(3pix) in F555W to separate point sources from extended sources. For the three galaxies here, the CI threshold is between $\geq$ 1.2 and 1.4, depending on distance of the galaxy and the camera used to obtain the F555W imaging (i.e., ACS or WFC3).

All candidates are visually inspected by three LEGUS team members, and placed into the following classes:

Class = 1: Symmetric, compact cluster

Class = 2: Concentrated object with some degree of asymmetry; possible color gradient

[2]Catalogs for NGC 4395 are based on updated models and will be posted in a future release.

Class = 3: Multiple peak system; compact association; could be confused with spurious sources if there are nearby stars along the line of sight

Class = 4: Spurious detection (e.g. foreground/background sources, single bright stars, artifacts)

Photometry is performed with apertures with radii of 4, 5, and 6 pixels for clusters in NGC 4395, NGC 7793, and NGC 1313, respectively. At the adopted distances of 4.30, 3.44, and 4.39 Mpc [28], these apertures subtend 3.3, 3.3, and 5.1 pc, respectively, given a WFC3 UVIS pixel scale of .04 arcseconds per pixel. To measure and subtract the background, a 1 pixel-wide sky annulus at a 7 pixel radius is used. An average aperture correction is estimated as the difference between the magnitude of the source measured at 20 pixels (with a 1 pixel-wide sky annulus at a 21 pixel radius) minus the magnitude of the source obtained using the smaller (4, 5, and 6 pixel) aperture for a set of bright isolated clusters. The total cluster magnitudes are corrected for foreground Galactic extinction [124].

Cluster SEDs are fitted based on the *HST* photometry with Yggdrasil SSP models [149], which include nebular flux via photoionization modeling with CLOUDY, assuming a covering fraction of 0.5.[3] The model grid used in the fitting is based on 46 time progressive steps from 1Myr to 10Gyr, and 150 fixed steps in reddening from 0.00 to 1.50. The "best values" used in this work are those corresponding to the minimum $\chi^2$ value. For each galaxy, the present-day metallicity of its young populations as derived from nebular abundances (listed in [28]) is adopted. This corresponds

[3]To validate the use of the models which include nebular emission to infer the ensemble properties of our star cluster sample, H$\alpha$ equivalent widths (EWs) are measured for isolated clusters with concentrated H$\alpha$ morphologies. For ages less than 4 Myr, the model values of log(EW[H$\alpha$] ()) range from ~2.7-3.25. The measured values are consistent within the measurement uncertainties: log(EW[H$\alpha$] ()) ranges from 2.6-3.6 with a median of 3.1. More detailed model validation is advised if examining the properties of individual objects, as opposed to the ensemble properties of interest here.

to a metallicity of Z = 0.02 (solar) for clusters in NGC 7793 and NGC 1313 while those in NGC 4395 assume a metallicity of Z = 0.004.

The errors of the ages, masses, and reddenings used in this study are based on the minimum and maximum values of the SED fitted parameters. Based on $1\sigma$ confidence levels of [93], all age and reddening values with corresponding $\chi^2 \leq \chi^2_{min} + 2.3$ are found, and from these values, minima and maxima are determined. In the cases where no other grid solution in the SED fitting procedure are found, the errors are half the size of the age step (1 Myr) or reddening step (0.01).

A total of twelve catalogs have been produced for each galaxy based on two stellar evolution models (Geneva and Padova), three extinction models (Milky Way extinction, starburst extinction, and differential starburst extinction), and two aperture correction methods (concentration index based and average aperture correction). In this work, we use the LEGUS "reference" catalogs [2], based on the Padova stellar evolution models, Milky Way extinction, and using standard average aperture correction, but it should be noted that the Geneva models are generally considered to better describe the youngest population of stars, and differences in the results of our analysis are discussed later in this paper. It should also be noted that the SED fitting results used in this analysis are only based on the broadband photometry and are independent of the narrow and medium band photometry. Information from the H$\alpha$ imaging only enters the analysis once, in the classification of the cluster H$\alpha$ morphologies.

For our study, we produce a sample of verified clusters by selecting all objects with mode class of 1, 2, 3 and excluding sources whose H$\alpha$ images were partially cut off by the edge of the field of view. We then narrow our sample down to those with best-fitted ages of 10 Myr or younger, leaving us with a total of 654 final cluster targets across all 6 pointings. Table 3.1 shows the total

| Galaxy | Total Detections | Verified Clusters | $\leq$ 10Myr | $\geq$ 5000 $M_{\odot}$ |
|---|---|---|---|---|
| NGC1313W | 3784 | 486 | 177 | 1 |
| NGC1313E | 5284 | 259 | 111 | 2 |
| NGC4395N | 291 | 39 | 23 | 14 |
| NGC4395S | 837 | 137 | 112 | 18 |
| NGC7793W | 2794 | 221 | 119 | 0 |
| NGC7793E | 899 | 191 | 112 | 7 |
| Totals | 13889 | 1333 | 654 | 42 |

Table 2.1: Number counts of total detections, visually-verified clusters (LEGUS mode class = 1, 2, or 3), verified clusters younger than 10 Myr, and verified clusters greater than 5000 $M_{\odot}$ for each of the six fields of view. Masses and ages are determined by comparing the measured broad-band photometry with the Yggdrasil models, and assuming Milky Way extinction, Padova stellar evolutionary tracks for an appropriate metallicity, and the average aperture correction procedure described in [2]

number of objects in the overall catalogs, as well as in our young cluster sample, for the galaxies in this study.

## 2.3 H$\alpha$ Morphology Classification

To aid our visual classification process, two sets of 150pc x 150pc postage stamps were created for each cluster. One set of stamps was made from an RGB image of the galaxy using combined NUV and U bands for the blue channel, combined V and I bands for the green channel, and the continuum-subtracted H$\alpha$ narrow band for the red channel. The second set of postage stamps was created solely from the continuum-subtracted H$\alpha$ narrow band image. Whereas the narrow band images clearly display the shape and extent of the HII regions, the RGB images are useful in showing the target cluster and its neighbors in relation to the surrounding gas.

As illustrated in Fig. 2.2, each individual stamp includes small cyan circles to indicate the positions of all clusters (including those older than 10 Myr). The radii of these circles represent the aperture sizes used for photometry in that particular field; i.e., whereas apertures with 6-pixel radii were used for sources in NGC 1313, 4-pixel and 5-pixel radii apertures were used for NGC 4395 and NGC 7793, respectively (see Section 2.2.2). These aperture sizes roughly correspond to a physical radius of 4pc. In addition, a white circle of radius 7.5pc is drawn around the central target as a reference to help determine the compactness of the HII region.

For reference, an O5 star producing ~5 x $10^{49}$ Lyman continuum photons per second[4] would create an idealized Strömgren sphere with a radius between ~1.1pc and 110pc for gas densities between $n_e \approx n_p$ = 1 cm$^{-3}$ (larger sphere) and $n_e \approx n_p = 10^3$ cm$^{-3}$ (smaller sphere). In the same range of gas densities, a B0 star producing ~5 x $10^{47}$ ionizing photons per second would create a Strömgren radius between ~0.25pc and 25pc. These numbers assume a uniform ISM rather than a more realistic clumpy ISM, but are used here as a guide.

Our morphological classification scheme is based on one used by [72], who defined three classes based on the presence and shape of the H$\alpha$ emission, similar to that of [139]:

1 **concentrated**, where the target star cluster has a compact HII region and where there are no discernable bubbles or areas around the cluster which lack H$\alpha$ emission,

2 **partially exposed**, where the target cluster shows bubble like/filamentary morphology covering part of the cluster and,

[4] [113]

3 **no emission**, where the target cluster does not appear to be associated with H$\alpha$. There is no H$\alpha$ emission within ~20pc of the cluster. The majority (62%) are clusters without any visible H$\alpha$ emission in their 150 parsec-wide postage stamps.

An important consideration in classifying clusters by their H$\alpha$ morphology is the detection limit for H$\alpha$ and the stars required to produce the ionizing radiation. The most straightforward way to characterize the sensitivity of the H$\alpha$ images is to compute the total flux of a point source at a specified detection limit. For the H$\alpha$ images used in this study, we find we that the 5$\sigma$ point source detection limit is between 5.0x10$^{-17}$ and 5.5x10$^{-17}$ ergs cm$^{-2}$ s$^{-1}$. At a distance of 4 Mpc, this gives an observed (i.e. no extinction corrections applied) luminosity of ~1.5x10$^{35}$ erg $^{-1}$. Given the model grid of [126], this luminosity corresponds to the ionizing flux of a B0.5V star (~10$M_{\odot}$), with the usual assumptions: solar metallicity, Case B recombination, nebular temperatures and densities of 10$^4$ K and 100 cm$^{-3}$ respectively, and that the nebular region is radiation bounded.

In addition to these three H$\alpha$ morphological classes, each cluster is also identified as either isolated or non-isolated. [62] compiled survey data for several thousand unbound stellar systems in Local Group galaxies and found that the average size of these stellar associations is ~70-90pc. Comparably, we define an isolated cluster to be one that does not have any neighboring clusters within 75pc. This is done to control for the potential impact of neighboring clusters on the clearing of a target cluster's gas, which may have a confounding effect on correlations between cluster properties and the H$\alpha$ morphology.

Our hypothesis in classifying the H$\alpha$ morphology of the young clusters in such a manner is that they represent HII region evolutionary stages. We are interested in testing for possible correlations between the H$\alpha$ morphology and cluster age, reddening, and mass. Fig. 2.2 shows RGB

postage stamps of examples from each of the three H$\alpha$ morphological classes, with the cluster ID in a given pointing labeled in the upper left-hand corner, its estimated age (in Myr) in the lower left-hand corner, and its estimated mass (in $M_{\odot}$) in the bottom right-hand corner. The isolated object in the upper-left panel (ID 84) is classified as concentrated, as the HII region has a size comparable to the 7.5pc radius circular marker and is fairly compact. The upper-right panel shows an isolated cluster with H$\alpha$ morphology classified as partially exposed (ID 1255), as there is little emission at the center of the HII region at the position of the cluster, creating an apparent bubble. The lower-left panel shows an isolated cluster without H$\alpha$ emission (ID 2674), as there is no HII region clearly associated with the cluster. Finally, the lower-right panel also shows a cluster with morphology classified as no emission (ID 764), as the H$\alpha$ is tens of parsecs away in every direction and it is not clear whether the cluster is contributing ionizing radiation responsible for the H$\alpha$ emission; this is also an example of a non-isolated cluster as there are several other clusters in the vicinity. We note that while our H$\alpha$ classification does not distinguish between the two no-emission examples in Fig. 2.2, the majority (>60%) of isolated clusters in this class showed no clear HII region associated with the cluster, resembling object ID 2674.

The number of clusters in each H$\alpha$ class and isolation category is shown in Table 3.2. The majority of clusters are classified as no-emission (~60%). Although the fractions of isolated and non-isolated clusters are comparable for the concentrated and no-emission classes, it is noteworthy that the partially exposed clusters of our sample show a much greater ratio of non-isolated to isolated clusters (~7:1). This possible reasons for this can be further examined in future work, upon expansion of the dataset.

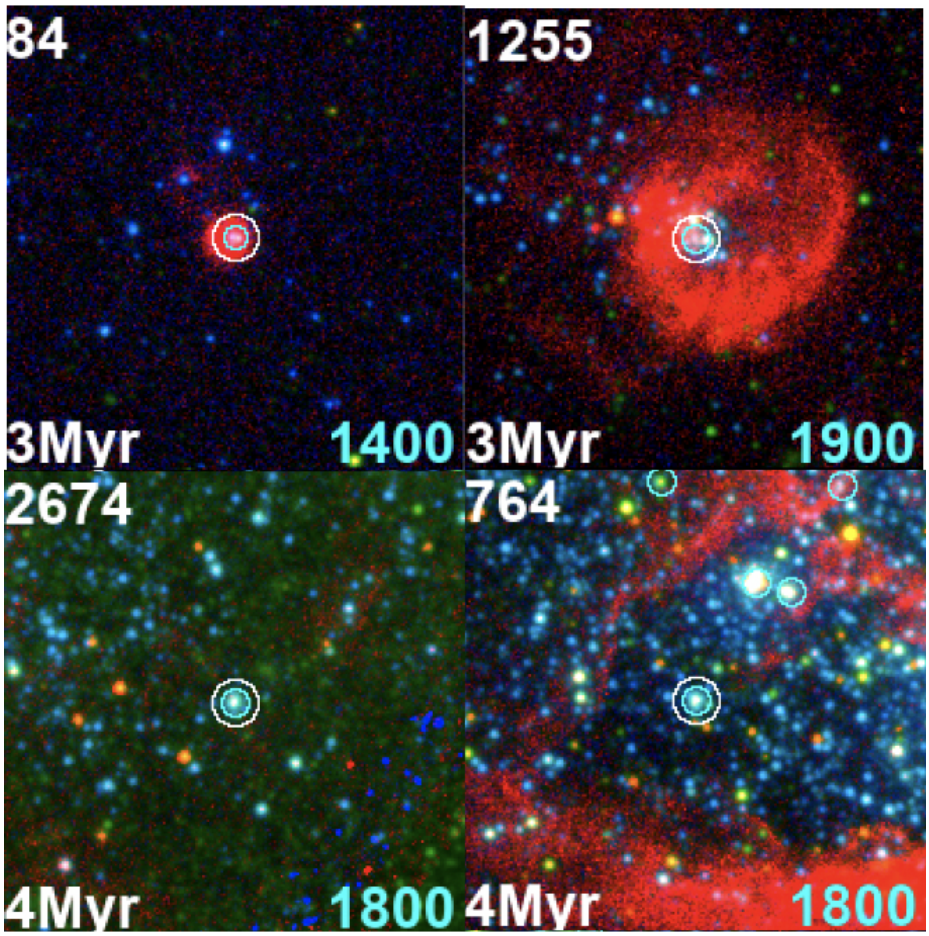


Figure 2.2: RGB postage stamps exemplifying the three HII region morphology classifications. The red in the images corresponds to continuum-subtracted H$\alpha$. In each stamp, the object ID is located in the upper left, age in the lower-left, and mass (in $M_{\odot}$) in the lower-right. White circles with radii of 7.5pc are drawn around the stamp's target cluster. Cyan circles represent the photometric aperture radii (~4pc). Clockwise from the upper-left panel: Object 84 from NGC 4395-N has an estimated age of 3 Myr and is classified as concentrated. Object 1255 from NGC 1313-E is also estimated to be 3 Myr and classified as partially exposed. Object 2674 from NGC 1313-E is ~4 Myr and is classified as no-emission. Object 764 from NGC 1313-E is also ~4 Myr and also classified as no-emission and is the only non-isolated cluster shown here. All postage stamps are oriented north-up, east-left.

| | Concentrated | | Partially Exposed | | No Emission | |
|---|---|---|---|---|---|---|
| Galaxy | Isolated | Non-Isolated | Isolated | Non-Isolated | Isolated | Non-Isolated |
| NGC1313W | 5 | 25 | 1 | 20 | 39 | 87 |
| NGC1313E | 10 | 15 | 1 | 25 | 29 | 31 |
| NGC4395N | 6 | 0 | 1 | 0 | 14 | 2 |
| NGC4395S | 9 | 16 | 4 | 23 | 20 | 40 |
| NGC7793W | 10 | 20 | 3 | 19 | 37 | 30 |
| NGC7793E | 11 | 15 | 4 | 11 | 47 | 24 |
| **Totals** | **51 (7.8%)** | **91 (13.9%)** | **14 (2.1%)** | **98 (15.0%)** | **186 (28.4%)** | **214 (32.7%)** |
| $\geq 5000\ M_{\odot}$ | 0 | 5 | 0 | 7 | 13 | 17 |

Table 2.2: Number counts of clusters in each of the three morphology classes (concentrated, partially exposed, no-emission) and further separated into isolated and non-isolated categories depending on the presence of neighboring clusters within 75pc. The total number of clusters (and their percentage of the total 654) and the number of clusters greater than or equal to 5000 $M_{\odot}$ in each of the six bins are provided in the bottom two rows.

## 2.4 Results

In this section, we examine the ages, masses and reddening of clusters in each morphological class and isolation category based on both the Padova and Geneva stellar evolutionary models. The mean and median age, reddening, and mass for each of these categories are summarized in Table 3.3. The following subsections detail the characteristics of the age and reddening distributions.

### 2.4.1 Age Statistics by Morphological Class

A key aspect in our analysis of young clusters is examining the age distributions as a function of H$\alpha$ morphological class. These ages can establish whether or not the morphological classes constitute an evolutionary sequence for HII regions. Fig. 2.3 shows the age distributions for

| | | | Padova | | | | Geneva | | |
|---|---|---|---|---|---|---|---|---|---|
| H$\alpha$ Class | Isolated? | N | Mean **Age** (Myr) | Median **Age** (Myr) | SD | N | Mean **Age** (Myr) | Median **Age** (Myr) | SD |
| Concentrated | Isolated | 51 | 3.3 | 3.0 [2.0, 4.0] | 1.6 | 51 | 2.6 | 3.0 [2.0, 3.0] | 1.0 |
| | Non-Isolated | 91 | 3.1 | 3.0 [1.0, 4.0] | 1.7 | 91 | 2.7 | 3.0 [2.0, 3.0] | 1.4 |
| Partially | Isolated | 14 | 3.9 | 4.0 [2.3, 5.0] | 2.1 | 14 | 3.0 | 3.0 [3.0, 3.0] | 0.9 |
| Exposed | Non-Isolated | 98 | 4.1 | 4.0 [3.0, 5.0] | 2.1 | 98 | 3.2 | 3.0 [3.0, 3.0] | 1.3 |
| No Emission | Isolated | 186 | 5.8 | 5.0 [4.0, 8.0] | 2.5 | 201 | 5.1 | 5.0 [3.0, 6.0] | 2.2 |
| | Non-Isolated | 214 | 4.7 | 4.0 [3.0, 6.0] | 2.4 | 229 | 4.0 | 3.0 [3.0, 5.0] | 2.0 |
| H$\alpha$ Class | Isolated? | N | Mean **E(B-V)** | Median **E(B-V)** | SD | N | Mean **E(B-V)** | Median **E(B-V)** | SD |
| Concentrated | Isolated | 51 | 0.19 | 0.17 [0.08, 0.28] | 0.16 | 51 | 0.21 | 0.19 [0.08, 0.29] | 0.16 |
| | Non-Isolated | 91 | 0.18 | 0.13 [0.05, 0.26] | 0.15 | 91 | 0.17 | 0.14 [0.05, 0.27] | 0.14 |
| Partially | Isolated | 14 | 0.10 | 0.07 [0.01, 0.15] | 0.11 | 14 | 0.10 | 0.06 [0.01, 0.11] | 0.14 |
| Exposed | Non-Isolated | 98 | 0.08 | 0.05 [0.00, 0.11] | 0.13 | 98 | 0.09 | 0.04 [0.00, 0.10] | 0.19 |
| No Emission | Isolated | 186 | 0.20 | 0.14 [0.05, 0.25] | 0.22 | 201 | 0.17 | 0.13 [0.05, 0.23] | 0.18 |
| | Non-Isolated | 214 | 0.14 | 0.08 [0.02, 0.18] | 0.19 | 229 | 0.16 | 0.09 [0.03, 0.21] | 0.22 |
| H$\alpha$ Class | Isolated? | N | Mean **Mass**($M_\odot$) | Median **Mass** ($M_\odot$) | SD | N | Mean **Mass**($M_\odot$) | Median **Mass** ($M_\odot$) | SD |
| Concentrated | Isolated | 51 | 1.1 E3 | 9.0 E2 [4.0E2, 1.5E3] | 900 | 51 | 1.0 E3 | 7.0 E2 [4.0E2, 1.3E3] | 800 |
| | Non-Isolated | 91 | 2.4 E3 | 1.0 E3 [6.0E2, 2.1E3] | 5700 | 91 | 2.4 E3 | 9.0 E2 [5.0E2, 2.1E3] | 6200 |
| Partially | Isolated | 14 | 8.0 E2 | 6.0 E2 [5.0E2, 1.3E3] | 500 | 14 | 9.0 E2 | 4.0 E2 [3.0E2, 1.1E3] | 1500 |
| Exposed | Non-Isolated | 98 | 1.9 E3 | 1.0 E3 [5.0E2, 1.8E3] | 3000 | 98 | 2.0 E3 | 9.0 E2 [4.0E2, 1.6E3] | 4100 |
| No Emission | Isolated | 186 | 2.2 E3 | 1.0 E3 [6.0E2, 2.0E3] | 3900 | 201 | 1.4 E3 | 7.0 E2 [4.0E2, 1.5E3] | 2000 |
| | Non-Isolated | 214 | 2.5 E3 | 1.2 E3 [7.0E2, 2.0E3] | 5600 | 229 | 2.8 E3 | 1.0 E3 [6.0E2, 1.9E3] | 6300 |

Table 2.3: Mean and median age, reddening, and mass for the clusters aggregated over all six fields in each of the three morphology classes, isolation category, and stellar population model (Padova vs. Geneva). The standard deviations of each distribution is also provided.

each of the H$\alpha$ morphological classes based on our reference catalog; the left and right plots show the distributions for the 251 isolated clusters and the 403 non-isolated clusters, respectively.

For the isolated Padova-based cluster sample, we find that the median best age [first quartile, third quartile] of the 51 clusters with concentrated HII regions is 3.0 [2.0, 4.0] Myr, while the ages for the 14 partially exposed clusters and 186 clusters with no H$\alpha$ emission are 4.0 [2.3, 5.0] Myr and 5.0 [4.0, 8.0] Myr, respectively. The non-isolated clusters provide roughly consistent results, with median best ages of 3.0 [1.0, 4.0] Myr, 4.0 [3.0, 5.0] Myr, and 4.0 [3.0, 6.0] Myr for the 91 concentrated, 98 partially exposed, and 214 no-emission H$\alpha$ morphologies, respectively. It is also important to note here that the median ages determined for clusters with no H$\alpha$ emission represent lower limits, due to the initial selection which eliminated clusters with estimated ages older than 10 Myr. While the Padova model shows some differences in the median ages which could possibly indicate an age progression, the Geneva model shows fewer differences, with equal median ages for the concentrated and partially exposed classes in both the isolated and not-isolated samples (3.0 Myr). Regardless of isolation criteria or stellar population model, the mean age of each morphological class does indicate a progression from concentrated to partially exposed to no-emission H$\alpha$ morphologies as expected, though the age differences are small, and often less than the SED time step of 1 Myr. We compare the widths of these distributions to the individual age uncertainties at the end of this section.

To test whether the age distributions for the three H$\alpha$ morphological classes are significantly different, we perform Kolmogorov-Smirnov (KS) tests in order to determine the probability that each class of objects originates from the same parent distribution, with the results summarized

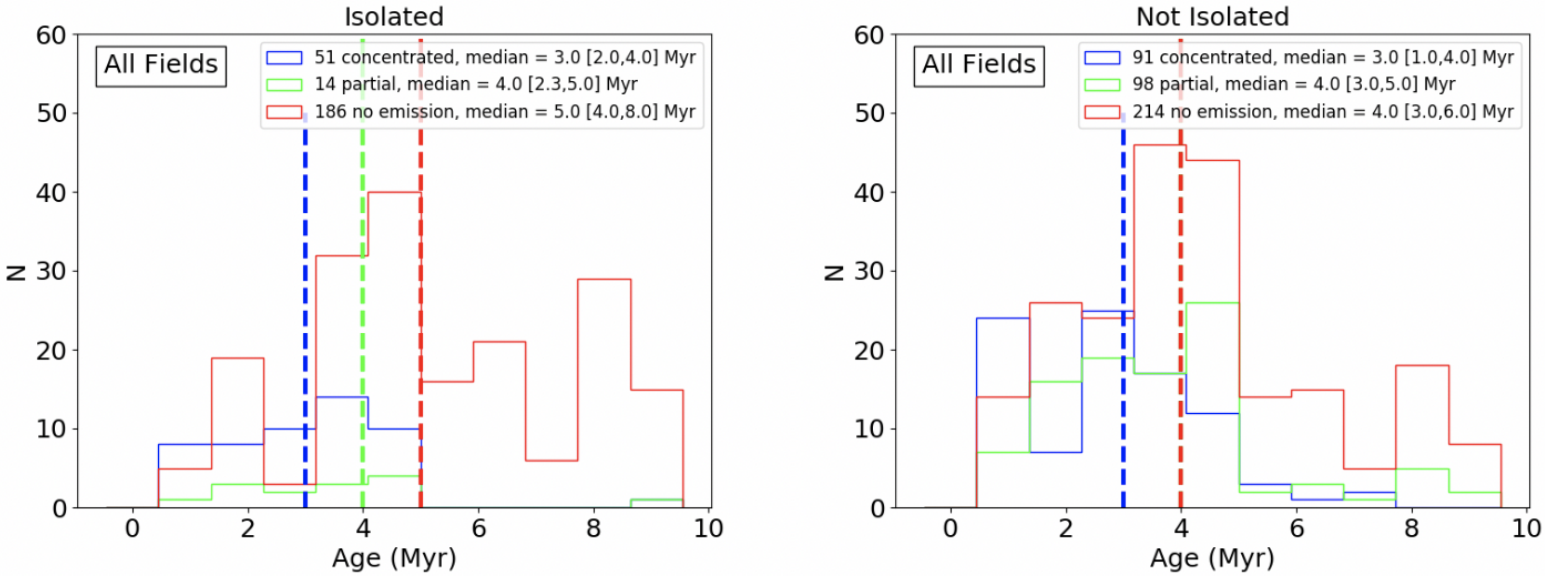


Figure 2.3: Histograms showing the age distribution of clusters across all the fields in the sample, using the Padova stellar evolutionary model. The left panel shows the 251 isolated clusters in the sample; the right panel shows the 403 clusters with neighboring clusters within 75 pc. The solid blue, green, and red lines represent clusters with H$\alpha$ emission that is concentrated, partially exposed, and absent (i.e., no emission), respectively. The number of clusters as well as the median cluster ages [first quartile, third quartile] for each of the three classes is displayed in the legend. Vertical dashed lines represent the medians for each class.

| | Isolated | | Not Isolated | | Total Sample | |
|---|---|---|---|---|---|---|
| H$\alpha$ Class | Padova | Geneva | Padova | Geneva | Padova | Geneva |
| 1 vs. 2 | 0.967 | 0.889 | 0.039 | 0.036 | 0.020 | 0.028 |
| 1 vs. 3 | $< p_{5\sigma}$ | $< p_{5\sigma}$ | $< p_{5\sigma}$ | 3.00E-04 | $< p_{5\sigma}$ | $< p_{5\sigma}$ |
| 2 vs. 3 | 0.024 | 1.00E-05 | 0.097 | 0.006 | 5.00E-05 | $< p_{5\sigma}$ |

Table 2.4: KS test results comparing the age distributions of each H$\alpha$ morphological class (1 = concentrated, 2 = partially exposed, 3 = no emission). p-values represent the corresponding probabilities that two samples share the same parent distribution; $p_{5\sigma}$ represents a p-value that corresponds to a confidence level greater than $5\sigma$.

in Table 3.4. We perform the test for both isolated and non-isolated cluster samples, as well as the two samples combined, to improve the overall number statistics.

Overall, when the cluster population is divided into isolated and non-isolated samples, we cannot reject the hypothesis that the age distributions for clusters with partially exposed H$\alpha$ morphologies have been drawn from the same parent sample as clusters with concentrated or absent H$\alpha$. As would be expected however, the clusters with no H$\alpha$ emission are found to be statistically different from those with concentrated H$\alpha$. When the isolated and non-isolated samples are combined to increase the sample sizes, the statistical differences between the age distributions of the concentrated and partially exposed classes versus the distribution for clusters without H$\alpha$ are significant at $\geq 3\sigma$ confidence, while the p-values remain at the $\sim 2\sigma$ confidence level between the age distributions for clusters with concentrated and partially exposed H$\alpha$ morphologies. These results hold regardless of the adopted stellar extinction model, except the confidence level drops to $\sim 1\sigma$ in distinguishing the distributions of clusters with concentrated and partially exposed H$\alpha$ morphologies when the starburst or differential-starburst extinction models are used.

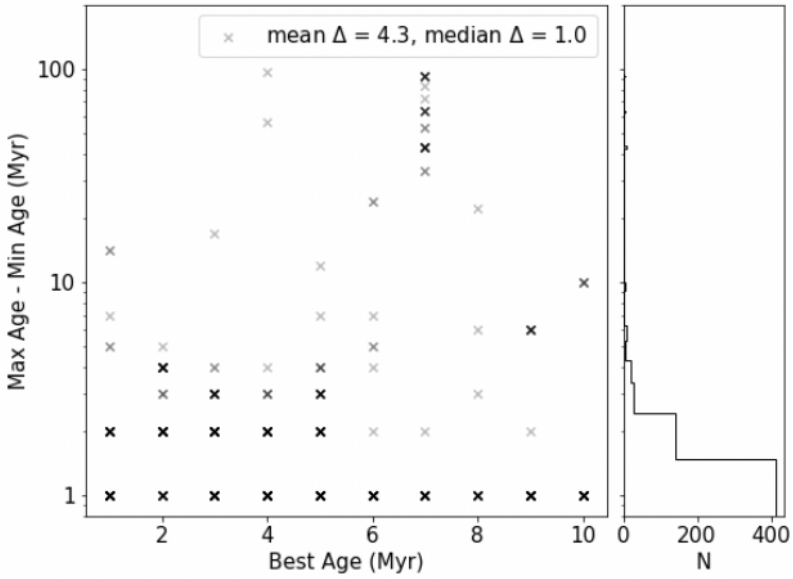


Figure 2.4: Distribution of SED errors in Padova-based cluster age for all 654 clusters, where the errors are the differences between each cluster's minimum and maximum age. Darkness represents a greater density of points.

To determine if the width of the distributions represent real variations in the cluster ages of each morphological class, we must compare the widths to the errors. Fig. 2.4 displays the errors in cluster age, which is shown as the difference between the maximum and minimum age, plotted against the best estimates. While we see the mean error is buoyed up to ~4 Myr due to extreme outliers, particularly due to the start of the red supergiant loop at 7 Myr in the SED models, the median error in age (1 Myr) is smaller than 10 of the 12 distributions' standard deviations, indicating that the errors are likely insufficient in describing the distribution widths. These results will be further discussed in Section 2.6.1.

### 2.4.2 Reddening Statistics by Morphological Class

The second parameter we examine is the reddening of the clusters in each morphological class, as a measure of dust in the region. Fig. 2.5 shows reddening histograms based on E(B-V) values derived from 5-band SED fitting for clusters across all six fields assuming Milky Way extinction [30], and divided into isolated (left) and non-isolated samples (right).

Interestingly, both isolated and non-isolated samples show that the clusters with partially exposed HII regions have the smallest median reddening, while the isolated concentrated and isolated no-emission H$\alpha$ morphologies have higher cluster reddening values. Regardless of the isolation category, stellar population model, extinction model, or using the mean or median values, we find consistent results.

Upon examination of the KS-test results of cluster reddening, the distributions are not found to be statistically different when the clusters are divided into isolated and non-isolated samples. After combining the samples, however, the KS tests show that all distributions are significantly different (>3$\sigma$) except for clusters with concentrated and no-emission H$\alpha$ morphologies, which are different at a $\sim$2$\sigma$ level, and these results are consistent across all stellar evolution and extinction models. The results of the KS tests are listed in Table 2.5.

Fig. 2.6 displays the error in cluster reddening, which is shown as the difference between the maximum and minimum reddening, plotted against the best estimates for each cluster. We find that both the mean error (0.08) and median error (0.06), are smaller than the standard deviation of every distribution (ranging from 0.11 to 0.22), regardless of isolation category or stellar population

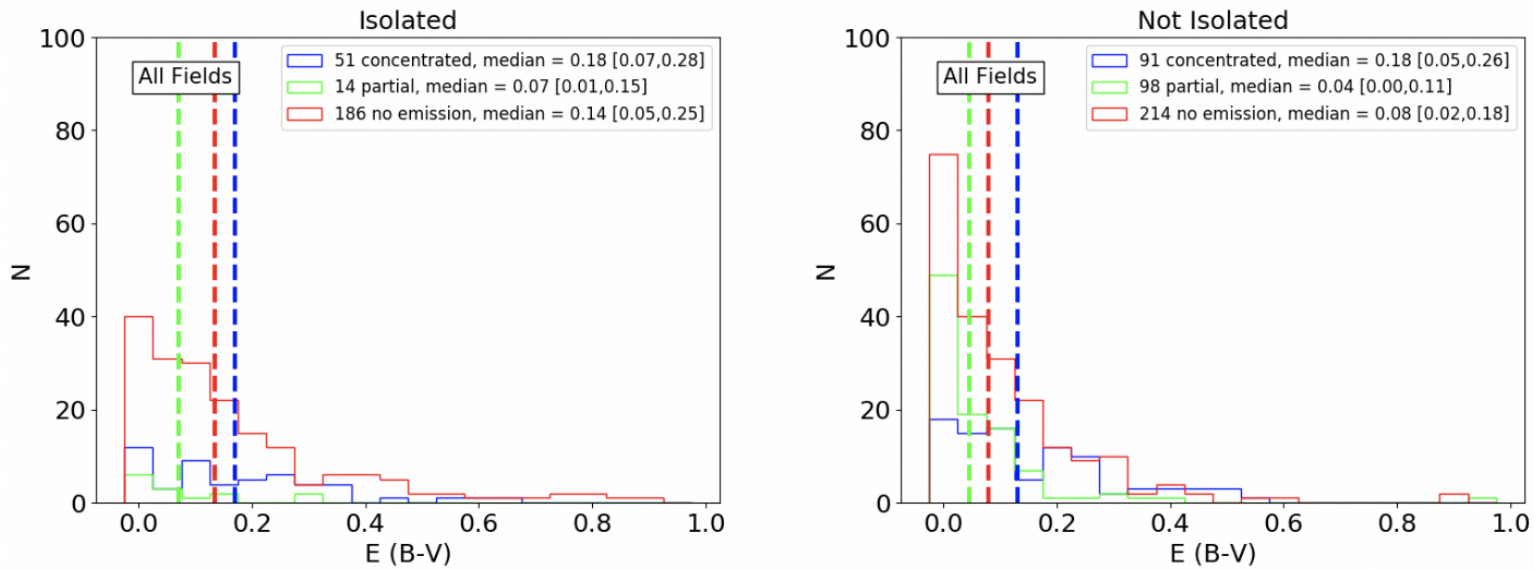


Figure 2.5: E(B-V) histograms for all clusters across all the fields in the sample, using the Padova stellar evolutionary model. The left plot shows the 251 isolated clusters in the sample while the right plot shows the 403 clusters with neighboring clusters within 75 pc. The solid blue, green, and red lines represent clusters with H$\alpha$ emission that is concentrated, partially exposed, and absent, respectively. The number of clusters as well as the median reddening [first quartile, third quartile] for each of the three classes is displayed in the legend. Vertical dashed lines represent the medians for each class.

| | Isolated | | Not Isolated | | Total Sample | |
|---|---|---|---|---|---|---|
| H$\alpha$ Class | Padova | Geneva | Padova | Geneva | Padova | Geneva |
| 1 vs. 2 | 0.107 | 0.006 | 7.00E-06 | 4.00E-06 | $< p_{5\sigma}$ | $< p_{5\sigma}$ |
| 1 vs. 3 | 0.665 | 0.092 | 0.016 | 0.089 | 0.016 | 0.021 |
| 2 vs. 3 | 0.290 | 0.014 | 0.013 | 0.002 | 9.00E-05 | 1.00E-06 |

Table 2.5: KS test results comparing the reddening distributions of each H$\alpha$ morphological class (1 = concentrated, 2 = partially exposed, 3 = no emission). p-values represent the corresponding probabilities that two samples share the same parent distribution.

model, again indicating that the error is insufficient in describing the width of the distributions. We will discuss these results in Section 2.6.3.

## 2.5 Stochasticity

Our sample is dominated by low mass clusters. The median mass of our entire cluster sample is 1100 $M_{\odot}$, with over 90% being less massive than 5000 $M_{\odot}$ (see also Table 3.3), the limit used by [72] to minimize the impacts of stochastic (i.e. random) sampling in their analysis of clusters in M83. At such masses, the initial mass function is not fully sampled and the relationship between physical and photometric properties is non-deterministic, which leads to a broad posterior probability distribution function (PDF) that is not well-characterized by a single best fit (e.g., [58, 87]). Here, we look for evidence of this stochasticity and explore methods to mitigate against its impact.

### 2.5.1 Color-Color Analysis

Color-color plots are useful tools in examining the quality of SED age estimates relative to a model as well as highlighting any potential outlier clusters. As examined by [59], the predicted

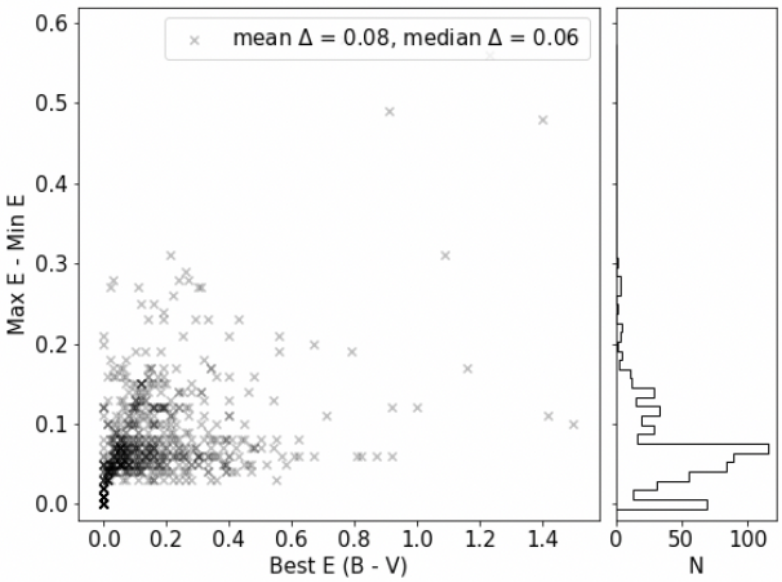


Figure 2.6: Distribution of errors in Padova-based cluster reddening for all 654 clusters, where the errors are the differences between each cluster's minimum and maximum reddening. Darkness represents a greater density of points.

optical fluxes of a Monte Carlo sample of star clusters are spread quite widely in color-color space, especially for clusters below $10^4$ $M_\odot$, where 96% of our sample lies. This is due to the fact that the integrated flux of such lower-mass clusters can be greatly influenced by the presence or absence of a few bright stars introduced by stochastic sampling of the IMF.

Fig. 2.7 shows observed (U-B) vs. (V-I) plots for all 654 young clusters across all six fields, split into isolated and non-isolated samples. There are a few notable features that are immediately apparent in these plots. As expected from the median age of each morphological class, we find clusters with no H$\alpha$ emission at the older end of the model predictions (red Xs), while the clusters with concentrated (blue circles) and partially exposed (green triangles) H$\alpha$ classes roughly overlap at the youngest end. In addition, while each class displays some spread in color space, we see that clusters with no H$\alpha$ emission have the largest degree of color spread. While the degree of spread

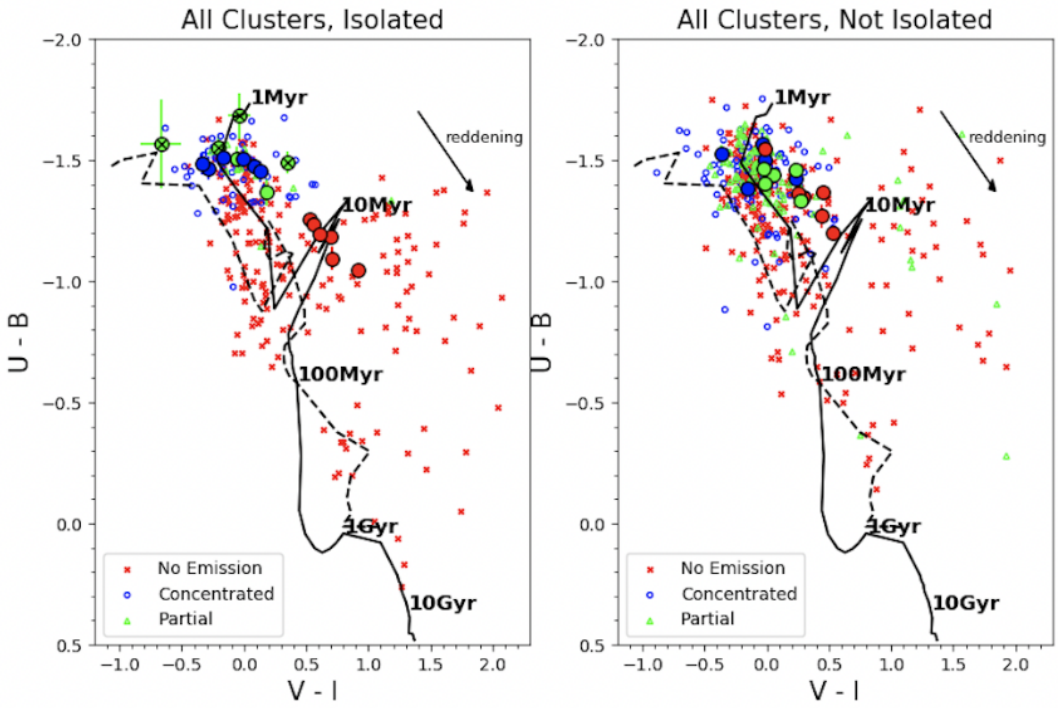


Figure 2.7: (U-B) vs. (V-I) diagrams for all 654 clusters across all six fields. U, B, V, and I represent the F336W, F435W (NGC 1313) or F438W (NGC 4395, NGC 7793), F555W, and F814W filters, respectively. The 251 isolated clusters are shown in the left plot while the 403 non-isolated clusters are plotted on the right. Z = 0.02 (solid line) and Z = 0.004 (dashed line) Yggdrasil model tracks are overplotted ([149]). Blue circles, green triangles, and red Xs represent clusters with H$\alpha$ morphologies classified as concentrated, partially exposed, and no-emission, respectively. An $A_V$ = 1.0 reddening vector is displayed in the upper-right corner of each plot. Large, black-outlined circular points represent the composite clusters from each field, provided here as an illustrative reference (see Section 2.5.3).

may be surprising given that the clusters were selected to be younger than 10 Myr, it is qualitatively similar to the spread found in the stochastic sampling model produced by [59, Figure 2].

### 2.5.2 Influence of Red Supergiants

The clusters in our sample without H$\alpha$ emission display a similar spread in (U-B) vs. (V-I) space to that observed by [59]. This prompts us to re-inspect the postage stamps of each cluster in

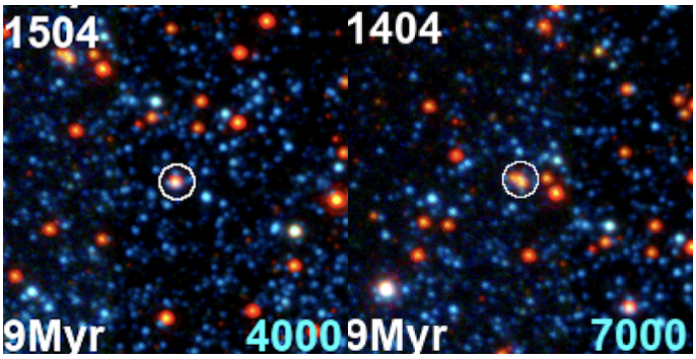


Figure 2.8: RGB images of isolated clusters with no H$\alpha$ emission which appears red in V-I due to the presence of one or more bright red sources within the aperture radius. These stamps have been modified to highlight the red sources (B = B, G = V, R = I) instead of (absent) H$\alpha$.

order to gain insight into the color-spread. Fig. 2.8 displays the postage stamps of two of the redder clusters with no H$\alpha$ emission.

We find that the flux from clusters without H$\alpha$ emission is significantly affected by the presence of bright red sources, which are presumably red supergiants. Of all the isolated clusters without H$\alpha$ emission, we find that each cluster located to the lower-right of the 10 Myr point on the model (V-I > 0.5, U-B < -0.5) was found to have at least one of these red sources within the photometric aperture. Overall, of all 400 clusters without H$\alpha$ emission in our sample, 134 (33%) contained one or more bright red point source.

Fig. 2.9 shows color-color diagrams for all clusters without H$\alpha$ emission in our sample. We see that those without a red source are much less spread out and have a loci much closer to the model track. Those with a red source display a large spread toward the reddest (V-I) colors, consistent with the expectation that the integrated flux of lower-mass clusters is greatly affected by the presence (or absence) of a few individual bright sources.

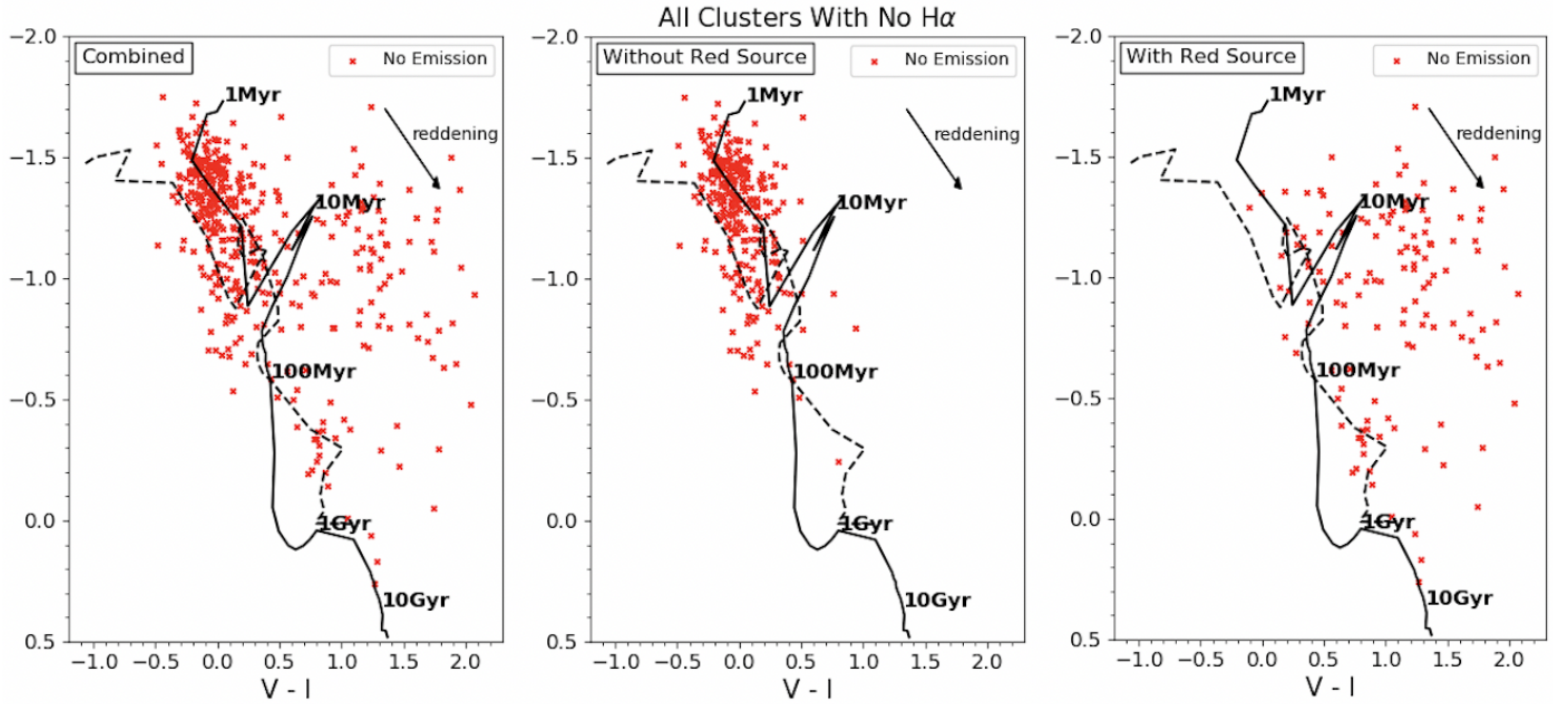


Figure 2.9: (U-B) vs. (V-I) diagrams for all clusters without H$\alpha$ emission across all six fields. The left plot displays all 400 clusters, the middle plot displays the 266 clusters containing no red source, and the right plot displays the 134 clusters containing a red source.

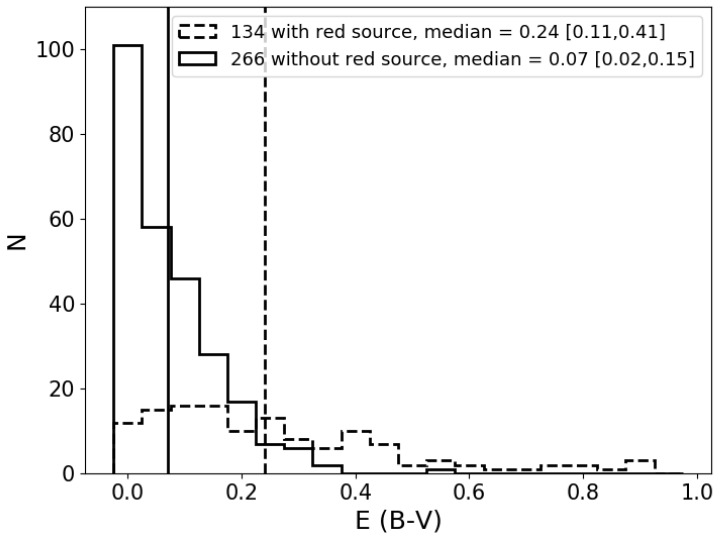


Figure 2.10: E(B-V) histograms of clusters without H$\alpha$ emission across all six fields. The dashed line represents the 134 clusters which were found to contain a red point source while the solid line represents the 266 clusters not found to contain a red source. The median reddening of each category is provided in the legend and is plotted with vertical lines.

We also find that these clusters containing one or more bright red source are correlated with higher cluster reddening. Fig. 2.10 shows the E(B-V) distributions based on our reference catalog for all 400 clusters without H$\alpha$ emission, separately displaying the samples with and without bright red sources. We find that the 134 clusters containing a red source have an apparent median reddening value (0.24) more than three times that of the 266 clusters without one (0.07) and over 30% greater than the median reddening value of isolated clusters with concentrated H$\alpha$ (~0.18). Analysis of clusters in NGC 4449 by Whitmore et al. (in prep.) similarly revealed a significant fraction of clusters whose red colors are due to the presence of a dominating red source.

Within the no H$\alpha$ emission class, applying a KS test to the reddening distributions of clusters with a red source versus clusters without a red source reveals a confidence level greater than $5\sigma$ that the two are not drawn from the same parent distribution.

### 2.5.3 Mitigating Stochastic Sampling Effects

The uncertainty in the determination of physical properties of low mass clusters due to stochastic sampling is a particular challenge for our study. To provide better constraints on cluster properties despite the low masses of our cluster sample, we examine two potential methods of minimizing stochastic sampling effects. First, we simply limit the analysis to clusters above the threshold mass used by [72], i.e. $\geq$ 5000 $M_{\odot}$. Fig. 2.11 shows color-color plots of all verified clusters with masses $\geq$ 5000 $M_{\odot}$, again divided by morphological class and isolation.

While simply selecting only clusters with masses $\geq$ 5000 $M_{\odot}$ results in a very small sample (13 isolated, 29 non-isolated clusters), the little data remaining is consistent with what we found for all clusters (Fig. 2.7), and still displays a significant spread in (U-B) vs. (V-I) space. Thus even when limiting to these higher mass clusters, stochasticity may still significantly impact the observed cluster properties: clusters with best fit ages $\leq$ 10 Myr can still be quite red and, in fact, all 13 of the isolated clusters above 5000 $M_{\odot}$ are amongst those found to contain one or more bright red source.

In our second strategy to address the impact of stochasticity, we stack the fluxes of all individual clusters according to their H$\alpha$ morphologies (i.e. isolated/non-isolated and concentrated/partially exposed/no-emission). Here we create thirty-six composite clusters - one for each morphological class, isolation type, and within each field (6 bins x 6 fields). We note that NGC 4395N does not have non-isolated clusters with concentrated or partially exposed H$\alpha$ morphologies,

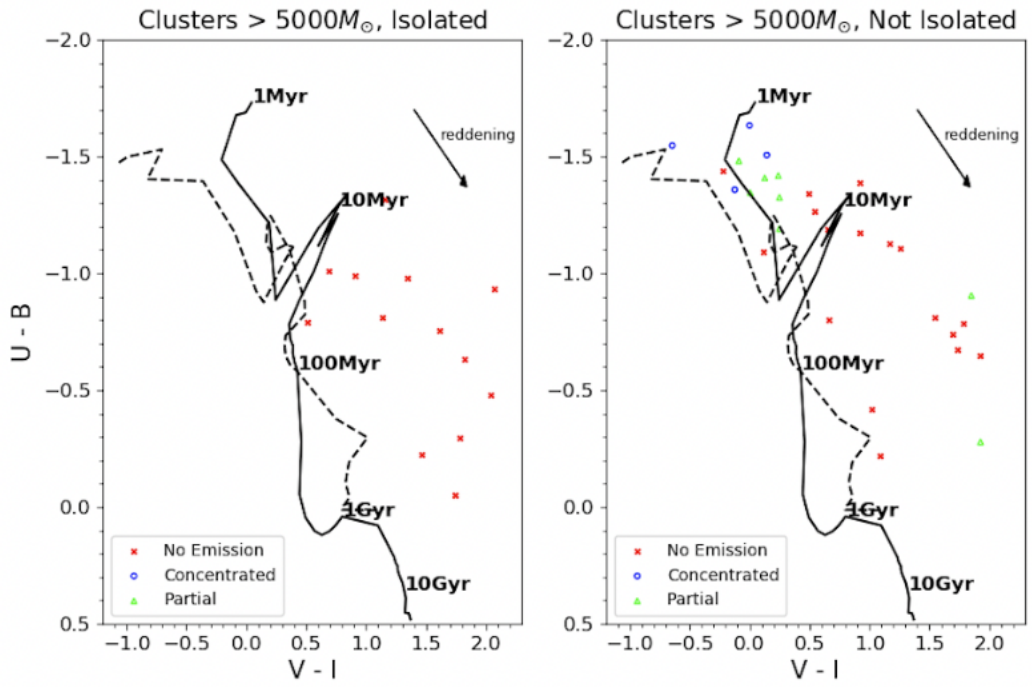


Figure 2.11: (U-B) vs. (V-I) diagrams for all 42 clusters above the stochastic limit across all six fields. The 13 isolated clusters greater than 5000 $M_\odot$ are plotted on the left and the 29 non-isolated clusters greater than 5000 $M_\odot$ are plotted on the right. Blue circles, green triangles, and red Xs represent clusters with H$\alpha$ morphologies classified as concentrated, partially exposed, and no-emission, respectively.

and three other bins contain only a single cluster (see Table 2.5.4) leaving us with 31 composite clusters. We sum the SED-determined masses of each of these composite clusters as an initial check on the composite mass. The summed masses range from 2.7x$10^3$ $M_\odot$ to 1.8x$10^5$ $M_\odot$ (see Table 2.5.4). For reference, 26 are above the 5000 $M_\odot$ limit used by Hollyhead et al. (2015).

Photometry for each of the NUV, U, B, V, and I bands are taken from the reference LEGUS catalog and converted into flux, utilizing the known zero points for each of the 8 *HST* filters: F = $10^{-0.4(m-m_z)}$, where $m_z$ is the zero-point magnitude. The cluster fluxes are summed in each of the 31 bins to produce the flux in the composite cluster. Photometric errors for composite clusters which are calculated by adding the constituent cluster errors in quadrature result in poor SED fitting. However, by using the median error for each composite cluster, the $\chi^2$ values for the SED fitting are comparable to the individual cluster $\chi^2$ values: the median $\chi^2$ is 2.1 and 1.4 for composite and individual clusters, respectively. The results of the fitting performed with the median errors are presented in Table 2.5.4 and provide the basis for our analysis.

We plot the stacked fluxes of these composite clusters in (U-B) vs. (V-I) space to examine their new positions relative to the model tracks (Fig. 2.12). Despite the significant percentage of individual clusters containing red sources (see Fig. 2.9 for their impact), the composite cluster sample is better behaved as they appear much closer to the model, likely due to the fact that stacking clusters diminishes the randomness in IMF sampling. The composite clusters with concentrated HII regions display some spread along the reddening vector while still being located at the youngest end of the model track. The composite isolated clusters without H$\alpha$ emission are located much closer to the model relative to their individual constituents, also displaying a much tighter locus found at the older end of the model, near the 10 Myr point. While the composite non-isolated clusters without H$\alpha$ also

display a tighter locus than their constituent clusters, they generally appear closer to the younger end of the model than the isolated sample. The clusters with partially exposed morphologies suffer the most from small-number statistics, but ignoring the composite clusters which were made up of so few clusters that their aggregate masses remained well below the $M_{\odot}$ threshold, the rest still roughly overlap with clusters with concentrated H$\alpha$, if not lie between the other two classes.

Whether or not we include the few clusters above 5000 $M_{\odot}$ as part of these composite clusters did not significantly affect our overall conclusions. In (U-B) vs. (V-I) space, Fig. 2.12 displays composite clusters which include all individual clusters (Fig. 2.12, left panels) with composite clusters which exclude the 42 individual clusters above 5000 $M_{\odot}$ (Fig. 2.12, right panels). In this comparison, we find no significant color change in the concentrated and partially exposed H$\alpha$ classes. The greatest difference is in the clusters with no H$\alpha$ emission, where the lower-mass composite clusters appear slightly less red than their more-massive counterparts. Regardless of the inclusion of individual clusters above 5000 $M_{\odot}$, the evolutionary pattern remains consistent.

### 2.5.4 Measurement of the Physical Parameters for Composite Clusters

We use SED fitting to calculate the age, mass, and reddening of each of our 31 composite clusters using the same method used to produce the physical cluster properties for the LEGUS catalogs [2]. The results of the SED fitting are shown for all 31 composite clusters in Table 2.5.4, where the number of clusters making up each composite is also provided. Median age and reddening values are reported with their first and third quartiles while summed SED mass errors are calculated by adding all individual errors in quadrature. Errors in composite SED age, reddening, and mass each represent their individual SED error.

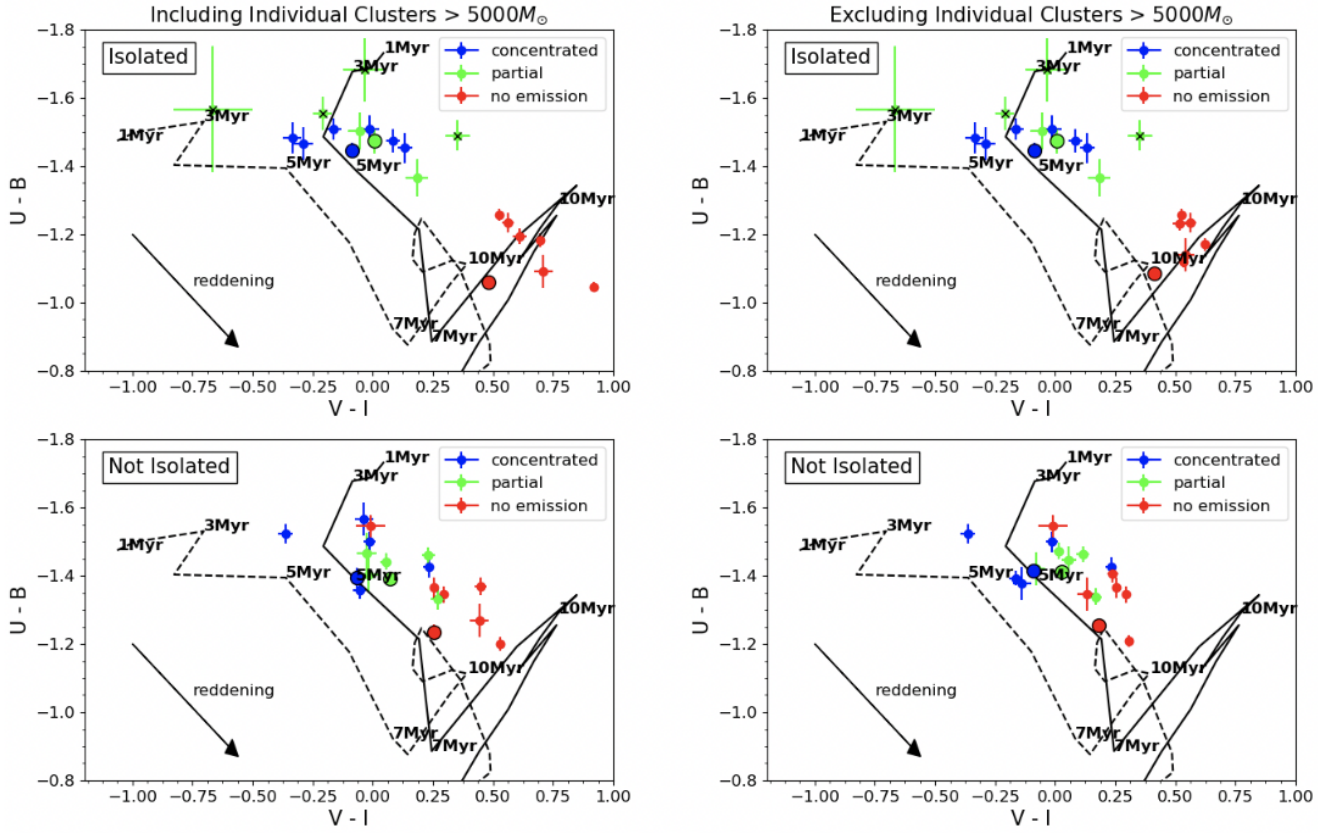


Figure 2.12: (U-B) vs. (V-I) diagrams for all 31 composite clusters. The left and right columns display composite clusters, respectively, including and excluding individual clusters above 5000 $M_\odot$. The top row shows the 18 isolated composite clusters and the bottom row shows the 16 non-isolated composite clusters. Blue, green, and red points represent composite clusters with HII regions that are concentrated, partially exposed, and absent, respectively. Error bars represent the constituent cluster errors added in quadrature. The four composite clusters which have aggregate masses well below the 5000 $M_\odot$ limit are marked with a black X. The larger, black-outlined circles are provided for reference and represent the unweighted mean position of each morphological class across all six fields. It is important to note that these mean positions are not exact, as the V-band for NGC 4395 and NGC 7793 is covered by F438W, while NGC 1313 uses F435W.

In examining the ages of the composite clusters, we first find a progression consistent with the analysis of the individual clusters: on average, the concentrated class comprises the youngest composite clusters (3.7 Myr isolated; 2.0 Myr non-isolated), the class without H$\alpha$ emission is the oldest (12.2 Myr isolated; 6.2 Myr non-isolated), and the partially exposed class lies between the two (6.3 Myr isolated; 4.6 Myr non-isolated), but the few data points we have overall show small differences between clusters with concentrated and partially exposed morphologies. It is also notable that 5 of the 6 composite clusters without H$\alpha$ emission have ages between 10 and 20 Myr, despite being comprised of *apparently* young ($\leq$ 10 Myr) clusters. While the SED-fitting of composite clusters assumes a single stellar population age, we are in fact stacking clusters with a range of ages, particularly for the no-emission class. Regardless of this fact, we see an older age for composite isolated clusters without H$\alpha$ than the apparent median age of their constituents.

| | Isolated, Concentrated | | | Non-isolated, Concentrated | | |
|---|---|---|---|---|---|---|
| Field | Number of Clusters | Median SED **Age** [25%, 75%] (Myr) | Composite SED **Age** ± Error (Myr) | Number of Clusters | Median SED **Age** [25%, 75%] (Myr) | Composite SED **Age** ± Error (Myr) |
| NGC1313W | 5 | 3.0 [3.0, 4.0] | 4.0 ± 0.5 | 25 | 3.5 [3.0, 4.0] | 3.0 ± 0.5 |
| NGC1313E | 10 | 4.0 [4.0, 4.0] | 4.0 ± 0.5 | 15 | 4.0 [2.0, 4.0] | 1.0 ± 1.0 |
| NGC4395N | 6 | 5.0 [3.5, 5.0] | 5.0 ± 0.5 | 0 | - | - |
| NGC4395S | 9 | 5.0 [3.0, 5.0] | 5.0 ± 0.5 | 16 | 3.0 [3.0, 5.0] | 3.0 ± 0.5 |
| NGC7793W | 10 | 3.0 [1.3, 4.0] | 2.0 ± 1.0 | 20 | 3.0 [2.0, 3.0] | 2.0 ± 0.5 |
| NGC7793E | 11 | 2.0 [1.0, 2.0] | 2.0 ± 0.5 | 15 | 1.0 [1.0, 2.0] | 1.0 ± 0.5 |
| | **Isolated, Partially Exposed** | | | **Non-isolated, Partially Exposed** | | |
| Field | Number of Clusters | Median SED **Age** [25%, 75%] (Myr) | Composite SED **Age** ± Error (Myr) | Number of Clusters | Median SED **Age** [25%, 75%] (Myr) | Composite SED **Age** ± Error (Myr) |
| NGC1313W | 1 | - | - | 20 | 4.5 [3.8, 7.0] | 1.0 ± 0.5 |
| NGC1313E | 1 | - | - | 25 | 4.0 [3.0, 4.0] | 3.0 ± 0.5 |
| NGC4395N | 1 | - | - | 0 | - | - |
| NGC4395S | 4 | 5.0 [5.0, 6.3] | 15.0 ± 0.5 | 23 | 5.0 [5.0, 5.0] | 15.0 ± 0.5 |
| NGC7793W | 3 | 2.0 [2.0, 3.0] | 2.0 ± 0.5 | 19 | 3.0 [2.0, 3.0] | 2.0 ± 0.5 |
| NGC7793E | 4 | 2.5 [1.8, 3.3] | 2.0 ± 0.5 | 11 | 2.0 [2.0, 3.0] | 2.0 ± 0.5 |
| | **Isolated, No Ha Emission** | | | **Non-isolated, No Ha Emission** | | |
| Field | Number of Clusters | Median SED **Age** [25%, 75%] (Myr) | Composite SED **Age** ± Error (Myr) | Number of Clusters | Median SED **Age** [25%, 75%] (Myr) | Composite SED **Age** ± Error (Myr) |
| NGC1313W | 39 | 5.0 [4.0, 8.0] | 15.0 ± 0.5 | 87 | 4.0 [3.0, 7.0] | 13.0 ± 0.5 |
| NGC1313E | 29 | 6.0 [4.0, 7.0] | 12.0 ± 0.5 | 31 | 4.0 [3.0, 4.0] | 1.0 ± 0.5 |
| NGC4395N | 14 | 8.5 [5.3, 10.0] | 10.0 ± 0.5 | 2 | 5.0 [5.0, 5.0] | 5.0 ± 0.5 |
| NGC4395S | 20 | 6.0 [5.0, 10.0] | 10.0 ± 0.5 | 40 | 5.0 [5.0, 6.0] | 15.0 ± 0.5 |
| NGC7793W | 37 | 5.0 [2.0, 6.0] | 6.0 ± 0.5 | 30 | 3.0 [3.0, 5.0] | 2.0 ± 0.5 |
| NGC7793E | 47 | 5.0 [4.0, 8.0] | 20.0 ± 3.5 | 24 | 4.0 [2.0, 4.3] | 1.0 ± 0.5 |

| | Isolated, Concentrated | | | Non-isolated, Concentrated | | |
|---|---|---|---|---|---|---|
| Field | Number of Clusters | Median SED **E(B-V)** [25%, 75%] | Composite SED **E(B-V)** ± Error | Number of Clusters | Median SED **E(B-V)** [25%, 75%] | Composite SED **E(B-V)** ± Error |
| NGC1313W | 5 | 0.26 [0.11, 0.30] | 0.15 ± 0.01 | 25 | 0.13 [0.09, 0.27] | 0.23 ± 0.01 |
| NGC1313E | 10 | 0.22 [0.17, 0.26] | 0.10 ± 0.01 | 15 | 0.22 [0.16, 0.30] | 0.12 ± 0.03 |
| NGC4395N | 6 | 0.05 [0.02, 0.15] | 0.13 ± 0.01 | 0 | - | - |
| NGC4395S | 9 | 0.01 [0.00, 0.08] | 0.06 ± 0.01 | 16 | 0.03 [0.00, 0.15] | 0.02 ± 0.01 |
| NGC7793W | 10 | 0.28 [0.13, 0.38] | 0.26 ± 0.02 | 20 | 0.11 [0.05, 0.17] | 0.11 ± 0.01 |
| NGC7793E | 11 | 0.20 [0.12, 0.37] | 0.22 ± 0.02 | 15 | 0.20 [0.10, 0.42] | 0.22 ± 0.01 |
| | **Isolated, Partially Exposed** | | | **Non-isolated, Partially Exposed** | | |
| Field | Number of Clusters | Median SED **E(B-V)** [25%, 75%] | Composite SED **E(B-V)** ± Error | Number of Clusters | Median SED **E(B-V)** [25%, 75%] | Composite SED **E(B-V)** ± Error |
| NGC1313W | 1 | - | - | 20 | 0.06 [0.03, 0.12] | 0.16 ± 0.02 |
| NGC1313E | 1 | - | - | 25 | 0.09 [0.03, 0.13] | 0.13 ± 0.01 |
| NGC4395N | 1 | - | - | 0 | - | - |
| NGC4395S | 4 | 0.00 [0.00, 0.04] | 0.00 ± 0.01 | 23 | 0.00 [0.00, 0.00] | 0.00 ± 0.01 |
| NGC7793W | 3 | 0.06 [0.04, 0.07] | 0.07 ± 0.01 | 19 | 0.07 [0.00, 0.14] | 0.13 ± 0.01 |
| NGC7793E | 4 | 0.14 [0.11, 0.22] | 0.18 ± 0.02 | 11 | 0.06 [0.03, 0.13] | 0.08 ± 0.02 |
| | **Isolated, No H$\alpha$ Emission** | | | **Non-isolated, No H$\alpha$ Emission** | | |
| Field | Number of Clusters | Median SED **E(B-V)** [25%, 75%] | Composite SED **E(B-V)** ± Error | Number of Clusters | Median SED **E(B-V)** [25%, 75%] | Composite SED **E(B-V)** ± Error |
| NGC1313W | 39 | 0.26 [0.13, 0.46] | 0.13 ± 0.01 | 87 | 0.14 [0.05, 0.21] | 0.00 ± 0.01 |
| NGC1313E | 29 | 0.18 [0.08, 0.33] | 0.06 ± 0.01 | 31 | 0.08 [0.04, 0.19] | 0.27 ± 0.01 |
| NGC4395N | 14 | 0.08 [0.04, 0.14] | 0.00 ± 0.01 | 2 | 0.01 [0.01, 0.02] | 0.00 ± 0.01 |
| NGC4395S | 20 | 0.01 [0.00, 0.06] | 0.00 ± 0.01 | 40 | 0.00 [0.00, 0.06] | 0.00 ± 0.01 |
| NGC7793W | 37 | 0.10 [0.05, 0.17] | 0.05 ± 0.01 | 30 | 0.10 [0.06, 0.14] | 0.21 ± 0.01 |
| NGC7793E | 47 | 0.13 [0.05, 0.22] | 0.00 ± 0.01 | 24 | 0.07 [0.04, 0.19] | 0.16 ± 0.01 |

| | **Isolated, Concentrated** | | | **Non-isolated, Concentrated** | | |
|---|---|---|---|---|---|---|
| Field | Number of Clusters | Summed SED **Mass** ± Error | Composite SED **Mass** ± Error | Number of Clusters | Summed SED **Mass** ± Error | Composite SED **Mass** ± Error |
| NGC1313W | 5 | 7.6 ± .4 E3 | 9.6 ± .3 E3 | 25 | 7.5 ± .3 E4 | 5.1 ± .1 E4 |
| NGC1313E | 10 | 1.2 ± .1 E4 | 1.0 ± .1 E4 | 15 | 1.0 ± .1 E5 | 7.7 ± 2.1 E4 |
| NGC4395N | 6 | 3.8 ± .3 E3 | 4.8 ± .2 E3 | 0 | - | - |
| NGC4395S | 9 | 3.9 ± .1 E3 | 4.1 ± .1 E3 | 16 | 8.0 ± .3 E3 | 6.0 ± .5 E3 |
| NGC7793W | 10 | 1.1 ± .1 E4 | 7.2 ± .1 E3 | 20 | 1.6 ± .1 E4 | 1.8 ± .2 E4 |
| NGC7793E | 11 | 1.9 ± .2 E4 | 1.7 ± .2 E4 | 15 | 2.5 ± .2 E4 | 2.2 ± .4 E4 |
| | **Isolated, Partially Exposed** | | | **Non-isolated, Partially Exposed** | | |
| Field | Number of Clusters | Summed SED **Mass** ± Error | Composite SED **Mass** ± Error | Number of Clusters | Summed SED **Mass** ± Error | Composite SED **Mass** ± Error |
| NGC1313W | 1 | - | - | 20 | 6.0 ± .4 E4 | 7.2 ± .7 E4 |
| NGC1313E | 1 | - | - | 25 | 5.2 ± .3 E4 | 4.6 ± .1 E4 |
| NGC4395N | 1 | - | - | 0 | - | - |
| NGC4395S | 4 | 2.7 ± .3 E3 | 5.7 ± .1 E3 | 23 | 2.6 ± .1 E4 | 7.0 ± .1 E4 |
| NGC7793W | 3 | 5.1 ± .1 E3 | 8.3 ± .3 E3 | 19 | 2.3 ± .1 E4 | 2.6 ± .1 E4 |
| NGC7793E | 4 | 4.8 ± .4 E3 | 4.4 ± .2 E3 | 11 | 2.6 ± .4 E4 | 3.0 ± .4 E4 |
| | **Isolated, No H$\alpha$ Emission** | | | Non-isolated, No H$\alpha$ Emission | | |
| Field | Number of Clusters | Summed SED **Mass** ± Error | Composite SED **Mass** ± Error | Number of Clusters | Summed SED **Mass** ± Error | Composite SED **Mass** ± Error |
| NGC1313W | 39 | 1.8 ± .2 E5 | 1.6 ± .1 E5 | 87 | 2.6 ± .2 E5 | 2.4 ± .1 E5 |
| NGC1313E | 29 | 8.8 ± 1.8 E4 | 9.5 ± .2 E4 | 31 | 1.1 ± .3 E5 | 1.4 ± .1 E5 |
| NGC4395N | 14 | 2.1 ± .1 E4 | 1.7 ± .1 E4 | 2 | 3.8 ± .3 E3 | 3.7 ± .1 E3 |
| NGC4395S | 20 | 3.4 ± .2 E4 | 3.4 ± .1 E4 | 40 | 1.0 ± .1 E5 | 1.6 ± .1 E5 |
| NGC7793W | 37 | 3.0 ± .6 E4 | 1.1 ± .1 E4 | 30 | 3.2 ± .4 E4 | 6.1 ± .1 E4 |
| NGC7793E | 47 | 5.9 ± .4 E4 | 7.3 ± 2.2 E4 | 24 | 2.8 ± .1 E4 | 3.8 ± .1 E4 |

Table 2.6: SED fitting results of all 31 composite clusters, separated into age results (top three tables), reddening results (middle three tabels), and mass results (bottom three tables). For each of the three metrics, the top table lists the twelve composite clusters with concentrated morphology, the middle table lists the twelve composite clusters with partially exposed morphology, and the bottom table lists the twelve composite clusters with no emission, each divided into isolated and non-isolated categories. The median age, median reddening, and sum total mass of individual clusters in each of the 31 composite clusters is provided adjacent to the corresponding composite SED result.

Fig. 2.13 shows plots comparing the SED-fit age, reddening, and mass of the composite clusters with the mean age, reddening, and mass of their constituent clusters. We find the masses determined from SED fitting for the composite clusters correlate well with their aggregate masses across all fields, classes, and isolation. There also seems to be a correlation between the age of composite isolated clusters versus the median values of their constituents for those with H$\alpha$ (concentrated and partially exposed classes), and we find similar agreement in those classes for reddening as well, albeit with wide distributions. Where we see the greatest discrepancy in cluster properties is in the ages and reddenings of clusters classified as no-emission. For the isolated sample, the mean and median ages of all individual clusters with no H$\alpha$ are $\sim$5 Myr, while the mean and median ages of the composite isolated clusters with no emission are $\sim$12 Myr, and all composite isolated clusters have best ages $\geq$ the mean or median age of their constituent clusters. Correspondingly, the median reddening of isolated clusters drops significantly from 0.14 for the constituent clusters to $\sim$0.03 for the composite clusters, and all isolated composite clusters have less reddening than the median of their constituents.

The non-isolated sample of composite clusters without H$\alpha$, however, shows mixed results. While two of the composite clusters have significantly older ages and smaller reddening than the median values of their constituent clusters, as is the case for the isolated sample, three composite clusters show the opposite result, namely that they have younger ages ($\lesssim$ 2x; all 1-2 Myr) and correspondingly larger reddening (>2x) than the medians of their constituents. This is puzzling because, although they do appear closer to the younger end of the model than the isolated sample in (U-B) vs. (V-I) space (Fig.2.12), the reddening vector would not appear to trace them back to

the 1Myr point in the model but rather $\gtrsim$ 3Myr. The implications of these results will be further discussed in Section 2.6.1.

## 2.6 Discussion

### 2.6.1 H$\alpha$ Morphology Evolution and Timescales

Examination of the age distributions of the individual star clusters as a function of H$\alpha$ morphological class (Section 3.4.1) shows that although the distributions are broad and overlap each other, the mean and median ages provide evidence for a temporal progression in H$\alpha$ morphology. The star clusters with concentrated H$\alpha$ have the youngest average ages ($\sim$3 Myr), those with partially exposed morphology are older ($\sim$4 Myr), and those with no H$\alpha$ emission are the most evolved (>5Myr). Consistent results are found when the sample is divided into clusters that are isolated, and those that have a neighbor (within 75 pc).

When KS tests are performed on isolated and non-isolated cluster sub-samples separately, we find that the null hypothesis that the age distributions for the clusters with concentrated and partially exposed H$\alpha$ morphologies are drawn from the same parent sample cannot be rejected with high certainty ($\sim 2\sigma$), and the same is true for clusters without H$\alpha$ and those with partially exposed H$\alpha$ morphologies. When the samples are combined, however, KS tests reveal greater confidence levels in the uniqueness of all distributions, and while the confidence level is only just above $2\sigma$ for the distributions of clusters with concentrated and partially exposed H$\alpha$ morphologies, which indicates a short clearing timescale ($\lesssim$ 1 Myr), each of the other distributions are found to be statistically different ($>3\sigma$). This is primarily a consequence of the decreased sizes of the subsamples

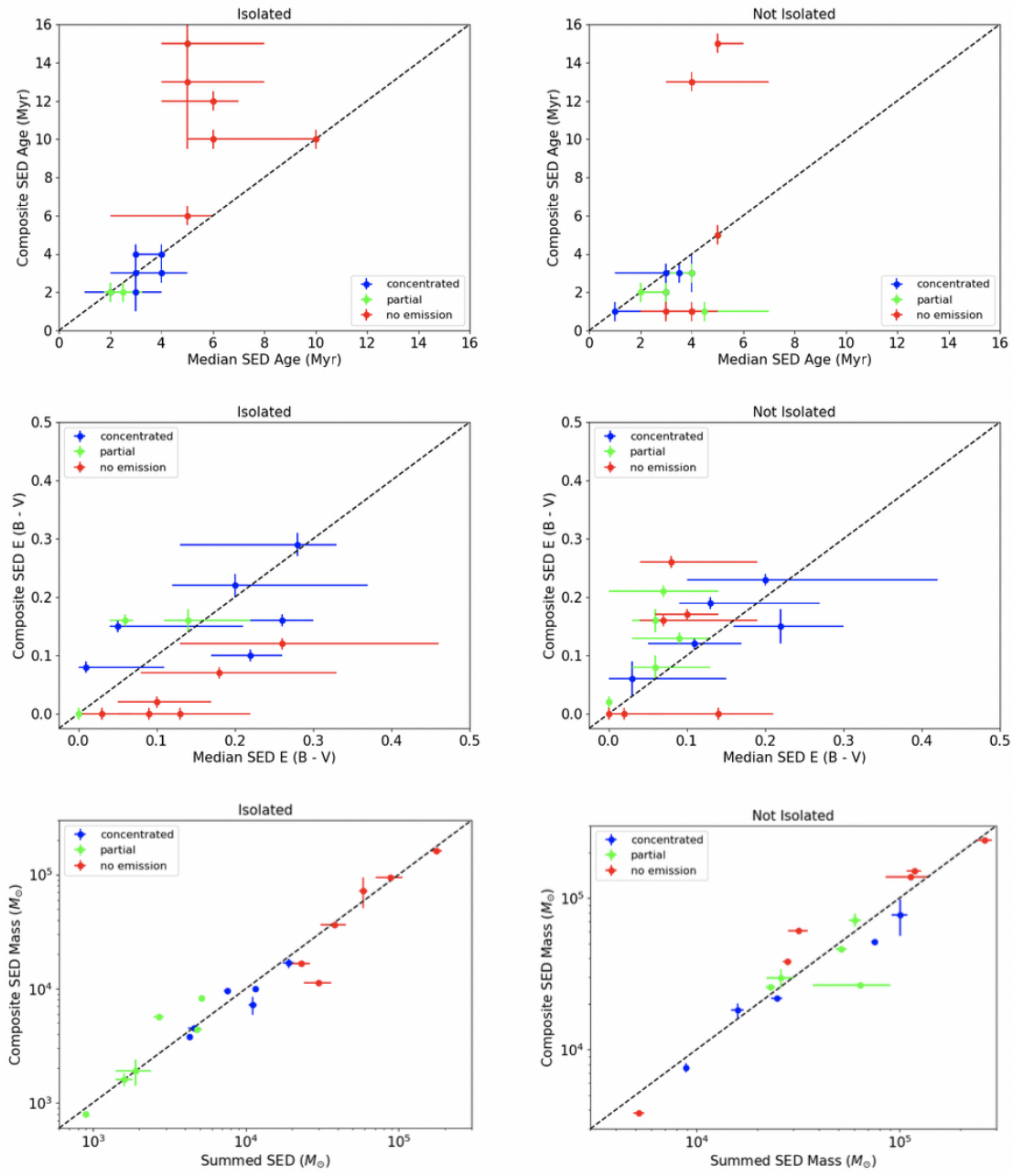


Figure 2.13: Cluster age, reddening, and mass plots comparing the composite cluster SED results with the median constituent cluster SED values. Blue, green, and red points represent concentrated, partially exposed, and no-emission H$\alpha$ morphologies, respectively. Top row: SED age of composite clusters vs. Median SED age of their constituents. Middle row: SED reddening of composite clusters vs. Median SED reddening of their constituents. Bottom row: SED mass of composite clusters vs. Summed SED mass of their constituents. The left and right columns display the isolated and non-isolated samples, respectively. Horizontal error bars for age and reddening represent the 25% and 75% quartile values for constituent clusters; horizontal errors for mass depict the standard deviation in the distribution. Vertical error bars represent the SED error for the composite cluster.

(Table 3.2). Hence, the overall sample size must be increased to properly study the possible impact of nearby neighbors on HII region morphologies and gas clearing timescales.

Nevertheless, the age distributions for each of the H$\alpha$ morphological classes are wider than the formal uncertainties alone would allow. This likely indicates that H$\alpha$ morphology (and the gas removal process) depends on multiple parameters beyond the age of the parent star cluster, (e.g. nearby neighbors/local star formation density; dependence on metallicity; confining pressure of the ISM).

The age progression results just discussed are model dependent, and are based on the Padova models adopted for the LEGUS "reference" catalogs of star cluster properties, and using the Milky Way extinction model [2]. When ages are instead derived from SED fitting to Geneva models or alternate extinction models (i.e. starburst, differential-starburst), the age distributions of the clusters with concentrated and partially exposed H$\alpha$ morphologies have consistent means and medians (~3-3.5 Myr). KS tests confirm that the null hypothesis that these ages have been drawn from the same parent sample cannot be rejected with high certainty ($\lesssim 2\sigma$). Of course, the statistical differences between the age distributions for those clusters with H$\alpha$ emission (whether concentrated or partially exposed) and those with no H$\alpha$ emission remain significant.

Independent of the age distributions for each of the H$\alpha$ morphological classes, we can infer the lifetimes of the classes by examining their relative fractions, assuming that our sample is statistically representative of all clusters $\leq$ 10 Myr. As shown in Table 3.5, we see that the time a cluster spends in the concentrated H$\alpha$ stage is ~2 Myr for the total sample as well as for the isolated and non-isolated sub-samples. While there are greater discrepancies between the isolated and non-isolated samples for the partially exposed class, we can infer a range of timescales, ~0.5-2.5

| | Isolated | | Non-Isolated | | Combined | |
|---|---|---|---|---|---|---|
| H$\alpha$ Class | % | Length of Stage | % | Length of Stage | % | Length of Stage |
| Concentrated | 20.5 | 2.1 Myr | 22.5 | 2.3 Myr | 21.7 | 2.2 Myr |
| Partially Exposed | 5.5 | 0.6 Myr | 24.7 | 2.5 Myr | 17.3 | 1.7 Myr |
| No-Emission | 74 | 7.4 Myr | 52.8 | 5.3 Myr | 61 | 6.1 Myr |

Table 2.7: Relative fractions of, and inferred length of time spent in, each morphological class for the 251 isolated clusters, 403 non-isolated clusters, and the entire 654 cluster sample.

Myr, for this stage. This could be due to a number of environmental factors and perhaps is worthy of future investigation. The "length of time" spent in the no-emission class is then simply the remaining time left in the cluster's first 10 Myr, not the total length of time spent without H$\alpha$ emission. For the total sample, the implied average ages for the clusters with concentrated H$\alpha$ and partially exposed morphologies are ~1 Myr and ~3 Myr, which are somewhat lower than the averages determined from analysis of the age distribution.

The characteristic ages of the H$\alpha$ morphological classes measured from SED fitting of the composite clusters (Table 2.5.4) yields a picture which is generally consistent with the analysis of the age distributions of the individual clusters, and the lifetimes inferred from the relative fractions of clusters in each class. The composite clusters with concentrated H$\alpha$ morphologies show the youngest average ages (~3 Myr) and those where the cluster is partially exposed have slightly older ages (~5 Myr). For the composites constructed from the isolated clusters with no H$\alpha$ emission, the ages are between 6 and 20 Myrs. Interpretation of the non-isolated composite clusters without H$\alpha$ emission is less straightforward. The positions of the non-isolated composite clusters on a color-color diagram (Fig. 2.12, bottom panels) show that those without H$\alpha$ emission are generally redder (and presumably older) than the composites with concentrated or partially exposed H$\alpha$ morphologies.

Yet, three of these composites have SED fit ages of 1-2 Myr, while the other three have ages between 5 and 15 Myr. More work is needed to understand why the SED-fit ages for these composites are so low. If the low ages are robust, a speculation is that this might be due to the confounding effects cluster neighbors have on gas clearing (i.e., clusters that are young and still have ionizing OB stars may have had their gas pushed away by other nearby stellar populations).

Taken altogether, this analysis suggests that gas clearing begins early ($\lesssim$ 3 Myr) and occurs quickly ($\lesssim$ 1 Myr). Such timescales provide evidence that young star clusters begin clearing their gaseous surroundings prior to the onset of the first SNe, due to radiation pressure and winds from their massive stars. These findings are consistent with a range of previous results.

In a similar analysis with HST H$\alpha$ images for 91 clusters in M83, [72] study found that clusters initially begin to remove gas at an age of ~2Myr, and also found that the median cluster ages of their equivalent concentrated, partially exposed, and no-emission H$\alpha$ morphologies to be ~4Myr, ~5Myr, and ~6Myr, respectively.

[67]'s study of the LEGUS galaxy NGC 7793 examines clearing timescales by associating star clusters with their nearest GMC based on ALMA CO data. They determine the clearing timescale by tracking how the distribution in the age of the cluster populations changes as a function of their distance from the center of every GMC, and thus determine that clusters dissociate from their GMCs at ages of 2-3 Myr.

[86] applied a statistical method to the combined observations of molecular gas and H$\alpha$ emission from young star clusters in NGC300, and subsequently applied the method to 9 other nearby spiral galaxies in Chevance et al. (in prep.), in order to characterize the correlation between GMCs and star formation. For NGC300, they found that GMCs and HII regions coexist on average

for 1.5 ± 0.2 Myr while the larger sample showed coexistence timescales between 1-5Myr, both of which support the conclusion that feedback prior to the onset of supernovae, such as stellar winds and radiation pressure, plays an important role in the dispersal of a star cluster's natal cloud.

Simulations also support this scenario. [83] modeled the dispersal of GMCs by photoionization and radiation pressure and found a range of cloud destruction times between 2 and 10 Myr after the onset of radiation feedback. For their fiducial model (initial cloud radius = 20pc, mass = $10^5$ $M_\odot$, $t_{ff}$ = 4.7 Myr), they found that ~50% of their simulation box (80pc x 80pc) was filled with ionized gas within 0.8Myr after the first stars were formed, and had mostly cleared all dense gas within a 10pc radius of the cluster within 1 $t_{ff}$ (4.7 Myr). This was performed without the aging of the stellar populations and thus these timescales serve as lower limits for radiation feedback. However, this model also does not include SNe, which would produce their own feedback as early as ~3Myr.

[134] used 1D expansion models to investigate the development of HII regions around young star clusters using isochrone-based age estimates. By testing their models on the Rosette, M16, RCW79, and RCW36 HII regions (which would either have concentrated or partially exposed Halpha morphologies in this study), they found their dynamical ages to agree with photometric ages from previous results, and to support the early onset of gas clearing by 2Myr. Furthermore, they found that for these four HII regions, a larger cloud radius correlated with an older age. Correlations of age with HII region size has also reported by [72], and [139] and would be interesting to investigate in future work.

It is interesting to note that when we examine the fields individually (see Table 6), we see that galaxies with higher metallicity (NGC 1313, NGC 7793; Z = 0.02) have younger median

ages for clusters with concentrated and partially exposed H$\alpha$ morphologies (~2-4Myr) than those of the lower-metallicity galaxy (Z = 0.004), NGC 4395 (~5Myr). A speculation is that longer clearing timescales are associated with lower metallicity systems, as winds would be weaker for lower metallicity stellar populations [102]. Detailed studies of individual young clusters in metal-rich galaxies such as Westerlund 2 [150] and NGC 3603, both of which are located in the Milky Way, [115] have shown early signs of gas clearing. Images of these clusters ([150, Figure 2]; [115, Figure 4]) show a cavity formed around the central stars of at least ~1-2pc (corresponding to our partially exposed class) while their estimated ages are ~1-2 Myr.

### 2.6.2 Cluster Mass and Stochasticity

Since young clusters should have O-type stars ionizing their natal gas, it may be surprising that we find clusters that have estimated ages younger than 3 Myr (before the onset of SNe) with no immediate H$\alpha$ emission. Fig. 2.14 shows postage stamps of four of the youngest of these clusters classified as no-emission, each of which have SED-determined ages of 1 Myr. There are at least three possible explanations for this phenomenon: 1) the SED determined ages for these clusters are incorrect, 2) these low-mass clusters are young but did not produce an O-type star, or 3) the density of HII is so low that the surface brightness of the H$\alpha$ emission is below our detection limit.

The mass distribution of clusters without H$\alpha$ emission may provide some insight. The mass histogram of two age bins in Fig. 2.15 shows that there is a small difference in median mass between those younger than 3 Myr (800 $M_{\odot}$) and those older than 3 Myr (1200 $M_{\odot}$). This could support the notion that the lower-mass clusters have a higher probability to not produce an O-type star to ionize its natal hydrogen gas. It is also plausible, however, that the low-mass nature of these

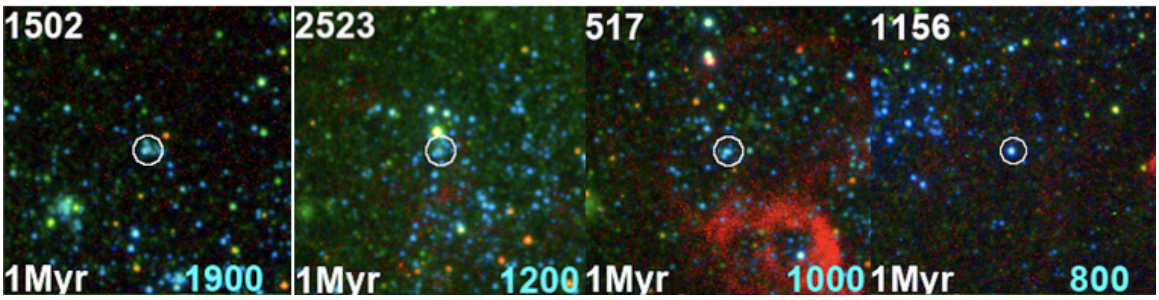


Figure 2.14: Four 150pc x 150pc RGB postage stamps of the youngest (1 Myr) isolated clusters with HII regions classified as no-emission. Cluster ID is located in the upper left, age in the lower-left, and mass (in $M_{\odot}$) in the lower-right.

clusters contribute to a longer dynamical timescale for the formation of each cluster and hence may add another confounding effect, as our models assume a single stellar population age for the entire cluster.

We also find clusters with best-fit ages $\geq 5$ Myr which show concentrated H$\alpha$ morphologies, after the typical 3-4 Myr timescale for SNe to begin clearing. 3 of the 6 isolated clusters with best ages $\geq$ 5 Myr and concentrated HII regions have their postage stamps shown in Fig. 2.16. All of these older concentrated clusters were found in NGC 4395, the lowest-mass galaxy in our sample, and none were found in NGC 7793 and NGC 1313. The clusters themselves are relatively lower mass as well (from 200-500 $M_{\odot}$), thus stochastic effects may introduce larger uncertainties into the age determinations.

### 2.6.3 Cluster Reddening and Stochasticity

Overall, in all three galaxies, we find relatively low reddening values for our clusters, where the range of our median E(B-V) values across the different morphological classes correspond to $A_V$ values between 0.3 and 0.6. [75]'s examination of extinction versus neutral H column density

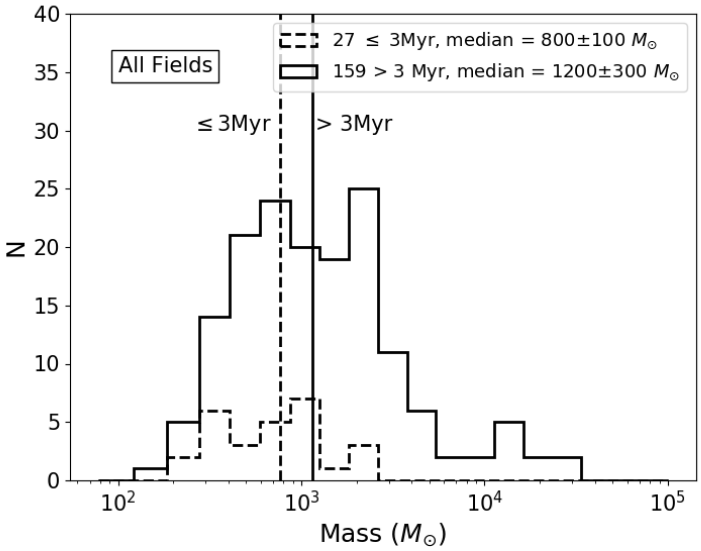


Figure 2.15: Mass histogram of all 186 isolated clusters without H$\alpha$ emission. Clusters $\leq$ 3 Myr are plotted with a dashed line while clusters > 3 Myr are plotted with a solid line. The number of clusters as well as the median mass values for these two bins is provided in the legend and the medians are plotted with vertical lines.

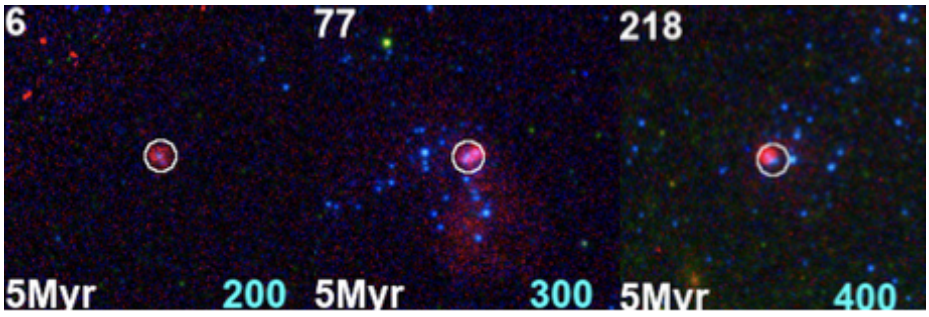


Figure 2.16: 150pc x 150pc RGB postage stamps of isolated clusters $\geq$ 5 Myr with concentrated HII regions. Cluster ID is located in the upper left, age in the lower-left, and mass (in $M_\odot$) in the lower-right.

for NGC 7793 revealed similarly small extinction values, with the vast majority between $A_V$ values of 0.3 and 0.6, consistent with what we find in our cluster sample.

A comparison of the color-color plots of our sample with the massive M83 clusters examined by [139] and [72] show interesting differences. In the M83 studies, clusters with concentrated H$\alpha$ emission showed a high degree of reddening, with some clusters lying near the 10 Gyr point on the model, while the clusters with no H$\alpha$ emission had the bluest colors and the tightest locus. As cluster age increases, the concentration of gas, H$\alpha$ emission, and thus reddening are expected to decrease [15]. This is supported by the observations of [72]; namely that the clusters of M83 without H$\alpha$ emission were not nearly as spread out due to reddening as the clusters with concentrated H$\alpha$. In our sample, however, we see that clusters with no H$\alpha$ are the ones that have the reddest colors because a significant fraction of them contain a bright red source. Additionally, we find that clusters without H$\alpha$ have reddening values that are comparable to those which show concentrated H$\alpha$ morphologies. This could be a result of overestimated reddening and corresponding underestimated ages, as also found by [139] and Whitmore et al. (in prep.) in the analysis of low mass clusters without H$\alpha$ in M83 and NGC 4449.

Further for NGC 7793 we have compared the reddening values of these clusters based on SED fitting with extinction maps made from the Balmer decrement (H$\alpha$/H$\beta$) using VLT-MUSE (Multi Unit Spectroscopic Explorer) data (Della Bruna et al. in prep). There are 65 clusters in our young cluster sample ($\leq$ 10Myr) which have MUSE coverage. For all 65 clusters, the median best SED-fit reddening is 0.11 while the median reddening determined with H$\alpha$/H$\beta$ via the MUSE data is 0.36. It is notable that only 7 of these 65 clusters have a best SED-fit E(B-V) greater than the Balmer calculated E(B-V) and each of those 7 clusters contain a bright red source. While clearly

suffering from small number statistics, the data do seem to suggest that clusters containing a bright red source correlate with a larger SED-fit E(B-V) than the H$\alpha$/H$\beta$ determined E(B-V).

The uniqueness of the reddening distributions of clusters with and without bright red sources (Fig. 2.10), and comparison with the local gas extinction lead us to conclude that the presence of bright red sources produces a significant impact on the SED-fit reddening of a cluster. Thus we find that our sample of clusters with no H$\alpha$ emission have red colors, which are not necessarily due to dust, but rather because there is a bright red source within the aperture.

Lastly, this likely overestimation of reddening for our clusters appears to be corrected by our stacking procedure. Compared to their constituent clusters, the older ages and smaller reddening values for our isolated composite clusters are more consistent with a cleared-out environment and thus potentially mitigates stochastic effects. As such, this procedure appears to provide a promising avenue for analyzing isolated clusters with stellar masses below the stochastic limit. More care must be taken when stacking non-isolated clusters, which show dichotomous results (see Section 2.6.1 for this discussion).

## 2.7 Summary and Future Work

We examine ~700 young ($\leq$ 10Myr) star clusters in the nearby spiral galaxies NGC 7793, NGC 1313, and NGC 4395 (d $\approx$ 4Mpc). We study the H$\alpha$ morphology of the HII regions surrounding the clusters in relation to cluster age, reddening, and mass derived through SED-fitting of *HST* NUV, U, B, V, I photometry. The SED-fit properties are available via the LEGUS star cluster catalogs which have been publicly released through MAST. The ultimate objective is to use the H$\alpha$ morphology around young star clusters to gain insight into the timescales, and thus the physical processes at

work, in the clearing of a cluster's natal gas. We classify the clusters in the sample according to: 1) visually-determined H$\alpha$ morphology (concentrated, partially exposed, and no-emission) and 2) whether they have neighboring clusters, which could affect the clearing timescales. A summary of our main results are as follows:

1 The distributions of cluster ages for each of the H$\alpha$ morphological classes are consistent with the expected evolutionary sequence, as also found by studies of young star clusters in M83 ([139, 72]). For the combined samples of isolated and non-isolated clusters, the median age of clusters (1) with concentrated H$\alpha$ is the lowest at ~3 Myr; (2) which are partially exposed by their H$\alpha$ emission is ~4 Myr; and (3) with no H$\alpha$ emission is the highest at > 5 Myr. The distinction between the ages of clusters with concentrated and partially exposed H$\alpha$ morphologies is model dependent, however. The mean and median ages of these classes based on the Geneva stellar evolution model (as opposed to our reference catalog, which uses the Padova model) or with alternate extinction models (i.e. starburst or differential-starburst extinction instead of Milky Way extinction) are consistent (~3-3.5Myr). Overall, this indicates that the clearing timescale is short – on the order of or less than our SED time step of 1Myr.

2 When the isolated and non-isolated samples are treated separately, KS tests cannot confirm with high certainty (~2$\sigma$) that the age distributions for all three morphological classes are statistically different. When the isolated and non-isolated samples are combined, however, the likelihood that they do not share a parent distribution is stronger ($\gtrsim 3\sigma$). These results indicate that a larger sample size is needed to properly study the possible impact of nearby neighbors on HII region morphologies and gas clearing timescales.

3 In contrast to previous studies and expectation, which find that clusters without H$\alpha$ emission are less reddened (e.g. [139, 72, 15]), we find comparable median E(B-V) values for clusters with concentrated H$\alpha$ and no H$\alpha$ emission (0.18 vs. 0.14, respectively). However, the clusters with no H$\alpha$ tend to contain bright red point-like sources, and are significantly redder in the (U-B) vs. (V-I) diagram than clusters with concentrated H$\alpha$. Given that these clusters have very low masses (several hundred $M_{\odot}$), we posit that this is the result of stochasticity in IMF sampling, and that the reddening has been overestimated for clusters containing bright red sources.

Our experiments to mitigate stochastic effects by summing the fluxes of the clusters in each H$\alpha$ morphological class to synthesize more massive composite sources have yielded promising results. From the observed properties of the composite clusters along with the ages, masses, and reddenings from SED fitting, we find that:

1 The colors of the composite clusters lie close to the evolutionary model track of a single-age population, and in general, have an age progression consistent with results based on the analysis of individual clusters.

2 The ages and reddening of composite clusters with concentrated and partially exposed morphologies are comparable to their constituents.

3 Isolated composite clusters with no H$\alpha$ are over twice as old (~12 Myr vs. ~5 Myr) and have significantly less reddening (~5x) than their constituent clusters, which is more consistent with a cleared-out environment. The non-isolated sample, however, shows mixed results. While two of the composite clusters similarly have older ages and smaller reddening than their

constituents, three composite clusters show the opposite result, namely having younger ages (all 1-2 Myr) and larger reddening (>2x) than their constituents. This is especially puzzling because of their position in (U-B) vs. (V-I) space: while they do appear closer to the younger end of the model than the isolated sample, the reddening vector would not appear to trace them back to the 1Myr point in the model but rather $\gtrsim$ 3Myr. We speculate that this could be the result of confounding effects cluster neighbors have on gas clearing.

In this work, we have designed the analysis to rely on the LEGUS star cluster catalogs. The star clusters, which are effectively single aged stellar populations, act as clocks which can be used to time the evolution of the HII region H$\alpha$ morphologies and clearing of the gas. While this provides a statistically complete sample of star clusters for study, it does not allow us to answer questions about the fraction of the overall HII region population that are associated with star clusters, or to check whether the HII regions associated with the clusters studied here are a representative sample of the population. Such questions require complete HII region catalogs to be developed (e.g., [132, 84]), and will be pursued in future work (e.g., Della Bruna et al., in prep).

Additionally, one of us (SH) visually classified the H$\alpha$ morphology of the clusters. The usual drawbacks with human visual classification include the time consuming nature of the task, and the relative subjectivity of classification. In the future, a more quantitative approach, which includes measurement of the concentration index of the H$\alpha$ emission, could be pursued. A cursory examination of concentration indices of H$\alpha$ relative to the total H$\alpha$ flux for our sample confirms photometric differences between the morphological classes. Machine learning techniques could also be pursued using the classifications established here as the foundation of a training sample. Robust training of neural networks would require larger samples with human classifications than used here.

Such approaches could be used to classify the many thousands of additional young clusters in the full H$\alpha$ LEGUS galaxy sample, and facilitate future study of possible environmental dependences of HII region evolution timescales.

## Acknowledgements

Based on observations with the NASA/ESA/CSA Hubble Space Telescope which were retrieved from MAST at the Space Telescope Science Institute, operated by the Association of Universities for Research in Astronomy, Incorporated, under NASA contract NAS5-26555. The observations were obtained through *HST* programs #13364 and #13773. Support for these programs was provided through a grant from the STScI under NASA contract NAS5-26555.

# Chapter 3

# H$\alpha$ Morphologies of Star Clusters in 16 LEGUS Galaxies: Constraints on HII region evolution timescales

## 3.1 Introduction

Clouds of cold gas coalesce to form stars, most of which are thought to form in clustered regions within giant molecular clouds (GMCs; [92]). Thus an understanding of the star formation cycle in galaxies must encompass a model for the complete evolution of these GMCs, including the formation of stars and star clusters as well as subsequent dispersal of the stars into the "field" (e.g., [138]). One of the key observations regarding GMCs is that the timescale on which these clouds convert all of their gas into stars (i.e. depletion time) has been observed to be much longer than the

dynamical time of the cloud. In fact only a few percent of GMC mass is converted into stars before the clouds are disrupted [152, 146, 54, 91, 55].

Despite the long-standing history of these observations, the exact processes that govern these cloud-scale dynamics are still debated, and stellar feedback in general is at the forefront of the discussion (see [90] for a review). Stellar feedback such as supernovae (SNe) explosions, stellar winds, photoionization, and radiation pressure have been shown to be capable of disrupting the parent molecular cloud, thus halting star formation and adequately limiting star formation efficiency to the observed degree (e.g. [6, 39, 74, 86]). Further, when simulations exclude stellar feedback, the resulting star formation rate and efficiency are far greater than the aforementioned observations ([22, 131, 73, 45, 89]).

These feedback mechanisms influence the interstellar medium (ISM) through the transfer of energy and momentum, which contribute to the observed dynamical equilibrium in the ISM [129] among other galactic-scale properties (e.g., [105, 63, 114, 88]). Importantly, these feedback processes occur on different timescales. Here, we seek to provide constraints on the timescale for gas clearing in order to illuminate the primary feedback mechanism(s) responsible for cloud dispersal, as this process influences the properties of the stellar population (see [46] & [2] for reviews), ISM, and of galaxy evolution as a whole [123].

One of the methods to constrain such timescales is through the study of nebular H$\alpha$ emission in conjunction with the parent star clusters (e.g. [139, 72, 68]). Upon the formation of star clusters within molecular clouds, massive OB-type stars within the clusters will ionize their natal gas cloud and produce HII regions. A large diversity in the size, shape, and extent of HII regions has been observed via H$\alpha$ imaging (e.g. [77, 37, 139, 9, 68]), and has been attributed to factors

including gas density distributions and the aforementioned stellar feedback mechanisms ([90]). We can then connect the HII morphologies to the parent star clusters' properties such as age, whereby the clusters can effectively be used as clocks to age-date the evolutionary state of the HII regions. Comparison between the morphologies of HII regions and the properties of their parent star clusters can therefore inform us about the HII region evolutionary sequence and its timescale, thus helping us better understand the gas clearing process.

Previous studies have examined correlations between H$\alpha$ morphology and star cluster properties (e.g. [139, 72, 68]). In particular, in [68], we use imaging from the Hubble Space Telescope (*HST*), to study ~700 young ($\leq$ 10 Myr) star clusters in the three nearest (d $\approx$ 4 Mpc) spiral galaxies (NGC 1313, NGC 4395 and NGC 7793) from the Legacy Extragalactic UV Survey (LEGUS; [28]). There we found that star clusters with young ages (~3 Myr) are associated with concentrated H$\alpha$ emission. We confirmed the presence of an evolutionary sequence from concentrated HII regions to more bubble-like regions as reported by [139] and [72]. By comparing the median ages of clusters with these two types of H$\alpha$ morphologies, we also confirmed that the clearing of gas around star clusters begins early (cluster age $\lesssim$ 3 Myr) and takes place over a short interval ($\lesssim$ 1 Myr).

Beyond the study of H$\alpha$ emission, [67] and [64] compared ALMA (*Atacama Large Millimeter Array*) CO detections of giant molecular clouds (GMCs) with the positions of star clusters in NGC 7793 (one of the galaxies in this study) and found that the timescale for star clusters to dissociate from their natal clouds is similarly short, between 2-4 Myr. This is also roughly consistent with the timescales found based on ALMA CO data for the Antennae galaxies [107] as well as with [81], who studied CO(1-0), Spitzer 24$\mu$m, and H$\alpha$ emission in tandem for nearby galaxies. As supernovae (SNe) typically ignite after ~3.5 Myr (e.g. [6]), these studies support the

notion that SNe cannot be the sole driver of gas removal and thus suggest the importance of other clearing mechanisms such as stellar winds, direct radiation pressure, thermal pressure from $10^4$ K gas, and dust processed radiation pressure (e.g. [17] and references therein).

A notable challenge in this type of analysis is that star cluster properties can be affected by stochastic sampling of the upper part of the initial mass function (IMF), following the predictions of previous modeling (e.g. [13, 61, 94, 25, 31, 44]). These sampling effects greatly affect the luminosity and color distributions of star clusters, which depend strongly on the mass distribution of stars within them ([58, 59]). For example, [68] found that ~33% of their star clusters without H$\alpha$ contained one or more bright red point-like sources, presumably red supergiants, within their photometric apertures. These luminous stars can dominate the flux of lower-mass clusters, resulting in an overestimate of the reddening and an underestimate of their ages. Stochastic sampling effects have motivated previous star cluster studies (e.g. [139]; [72]; [2]) to employ a $\geq 5000$ $M_\odot$ limit, as these more massive clusters more completely sample the IMF and thus their SEDs should be less affected by individual bright stars.

One of the major disadvantages of the [68] sample is the lack of these “massive" clusters – only 42 clusters were found to have stellar masses above 5000 $M_\odot$, including a mere 12 clusters with concentrated or partially exposed H$\alpha$ morphologies. Further, none of those 12 were isolated from other nearby clusters (defined as clusters with no other clusters within 75 pc), which can produce confounding effects in the presence and clearing of HII regions. To address this, we build upon the sample from [68], where the present study quadruples the number of young, massive clusters.

Also, the analysis of [68] ignores all star clusters with SED ages > 10 Myr under the assumption that H$\alpha$ will only be present when the clusters have ages < 10 Myr (e.g. [49, 139, 138,

72]). However, such an assumption ignores the impact of the age-reddening degeneracy, and studies including [68], [140], and [135] have all identified star clusters for which SED ages and E(B-V) appear to be poorly estimated (e.g. age is overestimated while reddening is underestimated and vice versa). [140] further report their age estimates to have an uncertainty of ~0.3, or a factor of 2 in most cases, but much larger for older clusters such as globular clusters. By examining all clusters regardless of SED age, the present study may prove valuable in checking the reliability of SED-fit ages, and obtaining new insights regarding timescales associated with gas clearing.

This paper is organized as follows. In Section 3.2 we summarize the observations and the star cluster catalogs used in the study. Section 3.3 reviews the visual classification scheme used to determine H$\alpha$ morphologies, as also employed in [68]. Section 3.4 examines the SED-estimated cluster age, reddening, and mass distributions as a function of H$\alpha$ morphological class. Sections 3.5 & 3.6 examine manifestations of stochastic sampling and the accuracy of SED-fit ages for two subsets of clusters. The recoverability of star cluster properties as well as resolution dependence on H$\alpha$ morphological classification are examined in Section 3.7. Section 3.8 provides an overall summary of the work.

## 3.2 Data

The data used in this study are taken from LEGUS [28], which combines WFC3 (GO-13364; F275W, F336W, F438W, F555W, and F814W) and archival ACS[1] (F435W, F555W, F606W, and F814W) *HST* imaging to provide full five-band NUV-U-B-V-I coverage for 50 nearby ($\lesssim$ 11 Mpc) galaxies. The LEGUS-H$\alpha$ follow-up survey (GO-13773; PI R. Chandar) provides coverage of

[1]To produce consistent final data products, the ACS/WFC images, with a native pixel scale of 0.049, are aligned to the UVIS WCS reference frame and re-drizzled to the UVIS pixel scale of 0.0396 [28].

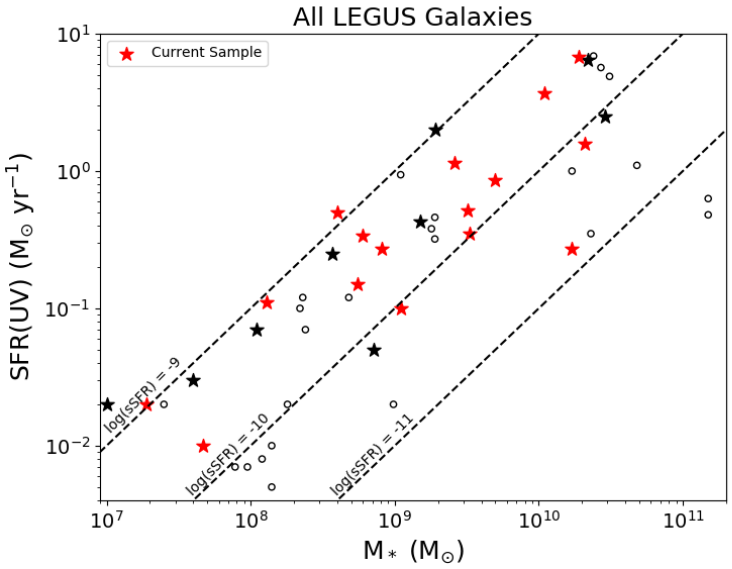


Figure 3.1: Star Formation Rate (SFR) vs. Stellar Mass ($M_*$) for the 16 galaxies studied in this paper (red stars). The parent sample of 50 LEGUS galaxies [28] are shown while the stars represent the galaxies observed in the LEGUS-H$\alpha$ *HST* follow-up survey, which have relatively higher sSFRs. The 16 red stars show the specific galaxies in this study while the 9 black stars represent galaxies with LEGUS H$\alpha$ imaging but lack available star cluster catalogs. Our sample spans the full range of LEGUS-H$\alpha$ galaxies. The black circles represent the remaining 25 LEGUS galaxies which were not part of LEGUS-H$\alpha$. Dashed lines at log(sSFR) = -9, -10, and -11 are provided for reference.

the H$\alpha$ emission-line with a narrow-band filter (F657N) as well as a medium-band filter sampling line-free continuum (F547M). This follow-up H$\alpha$ survey was completed for 25 LEGUS galaxies with higher specific star formation rates in the sample (Figure 3.1). The ~0.04 /pixel scale of *HST* imaging can resolve objects as small as ~1-3 pc across the distance range of the LEGUS galaxies (~3–11 Mpc), which allows us to effectively resolve ionizing star clusters and their HII regions, a necessary aspect of this analysis.

To produce H$\alpha$ emission-line images,[2] the F657N images are drizzled and aligned, and then an appropriate combination of F814W and F547M, scaled by their AB zeropoints relative to

[2]Note that the emission-line images also contain flux from the adjacent [NII] 6548,83 lines.

F657N and weighted by their relative pivot wavelengths, are subtracted as a representation of the continuum.

This study expands upon the work of [68], which examined only the three nearest spiral galaxies (6 fields) of the LEGUS sample: NGC 1313, NGC 4395, and NGC 7793. Here we have expanded the sample to include all LEGUS fields which have both cluster catalogs and LEGUS-H$\alpha$ emission-line and continuum imaging. NGC 5457 has also been included, however its cluster catalogs have instead been obtained via private communication and will be published in Linden et al. (in prep.). This has increased the number of galaxies from 3 to 16, and the total number of *HST* fields from 6 to 21. The current dataset also spans a much greater distance range, from ~3–10 Mpc, while the three spiral galaxies examined in [68] all have distances of ~3–4 Mpc. General properties for each of these galaxies including distance, position angle, inclination, and diameter, are provided in Table 3.1. $162 \times 162$ footprints of F657N (imaged with WFC3) are shown on $20 \times 20$ DSS images for all 16 galaxies in Figure 3.2.

As described in detail in [2], for each of the 21 fields, photometry is performed with aperture radii of 4, 5, or 6 pixels, which correspond to radii of 3.3-7.7 pc, given a pixel scale of 0.03962 /pixel for WFC3 UVIS. A 1-pixel-wide annulus at a 7-pixel inner radius is then used to subtract the background, with the final cluster magnitudes corrected for foreground Galactic extinction [124].

From the broadband *HST* photometry (i.e., excluding the narrow and medium bands), cluster SEDs are fitted to Yggdrasil SSP models [149] with 46 total ages consisting of 1 Myr steps from 1-15 Myr, 10 Myr steps from 20-100 Myr, 100 Myr steps up to 1 Gyr, and lastly 1 Gyr steps up to 14 Gyr. The models also include 150 fixed steps (0.01 mag) in E(B-V) from 0.00 to 1.50

**General Properties of Galaxies in the Sample**

| Field | Type | Distance (Mpc) | Position Angle (°) | Inclination (°) | $D_{25}$ (log(')) | Z | SFR(UV) ($M_\odot$ $yr^{-1}$) | $M_*$ ($M_\odot$) |
|---|---|---|---|---|---|---|---|---|
| NGC 1313* | SBd | 4.39 | 40 | 40.7 | 1.04 | 0.02 | 1.15 | 2.6e+09 |
| NGC 1433 | SBab | 8.3 | 88 | 24.5 | 0.27 | 0.02 | 0.27 | 1.7e+10 |
| NGC 1705 | SA0/BCG | 5.1 | 50 | 42.3 | 0.27 | 0.004 | 0.11 | 1.3e+08 |
| NGC 3344 | SABbc | 7.0 | 0 | 23.8 | 0.83 | 0.02 | 0.86 | 5.0e+09 |
| NGC 3351 | SBb | 10.0 | 13 | 47.4 | 0.86 | 0.02 | 1.57 | 2.1e+10 |
| NGC 4242 | SABdm | 5.8 | 25 | 40.4 | 0.58 | 0.02 | 0.10 | 1.1e+09 |
| NGC 4395* | SAm | 4.3 | 147 | 33.6 | 0.62 | 0.004 | 0.34 | 6.0e+08 |
| NGC 45 | SAdm | 6.61 | 142 | 46.1 | 0.79 | 0.02 | 0.35 | 3.3e+09 |
| NGC 4656 | SBm | 5.5 | 33 | 78.5 | 0.81 | 0.004 | 0.50 | 4.0e+08 |
| NGC 5457 | SABcd | 6.7 | 90 | 20.9 | 1.38 | 0.02, 0.008[a] | 6.72 | 1.9e+10 |
| NGC 5474 | SAcd | 6.8 | 0 | 26.5 | 0.38 | 0.02 | 0.27 | 8.1e+08 |
| NGC 628 | SAc | 9.9 | 25 | 25.2 | 1.00 | 0.02 | 3.67 | 1.1e+10 |
| NGC 7793* | SAd | 3.44 | 98 | 47.4 | 1.02 | 0.02 | 0.52 | 3.2e+09 |
| UGC 1249 | SBm | 6.9 | 150 | 63.4 | 0.81 | 0.02 | 0.15 | 5.5e+08 |
| UGC 7408 | IAm | 6.7 | 100 | 62.5 | 0.30 | 0.004 | 0.01 | 4.7e+07 |
| UGCA 281 | Sm | 5.9 | 95 | 40.7 | -0.11 | 0.004 | 0.02 | 1.9e+07 |

Table 3.1: General properties for the 16 galaxies examined in this study. This includes RC3 morphological type as listed in HyperLeda (http://leda.univ-lyon1.fr; **(author?)** 106), distance, star formation rate, and stellar mass [28], position and inclination angles [100], galactic diameter ($D_{25}$; **(author?)** 106, 40), and metallicity [2]. Distances and metallicities match those used to derive physical properties as published in the LEGUS star cluster catalogs. Asterisks indicate the galaxies studied in **(author?)** [68].
[a] Z = 0.02 for NGC 5457-NW1, Z = 0.008 for NGC 5457-NW2 and NGC 5457-NW3.

mag. These SSP models include nebular flux via photoionization modeling with CLOUDY [57], assuming a covering fraction of 0.5 as a fixed parameter [2]. Stellar libraries assume a fully-sampled [85] IMF with stellar masses between 0.1 and 100 $M_{\odot}$, and the fitting for each galaxy adopts the present day metallicity of its young stellar population as determined by nebular abundances [2].

The cluster ages, E(B-V)s, and masses presented in this work correspond to the minimum $\chi^2$ value of the fitting algorithm. Errors for these SED-fitted parameters are determined by the minimum and maximum values found amongst those with $\chi^2 \leq \chi^2_{min} + 2.3$, based on $1\sigma$ confidence levels [93]. Detailed descriptions of the SED-fitting algorithm and error analysis are given in [4] and [3], respectively.

A total of twelve cluster catalogs have been made for each of these fields, and each of the catalogs provides a unique set of SED-fit properties. Each catalog assumes one of two stellar evolutionary models (Padova or Geneva; see [102], [136]), one of three extinction models (Milky Way; [30], Starburst, or Differential Starburst; [29]), and one of two aperture correction methods [2, 38, average aperture correction or concentration index-based]. The rationale for these choices amongst other, more general details are described in [87] & [2]. In this study we examine star cluster properties based on the six models which use standard average aperture correction. It should also be noted that the catalogs using the starburst extinction model were made as a test, however their results are consistent with the other catalogs. A key difference between this study and [68] is that here we do not narrow the cluster sample to only include clusters with SED-fit ages $\leq$ 10 Myr; we consider all clusters in this analysis, regardless of SED-fit age.

For our study, we use all objects with a visually assigned cluster class of 1, 2, or 3, as determined by the mode of value provided by three classifiers. Cluster classes of 1, 2, and 3

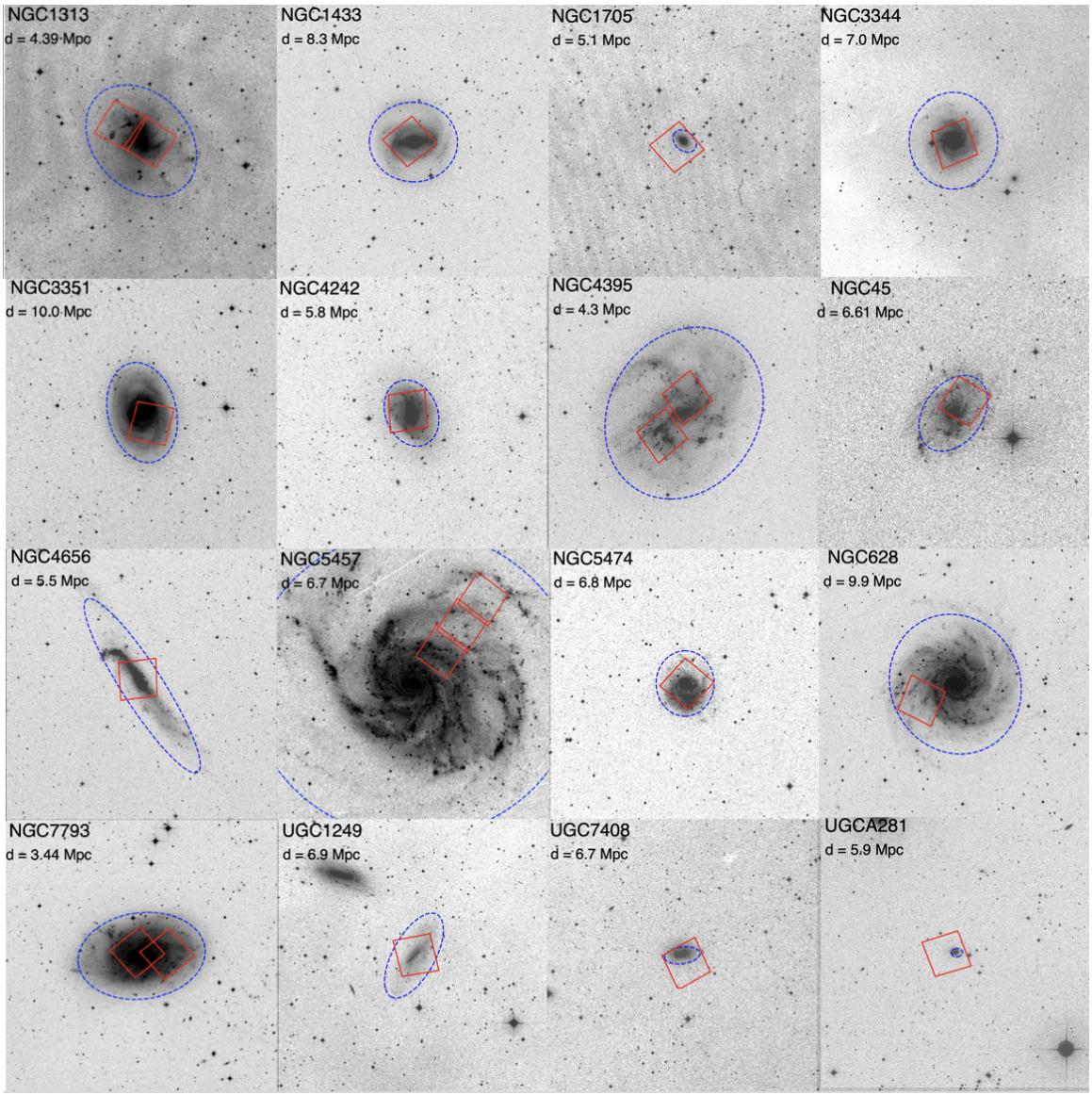


Figure 3.2: *HST* footprints on digitized sky survey (DSS) images for each of the 16 galaxies in this study. Red squares outline the fields of view for F657N (H$\alpha$+[NII] emission-line + continuum) WFC3 images, where galaxies with multiple squares indicate those with multiple fields. Galaxy name and distance are provided in the upper-left of each footprint, and the dashed blue ellipses trace the $R_{25}$ of each galaxy. The field of view of WFC3 is 162 $\times$ 162, and each DSS footprint is 20 $\times$ 20. Note that LEGUS has aimed to maximize sampling along galactic radii, which is perhaps most evident for NGC 5457.

represent symmetric, asymmetric, and multi-peaked star clusters, respectively. We are careful to note, however, that cluster class 3 objects are instead often referred to as compact associations of stars [90]. The term 'clusters' will be inclusive of these objects throughout this paper, except for explicitly stated comparisons. The cluster classes are provided in the LEGUS cluster catalogs ([2, 38]; Linden et al. in prep.) and reveal an even distribution of cluster class 1 (31.5%), 2 (35.9%), and 3 (32.6%) objects for the sample. For a more in-depth analysis on the distribution of these cluster morphologies in LEGUS galaxies, see [65, 66].

Overall, we present results based on 3757 final cluster targets across 16 galaxies totaling 21 fields for which we have H$\alpha$ emission-line data. This includes ~1900 clusters with SED ages $\leq$ 10 Myr and ~170 clusters with SED ages $\leq$ 10 Myr and stellar masses $\geq$ 5000 $M_{\odot}$. The total number of objects as well as the number of young and young+massive clusters for each of the fields in this study are shown in Table 3.2.

## 3.3 H$\alpha$ Morphology Classification

Following the visual classification process of [68], we create two sets of 150 pc $\times$ 150 pc images centered on each cluster, which we refer to as "postage stamps". One set of postage stamps shows only the continuum-subtracted H$\alpha$ in red, which allows us to most clearly determine the shape and extent of each HII region. The other set of stamps is made from a composite RGB image of the galaxy using combined NUV and U bands, combined V and I bands, and the continuum-subtracted H$\alpha$ narrow band for the blue, green, and red channels, respectively. These allow us to examine the HII regions in the context of the target cluster and any other neighboring objects. Examples of these postage stamps can be found throughout this paper, firstly in Figure 3.3.

**Detection & Cluster Counts by Field**

| Field | Total Detections | Verified Clusters | ≤ 10Myr | ≥5000 $M_\odot$ | ≥10000 $M_\odot$ |
|---|---|---|---|---|---|
| NGC1313E* | 5284 | 259 | 115 | 15 | 9 |
| NGC1313W* | 3784 | 486 | 180 | 19 | 13 |
| NGC1433 | 1099 | 168 | 123 | 14 | 8 |
| NGC1705 | 365 | 42 | 10 | 2 | 1 |
| NGC3344 | 1527 | 396 | 270 | 8 | 1 |
| NGC3351 | 1389 | 292 | 169 | 42 | 33 |
| NGC4242 | 1080 | 191 | 83 | 1 | 0 |
| NGC4395N* | 291 | 39 | 25 | 0 | 0 |
| NGC4395S* | 837 | 137 | 115 | 7 | 4 |
| NGC45 | 774 | 117 | 58 | 0 | 0 |
| NGC4656 | 1703 | 262 | 122 | 20 | 9 |
| NGC5457NW1 | 5891 | 283 | 92 | 5 | 3 |
| NGC5457NW2 | 3707 | 110 | 40 | 2 | 2 |
| NGC5457NW3 | 5390 | 36 | 18 | 3 | 1 |
| NGC5474 | 4275 | 177 | 89 | 2 | 0 |
| NGC628E | 593 | 259 | 120 | 21 | 6 |
| NGC7793E* | 899 | 191 | 117 | 2 | 1 |
| NGC7793W* | 2794 | 221 | 132 | 1 | 0 |
| UGC1249 | 1000 | 88 | 51 | 3 | 1 |
| UGC7408 | 305 | 46 | 13 | 0 | 0 |
| UGCA281 | 327 | 15 | 9 | 2 | 2 |
| **TOTAL** | **43314** | **3815** | **1951** | **169** | **94** |

Table 3.2: Number counts of total detections, visually-verified clusters (LEGUS mode class = 1, 2, or 3), verified clusters with SED age ≤10Myr, and verified clusters with SED age of ≤10Myr & stellar mass of either ≥5000$M_\odot$ or ≥10000$M_\odot$ for each of the 21 fields of view. The six fields which were studied in **(author?)** [68] are denoted with an asterisk. NGC 5457 catalogs have been obtained via private communication and are to be published by Linden et al. (in prep).

The definition of each of the three H$\alpha$ morphologies is as follows, as introduced in [139]:

1 **Concentrated (H$\alpha$ Class 1)**, where the target star cluster has H$\alpha$ emission covering it, and where there are no discernible bubbles or areas around the cluster which lack H$\alpha$ emission,

2 **Partially exposed (H$\alpha$ Class 2)**, where the H$\alpha$ surrounding the target cluster displays bubble like or filamentary morphology covering part of the cluster and,

3 **No emission (H$\alpha$ Class 3)**, where the target cluster appears to be clear of H$\alpha$, i.e. there is no H$\alpha$ emission within ~20 pc of the cluster. This includes those which have no visible H$\alpha$ emission in their entire 150 pc-wide postage stamps.

Clear examples of each of these H$\alpha$ morphologies can be found in Figure 2 of [68].

For reference, the 5$\sigma$ point source detection limit for the H$\alpha$ images used in this study is between 5.0x10$^{-17}$ and 5.5x10$^{-17}$ ergs cm$^{-2}$ s$^{-1}$. Across our distance range (~3–10 Mpc), the detectable observed luminosities are thus ~7.8x10$^{34}$ – 6.6x10$^{35}$ erg s$^{-1}$. Given the model grid of [127], these luminosities correspond to the ionizing fluxes of B0.5V and B0V stars for the nearest and furthest galaxies, respectively. These calculations assume solar metallicity, Case B recombination, nebular temperatures and densities of $10^4$ K and 100 cm$^{-3}$, respectively, and that the nebular region is radiation bounded.

During the initial classification of each postage stamp, the shape and position of H$\alpha$ relative to the target cluster is taken into consideration according to the above definitions of each of the classes. To facilitate this classification process, collages of postage stamps for all clusters in a given field, ordered by best-fit cluster age, are first examined. For ~80% of clusters, the classification of H$\alpha$ morphology is relatively unambiguous, such as when a cluster resides in a dense pocket of H$\alpha$

emission (concentrated morphology) or when there is hardly any H$\alpha$ emission in its entire postage stamp (no emission). However, the remaining ~20% are not so obvious, such as when the H$\alpha$ emission is faint or when the target cluster is found in a crowded region where the distribution of H$\alpha$ emission is uneven. An example of the latter case would be Object 260 (given an H$\alpha$ class of no emission; Figure 3.3), where there is plenty of H$\alpha$ emission in the vicinity due to a large number of clusters, but the H$\alpha$ is distributed quite irregularly and not in a circular pocket or bubble. This uneven distribution makes it more difficult to determine the origin and extent of the H$\alpha$ emission, and thus whether it should be identified as an H$\alpha$ class of 2 or 3. Object 1458 (Figure 3.3) shows what appears to be a cluster that is partially exposed from the H$\alpha$ in the RGB image, however upon inspection of the H$\alpha$-only image, one could argue that there are no obvious cleared regions within the H$\alpha$ emission and should be classified as an H$\alpha$ class 1 instead. Thus the faint H$\alpha$ emission of Object 1458 makes its classification difficult.

After these initial classifications are made, a second inspection is performed by the same person (SH). For each of the 21 fields, postage stamps are put into separate collages according to the three initial H$\alpha$ classes. In this manner, a more difficult case is able to be directly compared to the "obvious" cases in that particular H$\alpha$ class in order to discern whether the former in fact belongs in the class. Clear misidentifications are very occasionally made on the initial classifications and are subsequently corrected on this second pass. These corrections are performed until the H$\alpha$ morphologies in the collages for each of the classes are satisfactorily uniform. For the clusters in NGC 1313, NGC 4395, and NGC 7793, H$\alpha$ morphologies from [68] are treated as initial classifications and are thus subjected to this second inspection as well.

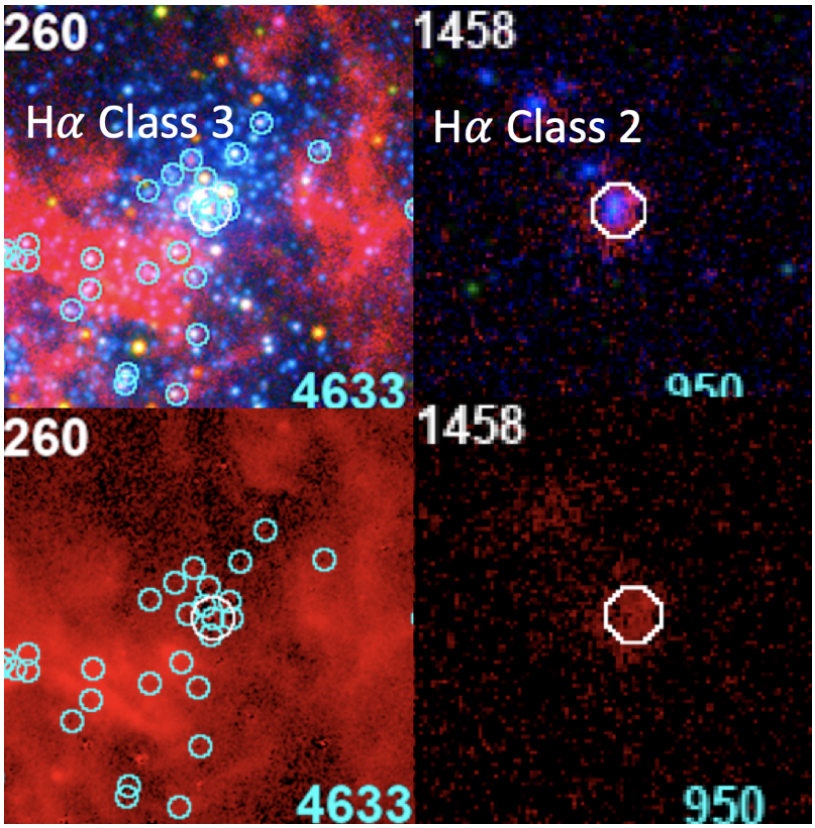


Figure 3.3: 150 pc × 150 pc postage stamps highlighting two of the more difficult H$\alpha$ morphology classifications, with the final classes indicated in the image. The top row is made up of the RGB images of the clusters while the corresponding continuum-subtracted H$\alpha$ is shown in the bottom row. Object IDs and cluster mass (in $M_{\odot}$) are provided in the upper-left and lower-right of each stamp, respectively. Crowded star cluster regions can produce widely dispersed and irregular H$\alpha$ emission which can make the distinction between an H$\alpha$ class of 2 versus 3 difficult for clusters such as Object 260. Faint emission can also make classifications harder to determine, such as Object 1458 which appears to show a small amount of clearing on the left side of the cluster.

**H$\alpha$ Morphology Reclassifications**

| H$\alpha$ Class Change | Isolated | Not Isolated |
|---|---|---|
| 1 to 2 | 2 | 6 |
| 1 to 3 | 0 | 2 |
| 2 to 1 | 4 | 13 |
| 2 to 3 | 1 | 0 |
| 3 to 1 | 0 | 1 |
| 3 to 2 | 1 | 18 |
| Total | 8 | 40 |

Table 3.3: A total of 48 clusters had their initial H$\alpha$ morphological class changed upon second inspection. The class changes for these objects are presented here, divided by isolation criteria and the specific class change. The 6 possible changes are shown in the first column (initial classification to new classification), where 1, 2, and 3 represent concentrated, partially exposed, and no emission H$\alpha$ morphologies, respectively.

By virtue of having the same person go through the classification process twice, an error rate can be drawn on the classification accuracy of the inspector themself. As shown in Table 3.3, 48 (1.3%) of the clusters in this sample had their H$\alpha$ morphology classes changed upon second inspection, 6 of which were obvious mistakes (0.2%). The majority (83%) of these changes occur for clusters that are not isolated, which is defined here as having at least one other star cluster within 75 pc.[3] Our figures indicate that, while the number of H$\alpha$ class changes that occur is quite small, the crowded regions naturally present the most difficulty. We have verified that these uncertainties do not affect the results discussed in following sections.

Table 3.4 lists the final overall distribution of H$\alpha$ morphological classes amongst the 3757 clusters in the sample. In total, there are 499 clusters with concentrated H$\alpha$ (180 isolated, 319 non-isolated), 372 clusters with partially exposed H$\alpha$ (108 isolated, 264 non-isolated), and 2886 clusters

[3]This separation is based on [62], who studied several thousand unbound stellar systems in Local Group galaxies and found that the average size of these stellar associations is ~70-90pc.

with no H$\alpha$ emission (1757 isolated, 1129 non-isolated). Looking at those that have best-fit ages $\leq$ 10 Myr and comparing them to the equally-defined cluster sample of [68], we find that the number of clusters with concentrated H$\alpha$, partially exposed H$\alpha$, and no emission have all roughly tripled, from 142 to 478 (3.4x), from 112 to 327 (2.9x), and to 400 to 1112 (2.8x), respectively. Thus the relative ratios of clusters in each H$\alpha$ morphological class have remained consistent across these two studies. Further, the ratio of isolated to non-isolated clusters within each H$\alpha$ morphological class has also remained roughly consistent: 36, 13, and 47 percent of clusters with concentrated H$\alpha$, partially exposed H$\alpha$, and no emission, respectively, were found to be isolated in [68] compared to 36, 30, and 54 percent of clusters in the present study. The most notable change is the relative increase in isolated clusters with partially exposed H$\alpha$, however this could be attributed to the smaller sample size of [68], which contained only 14 such clusters.

The complete list of H$\alpha$ classifications is provided as supplementary online material, and an abbreviated version of this table can be found in Appendix A.

## 3.4 Age, E(B-V), and Mass Distributions

To directly compare the results of this study to those of [68], we first limit the cluster sample to those which have best-fit SED ages $\leq$ 10 Myr as before. We then investigate the results without any age restrictions to examine the impact of including clusters with older age estimates, which may include young clusters with erroneous ages (e.g. [140]).

For each of the six LEGUS catalogs of SED-fit properties, we examine the statistics of cluster age, reddening, and mass, according to H$\alpha$ morphology, and whether the cluster is isolated. Our results are presented in the following subsections.

**H$\alpha$ Morphology Classifications by Field**

| | **Concentrated** | | **Partially Exposed** | | **No Emission** | |
|---|---|---|---|---|---|---|
| Field | Isolated | Not Isolated | Isolated | Not Isolated | Isolated | Not Isolated |
| NGC1313E | 8 | 19 | 2 | 28 | 94 | 101 |
| NGC1313W | 3 | 29 | 0 | 26 | 118 | 305 |
| NGC1433 | 13 | 19 | 13 | 26 | 69 | 28 |
| NGC1705 | 1 | 2 | 1 | 5 | 14 | 19 |
| NGC3344 | 37 | 60 | 17 | 38 | 136 | 97 |
| NGC3351 | 16 | 34 | 18 | 18 | 153 | 53 |
| NGC4242 | 6 | 12 | 4 | 6 | 126 | 37 |
| NGC4395N | 6 | 0 | 1 | 0 | 29 | 3 |
| NGC4395S | 4 | 27 | 3 | 30 | 32 | 41 |
| NGC45 | 9 | 5 | 3 | 2 | 90 | 8 |
| NGC4656 | 10 | 20 | 7 | 12 | 97 | 116 |
| NGC5457NW1 | 14 | 7 | 16 | 9 | 171 | 65 |
| NGC5457NW2 | 8 | 3 | 0 | 4 | 91 | 3 |
| NGC5457NW3 | 2 | 0 | 0 | 0 | 30 | 2 |
| NGC5474 | 12 | 12 | 6 | 5 | 115 | 26 |
| NGC628E | 9 | 20 | 5 | 11 | 165 | 37 |
| NGC7793E | 9 | 17 | 3 | 14 | 74 | 66 |
| NGC7793W | 5 | 23 | 4 | 23 | 71 | 85 |
| UGC1249 | 6 | 5 | 4 | 5 | 44 | 24 |
| UGC7408 | 0 | 0 | 0 | 0 | 33 | 13 |
| UGCA281 | 2 | 5 | 1 | 2 | 5 | 0 |
| **Total** | **180** | **319** | **108** | **264** | **1757** | **1129** |
| **$\leq$10Myr** | 171 | 307 | 99 | 228 | 601 | 511 |
| **$\geq$5000M$_\odot$** | 4 | 35 | 8 | 21 | 42 | 53 |
| **$\geq$10000M$_\odot$** | 1 | 26 | 5 | 13 | 22 | 26 |

Table 3.4: Number counts of clusters in each of the three H$\alpha$ morphology classes (concentrated, partially exposed, no emission) and further separated into isolated and non-isolated categories depending on the presence or absence of neighboring clusters within 75pc. Also included at the bottom of the table are the total number of clusters in each morphology & isolation bin that are $\leq$10Myr, $\leq$10Myr & $\geq$5000M$_\odot$, and $\leq$10Myr & $\geq$10000M$_\odot$. These numbers do not include 58 clusters which were found outside of the field of view for F657N.

### 3.4.1 Age Statistics

Analysis of the SED age distributions for each of the H$\alpha$ morphology classes is pertinent to understanding whether or not these classes constitute an evolutionary sequence. Figure 3.4 shows the age distributions for each of the H$\alpha$ morphological classes for clusters with SED ages $\leq$ 10 Myr based on our reference sample (i.e., SED fits assuming Padova stellar evolutionary model, Milky Way extinction).

For the reference sample of isolated clusters with SED ages $\leq$ 10 Myr, we find that the median best-fit age [first quartile, third quartile] of the 171 clusters with concentrated HII regions is 2.0 [1.0, 4.0] Myr, while the median ages for the 99 partially exposed clusters and 601 clusters with no H$\alpha$ emission are 2.0 [1.0, 3.0] Myr and 6.0 [4.0, 8.0] Myr, respectively. If we include all clusters regardless of best-fit age, we find that the median SED ages of the clusters with concentrated and partially exposed H$\alpha$ are unchanged (2.0 [1.0, 4.0] Myr, 2.0 [1.0, 4.0] Myr, respectively), while the median SED age of clusters without H$\alpha$ is significantly older (50.0 [7.0, 200.0] Myr), as would be expected. Additionally, we find relatively consistent results for the sample of non-isolated clusters.

Thus we find that the inclusion of clusters with SED ages > 10 Myr does not significantly affect the median ages of clusters with concentrated and partially exposed H$\alpha$, largely due to the fact that there are relatively few of these older clusters. 21 of the 499 clusters (4.2%) with concentrated H$\alpha$ and 45 of the 372 clusters (12.1%) with partially exposed H$\alpha$ have best-fit ages > 10 Myr. Although few, these clusters are of considerable interest as these ages are beyond the expected lifetime of ionizing stars, and are discussed in detail in Section 3.6.2.

Across all stellar evolutionary models (Padova, Geneva) and extinction/attenuation models (Milky Way, Starburst, Differential Starburst), and whether or not we differentiate between isolated

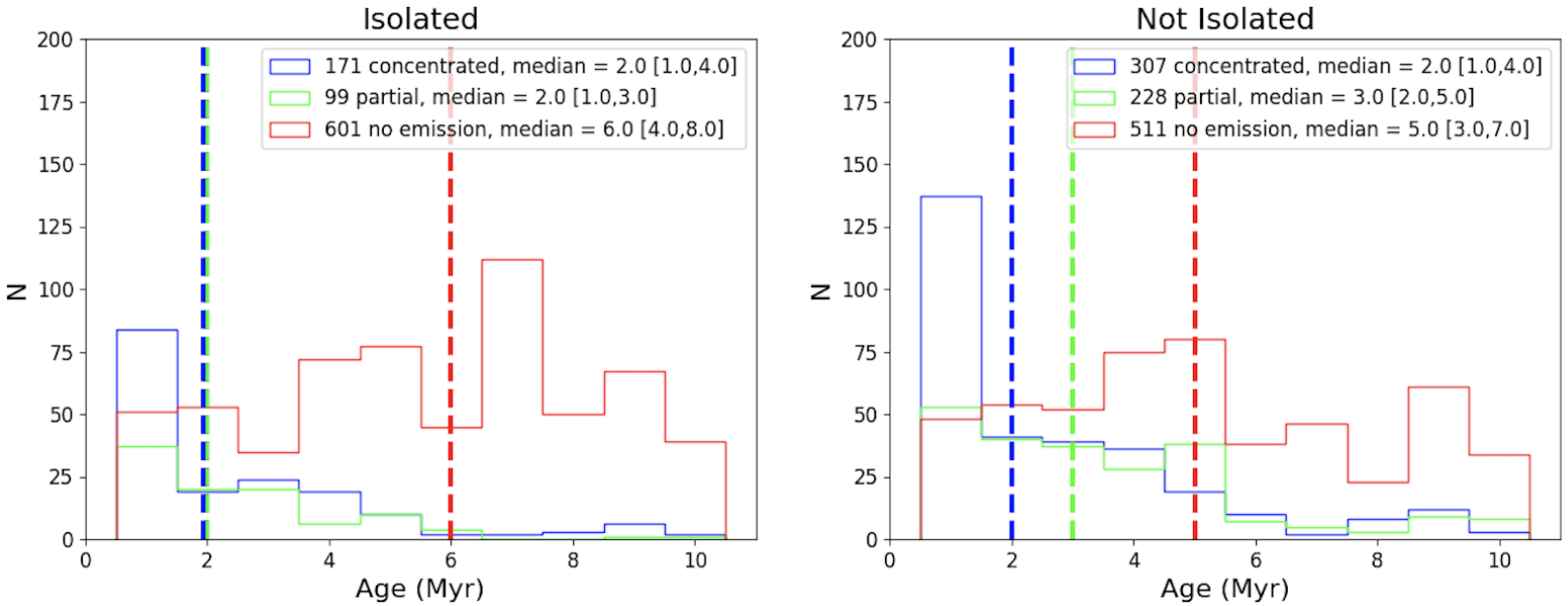


Figure 3.4: Age histograms for young ($\leq 10$ Myr) clusters with concentrated H$\alpha$ (blue), partially exposed H$\alpha$ (green), and no emission (red). The left and right plots show the distributions for isolated and non-isolated clusters, respectively. Vertical dashed lines show the median SED cluster age for each of the morphological classes, where the blue and green vertical lines overlap for isolated clusters due to the equal median ages of those with concentrated and partially exposed H$\alpha$ morphologies. While we find similarity in the age distributions of clusters with concentrated and partially exposed H$\alpha$, those with concentrated H$\alpha$ have an excess in the lowest age bin (1 Myr). As expected, those without H$\alpha$ have age distributions shifted to older ages.

and non-isolated clusters, we find a consistent progression for young clusters: those with concentrated H$\alpha$ have a median SED age of 1-2 Myr, those with partially exposed H$\alpha$ have a median SED age of 2-3 Myr, and those without H$\alpha$ have a median SED age of 3-6 Myr. We also note that the inclusion of 'compact associations' in our sample (Section 3.2) does not affect this progression. For an analysis on the robustness of the SED-fit ages, we guide the reader to Section 3.7.1.

If we take the error in a cluster's SED age to be the difference between its maximum and minimum age (see Section 3.2), we find that the median age error for each H$\alpha$ morphological class is 1 Myr. As this is smaller than each of the distributions' standard deviations, we determine that the errors are insufficient in describing the observed distribution widths, thus indicating that the distribution widths likely represent real variations in the cluster ages within each H$\alpha$ morphological class.

While the median SED ages reveal an age progression, we note that there is overlap in the age distributions, particularly for clusters with concentrated and partially exposed H$\alpha$ classes. To mathematically determine the uniqueness of the age distributions for all H$\alpha$ morphological classes, we perform Kolmogorov-Smirnov (KS) tests which calculate the probability that each individual distribution originates from the same parent distribution, with the results summarized in Table 3.5. KS tests are performed for isolated and non-isolated cluster samples separately, as well as for a combined sample of isolated + non-isolated clusters to improve the overall number statistics.

Overall, when the cluster population is divided into isolated and non-isolated samples, KS tests reveal that we cannot reject the hypothesis that the age distributions for clusters with partially exposed H$\alpha$ morphologies have been drawn from the same parent sample as clusters with concentrated H$\alpha$. The age distribution of clusters with no H$\alpha$ emission, however, are found to

**Model Comparison for Star Clusters ≤ 10Myr**

| Environment | Isolated | | Non-Isolated | | All | |
|---|---|---|---|---|---|---|
| | Padova | Geneva | Padova | Geneva | Padova | Geneva |
| H$\alpha$ Class | | | Age | | | |
| 1 vs. 2 | 0.322 | 0.019 | $<p_{3\sigma}$ | $<p_{3\sigma}$ | $<p_{3\sigma}$ | $<p_{5\sigma}$ |
| 1 vs. 3 | $<p_{5\sigma}$ | $<p_{5\sigma}$ | $<p_{5\sigma}$ | $<p_{5\sigma}$ | $<p_{5\sigma}$ | $<p_{5\sigma}$ |
| 2 vs. 3 | $<p_{5\sigma}$ | $<p_{5\sigma}$ | $<p_{5\sigma}$ | $<p_{5\sigma}$ | $<p_{5\sigma}$ | $<p_{5\sigma}$ |
| | | | E(B-V) | | | |
| 1 vs. 2 | $<p_{3\sigma}$ | $<p_{3\sigma}$ | $<p_{5\sigma}$ | $<p_{5\sigma}$ | $<p_{5\sigma}$ | $<p_{5\sigma}$ |
| 1 vs. 3 | $<p_{3\sigma}$ | $<p_{3\sigma}$ | 9.74E-03 | $<p_{3\sigma}$ | $<p_{3\sigma}$ | $p_{3\sigma}$ |
| 2 vs. 3 | $<p_{5\sigma}$ | $<p_{5\sigma}$ | $<p_{3\sigma}$ | $<p_{3\sigma}$ | $<p_{5\sigma}$ | $<p_{5\sigma}$ |
| | | | Mass | | | |
| 1 vs. 2 | 0.417 | 0.411 | 0.747 | 0.417 | 0.968 | 0.707 |
| 1 vs. 3 | 4.92E-02 | 0.136 | 0.549 | 0.182 | 0.634 | 1.12E-02 |
| 2 vs. 3 | 0.642 | 0.274 | 0.871 | 0.920 | 0.889 | 0.280 |

Table 3.5: p-values from KS tests to compare the H$\alpha$ morphological classes of clusters with SED ages ≤10Myr based on their distributions of cluster age (top), reddening (middle), and mass (bottom). These are split based on environment (Isolated, Not Isolated, and All clusters (i.e. regardless of isolation)) as well as whether the Padova or Geneva stellar evolutionary model was used, each assuming Milky Way extinction. "$p_{3\sigma}$" and "$p_{5\sigma}$" represent p-values below 2.70E-03 and 5.73E-07, respectively, indicating that the null hypothesis that the two samples are drawn from the same distribution can be rejected at a >3$\sigma$ or >5$\sigma$ confidence level according to the Gaussian error function.

be statistically different ($\geq 5\sigma$ confidence) from those of the concentrated and partially exposed H$\alpha$ classes, as expected. When the isolated and non-isolated samples are combined to increase the sample sizes, the statistical differences between the age distributions of the concentrated and partially exposed H$\alpha$ classes versus the distribution for clusters without H$\alpha$ remain at the $\geq 5\sigma$ confidence level, while the p-values improve to the $\sim 4\sigma$ confidence level between the age distributions for clusters with concentrated and partially exposed H$\alpha$ morphologies, similar to the confidence levels for non-isolated clusters. These results are also consistent across all stellar evolutionary models and extinction models.

The similarity in both the age distributions and median ages of star clusters with concentrated and partially exposed H$\alpha$ morphologies indicate that the gas clearing timescale is $\lesssim 1$ Myr, in agreement with [68]. Additionally, we can also determine a clearing timescale based on mean ages. Clusters with concentrated H$\alpha$ have a mean age of 2.7 and 2.3 Myr according to the Padova and Geneva models, respectively, while the clusters with partially exposed H$\alpha$ have a mean age of 3.2 and 2.8 Myr, respectively. If we subtract the ages of each H$\alpha$ class in quadrature (assuming simple gaussian statistics are a reasonable approximation for uncertainties such as differences in physical clearing times, measurement uncertainties, and number statistics), we find an age difference between clusters with concentrated and partially exposed H$\alpha$ of 1.7 and 1.6 Myr based on the Padova and Geneva models, respectively. This provides a rough estimate of the clearing time based on our measurements. Splitting the sample into isolated & non-isolated groups reveals that most of this difference in mean age comes from non-isolated clusters, for which the same calculation yields age differences between the two H$\alpha$ classes of 2.1 and 1.9 Myr for the Padova and Geneva models, respectively. These figures therefore suggest a clearing timescale of 1-2 Myr rather than $\lesssim 1$ Myr.

Further, we note that the 10 Myr cutoff is simply a construction of the initial analysis used to limit the number of clusters which require visual inspection for classification (based on the assumption that no H$\alpha$ emission would be found for older clusters), and more significant differences in the age distributions are apparent at the youngest ages (e.g., the peak at 1 Myr for clusters with concentrated H$\alpha$, see Figure 3.4). If we instead consider only clusters with SED ages $\leq$ 5 Myr, which marks the 80th percentile in age for clusters with H$\alpha$ (either concentrated or partially exposed), we find that the median SED ages of these clusters become more distinguished: 1.0 [1.0, 3.0] Myr for clusters with concentrated H$\alpha$, and 2.0 [1.0, 4.0] Myr for clusters with partially exposed H$\alpha$. We also see this reflected in KS tests; the p-values comparing the age distributions for class 1 and 2 H$\alpha$ morphologies are reduced by a factor of ~2, although this remains below the 2-sigma confidence level for the isolated sample of clusters. With these considerations, we report more generally that the gas clearing timescale is 1-2 Myr, in agreement with other recent works such as [36].

As done in [68], we can alternatively infer the lifetimes of the H$\alpha$ classes by examining their relative fractions, with the assumption that our sample is statistically representative of all clusters $\leq$ 10 Myr. For these objects with SED ages $\leq$ 10 Myr, the fraction of clusters with class 1, 2 and 3 H$\alpha$ morphologies is 20-30%, 10-20%, and 50-70%, respectively, where the ranges reflect the use of isolated or non-isolated clusters. These fractions imply a lifetime of 2-3 Myr for concentrated H$\alpha$ morphologies, which indicates when the clusters begin to clear their natal gas, and also a lifetime of 1-2 Myr for partially exposed morphologies, which corresponds to the duration of the gas clearing process. Both of these findings are consistent with the results from the median SED ages of each H$\alpha$ class.

It is important to note, however, that our sample is likely not complete amongst clusters embedded within their natal gas clouds (akin to a concentrated H$\alpha$ morphology) as they can be obscured beyond detection (e.g. [110], [81]), though a more detailed analysis would be necessary than is available here and is thus addressed in future opportunities (Section 3.8).

### 3.4.2 Reddening Statistics

We now examine the reddening of star clusters in each H$\alpha$ morphological class. E(B-V) measures the extinction of a star cluster due to dust, and considering cluster environment and H$\alpha$ morphology, can help to inform us as to the accuracy of the SED-fitting. Figure 3.5 shows distributions of E(B-V) values, used to measure the presence of dust, for each of the H$\alpha$ morphological classes for clusters with best-fit ages $\leq$ 10 Myr. These values are derived from five-band SED fitting, assuming Milky Way extinction [30].

Contrary to the expectation that H$\alpha$ traces dust content, we find clusters with concentrated H$\alpha$ and those without H$\alpha$ to have comparable reddening estimates, while those with partially exposed H$\alpha$ show the least reddening. For the reference (Padova, Milky Way extinction) sample of isolated clusters with SED ages $\leq$ 10 Myr, the median E(B-V) [first quartile, third quartile] of the 171 clusters with concentrated H$\alpha$ is 0.16 [0.08, 0.27] mag, while the E(B-V) for the 99 partially exposed clusters and 601 clusters with no H$\alpha$ emission are 0.06 [0.01, 0.14] and 0.20 [0.06, 0.43] mag, respectively. If we include all clusters regardless of SED-fit age, we find similar results: E(B-V)s of 0.15 [0.07, 0.26], 0.06 [0.01, 0.15], 0.14 [0.04, 0.33] mag are found for clusters with concentrated, partially exposed, and absent H$\alpha$, respectively. The biggest difference in median E(B-V) here is again between clusters without H$\alpha$, as the inclusion of older clusters triples their sample size, however their median

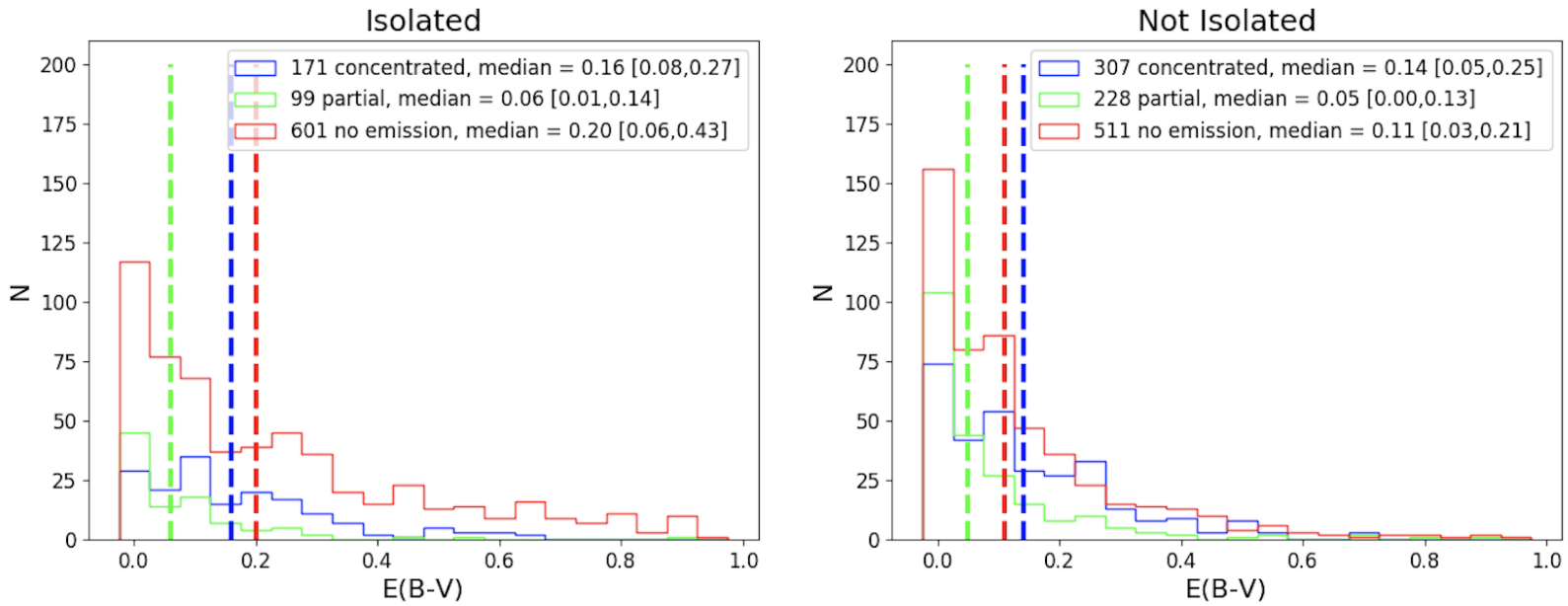


Figure 3.5: Reddening (E(B-V)) histograms for clusters with SED ages $\leq$ 10 Myr and with concentrated H$\alpha$ (blue), partially exposed H$\alpha$ (green), and no emission (red). The left and right plots show the distributions for isolated and non-isolated clusters, respectively. Vertical dashed lines show the median cluster reddening for each of the morphological classes. Comparable reddening distributions are unexpectedly found amongst clusters with concentrated and absent H$\alpha$.

E(B-V) remains larger than that of clusters with partially exposed H$\alpha$ and similar to that of clusters with concentrated H$\alpha$. As also observed in Section 4.1, the sample of non-isolated clusters reveal qualitatively consistent results.

Across all stellar evolutionary models (Padova, Geneva) and extinction models (Milky Way, Starburst, Differential Starburst), and whether or not we delineate between isolated and non-isolated clusters, we find consistent results: clusters with partially exposed H$\alpha$ have the smallest median E(B-V) (0.05-0.08 mag), while those with concentrated H$\alpha$ (0.13-0.16 mag) or no emission (0.11-0.22 mag) have higher, comparable cluster reddening values. These results are also consistent regardless of whether we include compact associations in the cluster sample.

If we take the error in E(B-V) to be the difference between the maximum and minimum E(B-V) value for an individual cluster (see Section 3.2), we find that the errors are greater for clusters without H$\alpha$ (0.09-0.10 mag) than for clusters with concentrated (0.06 mag) and partially exposed (0.05) H$\alpha$ morphologies. These greater errors indicate that the relatively large E(B-V) for clusters without H$\alpha$ may not be physical, as discussed in Section 3.5.

Upon examination of the KS-test results of cluster reddening (Table 3.5), the distributions of E(B-V) for clusters with partially exposed H$\alpha$ and no emission appear statistically different ($\gtrsim 5\sigma$) regardless of whether the cluster is isolated. Clusters with concentrated and partially exposed H$\alpha$ morphologies also appear statistically unique at a $> 3\sigma$ confidence level for all models. The E(B-V) distributions for clusters with concentrated H$\alpha$ and no emission, however, are a bit different: When the sample is divided into isolated and non-isolated samples, we find that while some models show $\sim 3\sigma$ confidence that they are statistically unique, others show significantly lower confidence ($\lesssim 1\sigma$) for both divisions. When we combine the isolated and non-isolated samples, KS tests show that

all distributions are significantly different ($> 5\sigma$) except for clusters with concentrated H$\alpha$ and no emission ($\gtrsim 3\sigma$). The comparable reddening estimates found between these two H$\alpha$ classes are examined further in Section 3.5.

### 3.4.3 Mass Statistics

Lastly, we examine the stellar mass of our star clusters. More massive clusters will more completely sample the IMF and hence be more likely to include massive OB stars. These stars are necessary in this study because they ionize their surrounding gas, which produces the H$\alpha$ emission we use to classify HII region morphologies.

For clusters with best-fit SED ages $\leq$ 10 Myr, the median cluster mass is $\sim$1000 $M_{\odot}$, regardless of the H$\alpha$ classification and whether or not the cluster is isolated. For star clusters of this mass, we are likely to observe effects due to stochastic sampling of the IMF as the colors of the clusters may be disproportionately represented by individual bright stars (e.g. [59]), which in turn can affect the estimated age and E(B-V) determined by the SED-fitting algorithm (e.g. [68]), which assumes a fully populated IMF. We investigate these effects further in Section 3.5.

When we include clusters with SED ages $>$ 10 Myr, we find that the median mass of clusters with concentrated and partially exposed H$\alpha$ remain unchanged ($\sim$1000 $M_{\odot}$), while clusters without H$\alpha$ see their median mass increase to $\sim$4000 $M_{\odot}$. This is likely a selection effect, however, as older objects become less luminous as they age, and thus the minimum detectable cluster mass increases with age for a given magnitude limit (e.g. [2]). A potential complicating factor here is that amongst these more massive objects are likely to be old, globular clusters, as indicated by the significant fraction ($\sim$50%) of clusters without H$\alpha$ which are symmetric (cluster class = 1). The inclusion of globular clusters is notable because SED-fitting has shown particular difficulty in

accurately estimating their ages and reddening ([135, 140]), and with sufficiently underestimated ages, the globular clusters can contaminate our sample of truly young clusters. Examples of such age underestimations are studied further in Section 3.6.

## 3.5 H$\alpha$ morphologies and UBVI Color-Color Diagram

Examining the colors of individual clusters can provide useful insight into the SED-fitting procedure as well as highlight potential anomalies to further investigate. In Figure 3.5, we present color-color diagrams ((U-B) vs. (V-I)) for the full sample of clusters, classified by H$\alpha$ morphology, where the colored points represent clusters with SED ages $\leq$ 10 Myr and gray points show clusters with older SED ages ($>$ 10 Myr). In these plots, we note that clusters with concentrated (blue circles) and partially exposed (green triangles) H$\alpha$ morphologies, which have median SED ages of 1-3 Myr, overlap near the youngest end of the stellar evolutionary models. Clusters without H$\alpha$ emission, on the other hand, are found generally toward the older parts of the SSP model track, as expected.

As in [68], we also observe manifestations of stochastic sampling of the IMF. Most notably, the positions of our clusters in UBVI space are consistent with those predicted by the stochastic modeling of low-mass clusters by [58], [59], and also [112]. Figure 2 of [59] provides an example of these predicted positions in the same color space as Figure 3.5, highlighted by a spray of points to the lower-right of the 10 Myr point of the model SSP track. Despite all of the colored points in Figure 3.5 representing clusters with SED-fit ages $\leq$ 10 Myr, some are found as far along the SSP model as around its 10 Gyr point, and are interspersed amongst the clusters with SED ages $>$ 10 Myr (gray points).

In the upper-right corner of each plot, we provide a reddening vector of $A_V$ = 1.0 [30] which, in principle, indicates that the more a cluster is reddened, the further the cluster will be moved from the model, along the direction of that vector (down and to the right). Typically, this reddening is due to dust covering parts or all of the cluster (see Figure 5 of [72]), however we find in our sample that the clusters with the least evidence of dust (i.e. lacking H$\alpha$ emission) are in fact the ones which appear the most reddened. These occupy the same region as the aforementioned stochastically sampled clusters, and in fact, the color-color plots in Figure 9 of [68] and Figure 9 of [140] show that this phenomenon is indeed at least partly attributable to stochastic sampling effects. In those cases, the fluxes of clusters in this region are dominated by the presence of bright red point-like sources, presumably red supergiants. In this study, at least one bright red point-like source was found within the photometric aperture of ~24% of all clusters with SED ages < 10 Myr and without H$\alpha$. This fraction ranges between ~20-40% with no dependence on galaxy distance. Of all clusters found to the lower-right of the 10 Myr point on the Yggdrasil model (V-I > 0.8, U-B > -1.3), ~70% contain a bright red point-source.

In turn, these clusters containing bright red sources are found to have a median E(B-V) ~2.5x larger than the clusters without a bright red star (0.26 vs. 0.11 mag, respectively). This indicates that the SED algorithm is likely interpreting the red color from bright stars within a cluster as reddening due to dust, which results in an overestimate of E(B-V) while underestimating its age as a consequence of the age-extinction degeneracy. As noted in Section 3.4.2, we see ~2x greater errors in E(B-V) for clusters without H$\alpha$ compared to those with H$\alpha$ (see also [140] & [135]), and we further find that, of the clusters without H$\alpha$, those containing red point-like sources have a median reduced $\chi^2$ value 3x greater than clusters without red sources. These errors indicate that the

stochastic sampling of bright red stars results in poorer fitting of a cluster's SED. It is also noteworthy that these effects are seen even when limiting the sample to clusters $\geq$ 5000 $M_{\odot}$ (middle column of Figure 3.5) and $\geq$ 10000 $M_{\odot}$ (right column), although the sample sizes are small. Beyond the age-extinction degeneracy, the poor fitting we observe may also be due to the assumption of a fixed metallicity for each galaxy, as older clusters are metal-poor relative to the younger population on which the SED-fitting is based (also see [41]).

Another point which was not addressed in [68] is that we find clusters blueward of the SSP models (V-I $\lesssim$ -0.3), approximately half of which belong to galaxies with sub-solar assumed metallicities. These clusters are of particular interest because they should be able to be traced backward along the reddening vector (up and to the left) to the SSP model. However, these clusters cannot be traced back in such a fashion as they are already upward and/or leftward of the model. Even more interesting is that nearly all of these clusters have concentrated H$\alpha$, and would thus likely be reddened. We suggest two possible causes for the very blue color of these clusters:

1) As the model tracks assume a gas covering fraction of 0.5, there could be additional contributions from nebular emission if the covering fraction is higher, which would push the color of these clusters blueward, and would especially affect those with sub-solar metallicities. This effect is demonstrated in Figure 1 of [148], where model predictions of V-I and U-B colors are found to be as much as 0.5 mag less and 0.5 mag greater, respectively, for young clusters which use a covering fraction of 1.0 versus 0.5.

2) Stochastic effects may result in the undersampling of low-mass stars which results in the flux-dominance of massive ionizing blue stars. To this end, [112] find in their models that the presence of two Wolf-Rayet stars (types WC or WNE) within low-mass clusters ($10^3$ $M_{\odot}$) can

produce this effect. Notably, all of the clusters from our sample which are in this region have masses $\leq 5000\ M_{\odot}$.

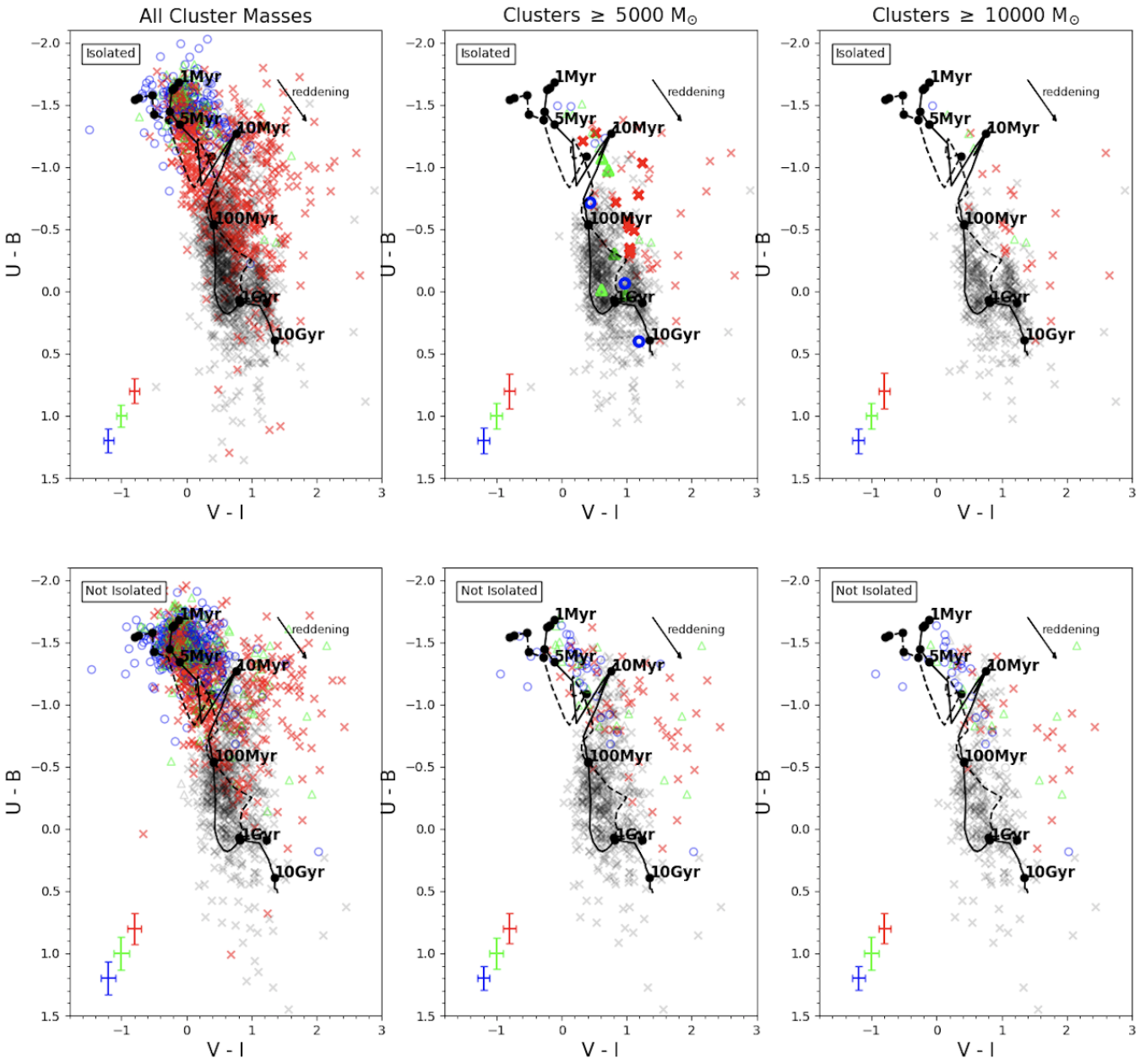
All Cluster Masses
Clusters ≥ 5000 M⊙
Clusters ≥ 10000 M⊙
Isolated
Not Isolated
reddening
1Myr
5Myr
10Myr
100Myr
1Gyr
10Gyr
U - B
V - I

Figure 3.6: (U-B) vs. (V-I) plots of star clusters across all 16 galaxies of the sample. Yggdrasil model tracks (solid line for Z=0.02; dashed line for Z=0.004) used for the fitting of these clusters are included (Table 3.1 lists the metallicity used for each galaxy). 1 Myr, 5 Myr, 10 Myr, 100 Myr, 1 Gyr, and 10 Gyr points along each track are indicated by solid black circles. Blue circles and green triangles, which represent clusters with SED ages ($\leq$ 10 Myr) and concentrated or partially exposed H$\alpha$ morphologies, respectively, are both largely focused near the youngest end of the models. Red Xs, representing clusters with SED ages ($\leq$ 10 Myr) without H$\alpha$, are much more widely dispersed along older sections of the model, as expected. Gray circles, triangles, and crosses represent the same H$\alpha$ morpholgies, but have best-fit ages $>$ 10 Myr. The top and bottom rows of plots show clusters that are isolated and not isolated, respectively. The columns show clusters with no mass limit (left), clusters above 5000 $M_{\odot}$ (middle), and clusters above 10000 $M_{\odot}$ (right). Median photometric errors for each H$\alpha$ morphological class are indicated by crosses in the lower-left of each plot. Bold, colored points in the upper middle plot indicate clusters for which the SED-fit ages seem to be inconsistent with the presence or absence of H$\alpha$; i.e., clusters with SED ages $\leq$ 3 Myr yet no H$\alpha$, and those with associated H$\alpha$ & SED ages $>$ 10 Myr, as further discussed in Section 3.6.

## 3.6 Accuracy of SED-fit Ages

Because key conclusions from this study are based on small differences (1 Myr) in median ages, one of the questions we must ask is how accurate the SED ages are. To investigate this accuracy for individual clusters, we look into two particular cases where the data do not align with expectation: 1) very young (SED age $\leq$ 3 Myr) clusters without H$\alpha$ and 2) older (SED age $>$ 10 Myr) clusters with H$\alpha$. The number of these cases in each field are listed in Table 3.6, where the totals and percentages of their relevant population in the sample are also shown.

### 3.6.1 "Young" Massive Clusters without H$\alpha$

We first examine isolated, massive ($\geq$ 5000 $M_{\odot}$) clusters that do not have H$\alpha$ emission, yet have very young ($\leq$ 3 Myr) SED-fit ages. These are interesting because we expect clusters of these ages and masses to have pre-supernova, massive ionizing stars, and thus to have HII regions. We specify isolated clusters in order to avoid confounding effects neighboring clusters could have on the clearing of a cluster's natal gas and hence the morphological class of H$\alpha$. As shown in Table 3.6, there are only 12 such cases across all 21 fields, however this age restriction means that this represents a lower limit to the overall number of clusters with younger-than-expected SED ages (e.g. [140, 135]).

While these clusters represent the youngest massive clusters without H$\alpha$, we also find that their estimated E(B-V)s are much greater than the larger population. Figure 3.7 shows the age, E(B-V), and mass distributions of all massive, isolated clusters without H$\alpha$, where the filled distributions indicate the 12 with SED ages $\leq$ 3 Myr. The reddening distribution (middle panel) shows that these clusters have a median E(B-V) over 7 times that of the greater sample (1.07 vs.

| | Clusters ≤3Myr without H$\alpha$ | | Clusters >10Myr with H$\alpha$ | |
|---|---|---|---|---|
| Field | Isolated | Not Isolated | Isolated | Not Isolated |
| NGC1313E | 0 | **3** | **1** | **2** |
| NGC1313W | 0 | 0 | 0 | **4** |
| NGC1433 | **8** | 0 | 0 | **4** |
| NGC1705 | 0 | 0 | **1** | **4** |
| NGC3344 | 0 | 0 | 0 | **2** |
| NGC3351 | **2** | **4** | **4** | **5** |
| NGC4242 | 0 | 0 | 0 | 0 |
| NGC4395N | 0 | 0 | 0 | 0 |
| NGC4395S | 0 | **1** | 0 | **1** |
| NGC45 | 0 | 0 | 0 | 0 |
| NGC4656 | 0 | **2** | **1** | 0 |
| NGC5457NW1 | 0 | 0 | **1** | **1** |
| NGC5457NW2 | 0 | **1** | 0 | 0 |
| NGC5457NW3 | 0 | 0 | 0 | 0 |
| NGC5474 | 0 | 0 | 0 | 0 |
| NGC628E | **1** | **2** | 0 | 0 |
| NGC7793E | 0 | 0 | 0 | **1** |
| NGC7793W | 0 | 0 | 0 | **1** |
| UGC1249 | **1** | 0 | 0 | 0 |
| UGC7408 | 0 | 0 | 0 | 0 |
| UGCA281 | 0 | 0 | 0 | **1** |
| **TOTALS** | **12 (63%)** | **13 (26%)** | **8 (40%)** | **26 (32%)** |

Table 3.6: Number counts of massive (≥5000 $M_\odot$) clusters with best-fit ages ≤ 3 Myr without H$\alpha$, and massive clusters with best-fit ages > 10 Myr with H$\alpha$ (concentrated or partially exposed H$\alpha$ morphology). These are organized by field and whether they are isolated, with their totals shown at the bottom. 63% and 26% of massive, young (≤3Myr; before the onset of supernovae) isolated and non-isolated clusters, respectively, are classified as no emission. 40% and 32% of massive, isolated and non-isolated clusters with H$\alpha$, respectively, have best-fit ages > 10 Myr, beyond the expected limit for H$\alpha$ association.

0.15 mag). The stellar masses of these clusters, however, show a relatively flat distribution across the observed mass range, indicating that they do not have relatively lower masses, which would have suggested a greater likelihood of lacking OB stars and hence H$\alpha$ emission.

By visually inspecting each of these clusters, we can determine how trustworthy their age & E(B-V) estimates are. Figure 3.8 displays the 150 pc $\times$ 150 pc RGB postage stamps for each of the 12 clusters. Here we note that these 12 objects of interest are spread across 4 galaxies (NGC 628E, UGC 1249, NGC 1433, and NGC 3351), with two-thirds of them coming from NGC 1433. In two of the postage stamps (objects 887 of NGC 3351 and 114 of NGC 628E), we find evidence in support of their young SED ages: 1) their blue (F275W + F336W) color, 2) their proximity to other blue stars, and 3) H$\alpha$ emission is in the vicinity (within the 75 pc radius of the stamp). For these clusters, it is possible that they have already cleared their natal gas and/or more proximal H$\alpha$ emission is too faint to detect.

The remaining 10 clusters, however, have colors consistent with older star clusters and do not display any of the above characteristics. That is, they show little to no blue emission themselves, lack neighboring blue stars (with the exception of object 865 of NGC 1433, which only has a couple), and do not show any nearby H$\alpha$ emission. Additionally, 9 of these objects are classified as symmetric clusters (cluster class = 1), consistent with old, globular clusters. The clusters found in NGC 1433 are displayed in Figure 3.9, which highlights that many are proximal to the galaxy's bulge, where globular clusters are typically found. Despite the consistencies between these objects and older clusters, we find that the errors in their SED ages are limited: the SED-fitting algorithm

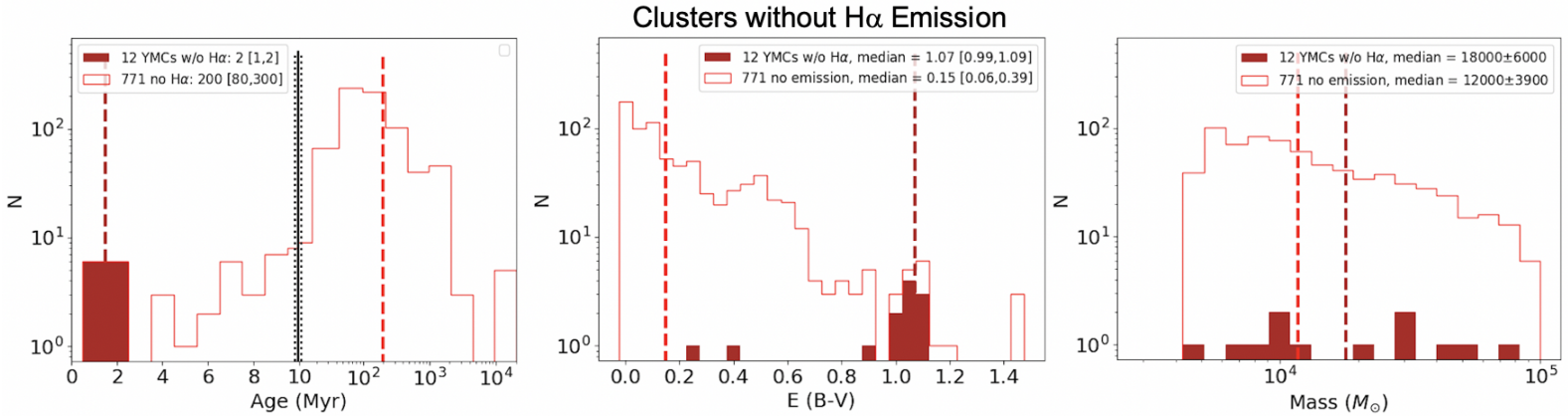


Figure 3.7: Age, E(B-V), and mass histograms of isolated, massive (≥5000 $M_\odot$) clusters without H$\alpha$. The light red outline represents the distribution of all of these clusters while the filled, dark red distribution represents our objects of interest: the youngest (SED age ≤ 3 Myr), massive clusters without H$\alpha$. The dashed, vertical light red and dark red lines represent the medians of all and young massive clusters without H$\alpha$, respectively. While there is not a strong distinction in the stellar mass of these clusters, the clusters with SED ages ≤ 3 Myr are found to have relatively high E(B-V). Note in the leftmost plot that the scale on the x-axis transitions from linear to logarithmic at 10 Myr.

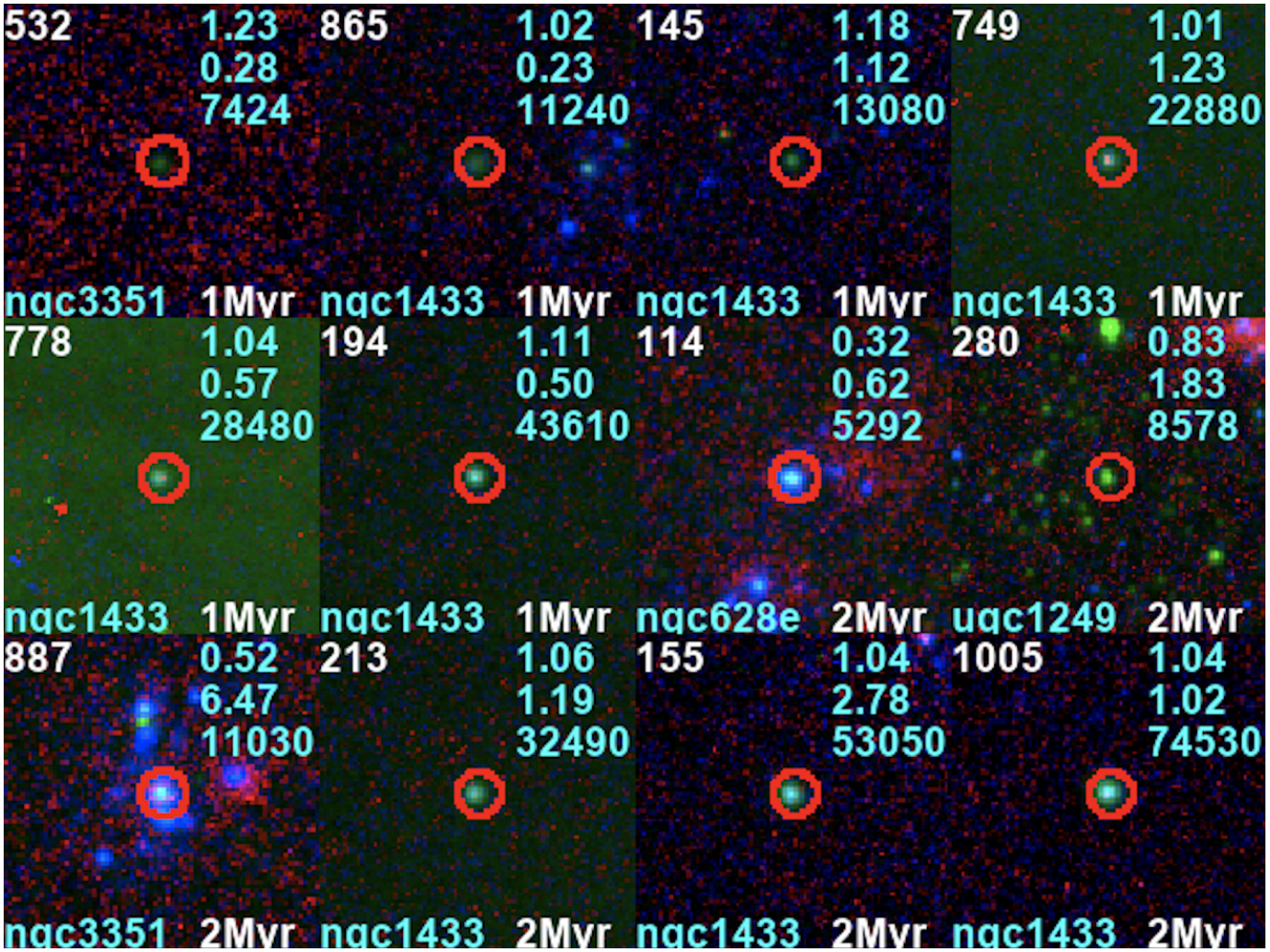


Figure 3.8: 150 pc × 150 pc RGB postage stamps for each of the 12 massive, isolated clusters classified as no emission. Object ID is in the upper-left, field in the lower-left, and SED age in the lower-right of each stamp. In the upper-right corner of each stamp are the E(B-V), $\chi^2$ fit, and mass, from top to bottom.

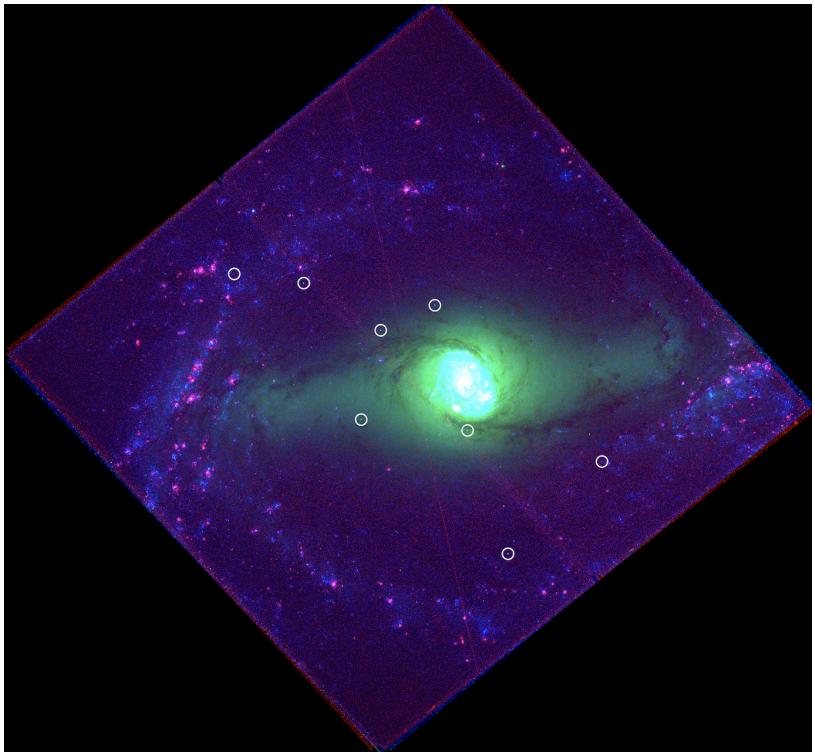

Figure 3.9: Field view of NGC 1433. The locations of clusters without H$\alpha$ but with SED ages $\leq$ 2 Myr and masses $\geq$ 5000 $M_{\odot}$ are denoted by white circles. Proximity to the galaxy's bulge indicates enhanced likelihood that clusters are likely old, globular clusters rather than young clusters.

has determined maximum ages of $\leq 8$ Myr for all of the globular cluster candidates, 7 of which have a maximum age $\leq 3$ Myr.

The positions of these clusters in UBVI space are also consistent with older clusters. Figure 3.5 displays these objects in (U-B) vs. (V-I) space as bold, red Xs in the top, middle panel, where we find all 10 of the older-appearing clusters down and to the right of the 10 Myr point in the SSP model, amongst the clusters with SED ages $> 10$ Myr (gray points). Here we can see that the SED-fitting algorithm is determining these clusters to be young and highly reddened, as indicated by how far they must be traced in the reverse direction of the reddening vector (up and to the left) to reach the youngest end of SSP model, rather than tracing them to the nearest point on the model, which would result in older ages and smaller E(B-V). As noted in Sections 3.2 and 3.5, all of the clusters within a galaxy are fitted assuming the present-day metallicity of its young stellar population, and thus these poor estimates may be due to the fact that these older clusters are fit to an incongruent metallicity model.

Overall, we find that most of these massive clusters with SED ages $\leq 3$ Myr and without H$\alpha$ are consistent with globular clusters, and thus indicate that their ages and E(B-V) are poorly estimated, in agreement with [140] and [135]. While we impose an age cut for these individual inspections, [140] find that there are likely to be several times more globular clusters with older, yet still poorly estimated SED ages, and thus the 12 objects studied here serve as a lower limit for clusters with underestimated ages. The statistical properties of all massive clusters, including these apparently mismeasured ones, are examined in Section 3.6.3.

### 3.6.2 "Old" Massive Clusters with H$\alpha$

The second subset of clusters we examine are those that are massive ($\geq$ 5000 $M_{\odot}$), with H$\alpha$ emission (i.e. either concentrated or partially exposed H$\alpha$ morphologies), and which have SED ages > 10 Myr. As listed in Table 3.6, there are a total of 34 such cases in the sample, which account for 33% of all massive clusters with H$\alpha$. Older objects with H$\alpha$ are of interest because we generally expect clusters > 10 Myr to not be producing ionizing photons, as massive O-stars will have died within this timeframe.

Upon visual inspection of these objects, we find that many appear to display characteristics consistent with young clusters. As seen in the RGB postage stamps (Figure 3.11) for each cluster, there are nearby blue stars within the 75 pc radius of each of the postage stamps, signifying that they share a local space with a young stellar population. This is in addition to the clear presence of H$\alpha$ emission, which is produced by young, ionizing stars. For the clusters which lack strong blue emission (e.g. Object 207), dust could be responsible for obscuring this light, however we would need additional data, such as CO (2-1) maps from ALMA (e.g. [104]), to confirm.

The distribution of properties for these clusters suggest that the potential age overestimation for these clusters is again due to the age-extinction degeneracy. Figure 3.10 highlights the age, E(B-V), and mass distributions of these clusters with H$\alpha$ and SED ages > 10 Myr (cyan-filled) relative to the distributions for all massive clusters with H$\alpha$ regardless of SED age (blue-outlines). While there is no clear correlation with the stellar mass of these clusters, we find that the median SED age of the "older" clusters (50 Myr) is obviously well-beyond the median SED age of all massive clusters with H$\alpha$ (4 Myr). Ionizing flux can be sustained beyond 10 Myr in massive binary systems ([147], [50]), however we also see that these clusters have relatively low E(B-V), with a median reddening ~3x less

than the median reddening of all massive clusters with H$\alpha$ (0.07 vs. 0.20 mag). Despite the clear presence of H$\alpha$, 10 of these clusters (30%) have best-fit E(B-V) = 0.0 mag. Thus we find that the ages of these clusters appear to be overestimated while their E(B-V) is underestimated. Of concern is that the SED errors are limited, as was also observed amongst the "young" clusters without H$\alpha$ (Section 3.6.1). Only 7 of these clusters (20%) have minimum SED ages $\leq$ 10 Myr, none of which belong to the sample of isolated clusters displayed in Figure 3.11, and only 3 have minimum ages $<$ 7 Myr.

The age-extinction degeneracy can also be observed for these clusters in color space. Upon examination of their positions in (U-B) vs. (V-I) space (top, middle panel of Figure 3.5), where the bold blue cirlces and bold green triangles denote these "old" massive clusters with H$\alpha$, we find that they mostly occupy a region with clusters of SED ages $>$ 10 Myr (gray points). This, however, is not unexpected for clusters with these H$\alpha$ morphologies, as the presence of H$\alpha$ typically correlates with higher extinction (e.g. [72]). The SED-fitting could theoretically trace them back to the SSP model below 10 Myr given a large enough E(B-V), as was the case for the "young" clusters without H$\alpha$ from Section 3.6.1 (bold red Xs), however in these cases, better SED fits were found for more proximal (i.e. older) points along the SSP model.

Thus we observe the opposite effect of the age-extinction degeneracy amongst these "old" clusters with H$\alpha$ compared to those discussed in Section 3.6.1, where the SED ages of these clusters appear to be overestimated while E(B-V) is correspondingly underestimated. Although we identify two specific cases of poor SED age-estimates in this section and Section 3.6.1, we note that there are other types of questionable SED ages that the current study is not sensitive to, since they do not involve the presence or absence of H$\alpha$. The total number of bad ages for previous SED fitting

studies such as [140, 135] have been found to be around 10-20%, and thus the 46 of 1408 massive clusters (3%) we investigate in the current study represent a lower limit. The impact of mismeasured properties on the overall statistical properties of the sample are discussed in the following subsection.

### 3.6.3 Statistics of Massive Clusters

Previous studies between star clusters and H$\alpha$ morphology (e.g. [139, 72]) have adopted a mass limit of 5000 $M_{\odot}$ in an attempt to reduce stochastic sampling effects such as those observed in Section 3.5, where bright red point sources can mimic the effects of reddening due to dust. Even amongst these massive clusters, however, we find that the SED-fitting algorithm can still have difficulty in accurately estimating a cluster's age and reddening, as discussed in Sections 3.6.1 & 3.6.2. With these considerations, it is important to examine how the statistical properties of massive clusters compare to the results from our overall sample.

Following [139] & [72], we define our sample of massive clusters to be those that are greater than 5000 $M_{\odot}$. Upon employing this mass limit, we find ~170 of these massive clusters to have SED ages $\leq$ 10, which represents an increase in sample size by a factor of ~4 compared to our previous analysis [68].

For clusters with SED ages $\leq$ 10 Myr, the median age of massive clusters are consistent with the overall sample for each of the H$\alpha$ morphological classes. Isolated clusters with concentrated H$\alpha$, partially exposed H$\alpha$, and no emission have median ages of 1.5 [1.0, 3.8] Myr, 3.0 [1.8, 5.0] Myr, and 7.0 [2.0, 9.0] Myr, respectively. Non-isolated clusters have median ages of 2.0 [1.0, 4.0] Myr, 2.0 [1.0, 4.0] Myr, and 8.0 [4.0, 9.0] Myr for clusters with concentrated H$\alpha$, partially exposed H$\alpha$, and no emission, respectively.

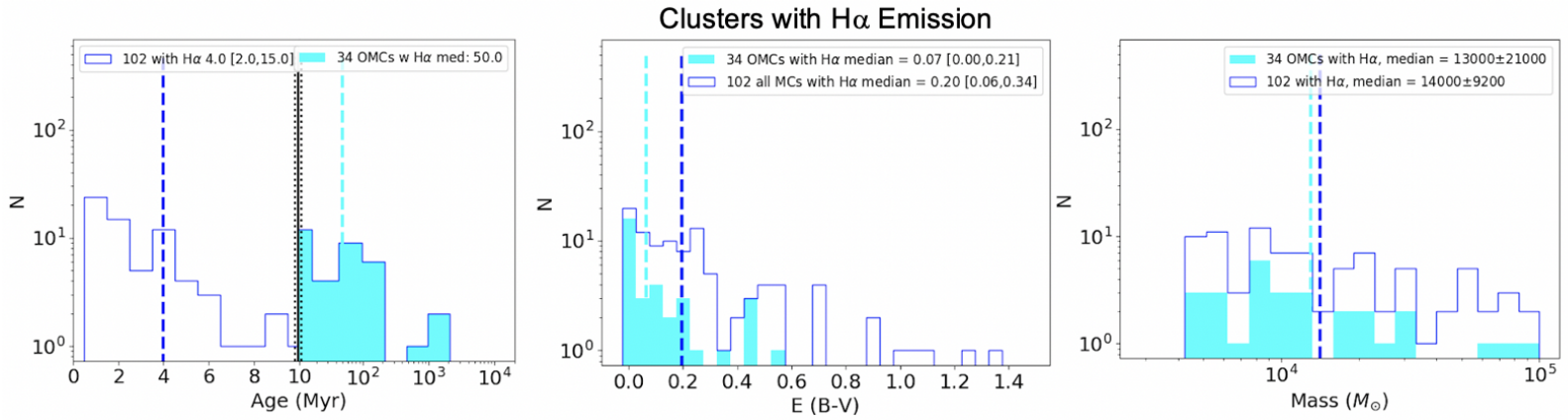


Figure 3.10: Age, E(B-V), and mass histograms of massive ($\geq 5000$ $M_\odot$) clusters with H$\alpha$ (i.e. with either concentrated or partially exposed H$\alpha$ morphologies; labeled as "OMCs"). The dark blue outline represents the distribution of all of these clusters while the cyan-filled distribution represents the oldest (SED age > 10 Myr) massive clusters with H$\alpha$. The dashed, vertical dark blue and cyan lines represent the medians of all and old massive clusters with H$\alpha$, respectively. Note in the leftmost plot that the scale on the x-axis transitions from linear to logarithmic at 10 Myr.

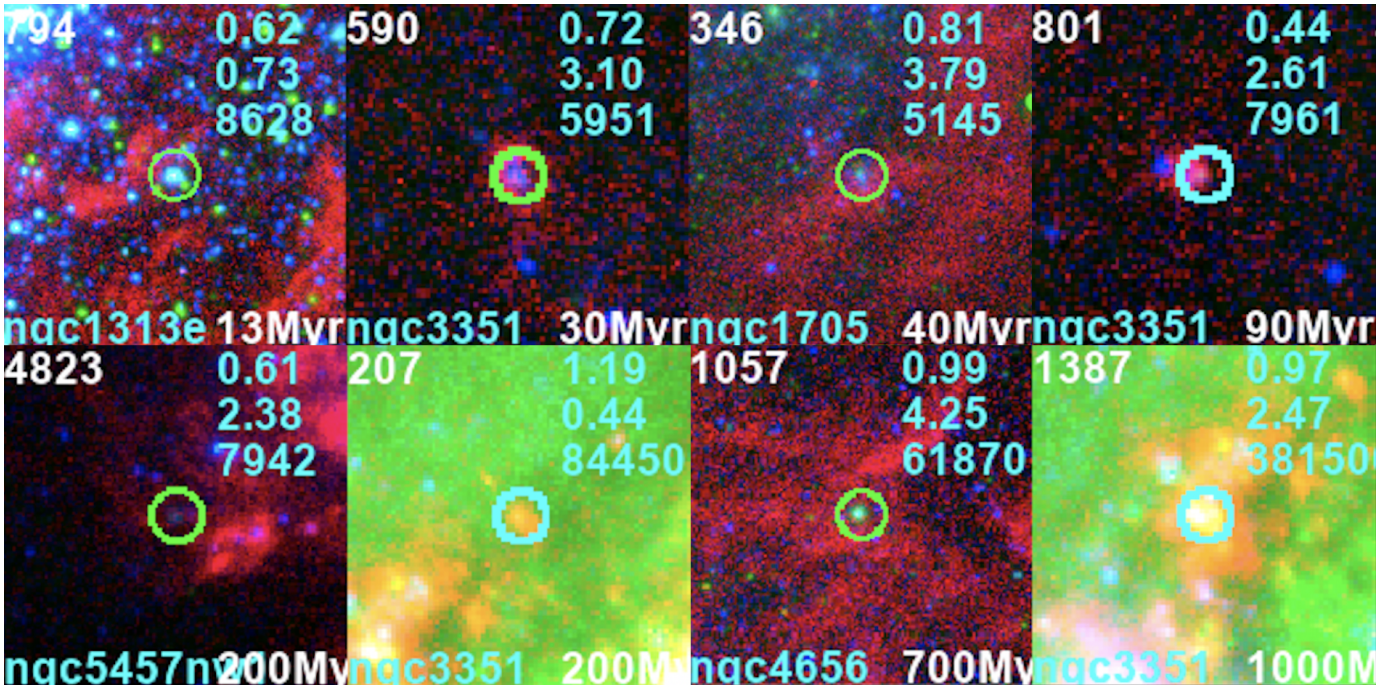


Figure 3.11: 150 pc × 150 pc RGB postage stamps for each of the 8 massive, isolated clusters with H$\alpha$ morphology classifications as either concentrated or partially exposed. Object ID is in the upper-left, field in the lower-left, and SED age in the lower-right of each stamp. In the upper-right corner of each stamp are the E(B-V), $\chi^2$ fit, and mass, from top to bottom. The bright backgrounds of Objects 207 and 1387 are due to their location at the center of NGC 3351.

If we include clusters with SED ages > 10 Myr as highlighted in Section 3.6.2, we find that those with concentrated H$\alpha$ overall retain a median SED age of ~2.0 Myr regardless of the SED model used, which is consistent with our prior results. For clusters with partially exposed H$\alpha$, we find that the isolated sample has a median SED age ranging from 2.0-5.0 Myr, depending on the adopted SED model, which is also roughly consistent with the results of our overall sample. The non-isolated sample shows a larger range in median SED age (2.0-13.5 Myr), although only one of the six models (Padova stellar evolution; Milky Way extinction) produces a median SED age > 4 Myr for this group of clusters, and thus we mostly find good agreement between the SED ages of these massive clusters and those of the overall sample.

As for the reddening of clusters, we find that E(B-V) is generally larger for the massive cluster sample. E(B-V) for massive clusters with partially exposed H$\alpha$ (~0.25 mag) is about five times larger than for the overall sample, regardless of the adopted SED model and whether or not the clusters are isolated. Massive clusters with concentrated H$\alpha$ show higher variance in median E(B-V) between SED models due to the fact that there are only 4 such isolated clusters, but if we combine the isolated & non-isolated clusters for a larger sample (N≈40), the median E(B-V) based on each of the models is ~0.25 mag, or about 70% larger than for the overall sample. We also find that massive clusters without H$\alpha$ have a median E(B-V) (~0.75) about four times larger than for the overall sample (~0.20).

Whereas the overall sample shows that clusters with concentrated H$\alpha$ have ~3 times larger E(B-V) than clusters with partially exposed H$\alpha$, we find that the E(B-V)s are comparable between the two classes for the massive cluster sample, which may further indicate the similarity between the two H$\alpha$ classes. Additionally, the relative increase in E(B-V) for both of these H$\alpha$ classes

could be explained by the fact that massive clusters are more likely to remain detectable with larger attenuation. For the clusters without H$\alpha$, we find in both the massive sample and the overall sample that their E(B-V) is overestimated. While we found bright red point sources to be responsible for their overestimated E(B-V) in Section 3.5, we find that globular clusters are likely responsible for the overestimated E(B-V) in the massive sample, as discussed in Section 3.6.1, and in agreement with similar star cluster studies [140, 135].

Further, the relative fraction of massive clusters in each H$\alpha$ class is also consistent with our overall sample. For clusters with SED ages $\leq$ 10 Myr, the percent of clusters with concentrated and partially exposed H$\alpha$ classes are ~25% and ~15-20%, respectively, which imply that the onset of gas clearing begins early ($\lesssim$ 3 Myr) and takes place over a short interval (1-2 Myr). Considering the clusters with apparently mismeasured SED ages, if we exclude the clusters without H$\alpha$ which appear much older than their SED ages (Sections 3.6.1) and include those with H$\alpha$ and overestimated SED ages (3.6.2), the resultant percentages of isolated clusters with concentrated and partially exposed H$\alpha$ morphologies is roughly consistent with the above values – ~15% & ~23%, respectively.

Thus we find in our analysis of the massive star cluster sample that despite the presence of objects with apparently mismeasured SED ages (Sections 3.6.1 & 3.6.2), we still find overall good agreement between the statistical ages of the massive cluster sample and those of the total sample, and therefore our reported gas clearing timescales are upheld.

## 3.7 Uncertainties

### 3.7.1 LEGUS vs. CIGALE SED-fitting

In our statistical presentation of star cluster properties, we have found that there are sometimes small or even no differences between the median ages, E(B-V)s, and masses of clusters within each H$\alpha$ morphological class. Especially considering the the difficulty that SED-fitting may have with the age-extinction degeneracy (Section 3.6), our confidence level in these star cluster properties and their distinctions is pertinent to drawing meaningful conclusions from their comparisons.

To this point, we have only considered the best-fit properties (those that minimize $\chi^2$) derived from a single SED-fitting algorithm as outlined in Section 3.2. As one way of testing the robustness of these properties, we follow the method of [135] in which we use an independent SED-fitting algorithm, Code Investigating GALaxy Emission (CIGALE; [26, 111, 21]), to produce new catalogs of properties for our sample of star clusters. For valid comparison, CIGALE allows us to input the same assumptions made by LEGUS, namely Yggdrasil SSP models, a Kroupa IMF, Milky Way extinction, and a covering fraction of 0.5.

With these same input parameters, we produce two new star cluster catalogs with CIGALE. For the first of these, we simply use the LEGUS broadband photometry as direct input for CIGALE to perform the SED-fitting. From this fitting, CIGALE will output not only the desired star cluster properties, but also the photometry of the best model fit for each cluster. For the second catalog, fluxes for each cluster are randomly chosen from Gaussian distributions centered on its best model fit, where the standard deviations are based on the individual photometric errors. Once all fluxes are thus determined, they are then fed back into CIGALE to produce new star cluster properties. In this manner, we have 1) a direct comparison of SED-fitting algorithms using the same photometry, and

2) a set of "mock clusters" for comparison. To note, the age grids of sub-solar metallicity models in CIGALE are truncated relative to the LEGUS models, thus our re-fitting is performed for the 13 fields for which LEGUS assumes solar metallicity (see Table 3.1). This accounts for 2787 of the 3757 (73%) star clusters of our sample, for which we present the following analysis.

Overall, the median difference in each of the cluster properties between the catalogs is small, although we note that there is considerable scatter. Figure 3.12 displays the plots comparing each of the three star cluster properties according to the three catalogs. The top row shows the comparisons between LEGUS fitting and the initial CIGALE fitting while the bottom row compares the initial CIGALE fitting to the mock cluster fitting. To the right of each of these plots is a histogram corresponding to the true distribution of points, which serves to highlight that although some clusters show large (e.g. up to ~2 dex in age) disagreements between the star cluster catalogs, the vast majority of clusters show small or no discrepancies. As a result, we find that the overall differences between the catalogs are quite small: the median ratio of cluster ages is less than 0.005 dex for each H$\alpha$ morphological class and for each catalog comparison, while the median ratio of cluster mass is less than 0.05 dex for each of the comparisons. The median difference in E(B-V) is no more than 0.02 mag across each H$\alpha$ class and catalog, and the majority of these comparisons have no difference in median E(B-V). These results are consistent with [135], who found median age and mass ratios of 0.001 and 0.003 dex, respectively, when comparing LEGUS & CIGALE catalogs for the 292 clusters of NGC 3351, one of the galaxies in our sample. While these median differences are small, scatter is considerable: the standard deviation in the sample of properties are ~0.35, ~0.10, and ~0.20 for age, E(B-V), and mass, respectively.

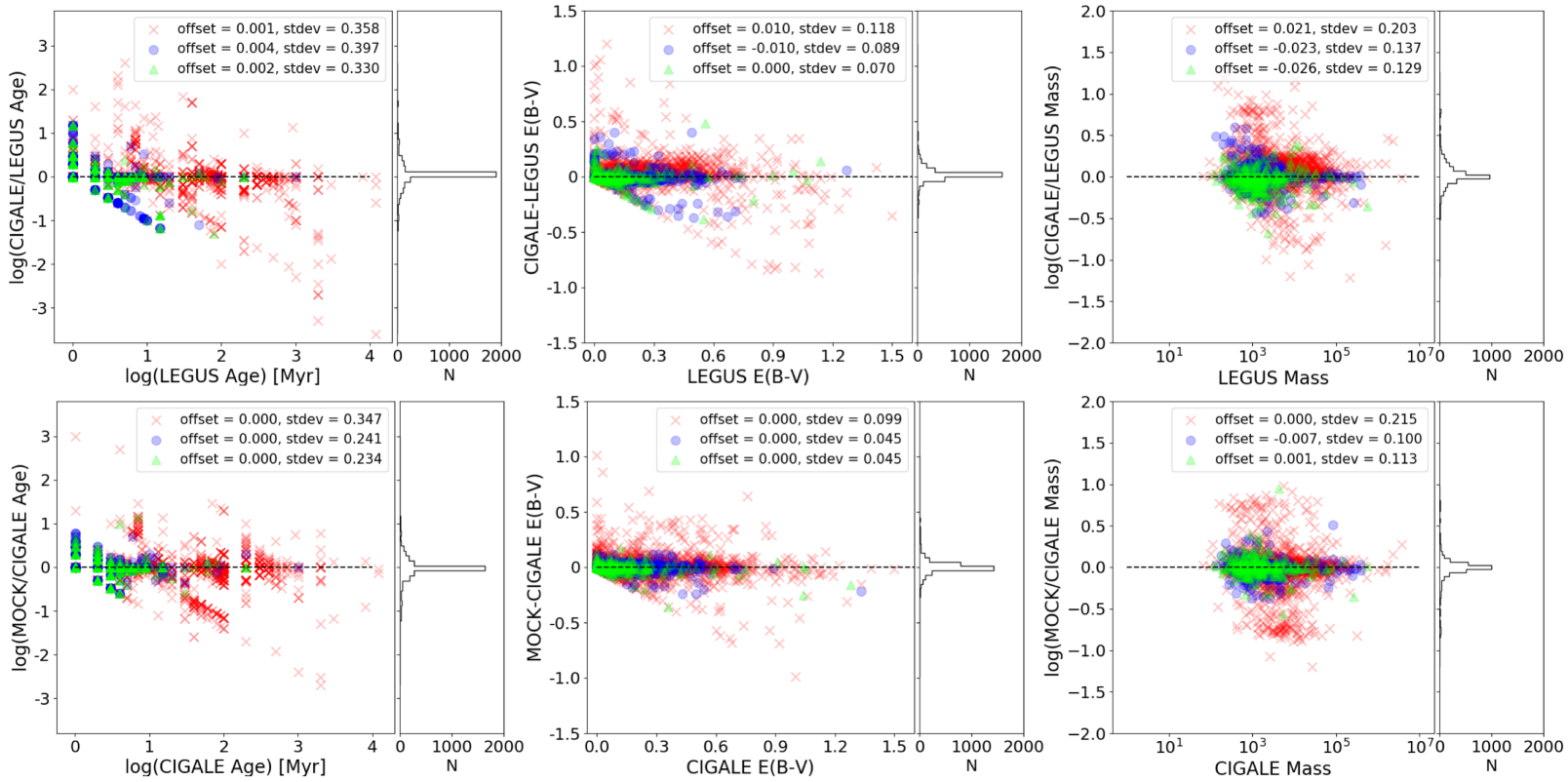


Figure 3.12: Comparison of star cluster properties (age, E(B-V), and mass in columns from left to right) between three SED-fitting methods. The top row compares LEGUS results (as reported throughout this paper) with the results of CIGALE's SED-fitting of the same LEGUS photometry, while the bottom row compares these initial CIGALE results with a set of Gaussian-determined "mock clusters" also fitted with CIGALE. While there appears to be considerable scatter amongst these points, the histograms provided to the right of each plot indicate that the vast majority of clusters have consistent properties between the three methods. The median offset and standard deviation for each property, separated by H$\alpha$ morphology, are shown in the legend of each plot and highlight the small overall differences between methods.

The observed scatter can in part be attributed to systematic effects. The diagonal striping that can be seen in the age comparisons in the left column of Figure 3.12 is due to the discrete nature of the allowed ages in the LEGUS and CIGALE models (i.e., 1, 2, 3, 4 . . . Myr), as can be seen by the discrete vertical lines. For example, in the upper left panel, the lowest diagonal represents values of LEGUS = 1, 2, 3, 4, . . . Myr and CIGALE = 1 Myr. The next higher diagonal stripe represents LEGUS = 1, 2, 3, 4 . . . Myr and CIGALE = 2 Myr. The discrete ages also produce systematic shifts in the ages and E(B-V)s of clusters at the extreme ends of our fixed grids, where a cluster with LEGUS age = 1 Myr must have a CIGALE age $\geq$ 1 Myr, which contribute to the standard deviations shown in the legends of Figure 3.12.

These systematic effects as well as random uncertainties are reflected in the standard deviations, where we glean that cluster ages are consistent between the SED-fitting algorithms to within ~0.35 dex or about a factor of 2, as was also found in previous studies such as [140]. While we do find a few more extreme discrepancies as high as 3 dex, these objects are mostly clusters without H$\alpha$, which include globular clusters (see also [140]. These objects are the subject of discussion in Section 3.6.1.

Despite the notable scatter in our comparisons, we still see very small overall shifts in the statistical properties of star clusters, and do not affect the results we presented in Section 3.4. The median SED ages of clusters with concentrated (1-2 Myr), partially exposed (2-3 Myr), and absent H$\alpha$ (4-5 Myr), as given by the two CIGALE-based catalogs, are consistent with what we have found based on the LEGUS catalogs. This consistency similarly holds for cluster reddening, where the median E(B-V)s of clusters with concentrated, partially exposed, and absent H$\alpha$ are 0.15, 0.04-0.05, and 0.14-0.15 mag, respectively.

Overall, this exercise demonstrates that the SED-fitting algorithms used by PHANGS-HST and LEGUS are consistent, however this does not mean that the age estimates themselves are all correct, only that they are reproducible. In fact, the clusters with apparently mismeasured ages which we investigate in Sections 3.6.1 & 3.6.2 have similarly poor age estimates when fitted with CIGALE instead. As discussed in Section 3.5 above, and in more detail in [140] & [135], the SED ages appear to be underestimated in as much as ~25% of the older cluster population in favor of overestimated E(B-V), based on the number of clusters without H$\alpha$ and young age estimates either due to red point sources or an overall red color. For a more detailed analysis of the SED-fitting algorithms presented in this Section for the star clusters of one of our galaxies (NGC 3351), we refer the reader to [135].

### 3.7.2 Resolution

The galaxies in our sample span a range of distances from ~3–10 Mpc. Because the nearest galaxies in the sample will have ~3x better physical resolution than the most distant ones, an important question to address is whether the H$\alpha$ morphological classifications are dependent on the resolution of our images. To test this, we degrade H$\alpha$ imaging of our nearest galaxy (NGC 7793; 3.44 Mpc) such that it appears as though we observed it at the distance of our furthest galaxy (NGC 3351; 10.0 Mpc), and then reclassify each of the clusters according to the morphology of their degraded H$\alpha$ emission. To further examine the limits of this type of morphological analysis, we also perform reclassifications for H$\alpha$ reprojected to a distance of 20.0 Mpc as well as for ground-based H$\alpha$ imaging.

The first step in the degradation process is to smooth the image to the appropriate full width at half maximum (FWHM), which we do by convolving the image with a 2D Gaussian function with a standard deviation corresponding to the difference in quadrature between the FWHM of the

original image and the expected FWHM of the new image. In order to retain a consistent pixel scale, we then reproject the image onto a smaller grid to match that of the galaxy at a projected distance of 10.0 or 20.0 Mpc. At this point it is important to subtract the background from the image, as the previous steps produce a smoothing effect that reduces noise. With the background subtracted, we scale down the signal of the image by a factor of the relative distance squared to obey the inverse square law. Next, we reintroduce the original background to the image. We reproduce this background by drawing from a Gaussian distribution such that the final image's background level and its standard deviation match those of the original image. Finally, we introduce slight pixel-to-pixel correlation by convolving the image with a compact Gaussian.

Figure 3.13 illustrates the results of such image degradation in comparison to the original *HST* image for NGC 7793W as well as overlapping ground-based H$\alpha$ taken with the Cerro Tololo Inter-American Observatory (CTIO) 1.5m telescope as part of the Spitzer Infrared Nearby Galaxies Survey (SINGS) program [79]. The top row of images share an angular scale ($1 \times 1$) while the bottom row shows an example HII region at a shared physical scale of 150pc $\times$ 150pc. Compared to the original H$\alpha$ image (leftmost column), we see in the top row that the two degraded images (middle columns) appear to have a similar background level, while the brightest regions become expectedly smaller and fainter. When we zoom into the HII region shown in the bottom row, we note that the clearing at the center of the region, which is obvious in the original image, becomes smoothed over as the image degrades. The central dip in flux remains visible at a projected distance of 10 Mpc, but appears almost imperceptible at a projected distance of 20 Mpc, and is completely undetectable in the CTIO image (right column). On its short-axis, the cleared region at the center of bubble is $\sim$10 pixels in diameter in the original image, which is commonly observed for these

bubble-like morphologies in this analysis. At a projected distance of 20 Mpc, these same areas of clearing would be less than 2 pixels wide, hence why it appears that this distance represents a natural limit to identifying these structures. The CTIO image has an approximate angular resolution of 1, which is $> 10$ worse than the resolution of the *HST* image (~0.08) and is thus simply unable to resolve structures of this scale.

Once all of the images are produced, we reclassify all 221 clusters within the NGC 7793W field according to the H$\alpha$ emission from each image. The classification procedure is similar to that outlined in Section 3.2: we create 150 pc $\times$ 150 pc postage stamps centered on each cluster from the LEGUS catalog and assemble the stamps into a single collage ordered by their best-fit SED age, and then into separate collages based on their initial H$\alpha$ classification. However, rather than using RGB images to aid in classification, here we simply use the continuum-subtracted H$\alpha$ to determine each cluster's H$\alpha$ morphology. Examples of H$\alpha$ morphologies which receive the same classification according to all of the images are shown in Figure 3.14.

Table 3.7 displays the results of the reclassifications in terms of what percent of the original H$\alpha$ classes are reclassified as a class 1, 2, or 3 (1 = concentrated, 2 = partially exposed, 3 = no emission) according to the each of the new images. Overall, we find relatively good agreement ($> 74\%$) between the original classes and those determined using the d = 10.0 Mpc image, and we note that this agreement decreases with decreasing resolution, as expected. We also find that the H$\alpha$ morphologies which receive a new class are almost exclusively given a more concentrated classification (e.g. a partially exposed morphology gets reclassified to a concentrated morphology), due to the smoothing effect discussed earlier, regarding the example HII region in Figure 3.13.

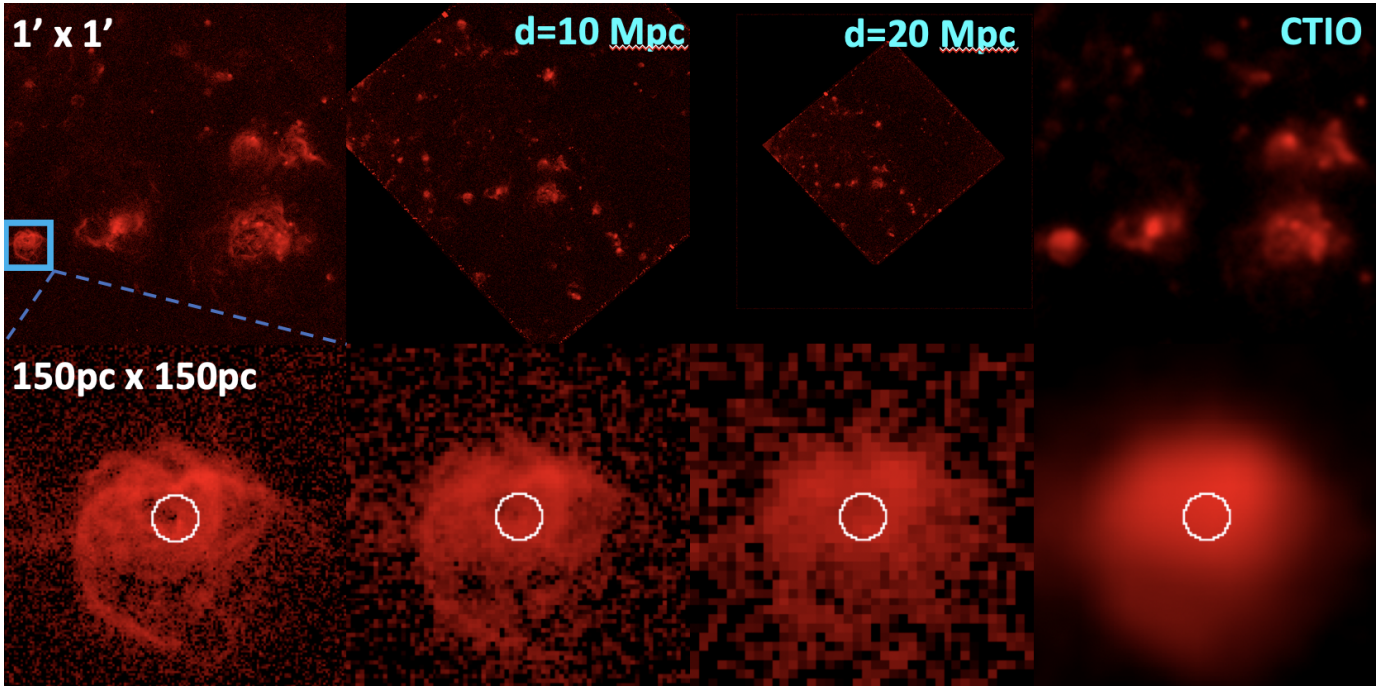


Figure 3.13: Continuum-subtracted H$\alpha$ images of NGC 7793W with varying physical resolution. From left to right, the columns display 1) images of the original *HST* data from LEGUS (~1.3 pc resolution), 2) the *HST* data degraded to resemble the data at a distance of 10.0 Mpc (~4.6 pc resolution), 3) the *HST* data degraded to resemble the data at a distance of 20.0 Mpc (~9.2 pc resolution), and 4) ground-based H$\alpha$ taken with the CTIO 1.5m telescope as part of the SINGS program ([79]; ~16.7 pc resolution). The top row shows images of the galaxy at the same angular scale (1 $\times$ 1) and the bottom row shows an example an example HII region at the same physical scale (150 $\times$ 150 pc).

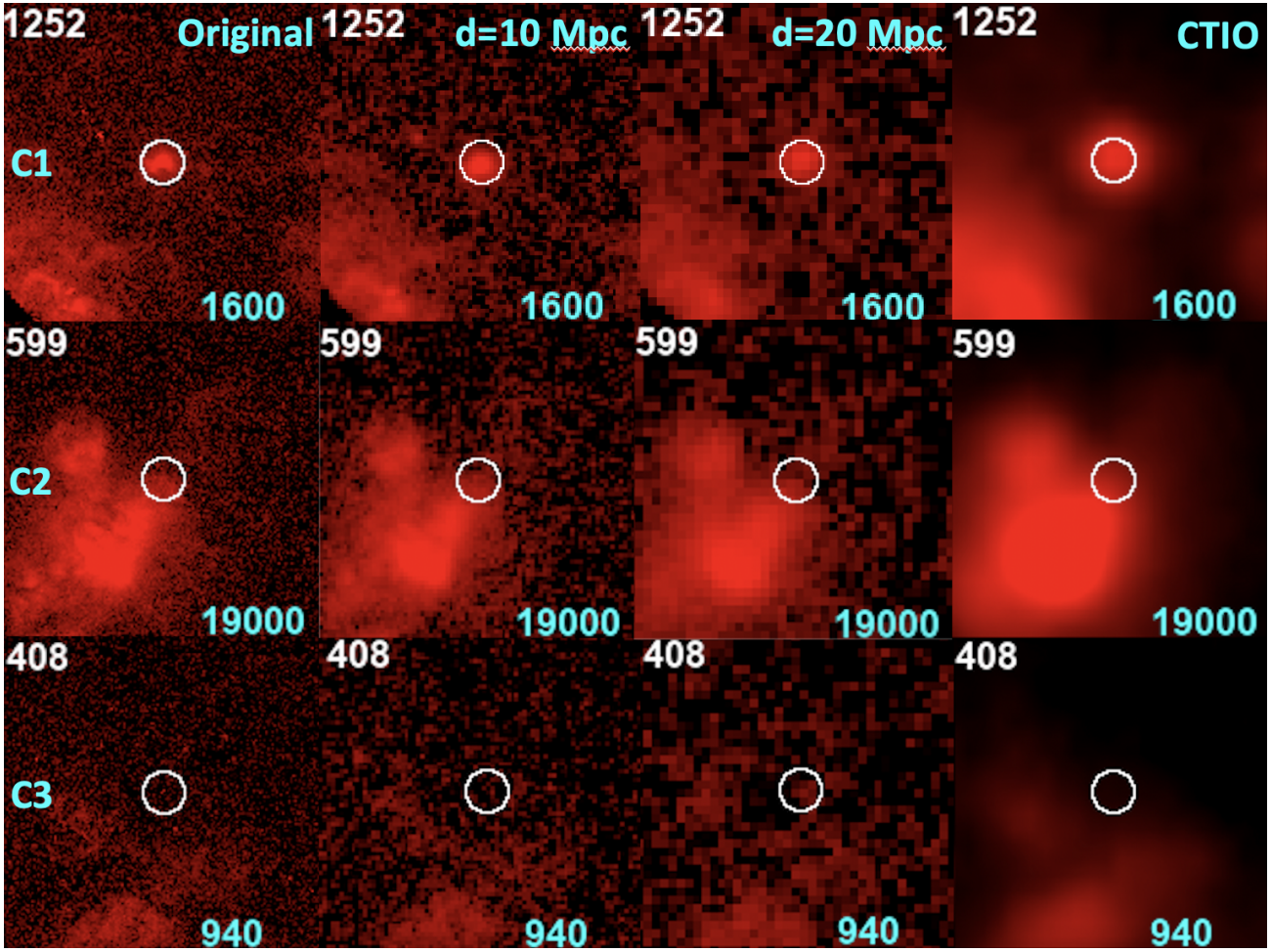


Figure 3.14: 150 pc × 150 pc postage stamps of continuum-subtracted H$\alpha$ comparing the original *HST* images of three NGC 7793 clusters (first column) with their images projected to 10.0 Mpc (second column), projected to 20.0 Mpc (third column), and with the CTIO image (fourth column). The top, middle, and bottom rows show an example class 1, 2, and 3 H$\alpha$ morphology, respectively, which received the same classification according to all four images. Stamps include the Object ID in the upper-left and stellar mass in the lower-right.

**Agreement Fractions for H$\alpha$ Reclassifications**

| | | d = 10.0 Mpc (~4.6 pc) | | | d = 20.0 Mpc (~9.2 pc) | | | SINGS (CTIO; ~16.7 pc) | | |
|---|---|---|---|---|---|---|---|---|---|---|
| | N | Class 1 | Class 2 | Class 3 | Class 1 | Class 2 | Class 3 | Class 1 | Class 2 | Class 3 |
| LEGUS Class 1 | 28 | **100.0%** | 0.0% | 0.0% | **100.0%** | 0.0% | 0.0% | **100.0%** | 0.0% | 0.0% |
| LEGUS Class 2 | 27 | 22.2% | **74.1%** | 3.7% | 29.6% | **63.0%** | 7.4% | 74.1% | **25.9%** | 0.0% |
| LEGUS Class 3 | 156 | 0.0% | 4.5% | **95.5%** | 0.0% | 5.8% | **94.2%** | 0.0% | 14.1% | **85.6%** |

Table 3.7: Comparison between H$\alpha$ morphological classifications for NGC 7793W based on the original *HST* H$\alpha$ image (LEGUS Classes) and 1) *HST* H$\alpha$ reprojected to a distance of 10.0 Mpc, 2) *HST* H$\alpha$ reprojected to d = 20.0 Mpc, and 3) ground-based CTIO data from the SINGS program [79]. The physical resolution for each is also included, compared to ~1.3 pc with the original image. Rows display the number of each of the original classifications and include the percentage of those that were reclassified as a class 1, 2, or 3 (1 = concentrated, 2 = partially exposed, 3 = no emission) according to each of the three new images. As physical resolution decreases, the recovery rate of the original classes decreases, as expected. This is due to the fact that the cleared regions immediately surrounding a cluster are often smoothed over, which results in a more concentrated classification, e.g. an HII region originally identified as class 2 appears instead as a class 1 according to the lower resolution image.

The H$\alpha$ class most affected by the reclassification process is the partially exposed class of objects, due to the fact that it requires the resolution of the smallest structures such as bubbles and filaments. When the galaxy is projected out to a distance of 10.0 Mpc, 74% of the partially exposed H$\alpha$ morphologies are retained, while 63% are retained when projected out to 20.0 Mpc, and only 26% are retained when using the ground-based imaging. The remaining clusters are almost all reclassified as having concentrated H$\alpha$, as the lower resolution smooths over small clearings, however a couple of HII regions become too faint for observation at their further projected distances and as such are reclassified as having no emission. Additionally, all of the clusters classified as having partially exposed H$\alpha$ according to the CTIO image are found at the edges of crowded regions (having neighboring clusters within 75 pc; see Object 599 in Figure 3.14); no clear bubble structures, as seen in the original image of Object 2099 (Figure 3.13), are identified with the ground-based H$\alpha$ image.

Better agreement is found amongst clusters without H$\alpha$, as $\lesssim$ 10% of these objects are given a new classification based on the lower-resolution images. Each of these objects are reclassified as partially exposed, as more distant H$\alpha$ is smoothed such that it appears closer to the cluster than originally observed. This effect can be seen for Object 408 in Figure 3.14, however in this case, the smoothed H$\alpha$ remains distinct enough to retain the cluster's H$\alpha$ class 3 label. Regardless of the H$\alpha$ image used, all of the clusters with an originally-determined concentrated morphology retained their classification, as smoothing does not affect this classification and the regions remained sufficiently bright for observation (e.g. Obejct 1252 in Figure 3.14).

Upon these reclassifications, it is important to examine their effects on our statistical results of cluster properties. In Table 3.8, we show the median age (top) and reddening (bottom) for clusters

with SED ages $\leq$ 10 Myr according to their respective classifications. For all of the images used to classify the H$\alpha$ morphologies, we find equivalent median ages for the three classes: 3 Myr for clusters with concentrated H$\alpha$, 3 Myr for clusters with partially exposed H$\alpha$, and 5 Myr for clusters without H$\alpha$, and the median ages of clusters with concentrated and partially exposed H$\alpha$ do not change when clusters with SED ages > 10 Myr are included. The age distributions for these clusters show that the majority ($\gtrsim$ 60%) of those which have changed classifications are between 2-5 Myr. Additionally, while we find a modest peak of clusters with concentrated H$\alpha$ at 3 Myr based on the *HST* H$\alpha$, the peak becomes much more pronounced as the physical resolution decreases, which also diminishes the peak of these clusters at 1 Myr which was much more clearly observed for the entire sample in Figure 3.4. Without a strong peak at 1 Myr, the median age of clusters with concentrated H$\alpha$ does not change based on whether we choose an age limit of 10 Myr or 5 Myr, regardless of the image used, contrary to what is observed for the whole sample (Section 3.4.1), though this could be an effect of the smaller sample size. Thus find even greater consistency amongst the ages of clusters with concentrated and partially exposed H$\alpha$ when the sample is reduced to a single field in NGC 7793W (median = 3 Myr).

Additionally, if we examine the relative fraction of H$\alpha$ morphologies with cluster SED ages $\leq$ 10 Myr as done in Section 3.4.1, we find that the percent of clusters with concentrated H$\alpha$ notably increases as resolution decreases. The classifications based on the original H$\alpha$ and the two degraded images show that 20-30% of clusters have concentrated H$\alpha$ morphologies, which implies that gas clearing begins at 2-3 Myr, consistent with our previous findings. The classifications based on the SINGS data, however, show that almost 40% of these clusters have concentrated H$\alpha$, which would indicate that clearing begins at an age (~4 Myr) older than previously discussed, and would

**Statistical Star Cluster Properties for H$\alpha$ Reclassifications**

| | Original H$\alpha$ | | d = 10.0 Mpc | | d = 20.0 Mpc | | SINGS (CTIO) | |
|---|---|---|---|---|---|---|---|---|
| | N | Median Age (Myr) | N | Median Age (Myr) | N | Median Age (Myr) | N | Median Age (Myr) |
| Concentrated | 28 | 3.0 [1.8,3.2] | 34 | 3.0 [2.0,3.0] | 39 | 3.0 [2.0,3.0] | 48 | 3.0 [2.0,3.0] |
| Partially Exposed | 25 | 3.0 [2.0,3.0] | 23 | 3.0 [2.0,3.5] | 19 | 3.0 [3.0,3.5] | 22 | 3.0 [2.2,4.8] |
| No Emission | 76 | 5.0 [3.0,7.0] | 72 | 5.0 [3.0,7.0] | 71 | 5.0 [3.0,7.0] | 59 | 5.0 [3.0,7.0] |
| | N | Median E(B-V) | N | Median E(B-V) | N | Median E(B-V) | N | Median E(B-V) |
| Concentrated | 28 | 0.12 [0.09,0.26] | 34 | 0.11 [0.06,0.23] | 39 | 0.11 [0.05,0.20] | 48 | 0.10 [0.05,0.17] |
| Partially Exposed | 25 | 0.06 [0.00,0.13] | 23 | 0.07 [0.01,0.13] | 19 | 0.10 [0.05,0.14] | 22 | 0.11 [0.07,0.14] |
| No Emission | 76 | 0.10 [0.06,0.18] | 72 | 0.11 [0.06,0.18] | 71 | 0.11 [0.06,0.18] | 59 | 0.11 [0.06,0.18] |

Table 3.8: Comparison of the age (top) and E(B-V) (bottom) statistics of clusters whose H$\alpha$ morphologies have been determined using, from left to right: 1) the original *HST* H$\alpha$ image, 2) *HST* H$\alpha$ reprojected to a distance of 10.0 Mpc, 3) *HST* H$\alpha$ reprojected to d = 20.0 Mpc, and 4) ground-based CTIO data from the SINGS program [79]. Statistics are shown for clusters with SED ages $\leq$ 10 Myr, however these results are largely unaffected when the age cut is removed (except for clusters without H$\alpha$, whose median age expectedly increases with the inclusion of older clusters).

also make a crucial change to our conclusions regarding the feedback mechanisms responsible for clearing, as this older age would then allow for supernovae to have already begun igniting and thus take emphasis away from other feedback mechanisms such as stellar winds and radiation pressure.

For cluster reddening, we find very small differences (~0.01 mag) between the original classifications and the 10.0 Mpc reprojection, though we also observe a notable converging of E(B-V) amongst the three classes as the physical resolution decreases. This convergence occurs due to clusters originally classified with partially exposed H$\alpha$ losing clusters with low E(B-V) to the concentrated class of objects while gaining clusters with relatively higher E(B-V) which were originally classified as having no emission.

Overall, we find good agreement in both the visual H$\alpha$ classifications and statistical properties of clusters in NGC 7793W at the original physical resolution and when the galaxy is projected out to a distance of 10.0 Mpc. This indicates that our analysis of H$\alpha$ morphologies across a distance range of ~3–10 Mpc is robust to resolution effects. We also project the galaxy out to a distance of 20.0 Mpc, where we appear to be around the limit for the resolution of fine bubble and filamentary structures commonly used in the classification of partially exposed morphologies. When we examine ground-based H$\alpha$ data, we find particularly poor agreement in identifying partially exposed H$\alpha$ morphologies, as it is impossible to resolve their common small structures, which serves to highlight the importance of *HST*'s resolution capability in identifying early stages of gas clearing and thereby understanding the mechanisms responsible for it.

## 3.8 Summary & Conclusions

To expand on our work in [68], we analyze 3757 star clusters in 21 *HST* WFC3/UVIS fields covering 16 galaxies (spanning a distance range of ∼3–10 Mpc) from the LEGUS sample (GO-13364; PI D. Calzetti). This study includes all LEGUS galaxies with both *HST* H$\alpha$ narrowband imaging (GO-13773; PI R. Chandar) and cluster catalogs containing SED-fit cluster properties [2] published as of 2022 January, plus an unpublished catalog of clusters in NGC 5457. We study all visually-identified cluster class 1, 2, and 3 objects corresponding to symmetric, asymmetric, and multi-peaked clusters, respectively. Relative to [68], the galaxy sample is increased by a factor of ∼4 and the star cluster sample increased by a factor of ∼6. One key addition in this study is that H$\alpha$ morphology classifications have been made for all star clusters regardless of SED age while [68] only considered clusters with SED ages $\leq$ 10 Myr.

By comparing different H$\alpha$ morphologies with the properties of their host star clusters, which effectively represent single-aged stellar populations, we seek to gain insight into the timescales, and thus the physical processes at work, in the clearing of a cluster's natal gas. A multi-stage process of visual inspection is employed to classify clusters according to their H$\alpha$ morphology (concentrated, partially exposed, or no emission), and the clusters are further categorized by whether they have neighboring clusters ($\leq$ 75 pc away), which could affect the clearing timescales.

Here we present a summary of our results:

1 Of the clusters with SED ages $\leq$ 10 Myr, those with concentrated H$\alpha$ have a median age of 1-2 Myr, those with partially exposed H$\alpha$ have a median age of 2-3 Myr, and those without H$\alpha$ have a median age of 3-6 Myr (ranges reflect differences resulting from various dust and stellar population models used in the SED fitting). These medians represent a shift to

slightly younger ($\leq$ 1 Myr) ages than was found in [68]. Together with the inferred ages from the relative fraction of each H$\alpha$ morphology, they support the two main conclusions of [68] and others: Firstly, the prevalence of clusters which show evidence of gas clearing (partially exposed H$\alpha$ class) and yet have SED ages younger than the possible onset of supernovae ($\leq$ 3 Myr) highlight the importance of pre-supernova gas clearing mechanisms such as stellar winds, radiation pressure, and photoionization during the first few Myr of a cluster's life (see also [36]). Secondly, the age difference between clusters with concentrated and partially exposed H$\alpha$ suggests short (1-2 Myr) clearing timescales.

2 Clusters with concentrated H$\alpha$ and those without H$\alpha$ emission share similar median E(B-V) values ($\sim$0.2 mag). With a median cluster mass of $\sim$1000 $M_{\odot}$, we find that the reddening of clusters without H$\alpha$ are likely overestimated due to the presence of bright red stars, a result of stochastic sampling of the IMF. We also see clusters with concentrated H$\alpha$ which are found blueward of the young end of the SSP models, potentially due to additional contributions from nebular emission [148], or the presence of two or more Wolf-Rayet stars (type WC or WNE; see [112]). These latter stochastic sampling effects instead have a bias toward bluer colors, and thus lower E(B-V).

3 We find that at least 46 of 1408 (3%) massive ($\geq$ 5000 $M_{\odot}$) clusters appear to have questionable SED ages, based on our H$\alpha$ study. These fall into two categories. The first group of anomalies consists of 12 isolated clusters with no H$\alpha$ emission, yet which have very young ($\leq$ 3 Myr) apparent SED ages. Upon visual inspection of each object's image, 10 of the 12 appear to have features consistent with much older clusters (i.e., globular clusters), including their color, symmetry, lack of nearby young stars, lack of H$\alpha$ emission, and presence in the bulge.

The second group of anomalies consists of 34 massive clusters with H$\alpha$ emission (2% of all massive clusters), but apparent SED age estimates that are old (> 10 Myr). We note that there are other types of questionable SED age estimates that the current study is not sensitive to, since they do not involve the presence or absence of H$\alpha$. Hence our estimates represent lower limits to the total number of poor age estimates (e.g., see [140] & [135], who find ~10-20% of clusters have poor estimates in NGC 4449 and NGC 3351, respectively).

4 The median ratios of cluster ages and masses between our standard LEGUS catalog and results derived using CIGALE with the parameters described in [135] are less than 0.005 dex and 0.05 dex, respectively, for all H$\alpha$ morphologies. For cluster E(B-V), we find the median difference to be less than 0.02 mag for all such comparisons and morphologies. These small offsets along with the fact that our statistical results (see point 1) remain unaffected indicate that our star cluster properties are robust to the adopted SED-fitting algorithm and thus support our reported timescales.

5 We find that the classification of H$\alpha$ morphologies does not change significantly over the distances spanned by the galaxies in this sample (3–10 Mpc). For our nearest galaxy (NGC 7793W; 3.44 Mpc), the majority (> 64%) of *HST*-based partially exposed classifications are recovered when we project the galaxy to be at a distance of our most distant galaxy (NGC 3351; 10.0 Mpc), and even to a distance of 20.0 Mpc, at which we appear to reach the resolution limit for our classifications. For both of these reprojections, the statistical properties of clusters according to their H$\alpha$ morphologies remain consistent with the original classifications. The use of ground-based H$\alpha$ data taken at CTIO as part of the SINGS program, however, is unfit for this analysis as it is simply unable to resolve small clearing structures necessary to identify

the early stages of gas clearing, and therefore we find that the resolution capability of *HST* is necessary to produce the analysis and results presented in this paper.

### 3.8.1 Future Work

Our analysis highlights issues due to the age-extinction degeneracy. While we identify instances in which ages of clusters with H$\alpha$ are overestimated and vice-versa, they do not occur frequently enough to affect the median ages of the different H$\alpha$ morphological classes.

To potentially break the observed age-extinction degeneracy in the SED fitting, there are a few avenues available to pursue: 1) there exists MUSE (*Multi Unit Spectroscopic Explorer*) data for fields overlapping with our sample with which we could create E(B-V) maps, as done by [42]. These would allow us to compare an independent measure of cluster reddening (via the Balmer decrement) to our SED-fitted reddening to check for consistency. Further, [75] additionally produced extinction maps for two of the LEGUS fields in our study by spatially binning the extinction of individual stars, based on isochrone matching of their broadband photometry, thus providing another check on cluster reddening. 2) We could utilize overlapping ALMA CO(2-1) maps (e.g. [104]), which would allow us to firstly determine the degree to which H$\alpha$ traces the molecular gas in a region. Secondly, we would be able to infer whether the clusters in our sample have foreground dust, which we could then use to support or oppose their SED-fitted dust reddening.

Another key uncertainty is the use of a fixed covering fraction of 0.5 in our SED-modeling, and a careful examination could be performed to determine how the use of a proper covering

fraction for each cluster (e.g Scheuermann et al., in prep.) might affect the ages we have presented here.

Lastly, stellar populations within denser natal clouds may go undetected in H$\alpha$, thus an analysis of our sample's completeness would be critical in determining more accurate cluster populations and distributions of cluster properties, particularly for clusters with concentrated H$\alpha$ (e.g. [110], [81]). Forthcoming infrared observations of nearby galaxies with the James Webb Space Telescope, such as described by [101], will provide inventories of dust embedded clusters to probe these earliest stages of star formation.

## Acknowledgements

Based on observations with the NASA/ESA/CSA Hubble Space Telescope which were retrieved from MAST at the Space Telescope Science Institute, operated by the Association of Universities for Research in Astronomy, Incorporated, under NASA contract NAS5-26555. The observations were obtained through *HST* programs #13364 and #13773. Support for these programs was provided through a grant from the STScI under NASA contract NAS5-26555. A.A. acknowledges the support of the Swedish Research Council, Vetenskapsrådet, and the Swedish National Space Agency (SNSA). ROD and AW acknowledge the support of UNAM via grant agreement PAPIIT no. IA-102120. ATB would like to acknowledge funding from the European Research Council (ERC) under the European Union's Horizon 2020 research and innovation programme (grant agreement No.726384/Empire).

## Data Availability

The broadband images and star cluster catalogs used in this study are taken from LEGUS ([28], [2]), which includes WFC3 (GO-13364; F275W, F336W, F438W, F555W, and F814W) and archival ACS (F435W, F555W, F606W, and F814W) *HST* imaging, and are publicly available via their website (`https://legus.stsci.edu`). The LEGUS-H$\alpha$ images (GO-13773; PI R. Chandar), which include the F657N narrow-band filter and F547M medium-band filter are available via MAST. The only exception is NGC 5457, whose star cluster catalogs have been obtained through private communication and are to be published in Linden et al. (in prep.); the images for NGC 5457 remain publicly available.

# Chapter 4

# Star Cluster Classification using Deep Transfer Learning with PHANGS-HST

## 4.1 Introduction

The evolution of star clusters is inherently linked to the evolution of their host galaxies. Most star formation occurs in clustered regions within giant molecular clouds [92], thus star clusters and associations represent a fundamental unit in tracing the overall star formation cycle, which in turn informs us of the larger-scale dynamical evolution of galaxies.

Collections of star clusters and their ensemble properties have thus served as the basis for many studies seeking to better understand these processes (see [5] for a review). For example, such studies inform us about the formation of globular cluster systems [143, 142, 99], the characterization of the star cluster luminosity function [145, 97] and initial cluster mass function [96, 33, 35, 108, 109], the spatial distribution of clusters and their hierarchical formation [19, 66, 52], correlations with

various galactic parameters such as surface brightness, morphological type [95, 98], star formation history [20], and the timescales for the clearing of the natal gas of stars [139, 72, 67, 64, 68, 110, 69], among many others. Physics at High Angular resolution in Nearby GalaxieS (PHANGS[1]; see PHANGS-HST [101], PHANGS-ALMA [104], and PHANGS-MUSE [53]) represents one of the newest and largest extragalactic surveys to systematically study these topics addressing the complete star formation cycle on the cluster scale across a broad range of galactic environments.

As these star cluster studies have evolved toward survey scales, the size of their cluster samples has grown dramatically, with PHANGS-HST the Legacy ExtraGalactic UV Survey (LEGUS; [28]), each containing tens of thousands of cluster candidates. In these surveys, clusters are categorized according to a four-class system based on morphology ([2]; see Section 4.2 for class definitions), which not only crucially differentiates clusters from artifacts, but has also shown correlations with the physical properties of star clusters including age and mass (e.g. [65, 66, 140, 141]). Critically, the classification of these objects has historically been performed by one or more humans, which is becoming increasingly time-consuming and thus effectively limits sample size.

Recently, however, there has been exploration in the use of machine learning techniques for the rapid classification of production-scale star cluster candidates. [64] created a generally successful classification model (~70% agreement with human classifications) using a bagged decision tree algorithm with star clusters from LEGUS [28], however it did not perform as well for more distant objects or for compact associations of stars. [137] and [117] then improved upon these models by utilizing deep learning with even larger samples of LEGUS galaxies, resulting in ~10x greater recovery rates for the compact associations. The accuracy of the deep learning models in particular (~70% overall) rival the consistency found between human classifiers, and thus highlight

[1] `https://www.phangs.org`

the viability of machine learning in producing cluster catalogs much more efficiently than with human classification.

While these models perform well for samples of objects from LEGUS, on which they were trained, they do not perform as well for the more recent cluster sample from PHANGS-HST. [137] and [141] use these LEGUS-based models to classify PHANGS-HST objects from NGC 1559 and NGC 1566, respectively, and find a 10–20% decrease in recovery rate relative to LEGUS samples for asymmetric clusters (Class 2) and compact associations (Class 3). One explanation for this is that in PHANGS-HST, the definition of Class 3 objects is more explicitly specified in order to avoid stellar pairs or triplets, which are sometimes categorized as Class 2 or 3 objects by LEGUS [141]. Another is that the PHANGS-HST cluster sample occupies a different distance range (4–23 Mpc; [7]) than the LEGUS sample (3–16 Mpc; [28]), and more distant objects have shown to be associated with lower model accuracy (e.g., [117]).

The present study seeks to address these issues with two primary experiments. First, we will train a new set of deep learning models based on the full, available PHANGS-HST sample of star clusters. This will allow us to not only compare model performance with previous models and varied galactic parameters, but also potentially provide a more reliable machine learning-based classification implemented into the PHANGS-HST cluster catalogs. Secondly, we will introduce a distance-dependent model system in which multiple models are trained based on the galactic distance of the star clusters.

The organization of this paper is as follows: Section 4.2 introduces the data used in this study, including the cluster sample, classification system, and model inputs. Section 4.3 examines the accuracy of the current ML-based classifications used by PHANGS-HST. Section 4.4 details

the experiments and procedure of the current study, while Section 4.5 presents our primary results regarding their performance. Section 4.6 examines additional correlations with model performance, and Section 4.7 provides a summary of this study as well as our overall conclusions.

## 4.2 Data

The PHANGS-HST survey [101] consists of 38 spiral galaxies at distances of 4–23 Mpc [7], observed with the Hubble Space Telescope in five broad bands ($NUV - U - B - V - I$), using either WFC3/UVIS or archival ACS/WFC images. Critically, we are able to effectively resolve star clusters at these distances. The ~0.04 /pixel scale of *HST* imaging can resolve objects with sizes between 1.7–9.0 pc across the distance range of the PHANGS-HST galaxies, which is consistent with the effective radii of compact star clusters (typically 0.5–10 pc; [118]; [120]).

These sources are initially detected using `DOLPHOT` [47] and are then photometrically selected as cluster candidates based on the measurement of multiple concentration indices and the use of model star clusters [133]. They are then visually inspected by co-author Brad Whitmore (BCW), who categorizes each object according to their morphology. Following previous works such as [65], [2], and [38], there are four primary morphological classes, which are displayed in Figure 4.1 and defined here:

1 Class 1: compact, symmetric, single central peak, radial profile more extended relative to point source

2 Class 2: compact, asymmetric, or non-circular (e.g., elongated), single central peak

3 Class 3: asymmetric, multiple peaks, sometimes superimposed on diffuse extended source

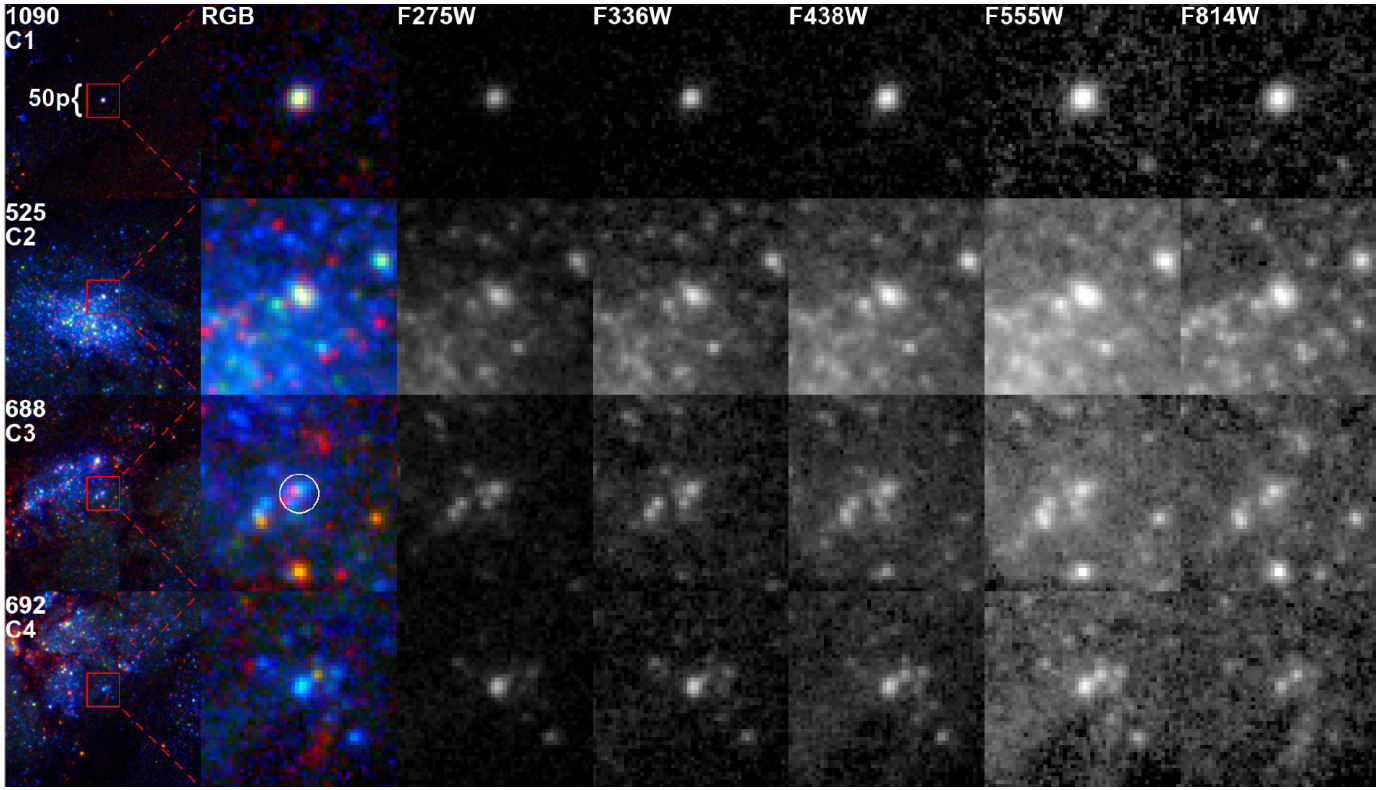


Figure 4.1: Examples of each of the four classes of training objects (Section 4.2) from a medium-distance galaxy within our sample (NGC 4321; $D \sim 15$ Mpc). A 50 x 50 pixel region, centered on each target object, is extracted from each of the five photometric bands and stored in a MEF file to be used for training. RGB images (R = F814W, G = F438W + F555W, B = F275W + F336W) are provided in the left two columns along with each Object ID and morphological class for reference.

4 Class 4: not a star cluster (image artefacts, background galaxies, single stars, pairs and multiple stars in crowded regions)

While these general definitions are used for both LEGUS and PHANGS-HST cluster samples, the Class 3 definition is further specified in PHANGS-HST to require at least four stars within a five-pixel radius. This can be seen for Object 525 in Figure 4.1, where at least two bluer and two redder stars are visible within the five-pixel radius (denoted by the white circle) in the RGB image. This is a key change which eliminates pairs (e.g., Object 692 in Figure 4.1) and triplets, as they may in fact be chance superpositions of individual stars within crowded regions. As later discussed, the effect of this change is reflected in the accuracy of the LEGUS-based models (Section 4.3) and PHANGS-based models (Section 4.5) in the classification of PHANGS-HST cluster candidates.

At the time of this project, visual classifications had been determined for cluster candidates in 23 galaxies (24 fields), providing a sample of over 20,000 objects for our study. Table 4.1 lists all of the galaxies used in this study along with the number of clusters in each morphological class, sorted by galaxy distance. Further information on the PHANGS-HST survey, data processing pipeline, and production of the star cluster catalogs which are used in this study can be found in [101].

### 4.2.1 Training Images

In order to perform deep transfer learning, we need to supply the neural networks with a set of images on which to train. For our dataset, we utilize the full, five-band $NUV-U-B-V-I$ coverage provided by the PHANGS-HST program, and ensure that our images are quantitatively similar to those on which our neural networks – `VGG19-BN` [125] and `ResNet18` [70] – have been pretrained.

**PHANGS Clusters**

| Field | Distance (Mpc) | Class 1 | Class 2 | Class 3 | Class 4 |
|---|---|---|---|---|---|
| IC5332* | 9.01 | 78 | 154 | 148 | 233 |
| NGC628E | 9.84 | 51 | 41 | 22 | 98 |
| NGC628C | 9.84 | 264 | 225 | 189 | 582 |
| NGC3351 | 9.96 | 140 | 177 | 173 | 1033 |
| NGC3627 | 11.32 | 462 | 312 | 184 | 546 |
| **Bin 1 Totals** | | **995** | **909** | **716** | **2492** |
| NGC5248 | 14.87 | 211 | 324 | 195 | 420 |
| NGC4571 | 14.9 | 61 | 101 | 100 | 200 |
| NGC4298* | 14.92 | 173 | 103 | 79 | 188 |
| NGC4689* | 15 | 130 | 214 | 166 | 265 |
| NGC1433 | 15.17 | 90 | 104 | 99 | 363 |
| NGC4321 | 15.21 | 436 | 279 | 235 | 421 |
| NGC4569 | 15.76 | 214 | 213 | 100 | 197 |
| NGC4535 | 15.77 | 202 | 203 | 127 | 435 |
| NGC1792 | 16.2 | 265 | 302 | 108 | 550 |
| NGC4548 | 16.22 | 96 | 99 | 76 | 142 |
| NGC4303 | 16.99 | 264 | 293 | 140 | 484 |
| NGC1566 | 17.69 | 394 | 291 | 166 | 911 |
| **Bin 2 Totals** | | **2536** | **2526** | **1591** | **4576** |
| NGC7496* | 18.72 | 105 | 158 | 110 | 245 |
| NGC1672 | 19.4 | 238 | 134 | 121 | 891 |
| NGC1559 | 19.44 | 420 | 303 | 218 | 641 |
| NGC1365 | 19.57 | 366 | 269 | 154 | 714 |
| NGC685* | 19.94 | 111 | 194 | 173 | 222 |
| NGC4654 | 21.98 | 256 | 360 | 243 | 409 |
| NGC2775 | 23.15 | 136 | 160 | 110 | 222 |
| **Bin 3 Totals** | | **1632** | **1578** | **1129** | **3344** |
| **Full Sample Totals** | | **4566** | **4190** | **2760** | **9259** |

Table 4.1: Number of objects in each of the four morphological classes for the 24 PHANGS-HST fields, as classified by BCW. The total number of clusters within each of the three distance bins is also given, as well as the totals for the "full" sample. Asterisks indicate galaxies which are not included in the training of the initial, distance-independent models. Distances compiled by **(author?)** [101] are listed.

The pre-training of these networks utilizes the `ImageNet`[2] dataset [43] consisting of 299 x 299 pixel images, which is far wider than the several pixels that the star clusters in our study typically subtend. To reduce the number of neighboring objects within each of our training images, we adopt the procedure of [137] by extracting a smaller region of 50 x 50 pixels[3], remaining centered on the original target object, and resize it to fit in a 299 x 299 pixel area.

For each target in the sample, these cutouts, which we refer to as “postage stamps", are produced for all five of the $NUV-U-B-V-I$ broadband images, and are then stored in individual header data units (HDUs) within a single Multi-Extension FITS (MEF) file. We note that if there is no observation of the object in one of the filters, all pixel values for that particular filter's postage stamp are set to zero. Lastly, all of the MEFs of objects within a particular cluster class are placed in a single file, which gives us four separate files for the four object classes.

## 4.3 Accuracy of Prior Models

The PHANGS-HST project has produced cluster catalogs complete with cluster classifications determined by a star cluster expert (BCW) for 23 galaxies (24 fields). Along with these human-verified cluster classifications, each of the cluster candidates have morphological classifications predicted by both the `VGG19-BN` and `ResNet18` models presented in [137]. As these models were trained on clusters from the LEGUS sample, we will henceforth refer to them as the “LEGUS-based" models.

To produce these machine learning classifications, MEF postage stamps of each of the objects in the PHANGS-HST cluster catalogs are first created as described in Section 4.2.1. The

[2] `http://www.image-net.org`

[3] For the range of galaxy distances in our sample, 50 pixels represents 87–224 pc.

full sample of objects is then fed through a single model for evaluation, the product of which is a list of predicted classes for all of the objects. The evaluation is repeated for each of the LEGUS-based models, consisting of 10 `VGG19-BN` and 10 `ResNet18` models. The mode class from each of the two neural network architectures is then chosen to represent the final classification for each object. These models, along with a Jupyter Notebook tutorial on how to use them to predict classifications for new catalogs of objects, have been made publicly available by the PHANGS-HST team via MAST (`https://archive.stsci.edu/hlsp/phangs-hst`).

Notably, the LEGUS-based models were trained on slightly different objects than those which make up the PHANGS-HST sample. Firstly, as noted in Section 4.2, the definition of a Class 3 object in PHANGS-HST has been further specified to eliminate pairs and triplets, which are sometimes included as Class 2 or 3 objects in LEGUS. Secondly, the LEGUS-based models were trained on a sample of objects which spans a nearer galactic distance range ($\sim 3 - 10$ Mpc) than the PHANGS-HST sample examined in this study ($\sim 9 - 24$ Mpc). By comparing the human-verified classes of PHANGS-HST objects with the classes predicted by the LEGUS-based models, we can examine the robustness of the models to these important distinctions.

Over the sample of ~20,000 objects used in this study, we find that the LEGUS-based models predict Class 1 and 4 objects from the PHANGS-HST sample with reasonable accuracy, however they do not accurately classify Class 2 and 3 objects. The agreement between BCW's classes ("True Label") and the machine learning classes ("Predicted Label") are displayed in the confusion matrices of Figure 4.2. The diagonal of each matrix represents the 1:1 agreement between the class determined by BCW and the class determined by the particular model. The left matrix displays the accuracy of the LEGUS-based models as tested on LEGUS objects [137]. The middle

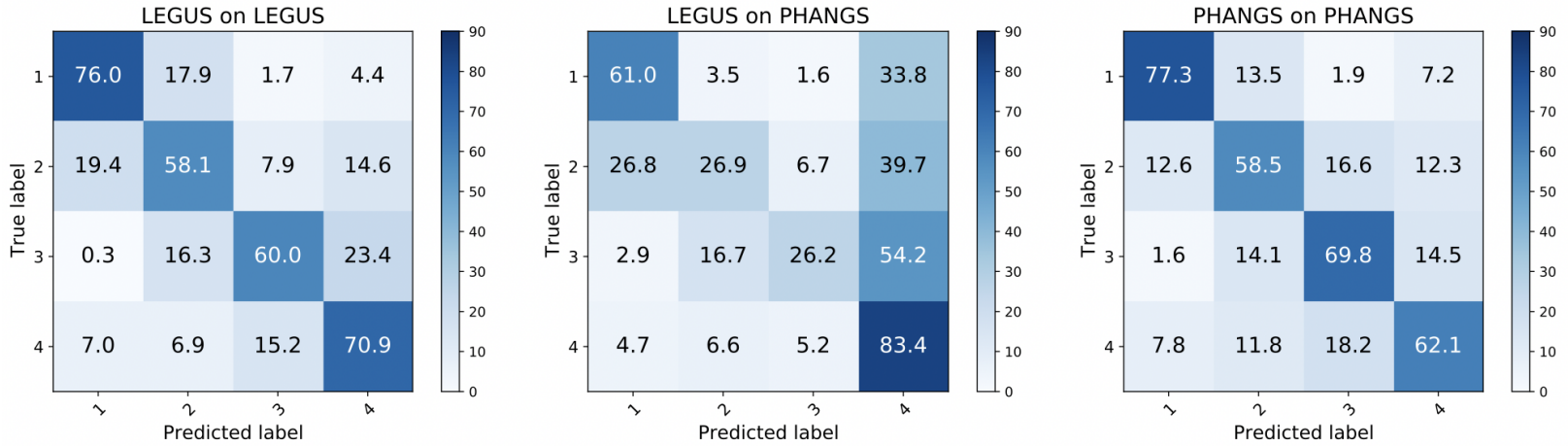


Figure 4.2: Comparison of classification accuracies for the LEGUS-based [137] and PHANGS-based models, with the model-determined labels and human-determined labels on the x-axes and y-axes, respectively. The left and middle confusion matrices display the accuracy of the LEGUS-based models in classifying LEGUS and PHANGS-HST candidate clusters, respectively, and the right matrix displays the accuracy of the PHANGS-based models in classifying PHANGS-HST candidates. While the LEGUS-based and PHANGS-based models classify objects from their respective samples with similar accuracy (~60-80%), the LEGUS-based models are notably poor at correctly classifying Class 2 and 3 PHANGS-HST objects. To note, the results presented here are specific to the `ResNet18` models from each study, however similar results are found for the `VGG19-BN` models which are discussed in the text.

matrix displays the accuracy of those same LEGUS-based models when classifying objects in the PHANGS-HST sample. As shown in the upper-left cell of this middle matrix, ∼60% of the PHANGS-HST objects identified by BCW as a Class 1 cluster have also been given a Class 1 label by the LEGUS-based models. Following the diagonals downward, we find that Class 2, 3, and 4 objects show such classification agreement between ∼30%, ∼30%, and ∼80% of PHANGS-HST objects, respectively.

For Class 2 and 3 objects, these percentages indicate poor agreement compared to the results of [137]. The recovery rate of Class 2 and 3 objects is cut in half when the LEGUS-based models are applied to PHANGS-HST objects, while we observe a more modest decrease in the recovery rate of Class 1 PHANGS-HST objects (15%). If we take a simple average of the accuracies for cluster objects (Class 1, 2, and 3), the LEGUS-based models drop from 65% accuracy when classifying LEGUS clusters to 38% for PHANGS-HST clusters.

If these models are to be used for production-scale cluster classifications, it is imperative that they can reliably delineate between cluster (Class 1, 2, 3) and non-cluster (Class 4), however we do not find this to be the case with the LEGUS-based models. We find that a significant fraction of Class 1, 2, and 3 PHANGS-HST objects are misclassified by the LEGUS-based models as non-clusters (Class 4). As shown in the rightmost column of the middle matrix, 30–50% of BCW Class 1, 2, and 3 objects have been misclassified by the models as Class 4. This is likely related to the observed good agreement for Class 4 objects (83%), which may be explained by the fact that the more-distant PHANGS-HST objects and nearby background sources appear less-resolved than those found in the LEGUS sample.

Thus we find that the current LEGUS-based models used to produce machine learning-based classifications for the PHANGS-HST sample of clusters do not achieve a sufficient level of accuracy, which motivates this study in training new machine learning models. Our results, shown in the rightmost matrix of Figure 4.2, will be discussed in Section 4.5.

## 4.4 Training Experiments

Considering the relatively poor performance of the LEGUS-based models in classifying PHANGS-HST clusters, we perform two experiments seeking to improve the reliability of such machine learning-based classification models for the PHANGS-HST sample of objects and potentially future star cluster samples.

For a direct comparison with the LEGUS-based models, we first train the neural networks using the full available sample of PHANGS-HST objects, which we refer to as our "distance-independent" models. At the time of this training, cluster catalogs with human-verified classifications were available for 18 galaxies (19 fields). These galaxies span a distance range of $\sim 10 - 23$ Mpc, and consisted of 20,775 objects.

To help illuminate whether the poor performance of the LEGUS-based models is due to the difference in galaxy distances in the samples, we divide our PHANGS-HST sample into three separate galaxy distance bins (9–12 Mpc, 14–18 Mpc, and 18–23 Mpc) and train the neural networks individually on each of the three samples. These models will be referred to as our "distance-dependent" models. The bins for these were determined based on the most natural breaks found in the galaxy distances in the sample. Because this training was performed subsequent to the distance-independent training, BCW classifications of cluster candidates for five additional galaxies

were made available for this distance-dependent experiment, for a total of 23 galaxies (24 fields). The 9–12 Mpc, 14–18 Mpc, and 18–23 Mpc distance bins consist of 5,112, 11,229, and 7,683 objects, respectively. Our smallest sample is thus comparable in size to those used for the BCW models from [137], which comprised of 5,147 objects.

Eighty percent of the objects in each sample are randomly chosen for their respective training set to be used for the machine learning process (Section 4.4.1), while the remaining 20% of objects are reserved as a validation set to evaluate the accuracy of the resultant models.

The complete list of galaxies along with each of their human-verified cluster populations for these two experiments are displayed in Table 4.1.

### 4.4.1 Training Procedure

For direct comparison of our newly trained models to those presented in [137], we employ the same training procedure outlined in their study.

In our experiments, we use two neural network architectures: `VGG19-BN`, which utilizes more of a standard series of convolutional layers and pooling layers feeding directly into each other [125], and `ResNet18`, which utilizes skip connections to pass information across layers with matrix addition to reduce the overall complexity of the network, ultimately resulting in more time-efficient training compared to `VGG` models [70].

Each of these neural networks have been pre-trained with the `ImageNet` dataset [43]. While the `ImageNet` dataset does not feature star cluster morphologies amongst its image classifications, its power resides in its scale, diversity and hierarchical nature. With over 14 million images, `ImageNet` allows the `VGG19-BN` and `ResNet18` models to learn lower-level features such as shapes, curves, and edges with accurate, high-quality data. Transfer learning is then implemented by replacing

the last layer of the models with randomly initialized weights which, upon training with a new dataset, will tailor the models to higher-level features specific to that particular input data – see [60**?** , 48, 1, 80, 14] for examples of astronomical applications. This method of transfer learning is particularly useful when the input dataset is small in comparison to the pretraining dataset, as is the case presented here – our sample of ∼20,000 objects is nearly 1000 times smaller than that of `ImageNet`. In our training, these pre-trained weights are provided by `PyTorch` [116].

To begin training, a number of objects from the training set are randomly selected as input to the models. This number is known as the batch size, which is 16 and 32 for the `VGG19-BN` and `ResNet18` models, respectively. These objects are then passed through the model and have their model-predicted classes compared to their human-verified classes. The accuracy of the model is then recorded as a cross-entropy loss function[4], which is used to determine how the weights are modified in order for the model to perform more accurately. The size of these modifications is determined by the learning rate, which we set to $10^{-4}$—a faster learning rate will make larger modifications to the weights, which may train a model faster, but may also result in a less accurate final model. These steps are then repeated for the desired number of batches, thus 10,000 batches correspond to 10,000 modifications to the initial model. Notably, it is possible to over-train the model, where the model becomes over-specified to classify the objects in the training sample and results in poorer accuracy for classifying objects outside of the sample.

Upon training one `ResNet18` and one `VGG19-BN` model for each of the samples and viewing their performance over time, we decide upon 5,000 and 10,000 batches for all `ResNet18` and `VGG19-BN` models, respectively. With the aforementioned batch sizes, this means that each of

[4]A loss function is used to evaluate and diagnose model optimization during training. The penalty for errors in the cross-entropy loss function is logarithmic, i.e., large errors are more strongly penalized.

the neural networks is exposed to 160,000 images during the training process, which is relatively large compared to our sample size. To reduce the number of identical images presented to the networks, when an object is selected in a batch, it is randomly rotated anywhere between 0 and 360 degrees, and also has a 50% chance of being reflected about its axes. Thus, it is rare for the model to train on the exact same array of pixel values (i.e., image) multiple times.

For an accurate representation of performance, 10 models, each with its own unique randomly-initialized weights in its final layer, are independently trained for each sample and architecture used. For the distance-independent sample, we train 10 models using the `ResNet18` architecture and 10 models using the `VGG19-BN` architecture. For each of the three distance-dependent samples, however, we choose to train 10 models using the `VGG19-BN` architecture only. This choice is primarily motivated by the relatively similar performance of the two architectures found for both our own distance-independent models as well as the models presented in [137]. With the training of 10 models for each sample and architecture, we are able to present their mean accuracies along with their standard deviations, which are presented in the following sections.

To note, the training and evaluation of every model in this study have been completed using Amazon Web Services (AWS), utilizing their EC2 p3.2xlarge instance. For additional details on deep transfer learning and its statistical foundations, we refer the reader to [137].

## 4.5 Results

Here we present the results of the training experiments described in Section 4.4.

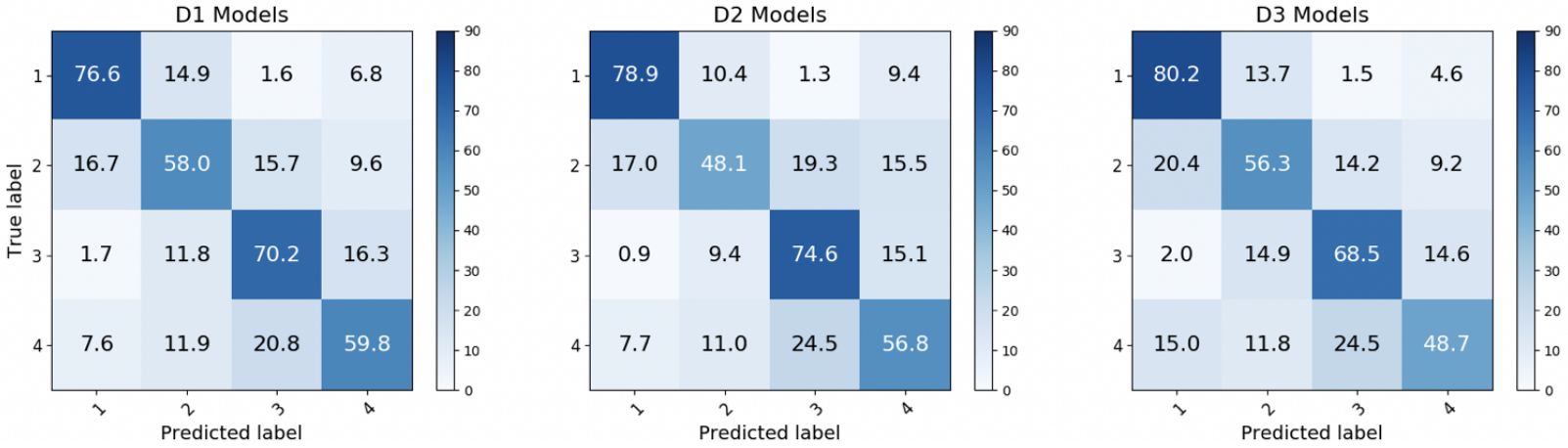


Figure 4.3: Confusion matrices showing the results of training separate machine learning models based on the galactic distance of PHANGS-HST objects. From left to right, the three sets of models are based on clusters between 1) 9–12 Mpc, 2) 14–18 Mpc, and 3) 18–24 Mpc. The averaged accuracies, as determined by classifying their respective validation set of PHANGS-HST objects, of 10 VGG-based models within each of the three distance bins are displayed.

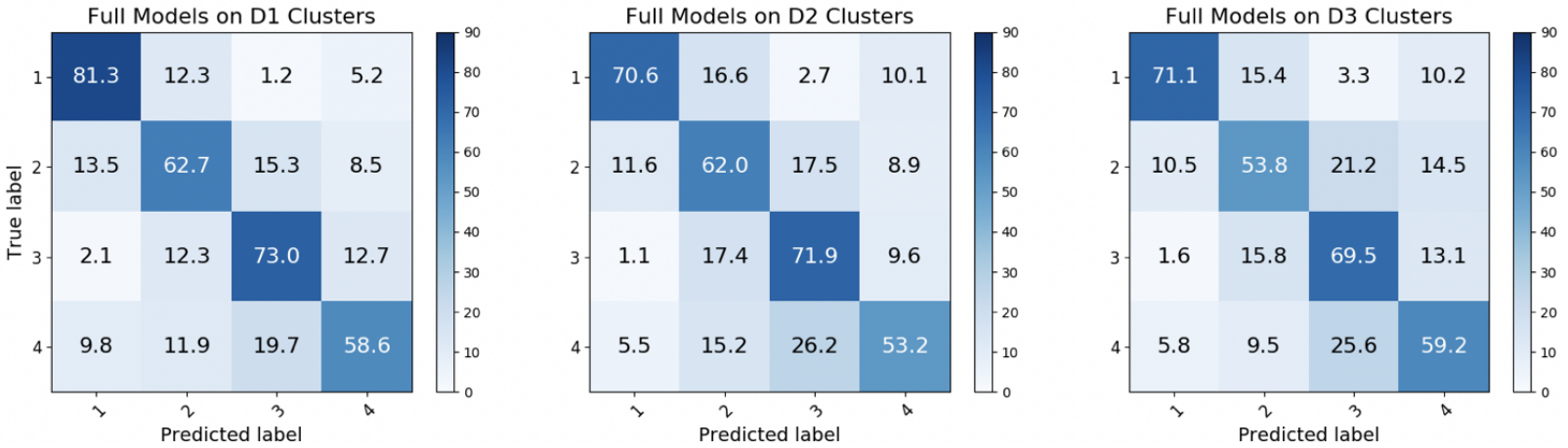


Figure 4.4: Confusion matrices showing the classification accuracies of our distance-independent models when classifying objects within the three distance bins shown in Figure 4.3 (9–12 Mpc, 14–18 Mpc, 18–24 Mpc). The similarity between these confusion matrices and those shown in Figure 4.3 indicate that training within distance bins does not significantly affect the accuracy of the classification models.

### 4.5.1 Distance-Independent Models

Considering the relatively poor accuracy of the LEGUS-based models in classifying PHANGS-HST clusters (Section 4.3), we first train a set of new models using only data from the PHANGS-HST sample, independent of galaxy distance. The results of this training are displayed in the rightmost confusion matrix in Figure 4.2, which measures the accuracy of our models in the classification of our validation set of clusters (Section 4.2). Figure 4.2 shows the percentage of objects from each of the human-verified classes (y-axis) which receive a specific classification as predicted by the `ResNet18` models (x-axis). Equivalent confusion matrices for the`VGG19-BN` models are not included because of their similarity to the `ResNet18` results, but are discussed below. Thus the diagonal in these plots represents clusters which received the same predicted class as their human-verified class. We remind the reader that these accuracies are based on the classifications of our validation set, the objects of which are not included in the training of the models.

Overall, we find marked improvement for our models over the LEGUS-based models in classifying PHANGS-HST objects, particularly for Classes 2 and 3. The accuracies averaged over our 10 `ResNet18` models (those presented in Figure 4.2), are 77 ± 7%, 58 ± 10%, 70 ± 5%, and 62 ± 6% for Class 1, 2, 3, and 4 objects, respectively, and the accuracies averaged over our 10 `VGG19-BN` models (not shown in Figure 4.2) are 74 ± 10%, 59 ± 12%, 71 ± 9%, and 57 ± 5%.

These accuracies are consistent with those presented in prior works as well. [137] reported 76–78%, 54–58%, 58–60%, and 66–71% accuracy for Class 1, 2, 3, and 4 objects using `ResNet18` models to classify LEGUS objects, and 71–76%, 54–64%, 57–60%, and 69% accuracy using `VGG19-BN` models. [117] report similar or slightly lower accuracies for their LEGUS-based sample

of cluster objects, with recovery rates of 78%, 55%, 45%, for Class 1, 2, and 3 objects, while their non-cluster (Class 4) accuracy is higher at 82%.

Most importantly, our newly trained models are classifying PHANGS-HST objects with much higher accuracy than the LEGUS-based models. The new models are identifying Class 2 and 3 PHANGS-HST objects with greater than twice the accuracy of the LEGUS-based models, and Class 1 PHANGS-HST objects are also identified with ~15% greater accuracy (Figure 4.2).

These results indicate that our new models are not only capable of classifying cluster morphology with accuracies that are comparable to previous machine learning studies as well as human-to-human variation ([117]; [137]), but can outperform them when classifying PHANGS-HST objects in particular and most notably for Class 2 and 3 clusters. Thus our models will be able to provide the most reliable machine learning classifications for cluster morphology for the PHANGS-HST sample, and can serve as a unique set of classification models moving forward.

### 4.5.2 Distance-Dependent Models

With the improved accuracy of our new models as well as the fact that the LEGUS-based models are trained on a cluster sample which spans a different galactic distance range ($\sim 4 - 10$ Mpc) than the PHANGS-HST cluster sample used in this study ($\sim 9 - 23$ Mpc), it is fair to question whether the classification accuracy of these machine learning models is dependent on galaxy distance. One way to examine this is to split our sample of galaxies into three separate distance bins and independently train three sets of models to allow us to compare the performance of each.

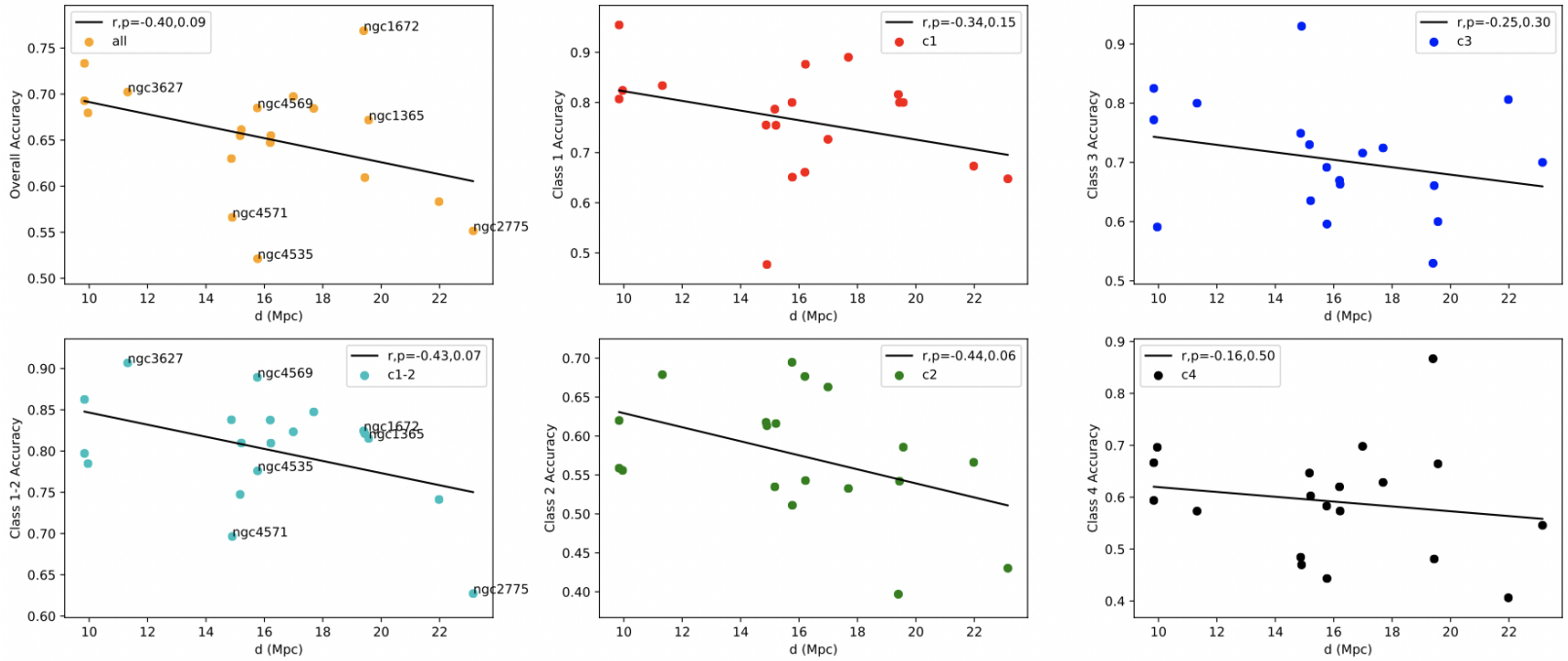


Figure 4.5: Classification accuracy vs. galactic distance [7]. Each of the points in these plots represents the prediction accuracy for objects within a particular galaxy. The top-left plot shows the percent of clusters which receive identical model- and human-determined classes. The bottom-left plot shows the percent of clusters which are classified as either Class 1 or 2 by both model and human. The right four plots show the percent of clusters which receive the same model- and human-determined classification for each of the four classes individually. Each plot includes a linear regression model with the Pearson correlation coefficients (r) and p-values included in the legend for reference. While model accuracy appears to generally decline with galactic distance, the correlation is not statistically significant.

When we examine the range of galaxy distances listed in Table 1, we find the most natural breaks between NGC 3627 and NGC 5248 ($\Delta D$ = 3.55 Mpc) and NGC 1566 and NGC 7496 ($\Delta D$ = 1.03 Mpc), and so we choose these to serve as the divisions in our sample. Upon this division, each of our three resultant samples contain more than 5,000 objects, which is comparable in size to the samples in previous star cluster classification studies [137, 117].

The results of this training are displayed in the confusion matrices in Figure 4.3, where the left, middle, and right plots show the accuracies of the 9–12 Mpc (D1 model), 14–18 Mpc (D2 model), and 18–23 Mpc (D3 model) bins, respectively.

Overall, we find that the accuracy of the three sets of models are consistent both with each other and with the distance-independent models. The accuracies averaged over the 10 `VGG19-BN` models for the three distance bins range from 77–80%, 48-58%, 68–75%, and 49–60% for Class 1, 2, 3, and 4 objects, respectively. We find that all of these agreement fractions, except that of Class 4 for the 18–24 Mpc model, fall within the standard deviations of the distance-independent `VGG19-BN` models.

Additionally, we find that the distance-independent models perform similarly when classifying the validation sets from each of the three distance bins. Figure 4.4 displays the results of this validation testing, where we find that the distance-independent models classify clusters within the three distance bins at accuracies of 71–81%, 54–63%, 69-73%, and 53–59% for Class 1, 2, 3, and 4 objects, respectively, which is consistent with the both the distance-dependent models (Figure 4.3) as well as the accuracy of the distance-independent models when tested on the overall sample (right matrix of Figure 4.2).

Thus we find that training separate models based on the galactic distance of the objects does not significantly affect their performance relative to the distance-independent models. Because of this, we determine that it is best to use the distance-independent models in the production-scale classification of PHANGS-HST objects, which is not only simpler, but will also help to avoid potential artificial correlations or discontinuities between the distance bins.

## 4.6 Additional Trends

The accuracies of our new models, presented in Section 4.5.1, are determined by using them to classify our validation set of cluster candidates, which is comprised of a randomly selected 20% of the overall sample. For each of these classified objects, we retain all of its information from the PHANGS-HST cluster catalogs, which allows us to investigate more potential correlations between the performance of the models and the properties of the objects themselves.

### 4.6.1 Galactic Trends

We begin by examining the model accuracies versus various galactic-scale properties of the objects. The properties we examine in this section have been taken from Table 1 of [101]. Using the distance-independent models to classify their validation set, we can then identify which of the 18 galaxies (19 fields) each object from the validation set belongs to. For each field, the validation set contains $\gtrsim 20$ objects in each of the four classes, except for NGC 628E which only has 11, 5, 4, and 16 Class 1, 2, 3, and 4 objects accounted for, respectively.

In Section 4.5.2, we examined the performance of models which were trained in three different distance bins, but we can also analyze our model performance on a more refined scale

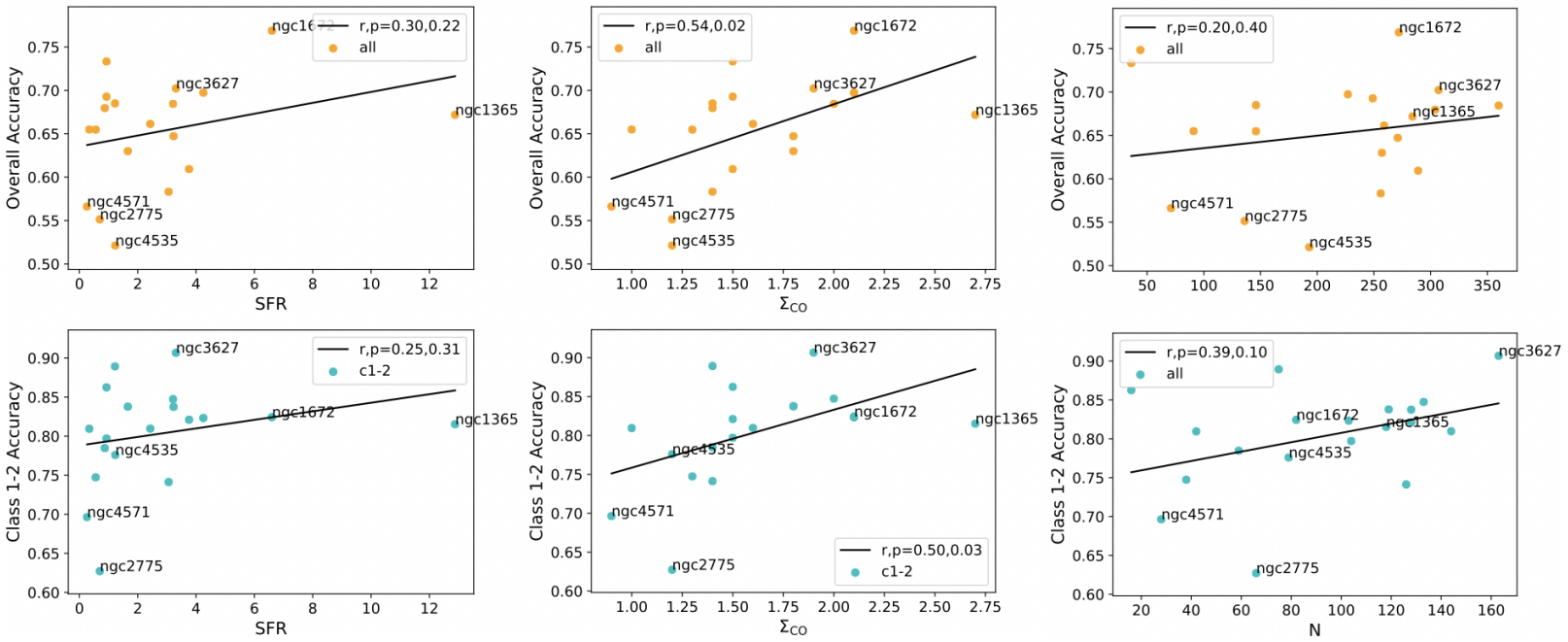


Figure 4.6: Classification accuracy vs. galaxy star formation rate (SFR; [122, 121, 103]; left), average molecular gas surface density ($\Sigma_{CO}$; [130]; middle), and total number of cluster candidates ($N$; right), based on the data provided in Table 1 of [101]. Each of the points in these plots represents the prediction accuracy for objects within a particular galaxy. Each plot includes a linear regression model with the Pearson correlation coefficients ($r$) and $p$-values included in the legend for reference. Labeled galaxies are discussed in Section 4.6.1

.

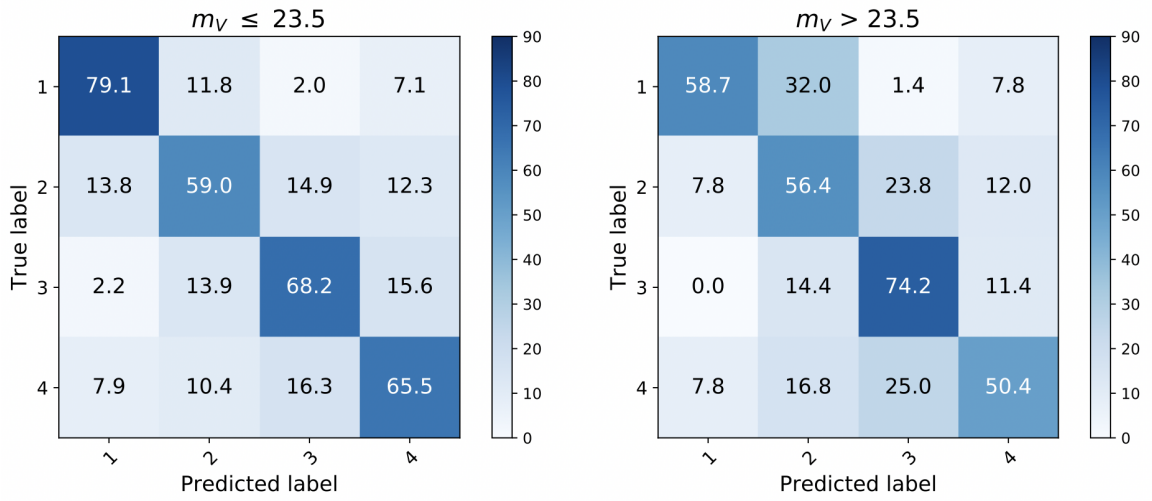


Figure 4.7: Classification accuracies of objects based on $m_V$ (VEGA). The left matrix displays model accuracies for objects with $m_V$ brighter than 23.5 mag while the right matrix displays model accuracies for objects fainter than 23.5 mag.

of individual galactic distances [7], where we find a slightly negative correlation between model accuracy and galaxy distance. Figure 4.5 displays classification accuracy versus galaxy distance, where each point represents a single field in the sample. Also included in each of these plots is a linear regression model, including its Pearson coefficient ($r$) and $p$-value to examine statistical significance, as well as a few galaxy labels for discussion.

Whether we look at the overall agreement regardless of class (top left plot of Figure 4.5), the agreement that an object is either Class 1 or 2 (bottom left plot), or the agreement for the individual classes (the remaining four plots), the lines of best fit appear to show that model accuracy declines as galaxy distance increases, however this correlation is not found to be statistically significant. While the overall accuracy and Class 1-2 accuracy (left plots) approach significance (p-values of 0.09 and 0.07, respectively), each of the p-values are ultimately above the commonly-used threshold used to

reject the null hypothesis ($p < 0.05$). This result is complementary to our finding that there were no obvious correlations when we trained our models in the more granular distance bins (Section 4.5.2).

In addition to the distance of each galaxy, the data provided in Table 1 of [101] allows us to investigate our model accuracy versus other galactic parameters, namely star formation rate (SFR; [122, 121, 103]) and molecular gas surface density ($\Sigma_{CO}$; [130]). Figure 6 displays the relationships between model accuracy and each of these properties for each of the galaxies in our sample. In each of these figures, we include plots for the overall accuracies regardless of cluster class (top row), as well as for the agreement that an object is Class 1 or 2 (bottom row). While data for each galaxy's stellar mass and inclination angle are also provided in [101], we did not observe any notable trends between them and model accuracy and thus do not include them here.

We identify a relatively weak, but statistically significant positive correlation between model accuracy and $\Sigma_{CO}$ ($r, p = 0.54, 0.02$). Furthermore, while there is not a statistically significant trend between accuracy and SFR, three of the galaxies with the highest SFRs (NGC 1365, NGC 1672, NGC 3627; labeled in Figures 4.5 & 4.6), which also have the highest $\Sigma_{CO}$, have three of the highest overall accuracies, regardless of distance (Figure 4.5). Similarly, three of the galaxies with the lowest SFRs and $\Sigma_{CO}$ (NGC 2775, NGC 4571, NGC 4535; also labeled in Figures 4.5 & 4.6) have the three lowest overall classification accuracies.

These observations may however be an artifact of our sample, as these galaxies with higher SFRs and $\Sigma_{CO}$ naturally contain more cluster candidates (right column of Figure 4.6), hence the models are exposed to more objects within those galaxies. Further, the three aforementioned galaxies with higher SFRs (NGC 1365, NGC 1672, NGC 3627) have higher percentages of Class 1 objects (Table 4.1), which the models are more accurate in classifying (Figure 4.2), whereas the other three

galaxies (NGC 2775, NGC 4571, NGC 4535) have a higher percentage of Class 2 and 3 objects, for which the models overall perform worse (Figure 4.2).

Overall, while it appears that model accuracy slightly decreases with individual galaxy distance, the correlation is not statistically significant, and is thus consistent with our findings for the distance-dependent models (Section 4.5.2). Additionally, while we find that our model accuracy improves for galaxies with higher $\Sigma_{CO}$, it may in fact be a result of bias in the training sample of clusters.

### 4.6.2 Individual Cluster Trends

In addition to the galactic trends discussed in the previous section, we are also able to investigate the accuracy of the models based on the properties of individual star clusters.

We first examine the accuracy as a function of cluster brightness. As described in [141], the standard limit for star cluster classification is $m_V$ = 23.5 mag for the PHANGS-HST sample of galaxies, however classifications were made for objects as faint as ~24.5 mag for testing. With this in mind, we divide our validation sample into clusters brighter than or fainter than $m_V$ = 23.5 mag.

Figure 4.7 shows the confusion matrices describing the model accuracy for each of these samples, where we observe relatively poor 1:1 accuracy for fainter Class 1 and 4 objects while Class 2 and 3 objects show no clear distinction. For the `ResNet18` models shown in the figure, Class 1 and 4 accuracy drops from 79% and 65% to 59% and 50%, respectively, while Class 2 and 3 accuracies remain within a standard deviation of each other. The `VGG19-BN` models perform similarly, with Class 1 and 4 accuracy dropping from 75% and 62% to 61% and 41%, respectively.

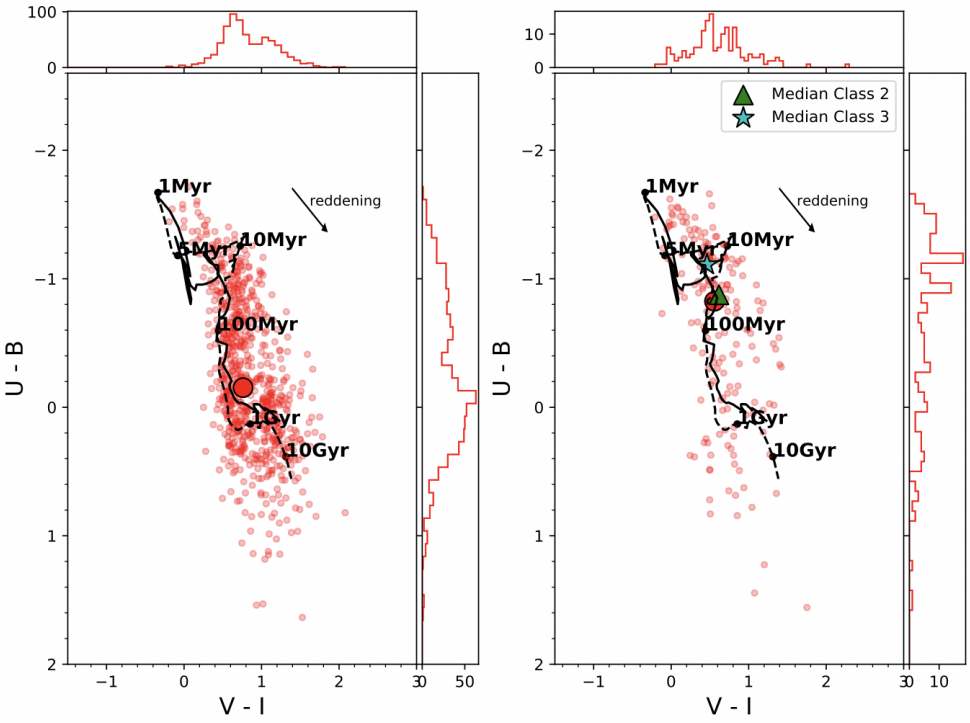


Figure 4.8: $(U-B)$ vs. $(V-I)$ plots comparing clusters for which human and machine learning models agree (left) and disagree (right) on classification. All of the clusters in the validation set which have Class 1 morphologies as determined by a human (BCW) are included as small red circles. The left plot contains the clusters for which the mode class from the 10 ResNet models is also 1, while the right contains the clusters which have a mode Class of 2, 3, or 4. [24] model tracks (dashed line for $Z = 0.02$; solid line for $Z = 0.004$) used for the fitting of these clusters are included with time stamps for reference. The median color for each sample is included as a larger, black-outlined circle, and histograms showing the distributions of colors are shown on each axis. Classification agreement appears to be higher for clusters which share the same color space as old, globular clusters (e.g. the median color in the left plot, near the 1 Gyr point), and is lower for objects sharing color space with younger clusters (e.g., the median color in the right plot, near the 50 Myr point) which is more consistent with the median colors of BCW Class 2 and 3 objects (denoted by a green triangle and blue star, respectively).

Although we do not observe the decline in Class 2 accuracy shown in [141], we do observe their other primary result from their equivalent analysis: when we consider Classes 1 and 2 together as a single class, the model accuracy is similar on both sides of the limit. For example, from the left matrix of Figure 4.7, 91% of brighter ($m_V \leq 23.5$), human-verified Class 1 clusters are classified by our `ResNet18` models as either Class 1 or 2 (79% + 12% = 91%). Similarly, 91% of fainter ($m_V > 23.5$), human-verified Class 1 clusters are classified by our `ResNet18` models as either Class 1 or 2 (59% + 32% = 91%). That is, the drop in accuracy for fainter Class 1 objects is due to more of them being classified as Class 2 clusters instead, and not as a Class 3 or 4. This is an important distinction because Class 1 and 2 clusters typically represent the standard sample in star cluster studies, and so such samples would be unaffected by whether an object is identified as Class 1 or 2. Together, the Class 1 and 2 accuracy is ~85% for both sets of models and both brightness bins, which is consistent with [141].

Color-color diagrams offer another useful tool for analyzing star clusters, particularly because they allow us to view them in relation to the single stellar population (SSP) model used for the fitting of their spectral energy distribution (SED), from which their age, $E(B-V)$, and mass can be derived. We utilize the multi-band photometry of PHANGS-HST to examine the positions of clusters in $(U-B)$ vs. $(V-I)$ space, as shown in Figure 4.8. In both of these figures, each red circle represents a cluster classified by BCW as Class 1. The left plot contains each of these clusters which also received a Class 1 label from the `ResNet18` models (as determined by the mode of the 10 models), while the right plot contains the clusters which received a different classification (i.e., Class 2, 3, or 4). Also included are the color distributions on each axis for each sample.

From these plots, we find that for Class 1 objects, the machine learning models are more likely to agree with the human-verified class for those which appear older than for those which appear younger. This is highlighted by the position of the median colors of each sample, denoted by the larger, black-outlined circles. Clusters which have been correctly classified (left plot) have median colors of $U - B \approx -0.2$ and $V - I \approx 0.8$, near the 1 Gyr point of the $Z = 0.02$ SSP model. Clusters which have been incorrectly identified (right plot), however, are much more concentrated toward the younger end of the SSP models, with median colors of $U - B \approx -0.8$ and $V - I \approx 0.6$, near the 50 Myr point.

Previous studies have also identified correlations between the colors of star clusters and morphological class (e.g., [2, 64, 135, 141]), and in particular, that older clusters tend to be both redder and more symmetric (i.e., Class 1-like). In fact, nearly all of the objects in our sample which occupy the section of $U - B$ vs. $V - I$ space which [141] designated for older clusters ($0.95 < V - I < 1.5; -0.4 < U - B < 1.0$) are found to have accurate classifications. Only 13 of the 206 BCW Class 1 clusters in this region (6.3%) received a different classification from the our models. Further, 8 of those 13 were labeled Class 2 instead, and would thus remain in standard star cluster samples.

While our models perform well in general for Class 1 clusters, and in particular for older-appearing clusters, the distribution in the right plot of Figure 4.8 shows that the relatively few problems it does have tend to be with younger-appearing clusters. With the median color near the 50 Myr point in the SSP model, BCW Class 1 clusters which have different model classifications are generally much younger looking than those which agree (median near 1 Gyr). Searching the [141]

box designated for the youngest objects ($-0.65 < V - I < 0.95$; $-1.8 < U - B < -1.1$), we find that 58 of 117 (~50%) of the BCW Class 1 clusters received a different classification from our models.

The color distributions offer an explanation for this, as there are more Class 1 objects found toward the older parts of this color space in general. Additionally, the younger-appearing Class 1 objects share the same color space of Class 2 and 3 objects, which have median colors of $U - B \approx -0.8$, $V - I \approx 0.6$ and $U - B \approx -1.1$, $V - I \approx 0.5$, respectively. What is reassuring again is that the majority of the reclassified Class 1 objects (34 of the 58) are determined to be Class 2 instead. Thus, even in this relatively problematic region, ~80% of Class 1 objects would still be retained in standard star cluster catalogs.

Further, we find that these observations in color-color space match how our model accuracy varies with SED age. These ages are derived by SED-fitting of the $NUV - U - B - V - I$ photometry of each object with Code Investigating GALaxy Emission[5] (CIGALE; [26, 111, 21]). The fitting uses the single-aged population synthesis models of [24] and assumes solar metallicity, a [32] initial mass function with limits of 0.1-100 $M_\odot$, and a [30] extinction curve with $R_V = 3.1$ (see [135] for more details on the SED-fitting of PHANGS-HST objects). Figure 4.9 displays the average model accuracies for each of the three classes of clusters (Class 1, 2, and 3), divided into four distinct age bins.

As discussed above, our models more accurately identify Class 1 objects which appear older, however not just in color-space, but also according to their SED age. Class 1 accuracy is lowest for the youngest objects (1-10 Myr; ~58%), and improves dramatically for the older objects: both the 100-1000 Myr and >1 Gyr age bins have Class 1 accuracies $\gtrsim 85\%$. Additionally, we observe the opposite effect for Class 3 objects, namely that as SED age increases, Class 3 accuracy decreases:

[5] `http://cigale.lam.fr`

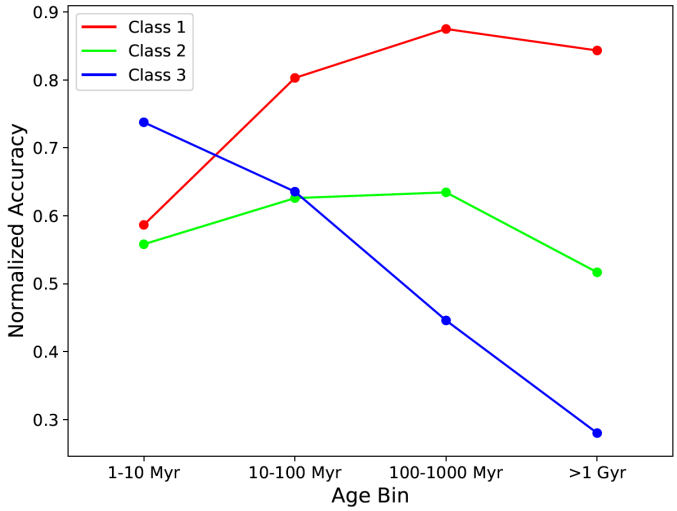


Figure 4.9: Average classification accuracies of PHANGS-HST clusters (Class 1, 2, and 3 objects), divided into four SED age bins (1-10 Myr, 10-100 Myr, 100-1000 Myr, >1 Gyr). Classification accuracy for Class 1 objects increases as the clusters become older, while accuracy decreases for Class 3 objects as they become older. The displayed normalized accuracies are based on the average of the 10 `ResNet18`-based distance-independent models tested on our validation set of clusters.

accuracy of these objects is best for the youngest clusters (71%) and dramatically *decreases* as they become older (28% accuracy for those with SED ages >1 Gyr). Class 2 objects reveal no such obvious correlations.

Overall, we observe reduced agreement between the BCW and our model classes for objects fainter than the standard magnitude limit ($m_V > 23.5$, particularly for Class 1 and 4) as well as those which appear younger in $U - B$ vs. $V - I$ space (Class 1), while also noting that the models correctly label BCW Class 1 objects which occupy the same color space as old, globular clusters with a very high degree of accuracy. This matches what we observe with the SED ages of objects as well, where we also find that Class 3 objects are most accurately classified for the youngest objects instead. Importantly, the instances where we do observe reduced accuracy for Class 1 objects are mostly disagreements between a Class of 1 or 2 label, and when we consider the two classes together

as many star cluster studies do, then the overall accuracy remains good ($\gtrsim$80%), consistent with our previous findings.

## 4.7 Summary

We present the results of new deep transfer learning for star cluster classification using the available data from the PHANGS-HST survey. Our sample consists of over 20,000 star cluster candidates, all of which have been visually inspected by a human (BCW), who has classified them according to their morphology. We utilize the cluster morphology classification system standard across LEGUS and PHANGS-HST studies amongst others, which includes four classes, briefly: 1) symmetric, 2) asymmetric, 3) multi-peaked, 4) non-cluster.

Our primary experiments use the `ResNet18` and `VGG19-BN` neural network architectures, and transfer their pretrained `ImageNet` knowledge to the task of classifying cluster morphology for the PHANGS-HST sample. In our first experiment, we use 80% of our overall sample (independent of galactic distance) to independently train 10 models using `ResNet18` and 10 models using `VGG19-BN`, and evaluate their performance by using them to classify the remaining 20% of clusters in the sample. Our second experiment instead divides the cluster sample into three separate bins based on galactic distance, where we use these three samples to independently train three sets of 10 models using the `VGG19-BN` architecture. We refer to these as our distance-independent and distance-dependent models, respectively.

The results are of these experiments are summarized here:

1 Our distance-independent models show considerable improvement over the current, LEGUS-based, machine learning models used to predict the classes of PHANGS-HST objects. Our

new models classify Class 1, 2, 3, and 4 objects with accuracies of ∼77%, ∼59%, ∼70%, and ∼62%, respectively, which is similar to previous star cluster classification studies (e.g. [64, 137, 117]). Moreover, this represents improvements of ∼16%, ∼32%, and ∼44% over the LEGUS-based models in the classification of PHANGS-HST Class 1, 2, and 3 objects (i.e., clusters).

2 The division of our sample into three separate distance bins does not significantly affect the accuracy of the models. The accuracies averaged over the 10 `VGG19-BN` models for the three distance bins range from 77–80%, 48–58%, 68–75%, and 49–60% for Class 1, 2, 3, and 4 objects, respectively. We have used our distance-independent models to classify each of these validation sets as well, with accuracies ranging from 71–81%, 54–63%, 69–73%, and 53–59% for Class 1, 2, 3, and 4 objects, respectively.

As a result of these experiments, we determine it best to use our distance-independent models in the production-scale classification of PHANGS-HST objects. These models show marked improvement over the LEGUS-based models, and along with simplicity, may also help to avoid potential artificial correlations between the samples of the similarly-accurate distance-dependent models.

Additionally, we compare model accuracy to a variety of galactic and individual cluster properties, upon which we find:

3 While it appears that model accuracy slightly decreases with individual galaxy distance, the correlation is not statistically significant, and is thus consistent with our findings for the distance-dependent models (Section 4.5.2). Additionally, while we find that our model

accuracy improves for galaxies with higher $\Sigma_{CO}$, it may in fact be a result of bias in the training sample of clusters.

4 The model accuracy for Class 1 objects is lower for faint objects as well as those which appear young in color-color space. The recovery rate for Class 1 objects fainter than $m_V$ = 23.5 mag is 20% lower than for objects brighter than $m_V$ = 23.5 mag. Additionally, we find that our models less accurately identify Class 1 objects which appear younger relative to SSP models. This is supported by the SED ages of the objects as well, where we find that the oldest Class 1 objects (> 100 Myr) are identified by our models with ~30% greater accuracy than those which are youngest (≤ 10 Myr). The opposite observation is made for Class 3 objects, which reveal that model accuracy is best for the youngest Class 3 objects (71%), and is significantly worse for the oldest objects (28% accuracy for objects with SED age > 1 Gyr).

   For both of these observations for Class 1 clusters, we find that the models are largely reclassifying these objects as Class 2 clusters instead, which provides reassurance as Class 1 and 2 objects together typically form the basis of star cluster studies, and hence none of these objects which appear more difficult for the models to classify would be left out of standard samples.

### 4.7.1 Future Work

As our newly trained models have been effective in classifying star clusters from PHANGS-HST, the next objective will be to to provide machine learning classifications for the full sample of PHANGS-HST objects using these models. We could then use our models to classify cluster samples outside of PHANGS-HST to inform us further of their performance and external viability.

To this end, there also remain opportunities to explore enhanced model performance. For example, newer neural networks such as Contrastive Language–Image Pre-training (CLIP; [119]) offer unique algorithms which have shown improved classification accuracy over `ResNet` models for objects outside of the dataset on which the the models were trained (i.e. `ImageNet`; [43]). Continuing to optimize the performance of classification models will be important as newer, larger samples are made available, such as the data which we have just begun receiving from JWST.

## Acknowledgements

Médéric Boquien gratefully acknowledges support by the ANID BASAL project FB210003 and from the FONDECYT regular grant 1211000. K.G. is supported by the Australian Research Council through the Discovery Early Career Researcher Award (DECRA) Fellowship DE220100766 funded by the Australian Government. K.G. is supported by the Australian Research Council Centre of Excellence for All Sky Astrophysics in 3 Dimensions (ASTRO 3D), through project number CE170100013.

# Chapter 5

# Conclusions

Star clusters represent a fundamental unit in the study of the star formation cycle. We investigate this cycle by studying the morphology of HII regions via their H$\alpha$ emission in relation to their host star cluster's age, reddening, and mass derived through SED-fitting of *HST* NUV, U, B, V, I photometry.

We first find that HII regions typically evolve from a concentrated morphology to a more dispersed, bubble-like morphology within the first 3 Myr of a cluster's life. This timescale is prior to the onset of supernovae, and so this finding indicates a significant role for pre-supernova feedback such as stellar winds, radiation pressure, and photoionization in the clearing of a cluster's natal gas. We also examine the effects of stochastic sampling of the initial mass function which typically occur with lower-mass cluster samples. Here we find evidence that red supergiants can influence the colors of clusters such that SED-fitting can misinterpret their naturally red flux as reddening due to dust, thus resulting in underestimated SED ages. To address this, we present a novel method of stacking the flux from numerous individual clusters in order to synthesize more massive clusters,

ultimately resulting in more appropriate SED ages and reddening. Additionally, we find that the degeneracy between cluster age and reddening is not limited to lower mass clusters, as we identify dozens of massive clusters with poorly estimated SED ages. Notably, despite the presence of these mismeasured clusters in our sample, their population is sparse enough that our reported timescales are upheld. Finally, we utilize deep transfer learning to provide more efficient classifications of star cluster morphologies for future studies. Here we find that our newly trained models outperform prior models in the morphological classification of PHANGS-HST star clusters, particularly for those which are asymmetric or are compact associations of stars.

## 5.1 Gas Clearing Timescales

As stellar feedback occurs on different timescales, constraining the time during which a star cluster clears its natal gas allows us to understand which feedback processes are responsible. To investigate this, we analyze 3757 star clusters in 21 *HST* WFC3/UVIS fields covering 16 galaxies (spanning a distance range of ∼3–10 Mpc) from the LEGUS sample (GO-13364; PI D. Calzetti), which represents all LEGUS galaxies with both *HST* H$\alpha$ narrowband imaging (GO-13773; PI R. Chandar) as well as cluster catalogs containing SED-fit cluster properties [2]. We visually classify each of these clusters according to their H$\alpha$ morphology, namely 1) concentrated, 2) partially exposed, and 3) no-emission.

We find that of the clusters with SED ages $\leq$ 10 Myr, those with concentrated H$\alpha$ have a median age of 1-2 Myr, those with partially exposed H$\alpha$ have a median age of 2-3 Myr, and those without H$\alpha$ have a median age of 3-6 Myr, where the ranges reflect differences resulting from various dust and stellar population models used in the SED fitting. Together with the inferred ages from the

relative fraction of each H$\alpha$ morphology, they support two main conclusions: First, the prevalence of clusters which show evidence of gas clearing (partially exposed H$\alpha$ class) and yet have SED ages younger than the possible onset of supernovae ($\leq$ 3 Myr) highlight the importance of pre-supernova gas clearing mechanisms such as stellar winds, radiation pressure, and photoionization during the first few Myr of a cluster's life (see also [36]). Secondly, the age difference between clusters with concentrated and partially exposed H$\alpha$ suggests short (1-2 Myr) clearing timescales, in agreement with other studies such as [139, 72, 67, 64, 107, 81].

Additionally, we find that our reported timescales are robust to the varying resolution of H$\alpha$ across our sample. For our nearest galaxy (NGC 7793W; 3.44 Mpc), the majority ($>$ 64%) of our original, *HST*-based partially exposed classifications are recovered when we project the galaxy to be at a distance of our most distant galaxy (NGC 3351; 10.0 Mpc), and even to a distance of 20.0 Mpc, at which we appear to reach the resolution limit for our classifications. For both of these reprojections, the statistical properties of clusters according to their H$\alpha$ morphologies remain consistent with the original classifications, thus upholding our reported timescales. The use of ground-based H$\alpha$ data taken at CTIO as part of the SINGS program, however, is unfit for this analysis as it is simply unable to resolve small clearing structures necessary to identify the early stages of gas clearing, and therefore we find that the resolution capability of *HST* is necessary to produce the analysis and results presented in Chapters 2 & 3.

## 5.2 Reliability of SED-fitting

As we report differences in star cluster age as small as 1 Myr, it is important to examine how well-constrained our star cluster ages are, especially considering effects due to stochastic sampling

of the IMF (e.g. [58, 59]) & the age-reddening degeneracy (e.g. [140, 135]). In each of the analyses detailed below, our timescales reported in 5.1 are upheld.

Regarding stochastic sampling, we find that for our entire sample, which has a median cluster mass of ~1000 $M_{\odot}$, clusters which lack evidence of nearby gas (classified as no-emission) have likely overestimated SED-fitted reddening: these clusters without H$\alpha$ have a median E(B-V) which is comparable to those with concentrated H$\alpha$ emission (~0.2 mag). Upon investigating these clusters further, we report that these overestimated E(B-V) values are due to the presence of bright red, point-like sources (likely red supergiants), which mimic the effects of cluster reddening. For clusters without H$\alpha$, those which contain one or more of these red source(s) have a median E(B-V) that is ~2.5x greater than those without red source(s) (0.26 mag vs. 0.11 mag). As overestimations of reddening result in underestimated SED ages, the median age of young clusters without H$\alpha$ (3-6 Myr) represent a lower-limit. To address this stochstic effect, we present a novel method of stacking the flux of individual clusters to synthesize more massive clusters and perform SED-fitting on them, which results in much more reasonable ages and E(B-V) values for these clusters. Importantly, this effect does not affect our clearing timescales reported in 5.1 as they are dependent on the ages of clusters with concentrated and partially-exposed H$\alpha$ morphologies.

We also find that the sensitivity of SED-fitting due to the age-extinction degeneracy is not limited to clusters of lower mass. In our sample, at least 46 of 1408 (3%) massive ($\geq$ 5000 $M_{\odot}$) clusters appear to have questionable SED ages based on our analysis of H$\alpha$. These clusters fall into two categories: The first group of anomalies consists of 12 isolated clusters with no H$\alpha$ emission, yet which have very young ($\leq$ 3 Myr) apparent SED ages. Upon visual inspection of each object's image, 10 of the 12 appear to have features consistent with much older clusters (i.e.,

globular clusters), including their color, symmetry, lack of nearby young stars, lack of H$\alpha$ emission, and presence in the bulge of the galax. Because we only examine objects with SED ages $\leq$ 3 Myr, we note that there are likely to be several times as many globular clusters with poor age estimates overall, based on the results of [140] and [135]. The second group consists of 34 massive clusters with H$\alpha$ emission (2% of all massive clusters), but apparent SED age estimates that are old ($>$ 10 Myr). While some of these clusters do not have a significant amount of flux in the bluest bands (F275W, F336W), they share a local space with other blue stars in addition to clearly displaying the presence of H$\alpha$. Notably, as these objects represent a small fraction of our overall sample of massive clusters, we find that the median ages of clusters $\geq$ 5000 $M_{\odot}$ for each H$\alpha$ class are consistent with those based on overall sample whether or not the objects in question are included. Here we note that there are other types of questionable SED ages that the current study is not sensitive too, since they do not involve the presence or absence of H$\alpha$, hence our estimates represent lower limits to the total number of bad ages.

The above apparent age-extinction degeneracy issues lead us to examine the robustness of our SED-fitting method by re-fitting them with an alternative algorithm (CIGALE; [135]), which yields consistent results. The median ratios of cluster ages and masses from our standard catalog and those derived using CIGALE are less than 0.005 dex and 0.05 dex, respectively, for all H$\alpha$ morphologies. For cluster E(B-V), we find the median difference to be less than 0.02 mag for all such comparisons and morphologies. These small offsets along with the fact that our statistical results remain unaffected indicate that our star cluster properties are robust to the adopted SED-fitting algorithm and thus support our reported timescales.

## 5.3 Classifying Star Cluster Morphology Using Machine Learning

The studies presented in Chapters 2 & 3, as well as many others regarding the star formation cycle, have historically relied on visual classification of star cluster morphology (i.e. symmetric (Class 1), asymmetric (Class 2), multi-peaked (Class 3), non-cluster (Class 4)) by one or more human(s) for the production of cluster samples. As these samples continue to grow, it becomes increasingly more time consuming to produce catalogs of star clusters, thus limiting their sample size. To address this, we utilize deep transfer learning to vastly improve the efficiency of star cluster classification using the available data from the PHANGS-HST survey [101], consisting of over 20,000 star cluster candidates. Here we present the results of our newly-trained models, which reveal considerable improvement upon prior models.

Our primary experiments use the `ResNet18` and `VGG19-BN` neural network architectures, and transfer their pretrained `ImageNet` [43] knowledge to the task of classifying cluster morphology for the PHANGS-HST sample. Our first set of models is trained on the overall cluster sample (independent of galactic distance), while our second set of models instead divides the cluster sample into three separate bins based on galactic distance. We refer to these as our distance-independent and distance-dependent models, respectively.

We find that our newly-trained models more accurately predict the classes of PHANGS-HST objects than LEGUS-based models. Our distance-independent models classify Class 1, 2, 3, and 4 objects with accuracies of ∼77%, ∼59%, ∼70%, and ∼62%, respectively, which is similar to previous star cluster classification studies (e.g. [137, 117]). Moreover, this represents improvements of ∼16%, ∼32%, and ∼44% over the LEGUS-based models in the classification of PHANGS-HST Class 1, 2, and 3 objects (i.e., clusters). Secondly, the division of our sample into three separate

distance bins does not significantly affect the accuracy of the models. The accuracies averaged over the 10 `VGG19-BN` models for the three distance bins range from 77–80%, 48–58%, 68–75%, and 49–60% for Class 1, 2, 3, and 4 clusters, respectively. In comparison, our distance-independent models classify the same test sets of clusters with accuracies ranging from 71–81%, 54–63%, 69–73%, and 53–59% for Class 1, 2, 3, and 4 clusters, respectively. Based on simplicity and to avoid potential artificial correlations between the samples of the distance-dependent models, we determine it best to use our distance-independent models in the production-scale classification of PHANGS-HST objects.

Additionally, we find that our models are potentially sensitive to a number of galactic and individual star cluster parameters. First, despite the consistency between our two sets of models, we actually find that the accuracy of our distance-independent models slightly decreases with galactic distance (∼10% over our distance range of 9-23 Mpc). We also observe that model accuracy appears to be higher for galaxies with greater star formation, as measured by SFR and $\Sigma_{CO}$. While we note that these trends are not the strongest, they may also be a result of our sample: the galaxies with the most star formation naturally have the most clusters on which the models have trained, and these galaxies also have a greater percentage of Class 1 objects, which the models are more adept at classifying.

When considering the properties of individual clusters, we find that model accuracy for Class 1 objects is lower for faint objects as well as those which appear young in color-color space. The recovery rate for Class 1 objects fainter than $m_V$ = 23.5 mag is 20% lower than for objects brighter than $m_V$ = 23.5 mag, and Class 1 objects with SED ages > 100 Myr are identified by our models with ∼30% greater accuracy than those with SED ages ≤ 10 Myr). The opposite observation

is made for Class 3 objects, which reveal that model accuracy is best for the young Class 3 objects (71%), and is significantly worse for the oldest objects (28% accuracy for objects with SED age > 1 Gyr). For these observations, we find that the models are reclassifying these Class 1 objects as Class 2 objects instead, which provides reassurance as Class 1 and 2 objects together typically form the basis of star cluster studies, and hence none of these objects which appear more difficult for the models to classify would be left out of standard samples.

## 5.4 Future Work

Chapters 2 & 3 of this work highlight the effects of the age-reddening degeneracy in the SED-fitting of star clusters. To potentially break the observed degeneracy, there are a number of avenues available to pursue: 1) while the SED-fitting in this work have only used NUBVI broadband photometry to predict the properties of star clusters, the inclusion of H$\alpha$ measurements has shown promise in better constraining cluster age [144, 12]. 2) There exists MUSE (*Multi Unit Spectroscopic Explorer*) data for fields overlapping with our sample with which we could create E(B-V) maps, as done by [42]. These would allow us to compare an independent measure of cluster reddening (via the Balmer decrement) to our SED-fitted reddening to check for consistency. Further, [75] produced extinction maps for two of the LEGUS fields in our study by spatially binning the extinction of individual stars, based on isochrone matching of their broadband photometry, thus providing another check on cluster reddening. 3) We could also utilize overlapping ALMA CO(2-1) maps (e.g. [104]), which would allow us to firstly determine the degree to which H$\alpha$ traces the molecular gas in a region. We would then be able to infer whether the clusters in our sample have foreground dust, which we could then use to support or oppose their SED-fitted dust reddening.

Additionally, our analysis relies on the detection of star clusters and visible H$\alpha$ emission. Stellar populations within denser natal clouds may go undetected, thus an analysis of our sample's completeness would be critical in determining more accurate cluster populations and distributions of cluster properties, particularly for clusters with concentrated HII regions (e.g. [110, 81]). With the advent of the James Webb Space Telescope, infrared observations of nearby galaxies will be able to provide inventories of dust embedded clusters to probe these earliest stages of star formation. More complete catalogs of HII regions (e.g. [132, 84, 16]) would also be necessary to provide a true representative sample of the star cluster population in these analyses.

Another key uncertainty is the use of a fixed covering fraction of 0.5 in our SED-modeling, and a careful examination could be performed to determine how the use of a proper covering fraction for each cluster (e.g Scheuermann et al., in prep.) might affect the ages we have presented here.

Chapter 4 relies on the use of two neural network architectures in `ResNet18` & `VGG-19BN` to produce models for star cluster classification. As these models have been effective in classifying star clusters from PHANGS-HST, the first objective will be to to provide machine learning classifications for the full sample of PHANGS-HST objects using these models. We could then use our models to classify cluster samples outside of PHANGS-HST to inform us further of their performance and external viability. To this end, there also remain opportunities to explore enhanced model performance. For example, newer neural networks such as Contrastive Language–Image Pre-training (CLIP; [119]) offer unique algorithms which have shown improved classification accuracy over `ResNet` models for objects outside of the dataset on which the the models were trained (i.e. `ImageNet`; [43]). Continuing to optimize the performance of classification models will be important

as newer, larger samples are made available, such as the data which we have just begun receiving from JWST.

# Appendix A

# Additional Information for Chapter 3

The analyses performed throughout this work are based on the H$\alpha$ classifications of 3757 total clusters, as described in Section 3.3. The complete list of classifications, including whether the cluster is isolated, is provided as supplementary online material alongside relevant identification information from the LEGUS cluster catalogs. An abbreviated version of this table is shown in Table A.1.

**Cluster Identification Information and H$\alpha$ Classes**

| ObjectID | LEGUS X | LEGUS Y | RA | Dec | H$\alpha$ Class | Isolated? | Field |
|---|---|---|---|---|---|---|---|
| 3 | 3077.165 | 4717.243 | 73.57212 | -53.3508 | 3 | TRUE | ngc1705 |
| 9 | 4140 | 4315.868 | 73.55252 | -53.35522 | 3 | TRUE | ngc1705 |
| 13 | 3472.717 | 4121.713 | 73.56483 | -53.35736 | 3 | TRUE | ngc1705 |
| 15 | 3227.907 | 4082.261 | 73.56934 | -53.35779 | 3 | TRUE | ngc1705 |
| 16 | 4137.33 | 4061.561 | 73.55257 | -53.35802 | 3 | TRUE | ngc1705 |
| 26 | 3791.484 | 3955 | 73.55895 | -53.35919 | 3 | TRUE | ngc1705 |
| 42 | 3726 | 3870.536 | 73.56016 | -53.36012 | 1 | FALSE | ngc1705 |
| 53 | 3869 | 3892.138 | 73.55752 | -53.35988 | 3 | FALSE | ngc1705 |
| 65 | 4002.706 | 3777 | 73.55505 | -53.36115 | 3 | FALSE | ngc1705 |
| 72 | 4045.371 | 3869.126 | 73.55427 | -53.36013 | 3 | TRUE | ngc1705 |
| ⋮ | ⋮ | ⋮ | ⋮ | ⋮ | ⋮ | ⋮ | ⋮ |

Table A.1: An abbreviated table of H$\alpha$ classifications for all 3815 clusters detected within the 21 fields in this study (1 = concentrated, 2 = partially exposed, 3 = no emission). In addition to these classes, we include whether the cluster is isolated (no neighboring clusters within 75pc), as well as relevant identification information taken from the LEGUS cluster catalogs (`https://legus.stsci.edu`). The full table is available online as supplementary material.

# Bibliography


[1] Sandro Ackermann, Kevin Schawinski, Ce Zhang, Anna K. Weigel, and M. Dennis Turp. Using transfer learning to detect galaxy mergers. *MNRAS*, 479:415–425, Sep 2018.

[2] A. Adamo, J. E. Ryon, M. Messa, H. Kim, K. Grasha, D. O. Cook, D. Calzetti, J. C. Lee, B. C. Whitmore, B. G. Elmegreen, L. Ubeda, L. J. Smith, S. N. Bright, A. Runnholm, J. E. Andrews, M. Fumagalli, D. A. Gouliermis, L. Kahre, P. Nair, D. Thilker, R. Walterbos, A. Wofford, A. Aloisi, G. Ashworth, T. M. Brown, R. Chandar, C. Christian, M. Cignoni, G. C. Clayton, D. A. Dale, S. E. de Mink, C. Dobbs, D. M. Elmegreen, A. S. Evans, J. S. Gallagher, III, E. K. Grebel, A. Herrero, D. A. Hunter, K. E. Johnson, R. C. Kennicutt, M. R. Krumholz, D. Lennon, K. Levay, C. Martin, A. Nota, G. Östlin, A. Pellerin, J. Prieto, M. W. Regan, E. Sabbi, E. Sacchi, D. Schaerer, D. Schiminovich, F. Shabani, M. Tosi, S. D. Van Dyk, and E. Zackrisson. Legacy ExtraGalactic UV Survey with The Hubble Space Telescope: Stellar Cluster Catalogs and First Insights Into Cluster Formation and Evolution in NGC 628. *ApJS*, 841:131, June 2017.

[3] A. Adamo, L. J. Smith, J. S. Gallagher, N. Bastian, J. Ryon, M. S. Westmoquette, I. S. Konstantopoulos, E. Zackrisson, S. S. Larsen, E. Silva-Villa, J. C. Charlton, and D. R. Weisz. Revealing a ring-like cluster complex in a tidal tail of the starburst galaxy NGC 2146. *MNRAS*, 426(2):1185–1194, October 2012.

[4] A. Adamo, G. Östlin, E. Zackrisson, M. Hayes, R. J. Cumming, and G. Micheva. Super star clusters in Haro 11: properties of a very young starburst and evidence for a near-infrared flux excess. *Monthly Notices of the Royal Astronomical Society*, 407(2):870–890, 09 2010.

[5] Angela Adamo, Peter Zeidler, J. M. Diederik Kruijssen, Mélanie Chevance, Mark Gieles, Daniela Calzetti, Corinne Charbonnel, Hans Zinnecker, and Martin G. H. Krause. Star clusters near and far. *Space Science Reviews*, 216(4), Jun 2020.

[6] O. Agertz, A. V. Kravtsov, S. N. Leitner, and N. Y. Gnedin. Toward a Complete Accounting of Energy and Momentum from Stellar Feedback in Galaxy Formation Simulations. *ApJ*, 770:25, June 2013.

[7] Gagandeep S Anand, Janice C Lee, Schuyler D Van Dyk, Adam K Leroy, Erik Rosolowsky, Eva Schinnerer, Kirsten Larson, Ehsan Kourkchi, Kathryn Kreckel, Fabian Scheuermann, Luca Rizzi, David Thilker, R Brent Tully, Frank Bigiel, Guillermo A Blanc, Mé déric Boquien, Rupali Chandar, Daniel Dale, Eric Emsellem, Sinan Deger, Simon C O Glover, Kathryn Grasha, Brent Groves, Ralf S. Klessen, J M Diederik Kruijssen, Miguel Querejeta,

Patricia Sánchez-Blázquez, Andreas Schruba, Jordan Turner, Leonardo Ubeda, Thomas G Williams, and Brad Whitmore. Distances to PHANGS galaxies: New tip of the red giant branch measurements and adopted distances. *Monthly Notices of the Royal Astronomical Society*, 501(3):3621–3639, nov 2020.

[8] P. Anders and U. Fritze-v. Alvensleben. Spectral and photometric evolution of young stellar populations: The impact of gaseous emission at various metallicities. *A&A*, 401:1063–1070, April 2003.

[9] L. D. Anderson, T. M. Bania, Dana S. Balser, V. Cunningham, T. V. Wenger, B. M. Johnstone, and W. P. Armentrout. THEWISECATALOG OF GALACTIC h II REGIONS. *ApJ*, 212(1):1, apr 2014.

[10] J. E. Andrews, D. Calzetti, R. Chandar, B. G. Elmegreen, R. C. Kennicutt, Hwihyun Kim, Mark R. Krumholz, J. C. Lee, Sean McElwee, R. W. O'Connell, and B. Whitmore. BIG FISH IN SMALL PONDS: MASSIVE STARS IN THE LOW-MASS CLUSTERS OF m83. *ApJ*, 793(1):4, aug 2014.

[11] Jennifer Andrews, D Calzetti, R Chandar, Janice Lee, Bruce Elmegreen, R C. Kennicutt, B Whitmore, Jeffrey S. Kissel, Robert L. da Silva, Mark R. Krumholz, R W. O'Connell, Michael Dopita, Jay Frogel, and Hwihyun Kim. An initial mass function study of the dwarf starburst galaxy ngc 4214. *ApJ*, 767:51, 03 2013.

[12] G. Ashworth, M. Fumagalli, M. R. Krumholz, A. Adamo, D. Calzetti, R. Chandar, M. Cignoni, D. Dale, B. G. Elmegreen, III Gallagher, J. S., D. A. Gouliermis, K. Grasha, E. K. Grebel, K. E. Johnson, J. Lee, M. Tosi, and A. Wofford. Exploring the IMF of star clusters: a joint SLUG and LEGUS effort. *MNRAS*, 469(2):2464–2480, August 2017.

[13] C. Barbaro and C. Bertelli. Integrated Colour Synthesis of Population I Clusters. *A&A*, 54:243, January 1977.

[14] P. H. Barchi, R. R. de Carvalho, R. R. Rosa, R. Sautter, M. Soares-Santos, B. A. D. Marques, and E. Clua. Machine and Deep Learning Applied to Galaxy Morphology - A Complete Classification Catalog. *arXiv e-prints*, page arXiv:1901.07047, Jan 2019.

[15] M. J. Barlow. Dust in Planetary Nebulae and in Post-AGB Objects. In R. Weinberger and A. Acker, editors, *Planetary Nebulae*, volume 155 of *IAU Symposium*, page 163, 1993.

[16] A. T. Barnes, S. C. O. Glover, K. Kreckel, E. C. Ostriker, F. Bigiel, F. Belfiore, I. Bešlić, G. A. Blanc, M. Chevance, D. A. Dale, O. Egorov, C. Eibensteiner, E. Emsellem, K. Grasha, B. A. Groves, R. S. Klessen, J. M. D. Kruijssen, A. K. Leroy, S. N. Longmore, L. Lopez, R. McElroy, S. E. Meidt, E. J. Murphy, E. Rosolowsky, T. Saito, F. Santoro, E. Schinnerer, A. Schruba, J. Sun, E. J. Watkins, and T. G. Williams. Comparing the pre-SNe feedback and environmental pressures for 6000 H II regions across 19 nearby spiral galaxies. *MNRAS*, 508(4):5362–5389, December 2021.

[17] Ashley T. Barnes, Steven N. Longmore, James E. Dale, Mark R. Krumholz, J. M. Diederik Kruijssen, and Frank Bigiel. Which feedback mechanisms dominate in the high-pressure environment of the central molecular zone? *MNRAS*, 498(4):4906–4923, November 2020.

[18] N. Bastian, A. Adamo, E. Zackrisson, M. Gieles, E. Silva-Villa, H. J. G. L. M. Lamers, S. S. Larsen, L. J. Smith, R. Kotulla, I. S. Konstantopoulos, and G. Trancho. Evidence for environmentally dependent cluster disruption in M83. *MNRAS: Letters*, 417(1):L6–L10, 10 2011.

[19] N. Bastian, M. Gieles, Yu. N. Efremov, and H. J. G. L. M. Lamers. Hierarchical star formation in M 51: star/cluster complexes. *A&A*, 443(1):79–90, November 2005.

[20] N. Bastian, M. Gieles, H. J. G. L. M. Lamers, R. A. Scheepmaker, and R. de Grijs. The star cluster population of M 51. II. Age distribution and relations among the derived parameters. *A&A*, 431(3):905–924, March 2005.

[21] M. Boquien, D. Burgarella, Y. Roehlly, V. Buat, L. Ciesla, D. Corre, A. K. Inoue, and H. Salas. CIGALE: a python Code Investigating GALaxy Emission. *A&A*, 622:A103, February 2019.

[22] Frédéric Bournaud, Bruce G. Elmegreen, Romain Teyssier, David L. Block, and Ivânio Puerari. ISM properties in hydrodynamic galaxy simulations: turbulence cascades, cloud formation, role of gravity and feedback. *Monthly Notices of the Royal Astronomical Society*, 409(3):1088–1099, 12 2010.

[23] W. Brandner, J. S. Clark, A. Stolte, R. Waters, I. Negueruela, and S. P. Goodwin. Intermediate to low-mass stellar content of Westerlund 1. *A&A*, 478:137–149, January 2008.

[24] G. Bruzual and S. Charlot. Stellar population synthesis at the resolution of 2003. *MNRAS*, 344:1000–1028, October 2003.

[25] G. Bruzual A. Stellar Populations in Star Clusters: The Rôle Played by Stochastic Effects. In D. P. Geisler, E. K. Grebel, and D. Minniti, editors, *Extragalactic Star Clusters*, volume 207 of *IAU Symposium*, page 616, 2002.

[26] D. Burgarella, V. Buat, and J. Iglesias-Páramo. Star formation and dust attenuation properties in galaxies from a statistical ultraviolet-to-far-infrared analysis. *MNRAS*, 360(4):1413–1425, July 2005.

[27] D. Calzetti, R. Chandar, J. C. Lee, B. G. Elmegreen, R. C. Kennicutt, and B. Whitmore. A METHOD FOR MEASURING VARIATIONS IN THE STELLAR INITIAL MASS FUNCTION. *ApJ*, 719(2):L158–L161, jul 2010.

[28] D. Calzetti, J. C. Lee, E. Sabbi, A. Adamo, L. J. Smith, J. E. Andrews, L. Ubeda, S. N. Bright, D. Thilker, A. Aloisi, T. M. Brown, R. Chandar, C. Christian, M. Cignoni, G. C. Clayton, R. da Silva, S. E. de Mink, C. Dobbs, B. G. Elmegreen, D. M. Elmegreen, A. S. Evans, M. Fumagalli, J. S. Gallagher, III, D. A. Gouliermis, E. K. Grebel, A. Herrero, D. A. Hunter, K. E. Johnson, R. C. Kennicutt, H. Kim, M. R. Krumholz, D. Lennon, K. Levay, C. Martin, P. Nair, A. Nota, G. Östlin, A. Pellerin, J. Prieto, M. W. Regan, J. E. Ryon, D. Schaerer, D. Schiminovich, M. Tosi, S. D. Van Dyk, R. Walterbos, B. C. Whitmore, and A. Wofford. Legacy Extragalactic UV Survey (LEGUS) With the Hubble Space Telescope. I. Survey Description. *AJ*, 149:51, February 2015.

[29] Daniela Calzetti, Lee Armus, Ralph C. Bohlin, Anne L. Kinney, Jan Koornneef, and Thaisa Storchi-Bergmann. The Dust Content and Opacity of Actively Star-forming Galaxies. *ApJ*, 533(2):682–695, April 2000.

[30] J. A. Cardelli, G. C. Clayton, and J. S. Mathis. The relationship between infrared, optical, and ultraviolet extinction. *ApJ*, 345:245–256, October 1989.

[31] M. Cerviño and V. Luridiana. Confidence limits of evolutionary synthesis models. IV. Moving forward to a probabilistic formulation. *A&A*, 451:475–498, May 2006.

[32] Gilles Chabrier. Galactic Stellar and Substellar Initial Mass Function. , 115(809):763–795, July 2003.

[33] R. Chandar, B. C. Whitmore, H. Kim, C. Kaleida, M. Mutchler, D. Calzetti, A. Saha, R. O'Connell, B. Balick, H. Bond, M. Carollo, M. Disney, M. A. Dopita, J. A. Frogel, D. Hall, J. A. Holtzman, R. A. Kimble, P. McCarthy, F. Paresce, J. Silk, J. Trauger, A. R. Walker, R. A. Windhorst, and E. Young. The Luminosity, Mass, and Age Distributions of Compact Star Clusters in M83 Based on Hubble Space Telescope/Wide Field Camera 3 Observations. *ApJ*, 719:966–978, August 2010.

[34] Rupali Chandar, S. Michael Fall, and Bradley C. Whitmore. New Tests for Disruption Mechanisms of Star Clusters: The Large and Small Magellanic Clouds. *ApJ*, 711(2):1263–1279, March 2010.

[35] Rupali Chandar, Bradley C. Whitmore, Daiana Dinino, Robert C. Kennicutt, L. H. Chien, Eva Schinnerer, and Sharon Meidt. The Age, Mass, and Size Distributions of Star Clusters in M51. *ApJ*, 824(2):71, June 2016.

[36] Mélanie Chevance, J. M. Diederik Kruijssen, Mark R. Krumholz, Brent Groves, Benjamin W. Keller, Annie Hughes, Simon C. O. Glover, Jonathan D. Henshaw, Cinthya N. Herrera, Jenny J. Kim, Adam K. Leroy, Jérôme Pety, Alessandro Razza, Erik Rosolowsky, Eva Schinnerer, Andreas Schruba, Ashley T. Barnes, Frank Bigiel, Guillermo A. Blanc, Eric Emsellem, Christopher M. Faesi, Kathryn Grasha, Ralf S. Klessen, Kathryn Kreckel, Daizhong Liu, Steven N. Longmore, Sharon E. Meidt, Miguel Querejeta, Toshiki Saito, Jiayi Sun, and Antonio Usero. Pre-supernova feedback mechanisms drive the destruction of molecular clouds in nearby star-forming disc galaxies. *arXiv e-prints*, page arXiv:2010.13788, October 2020.

[37] E. Churchwell, M. S. Povich, D. Allen, M. G. Taylor, M. R. Meade, B. L. Babler, R. Indebetouw, C. Watson, B. A. Whitney, M. G. Wolfire, T. M. Bania, R. A. Benjamin, D. P. Clemens, M. Cohen, C. J. Cyganowski, J. M. Jackson, H. A. Kobulnicky, J. S. Mathis, E. P. Mercer, S. R. Stolovy, B. Uzpen, D. F. Watson, and M. J. Wolff. The Bubbling Galactic Disk. *ApJ*, 649:759–778, October 2006.

[38] D. O. Cook, J. C. Lee, A. Adamo, H. Kim, R. Chand ar, B. C. Whitmore, A. Mok, J. E. Ryon, D. A. Dale, D. Calzetti, J. E. Andrews, A. Aloisi, G. Ashworth, S. N. Bright, T. M. Brown, C. Christian, M. Cignoni, G. C. Clayton, R. da Silva, S. E. de Mink, C. L. Dobbs, B. G. Elmegreen, D. M. Elmegreen, A. S. Evans, M. Fumagalli, J. S. Gallagher, D. A. Gouliermis,

K. Grasha, E. K. Grebel, A. Herrero, D. A. Hunter, E. I. Jensen, K. E. Johnson, L. Kahre, R. C. Kennicutt, M. R. Krumholz, N. J. Lee, D. Lennon, S. Linden, C. Martin, M. Messa, P. Nair, A. Nota, G. Östlin, R. C. Parziale, A. Pellerin, M. W. Regan, E. Sabbi, E. Sacchi, D. Schaerer, D. Schiminovich, F. Shabani, F. A. Slane, J. Small, C. L. Smith, L. J. Smith, S. Taibi, D. A. Thilker, I. C. de la Torre, M. Tosi, J. A. Turner, L. Ubeda, S. D. Van Dyk, R. AM Walterbos, and A. Wofford. Star cluster catalogues for the LEGUS dwarf galaxies. *MNRAS*, 484:4897–4919, Apr 2019.

[39] J. E. Dale, J. Ngoumou, B. Ercolano, and I. A. Bonnell. Before the first supernova: combined effects of Hii regions and winds on molecular clouds. *Monthly Notices of the Royal Astronomical Society*, 442(1):694–712, 06 2014.

[40] Gerard de Vaucouleurs, Antoinette de Vaucouleurs, Jr. Corwin, Herold G., Ronald J. Buta, Georges Paturel, and Pascal Fouque. *Third Reference Catalogue of Bright Galaxies*. 1991.

[41] Sinan Deger, Janice C. Lee, Bradley C. Whitmore, David A. Thilker, Mederic Boquien, Rupali Chandar, Daniel A. Dale, Leonardo Ubeda, Rick White, Kathryn Grasha, Simon C. O. Glover, Andreas Schruba, Ashley T. Barnes, Ralf Klessen, J. M. Diederik Kruijssen, Erik Rosolowsky, and Thomas G. Williams. Bright, relatively isolated star clusters in PHANGS-HST galaxies: Aperture corrections, quantitative morphologies, and comparison with synthetic stellar population models. *MNRAS*, November 2021.

[42] Lorenza Della Bruna, Adamo, Angela, Bik, Arjan, Fumagalli, Michele, Walterbos, Rene, Östlin, Göran, Bruzual, Gustavo, Calzetti, Daniela, Charlot, Stephane, Grasha, Kathryn, Smith, Linda J., Thilker, David, and Wofford, Aida. Studying the ism at pc scale in ngc 7793 with muse - i. data description and properties of the ionised gas. *A&A*, 635:A134, 2020.

[43] J. Deng, W. Dong, R. Socher, L.-J. Li, K. Li, and L. Fei-Fei. ImageNet: A Large-Scale Hierarchical Image Database. In *CVPR09*, 2009.

[44] V. Deveikis, D. Narbutis, R. Stonkutė, A. Bridžius, and V. Vansevičius. Simclust – a Program to Simulate Star Clusters. *Baltic Astronomy*, 17:351–361, 2008.

[45] C. L. Dobbs, A. Burkert, and J. E. Pringle. Why are most molecular clouds not gravitationally bound? *MNRAS*, 413(4):2935–2942, June 2011.

[46] C. L. Dobbs, M. R. Krumholz, J. Ballesteros-Paredes, A. D. Bolatto, Y. Fukui, M. Heyer, M. M. M. Low, E. C. Ostriker, and E. Vázquez-Semadeni. Formation of Molecular Clouds and Global Conditions for Star Formation. In Henrik Beuther, Ralf S. Klessen, Cornelis P. Dullemond, and Thomas Henning, editors, *Protostars and Planets VI*, page 3, January 2014.

[47] Andrew E. Dolphin. WFPC2 Stellar Photometry with HSTPHOT. , 112(776):1383–1396, October 2000.

[48] H. Domínguez Sánchez, Huertas-Company, et al. Knowledge transfer of Deep Learning for galaxy morphology from one survey to another. *ArXiv e-prints*, page arXiv:1807.00807, July 2018.

[49] Michael A. Dopita, Jörg Fischera, Ralph S. Sutherland, Lisa J. Kewley, Richard J. Tuffs, Cristina C. Popescu, Wil van Breugel, Brent A. Groves, and Claus Leitherer. Modeling the Pan-Spectral Energy Distribution of Starburst Galaxies. II. Control of the H II Region Parameters. *ApJ*, 647(1):244–255, August 2006.

[50] J. J. Eldridge, E. R. Stanway, L. Xiao, L. A. S. McClelland, G. Taylor, M. Ng, S. M. L. Greis, and J. C. Bray. Binary population and spectral synthesis version 2.1: Construction, observational verification, and new results. *Publications of the Astronomical Society of Australia*, 34, 2017.

[51] L. E. Ellerbroek, A. Bik, L. Kaper, K. M. Maaskant, M. Paalvast, F. Tramper, H. Sana, L. B. F. M. Waters, and Z. Balog. <ASTROBJ>RCW36</ASTROBJ>: characterizing the outcome of massive star formation. *A&A*, 558:A102, Oct 2013.

[52] Bruce G. Elmegreen, A. Adamo, M. Boquien, F. Bournaud, D. Calzetti, D. O. Cook, D. A. Dale, P. A. Duc, D. M. Elmegreen, J. Fensch, K. Grasha, Hwi Kim, L. Kahre, M. Messa, J. E. Ryon, E. Sabbi, and L. J. Smith. Spatial Segregation of Massive Clusters in Dwarf Galaxies. *ApJ*, 888(2):L27, January 2020.

[53] Emsellem, Schinnerer, Eva, Santoro, Francesco, Belfiore, Francesco, Pessa, Ismael, McElroy, Rebecca, Blanc, Guillermo A., Congiu, Enrico, Groves, Brent, Ho, I-Ting, Kreckel, Kathryn, Razza, Alessandro, Sanchez-Blazquez, Patricia, Egorov, Oleg, Faesi, Chris, Klessen, Ralf S., Leroy, Adam K., Meidt, Sharon, Querejeta, Miguel, Rosolowsky, Erik, Scheuermann, Fabian, Anand, Gagandeep S., Barnes, Ashley T., Besli´c, Ivana, Bigiel, Frank, Boquien, Médéric, Cao, Yixian, Chevance, Mélanie, Dale, Daniel A., Eibensteiner, Cosima, Glover, Simon C. O., Grasha, Kathryn, Henshaw, Jonathan D., Hughes, Annie, Koch, Eric W., Kruijssen, J. M. Diederik, Lee, Janice, Liu, Daizhong, Pan, Hsi-An, Pety, Jérôme, Saito, Toshiki, Sandstrom, Karin M., Schruba, Andreas, Sun, Jiayi, Thilker, David A., Usero, Antonio, Watkins, Elizabeth J., and Williams, Thomas G. The phangs-muse survey - probing the chemo-dynamical evolution of disc galaxies. *A&A*, 659:A191, 2022.

[54] II Evans, Neal J. Physical Conditions in Regions of Star Formation. *ARA&A*, 37:311–362, January 1999.

[55] II Evans, Neal J., Michael M. Dunham, Jes K. Jørgensen, Melissa L. Enoch, Bruno Merín, Ewine F. van Dishoeck, Juan M. Alcalá, Philip C. Myers, Karl R. Stapelfeldt, Tracy L. Huard, Lori E. Allen, Paul M. Harvey, Tim van Kempen, Geoffrey A. Blake, David W. Koerner, Lee G. Mundy, Deborah L. Padgett, and Anneila I. Sargent. The Spitzer c2d Legacy Results: Star-Formation Rates and Efficiencies; Evolution and Lifetimes. *ApJS*, 181(2):321–350, April 2009.

[56] S. M. Fall and R. Chandar. Similarities in Populations of Star Clusters. *ApJ*, 752:96, June 2012.

[57] G. J. Ferland, R. L. Porter, P. A. M. van Hoof, R. J. R. Williams, N. P. Abel, M. L. Lykins, G. Shaw, W. J. Henney, and P. C. Stancil. The 2013 Release of Cloudy. , 49:137–163, April 2013.

[58] M. Fouesneau and A. Lançon. Accounting for stochastic fluctuations when analysing the integrated light of star clusters. I. First systematics. *A&A*, 521:A22, October 2010.

[59] Morgan Fouesneau, Ariane Lançon, Rupali Chandar, and and Bradley C. Whitmore. Analyzing star cluster populations with stochastic models: The hubble space telescope/wide field camera 3 sample of clusters in m83. *ApJ*, 750:60, 04 2012.

[60] Daniel George, Hongyu Shen, and E. A. Huerta. Glitch Classification and Clustering for LIGO with Deep Transfer Learning. *arXiv e-prints*, page arXiv:1711.07468, November 2017.

[61] L. Girardi and E. Bica. Colour evolution models and the distribution of LMC clusters in the integrated UBV plane. *A&A*, 274:279–290, Jul 1993.

[62] Dimitrios A. Gouliermis. Unbound Young Stellar Systems: Star Formation on the Loose. , 130:072001, Jul 2018.

[63] F. Governato, C. Brook, L. Mayer, A. Brooks, G. Rhee, J. Wadsley, P. Jonsson, B. Willman, G. Stinson, T. Quinn, and P. Madau. Bulgeless dwarf galaxies and dark matter cores from supernova-driven outflows. *Nature*, 463(7278):203–206, January 2010.

[64] K. Grasha, D. Calzetti, A. Adamo, R. C. Kennicutt, B. G. Elmegreen, M. Messa, D. A. Dale, K. Fedorenko, S. Mahadevan, E. K. Grebel, M. Fumagalli, H. Kim, C. L. Dobbs, D. A. Gouliermis, G. Ashworth, J. S. Gallagher, L. J. Smith, M. Tosi, B. C. Whitmore, E. Schinnerer, D. Colombo, A. Hughes, A. K. Leroy, and S. E. Meidt. The spatial relation between young star clusters and molecular clouds in M51 with LEGUS. *MNRAS*, 483:4707–4723, Mar 2019.

[65] K. Grasha, D. Calzetti, A. Adamo, H. Kim, B. G. Elmegreen, D. A. Gouliermis, A. Aloisi, S. N. Bright, C. Christian, M. Cignoni, D. A. Dale, C. Dobbs, D. M. Elmegreen, M. Fumagalli, III Gallagher, J. S., E. K. Grebel, K. E. Johnson, J. C. Lee, M. Messa, L. J. Smith, J. E. Ryon, D. Thilker, L. Ubeda, and A. Wofford. The Spatial Distribution of the Young Stellar Clusters in the Star-forming Galaxy NGC 628. *ApJ*, 815(2):93, December 2015.

[66] K. Grasha, D. Calzetti, A. Adamo, H. Kim, B. G. Elmegreen, D. A. Gouliermis, D. A. Dale, M. Fumagalli, E. K. Grebel, K. E. Johnson, L. Kahre, R. C. Kennicutt, M. Messa, A. Pellerin, J. E. Ryon, L. J. Smith, F. Shabani, D. Thilker, and L. Ubeda. The Hierarchical Distribution of the Young Stellar Clusters in Six Local Star-forming Galaxies. *ApJ*, 840(2):113, May 2017.

[67] K. Grasha, D. Calzetti, L. Bittle, K. E. Johnson, J. Donovan Meyer, R. C. Kennicutt, B. G. Elmegreen, A. Adamo, M. R. Krumholz, M. Fumagalli, E. K. Grebel, D. A. Gouliermis, D. O. Cook, J. S. Gallagher, A. Aloisi, D. A. Dale, S. Linden, E. Sacchi, D. A. Thilker, R. A. M. Walterbos, M. Messa, A. Wofford, and L. J. Smith. Connecting young star clusters to CO molecular gas in NGC 7793 with ALMA-LEGUS. *MNRAS*, 481:1016–1027, Nov 2018.

[68] Stephen Hannon, Janice C Lee, B C Whitmore, R Chandar, A Adamo, B Mobasher, A Aloisi, D Calzetti, M Cignoni, D O Cook, and et al. H$\alpha$ morphologies of star clusters: a legus study of hii region evolution time-scales and stochasticity in low-mass clusters. *MNRAS*, 490(4):4648–4665, Oct 2019.

[69] Stephen Hannon, Janice C Lee, B C Whitmore, B Mobasher, D Thilker, R Chandar, A Adamo, A Wofford, R Orozco-Duarte, D Calzetti, L Della Bruna, K Kreckel, B Groves, A T Barnes, M Boquien, F Belfiore, and S Linden. H α morphologies of star clusters in 16 LEGUS galaxies: Constraints on h scpii/scp region evolution time-scales. *Monthly Notices of the Royal Astronomical Society*, 512(1):1294–1316, mar 2022.

[70] Kaiming He, Xiangyu Zhang, Shaoqing Ren, and Jian Sun. Deep residual learning for image recognition, 2015.

[71] Paul W. Hodge, Jeff Balsley, Ted K. Wyder, and Brooke P. Skelton. The HiiRegions of m33. II. a photometric catalog of 1272 newly identified emission regions. *Publications of the Astronomical Society of the Pacific*, 111(760):685–690, jun 1999.

[72] K. Hollyhead, N. Bastian, A. Adamo, E. Silva-Villa, J. Dale, J. E. Ryon, and Z. Gazak. Studying the YMC population of M83: how long clusters remain embedded, their interaction with the ISM and implications for GC formation theories. *MNRAS*, 449(1):1106–1117, 03 2015.

[73] Philip F. Hopkins, Eliot Quataert, and Norman Murray. Self-regulated star formation in galaxies via momentum input from massive stars. *MNRAS*, 417(2):950–973, October 2011.

[74] Philip F Hopkins, Andrew Wetzel, Dušan Kereš, Claude-André Faucher-Giguère, Eliot Quataert, Michael Boylan-Kolchin, Norman Murray, Christopher C Hayward, Shea Garrison-Kimmel, Cameron Hummels, and et al. Fire-2 simulations: physics versus numerics in galaxy formation. *Monthly Notices of the Royal Astronomical Society*, 480(1):800–863, Jun 2018.

[75] L. Kahre, R. A. Walterbos, H. Kim, D. Thilker, D. Calzetti, J. C. Lee, E. Sabbi, L. Ubeda, A. Aloisi, M. Cignoni, D. O. Cook, D. A. Dale, B. G. Elmegreen, D. M. Elmegreen, M. Fumagalli, III Gallagher, J. S., D. A. Gouliermis, K. Grasha, E. K. Grebel, D. A. Hunter, E. Sacchi, L. J. Smith, M. Tosi, A. Adamo, J. E. Andrews, G. Ashworth, S. N. Bright, T. M. Brown, R. Chand ar, C. Christian, S. E. de Mink, C. Dobbs, A. S. Evans, A. Herrero, K. E. Johnson, R. C. Kennicutt, M. R. Krumholz, M. Messa, P. Nair, A. Nota, A. Pellerin, J. E. Ryon, D. Schaerer, F. Shabani, S. D. Van Dyk, B. C. Whitmore, and A. Wofford. Extinction Maps and Dust-to-gas Ratios in Nearby Galaxies with LEGUS. *ApJ*, 855:133, Mar 2018.

[76] Mahmoud Kassab, Randa S. Asa'd, Alexandre Vazdekis, Michael A. Beasley, Miguel Cerviño, and Noelia E. D. Noël. Young LMC clusters: the role of red supergiants and multiple stellar populations in their integrated light and CMDs. *MNRAS*, 471(3):3599–3614, 07 2017.

[77] Jr. Kennicutt, R. C. Structural properties of giant H II regions in nearby galaxies. *ApJ*, 287:116–130, Dec 1984.

[78] Jr. Kennicutt, Robert C. The Global Schmidt Law in Star-forming Galaxies. *ApJ*, 498(2):541–552, May 1998.

[79] Robert C. Kennicutt, Jr., Lee Armus, George Bendo, Daniela Calzetti, Daniel A. Dale, Bruce T. Draine, Charles W. Engelbracht, Karl D. Gordon, Albert D. Grauer, George Helou, and et al. Sings: The sirtf nearby galaxies survey. *Publications of the Astronomical Society of the Pacific*, 115(810):928–952, Aug 2003.

[80] Asad Khan, E. A. Huerta, Sibo Wang, Robert Gruendl, Elise Jennings, and Huihuo Zheng. Deep Learning at Scale for the Construction of Galaxy Catalogs in the Dark Energy Survey. *Phys. Lett.*, B795:248–258, 2019.

[81] Jaeyeon Kim, Mélanie Chevance, J. M. Diederik Kruijssen, Andreas Schruba, Karin Sandstrom, Ashley T. Barnes, Frank Bigiel, Guillermo A. Blanc, Yixian Cao, Daniel A. Dale, Christopher M. Faesi, Simon C. O. Glover, Kathryn Grasha, Brent Groves, Cinthya Herrera, Ralf S. Klessen, Kathryn Kreckel, Janice C. Lee, Adam K. Leroy, Jérôme Pety, Miguel Querejeta, Eva Schinnerer, Jiayi Sun, Antonio Usero, Jacob L. Ward, and Thomas G. Williams. On the duration of the embedded phase of star formation. *MNRAS*, 504(1):487–509, June 2021.

[82] Jeong-Gyu Kim, Woong-Tae Kim, and Eve C. Ostriker. DISRUPTION OF MOLECULAR CLOUDS BY EXPANSION OF DUSTY h II REGIONS. *The Astrophysical Journal*, 819(2):137, mar 2016.

[83] Jeong-Gyu Kim, Woong-Tae Kim, and Eve C. Ostriker. Modeling UV radiation feedback from massive stars. II. dispersal of star-forming giant molecular clouds by photoionization and radiation pressure. *ApJ*, 859(1):68, may 2018.

[84] K. Kreckel, G. A. Blanc, E. Schinnerer, B. Groves, A. Adamo, A. Hughes, and S. Meidt. CHARACTERIZING SPIRAL ARM AND INTERARM STAR FORMATION. *ApJ*, 827(2):103, aug 2016.

[85] Pavel Kroupa. On the variation of the initial mass function. *MNRAS*, 322(2):231–246, April 2001.

[86] J. M. Diederik Kruijssen, Andreas Schruba, Mélanie Chevance, Steven N. Longmore, Alexander P. S. Hygate, Daniel T. Haydon, Anna F. McLeod, Julianne J. Dalcanton, Linda J. Tacconi, and Ewine F. van Dishoeck. Fast and inefficient star formation due to short-lived molecular clouds and rapid feedback. *Nature*, 569(7757):519–522, 2019.

[87] Mark R. Krumholz, Angela Adamo, Michele Fumagalli, Aida Wofford, Daniela Calzetti, Janice C. Lee, Bradley C. Whitmore, Stacey N. Bright, Kathryn Grasha, Dimitrios A. Gouliermis, Hwihyun Kim, Preethi Nair, Jenna E. Ryon, Linda J. Smith, David Thilker, Leonardo Ubeda, and Erik Zackrisson. Star Cluster Properties in Two LEGUS Galaxies Computed with Stochastic Stellar Population Synthesis Models. *ApJ*, 812:147, Oct 2015.

[88] Mark R. Krumholz, Blakesley Burkhart, John C. Forbes, and Roland M. Crocker. A unified model for galactic discs: star formation, turbulence driving, and mass transport. *MNRAS*, 477(2):2716–2740, June 2018.

[89] Mark R. Krumholz and Nickolay Y. Gnedin. A COMPARISON OF METHODS FOR DETERMINING THE MOLECULAR CONTENT OF MODEL GALAXIES. *The Astrophysical Journal*, 729(1):36, feb 2011.

[90] Mark R. Krumholz, Christopher F. McKee, and Joss Bland-Hawthorn. Star Clusters Across Cosmic Time. *ARA&A*, 57:227–303, August 2019.

[91] Mark R. Krumholz and Jonathan C. Tan. Slow Star Formation in Dense Gas: Evidence and Implications. *ApJ*, 654(1):304–315, January 2007.

[92] C. J. Lada and E. A. Lada. Embedded Clusters in Molecular Clouds. *ARA&A*, 41:57–115, 2003.

[93] M. Lampton, B. Margon, and S. Bowyer. Parameter estimation in X-ray astronomy. *ApJ*, 208:177–190, August 1976.

[94] A. Lançon and M. Mouhcine. Stochastic Fluctuations in the Spectrophotometric Properties of Star Clusters. In A. Lançon and C. M. Boily, editors, *Massive Stellar Clusters*, volume 211 of *Astronomical Society of the Pacific Conference Series*, page 34, 2000.

[95] S. S. Larsen. Young massive star clusters in nearby galaxies. II. Software tools, data reductions and cluster sizes. , 139:393–415, October 1999.

[96] S. S. Larsen. The mass function of young star clusters in spiral galaxies. *A&A*, 494(2):539–551, February 2009.

[97] Søren S. Larsen. The Luminosity Function of Star Clusters in Spiral Galaxies. *AJ*, 124:1393–1409, Sep 2002.

[98] Søren S. Larsen and Jean P. Brodie. Hubble Space Telescope Observations of Star Clusters in NGC 1023: Evidence for Three Cluster Populations? *AJ*, 120(6):2938–2949, December 2000.

[99] Søren S. Larsen, Jean P. Brodie, John P. Huchra, Duncan A. Forbes, and Carl J. Grillmair. Properties of Globular Cluster Systems in Nearby Early-Type Galaxies. *AJ*, 121(6):2974–2998, June 2001.

[100] Janice C. Lee, Armando Gil de Paz, Robert C. Kennicutt, Matthew Bothwell, Julianne Dalcanton, José G. Funes S. J., Benjamin D. Johnson, Shoko Sakai, Evan Skillman, Christy Tremonti, and et al. A galex ultraviolet imaging survey of galaxies in the local volume. *The Astrophysical Journal Supplement Series*, 192(1):6, Dec 2010.

[101] Janice C. Lee, Bradley C. Whitmore, David A. Thilker, Sinan Deger, Kirsten L. Larson, Leonardo Ubeda, Gagandeep S. Anand, Mederic Boquien, Rupali Chandar, Daniel A. Dale, Eric Emsellem, Adam K. Leroy, Erik Rosolowsky, Eva Schinnerer, Judy Schmidt, Jordan Turner, Schuyler Van Dyk, Richard L. White, Ashley T. Barnes, Francesco Belfiore, Frank Bigiel, Guillermo A. Blanc, Yixian Cao, Melanie Chevance, Enrico Congiu, Oleg V. Egorov, Simon C. O. Glover, Kathryn Grasha, Brent Groves, Jonathan Henshaw, Annie Hughes, Ralf S. Klessen, Eric Koch, Kathryn Kreckel, J. M. Diederik Kruijssen, Daizhong Liu, Laura A. Lopez, Ness Mayker, Sharon E. Meidt, Eric J. Murphy, Hsi-An Pan, Jerome Pety, Miguel Querejeta, Alessandro Razza, Toshiki Saito, Patricia Sanchez-Blazquez, Francesco Santoro, Amy Sardone, Fabian Scheuermann, Andreas Schruba, Jiayi Sun, Antonio Usero, Elizabeth Watkins, and Thomas G. Williams. The PHANGS-HST Survey: Physics at High Angular resolution in Nearby GalaxieS with the Hubble Space Telescope. *arXiv e-prints*, page arXiv:2101.02855, January 2021.

[102] Claus Leitherer, Daniel Schaerer, Jeffrey D. Goldader, Rosa M. González Delgado, Carmelle Robert, Denis Foo Kune, Duília F. de Mello, Daniel Devost, and Timothy M. Heckman. Starburst99: Synthesis Models for Galaxies with Active Star Formation. *ApJS*, 123(1):3–40, Jul 1999.

[103] Adam K. Leroy, Annie Hughes, Daizhong Liu, Jérôme Pety, Erik Rosolowsky, Toshiki Saito, Eva Schinnerer, Andreas Schruba, Antonio Usero, Christopher M. Faesi, Cinthya N. Herrera, Mélanie Chevance, Alexander P. S. Hygate, Amanda A. Kepley, Eric W. Koch, Miguel Querejeta, Kazimierz Sliwa, David Will, Christine D. Wilson, Gagandeep S. Anand, Ashley Barnes, Francesco Belfiore, Ivana Bešlić, Frank Bigiel, Guillermo A. Blanc, Alberto D. Bolatto, Médéric Boquien, Yixian Cao, Rupali Chandar, Jérémy Chastenet, I-Da Chiang, Enrico Congiu, Daniel A. Dale, Sinan Deger, Jakob S. den Brok, Cosima Eibensteiner, Eric Emsellem, Axel García-Rodríguez, Simon C. O. Glover, Kathryn Grasha, Brent Groves, Jonathan D. Henshaw, María J. Jiménez Donaire, Jaeyeon Kim, Ralf S. Klessen, Kathryn Kreckel, J. M. Diederik Kruijssen, Kirsten L. Larson, Janice C. Lee, Ness Mayker, Rebecca McElroy, Sharon E. Meidt, Angus Mok, Hsi-An Pan, Johannes Puschnig, Alessandro Razza, Patricia Sánchez-Bl'azquez, Karin M. Sandstrom, Francesco Santoro, Amy Sardone, Fabian Scheuermann, Jiayi Sun, David A. Thilker, Jordan A. Turner, Leonardo Ubeda, Dyas Utomo, Elizabeth J. Watkins, and Thomas G. Williams. PHANGS–ALMA data processing and pipeline. *The Astrophysical Journal Supplement Series*, 255(1):19, jul 2021.

[104] Adam K. Leroy, Eva Schinnerer, Annie Hughes, Erik Rosolowsky, Jérôme Pety, Andreas Schruba, Antonio Usero, Guillermo A. Blanc, Mélanie Chevance, Eric Emsellem, Christopher M. Faesi, Cinthya N. Herrera, Daizhong Liu, Sharon E. Meidt, Miguel Querejeta, Toshiki Saito, Karin M. Sandstrom, Jiayi Sun, Thomas G. Williams, Gagandeep S. Anand, Ashley T. Barnes, Erica A. Behrens, Francesco Belfiore, Samantha M. Benincasa, Ivana Bešlić, Frank Bigiel, Alberto D. Bolatto, Jakob S. den Brok, Yixian Cao, Rupali Chandar, Jérémy Chastenet, I-Da Chiang, Enrico Congiu, Daniel A. Dale, Sinan Deger, Cosima Eibensteiner, Oleg V. Egorov, Axel García-Rodríguez, Simon C. O. Glover, Kathryn Grasha, Jonathan D. Henshaw, I-Ting Ho, Amanda A. Kepley, Jaeyeon Kim, Ralf S. Klessen, Kathryn Kreckel, Eric W. Koch, J. M. Diederik Kruijssen, Kirsten L. Larson, Janice C. Lee, Laura A. Lopez, Josh Machado, Ness Mayker, Rebecca McElroy, Eric J. Murphy, Eve C. Ostriker, Hsi-An Pan, Ismael Pessa, Johannes Puschnig, Alessandro Razza, Patricia Sánchez-Blázquez, Francesco Santoro, Amy Sardone, Fabian Scheuermann, Kazimierz Sliwa, Mattia C. Sormani, Sophia K. Stuber, David A. Thilker, Jordan A. Turner, Dyas Utomo, Elizabeth J. Watkins, and Bradley Whitmore. Phangs-alma: Arcsecond co(2-1) imaging of nearby star-forming galaxies, 2021.

[105] Adam K. Leroy, Fabian Walter, Elias Brinks, Frank Bigiel, W. J. G. de Blok, Barry Madore, and M. D. Thornley. THE STAR FORMATION EFFICIENCY IN NEARBY GALAXIES: MEASURING WHERE GAS FORMS STARS EFFECTIVELY. *The Astronomical Journal*, 136(6):2782–2845, nov 2008.

[106] Dmitry Makarov, Philippe Prugniel, Nataliya Terekhova, Hélène Courtois, and Isabelle Vauglin. HyperLEDA. III. The catalogue of extragalactic distances. *A&A*, 570:A13, October 2014.

[107] Allison M. Matthews, Kelsey E. Johnson, Bradley C. Whitmore, Crystal L. Brogan, Adam K. Leroy, and Remy Indebetouw. Resolved star formation efficiency in the antennae galaxies. *ApJ*, 862(2):147, aug 2018.

[108] M. Messa, A. Adamo, G. Östlin, D. Calzetti, K. Grasha, E. K. Grebel, F. Shabani, R. Chandar, D. A. Dale, C. L. Dobbs, B. G. Elmegreen, M. Fumagalli, D. A. Gouliermis, H. Kim, L. J. Smith, D. A. Thilker, M. Tosi, L. Ubeda, R. Walterbos, B. C. Whitmore, K. Fedorenko, S. Mahadevan, J. E. Andrews, S. N. Bright, D. O. Cook, L. Kahre, P. Nair, A. Pellerin, J. E. Ryon, S. D. Ahmad, L. P. Beale, K. Brown, D. A. Clarkson, G. C. Guidarelli, R. Parziale, J. Turner, and M. Weber. The young star cluster population of M51 with LEGUS - I. A comprehensive study of cluster formation and evolution. *MNRAS*, 473(1):996–1018, January 2018.

[109] Matteo Messa, A. Adamo, D. Calzetti, M. Reina-Campos, D. Colombo, E. Schinnerer, R. Chandar, D. A. Dale, D. A. Gouliermis, K. Grasha, E. K. Grebel, B. G. Elmegreen, M. Fumagalli, K. E. Johnson, J. M. D. Kruijssen, G. Östlin, F. Shabani, L. J. Smith, and B. C. Whitmore. The young star cluster population of M51 with LEGUS - II. Testing environmental dependences. *MNRAS*, 477(2):1683–1707, June 2018.

[110] Matteo Messa, Daniela Calzetti, Angela Adamo, Kathryn Grasha, Kelsey E. Johnson, Elena Sabbi, Linda J. Smith, Varun Bajaj, Molly K. Finn, and Zesen Lin. Looking for Obscured Young Star Clusters in NGC 1313. *ApJ*, 909(2):121, March 2021.

[111] S. Noll, D. Burgarella, E. Giovannoli, V. Buat, D. Marcillac, and J. C. Muñoz-Mateos. Analysis of galaxy spectral energy distributions from far-UV to far-IR with CIGALE: studying a SINGS test sample. *A&A*, 507(3):1793–1813, December 2009.

[112] Rogelio Orozco-Duarte, Aida Wofford, Alba Vidal-García, Gustavo Bruzual, Stephane Charlot, Mark R. Krumholz, Stephen Hannon, Janice Lee, Timothy Wofford, Michele Fumagalli, Daniel Dale, Matteo Messa, Eva K. Grebel, Linda Smith, Kathryn Grasha, and David Cook. Synthetic photometry of OB star clusters with stochastically sampled IMFs: analysis of models and HST observations. *MNRAS*, 509(1):522–549, January 2022.

[113] D. E. Osterbrock and G. J. Ferland. *Astrophysics of gaseous nebulae and active galactic nuclei*. 2006.

[114] Eve C. Ostriker, Christopher F. McKee, and Adam K. Leroy. REGULATION OF STAR FORMATION RATES IN MULTIPHASE GALACTIC DISKS: A THERMAL/DYNAMICAL EQUILIBRIUM MODEL. *The Astrophysical Journal*, 721(2):975–994, sep 2010.

[115] Xiaoying Pang, Anna Pasquali, and Eva K. Grebel. A TWO-DIMENSIONAL MAP OF THE COLOR EXCESS IN NGC 3603. *AJ*, 142(4):132, sep 2011.

[116] Adam Paszke, Sam Gross, Soumith Chintala, Gregory Chanan, Edward Yang, Zachary DeVito, Zeming Lin, Alban Desmaison, Luca Antiga, and Adam Lerer. Automatic differentiation in pytorch. In *NIPS-W*, 2017.

[117] Gustavo Pérez, Matteo Messa, Daniela Calzetti, Subhransu Maji, Dooseok E. Jung, Angela Adamo, and Mattia Sirressi. StarcNet: Machine learning for star cluster identification. *The Astrophysical Journal*, 907(2):100, feb 2021.

[118] Simon F. Portegies Zwart, Stephen L. W. McMillan, and Mark Gieles. Young Massive Star Clusters. *ARA&A*, 48:431–493, September 2010.

[119] Alec Radford, Jong Wook Kim, Chris Hallacy, Aditya Ramesh, Gabriel Goh, Sandhini Agarwal, Girish Sastry, Amanda Askell, Pamela Mishkin, Jack Clark, Gretchen Krueger, and Ilya Sutskever. Learning transferable visual models from natural language supervision. In Marina Meila and Tong Zhang, editors, *Proceedings of the 38th International Conference on Machine Learning*, volume 139 of *Proceedings of Machine Learning Research*, pages 8748–8763. PMLR, 18–24 Jul 2021.

[120] J. E. Ryon, J. S. Gallagher, L. J. Smith, A. Adamo, D. Calzetti, S. N. Bright, M. Cignoni, D. O. Cook, D. A. Dale, B. E. Elmegreen, M. Fumagalli, D. A. Gouliermis, K. Grasha, E. K. Grebel, H. Kim, M. Messa, D. Thilker, and L. Ubeda. Effective radii of young, massive star clusters in two LEGUS galaxies. *The Astrophysical Journal*, 841(2):92, may 2017.

[121] Samir Salim, Médéric Boquien, and Janice C. Lee. Dust attenuation curves in the local universe: Demographics and new laws for star-forming galaxies and high-redshift analogs. *The Astrophysical Journal*, 859(1):11, may 2018.

[122] Samir Salim, Janice C. Lee, Steven Janowiecki, Elisabete da Cunha, Mark Dickinson, Médéric Boquien, Denis Burgarella, John J. Salzer, and Stéphane Charlot. iGALEX/i –SDSS i–WISE/i LEGACY CATALOG (GSWLC): STAR FORMATION RATES, STELLAR MASSES, AND DUST ATTENUATIONS OF 700,000 LOW-REDSHIFT GALAXIES. *The Astrophysical Journal Supplement Series*, 227(1):2, nov 2016.

[123] Joop Schaye, Robert A. Crain, Richard G. Bower, Michelle Furlong, Matthieu Schaller, Tom Theuns, Claudio Dalla Vecchia, Carlos S. Frenk, I. G. McCarthy, John C. Helly, Adrian Jenkins, Y. M. Rosas-Guevara, Simon D. M. White, Maarten Baes, C. M. Booth, Peter Camps, Julio F. Navarro, Yan Qu, Alireza Rahmati, Till Sawala, Peter A. Thomas, and James Trayford. The EAGLE project: simulating the evolution and assembly of galaxies and their environments. *MNRAS*, 446(1):521–554, January 2015.

[124] E. F. Schlafly and D. P. Finkbeiner. Measuring Reddening with Sloan Digital Sky Survey Stellar Spectra and Recalibrating SFD. *ApJ*, 737:103, August 2011.

[125] Karen Simonyan and Andrew Zisserman. Very deep convolutional networks for large-scale image recognition, 2014.

[126] J. A. Smith, D. L. Tucker, S. Kent, M. W. Richmond, M. Fukugita, T. Ichikawa, S.-i. Ichikawa, A. M. Jorgensen, A. Uomoto, J. E. Gunn, M. Hamabe, M. Watanabe, A. Tolea, A. Henden, J. Annis, J. R. Pier, T. A. McKay, J. Brinkmann, B. Chen, J. Holtzman, K. Shimasaku, and D. G. York. The u'g'r'i'z' Standard-Star System. *AJ*, 123:2121–2144, April 2002.

[127] Linda J. Smith, Richard P. F. Norris, and Paul A. Crowther. Realistic ionizing fluxes for young stellar populations from 0.05 to 2 Z. *Monthly Notices of the Royal Astronomical Society*, 337(4):1309–1328, 12 2002.

[128] C. Soubiran, G. Jasniewicz, L. Chemin, C. Zurbach, N. Brouillet, P. Panuzzo, P. Sartoretti, D. Katz, J.-F. Le Campion, O. Marchal, D. Hestroffer, F. Thévenin, F. Crifo, S. Udry, M. Cropper, G. Seabroke, Y. Viala, K. Benson, R. Blomme, A. Jean-Antoine, H. Huckle, M. Smith, S. G. Baker, Y. Damerdji, C. Dolding, Y. Frémat, E. Gosset, A. Guerrier, L. P. Guy, R. Haigron, K. Janßen, G. Plum, C. Fabre, Y. Lasne, F. Pailler, C. Panem, F. Riclet, F. Royer, G. Tauran, T. Zwitter, A. Gueguen, and C. Turon. Gaia Data Release 2. The catalogue of radial velocity standard stars. *A&A*, 616:A7, August 2018.

[129] Jiayi Sun, Adam K. Leroy, Eve C. Ostriker, Annie Hughes, Erik Rosolowsky, Andreas Schruba, Eva Schinnerer, Guillermo A. Blanc, Christopher Faesi, J. M. Diederik Kruijssen, Sharon Meidt, Dyas Utomo, Frank Bigiel, Alberto D. Bolatto, Mélanie Chevance, I-Da Chiang, Daniel Dale, Eric Emsellem, Simon C. O. Glover, Kathryn Grasha, Jonathan Henshaw, Cinthya N. Herrera, Maria Jesus Jimenez-Donaire, Janice C. Lee, Jérôme Pety, Miguel Querejeta, Toshiki Saito, Karin Sandstrom, and Antonio Usero. Dynamical Equilibrium in the Molecular ISM in 28 Nearby Star-forming Galaxies. *ApJ*, 892(2):148, April 2020.

[130] Jiayi Sun, Adam K. Leroy, Andreas Schruba, Erik Rosolowsky, Annie Hughes, J. M. Diederik Kruijssen, Sharon Meidt, Eva Schinnerer, Guillermo A. Blanc, Frank Bigiel, Alberto D. Bolatto, Mélanie Chevance, Brent Groves, Cinthya N. Herrera, Alexander P. S. Hygate, Jérôme Pety, Miguel Querejeta, Antonio Usero, and Dyas Utomo. Cloud-scale molecular gas properties in 15 nearby galaxies. *The Astrophysical Journal*, 860(2):172, jun 2018.

[131] Elizabeth J. Tasker. STAR FORMATION IN DISK GALAXIES. II. THE EFFECT OF STAR FORMATION AND PHOTOELECTRIC HEATING ON THE FORMATION AND EVOLUTION OF GIANT MOLECULAR CLOUDS. *The Astrophysical Journal*, 730(1):11, feb 2011.

[132] David A. Thilker, Robert Braun, and René A. M. Walterbos. HII[CLC]phot[/CLC]: Automated photometry of h [CSC]ii[/CSC] regions applied to m51. *ApJ*, 120(6):3070–3087, dec 2000.

[133] David A. Thilker, Bradley C. Whitmore, Janice C. Lee, Sinan Deger, Rupali Chandar, Kirsten L. Larson, Stephen Hannon, Leonardo Ubeda, Daniel A. Dale, Simon C. O. Glover, Kathryn Grasha, Ralf S. Klessen, J. M. Diederik Kruijssen, Erik Rosolowsky, Andreas Schruba, Richard L. White, and Thomas G. Williams. PHANGS-HST: new methods for star cluster identification in nearby galaxies. *MNRAS*, 509(3):4094–4127, January 2022.

[134] Tremblin, P., Anderson, L. D., Didelon, P., Raga, A. C., Minier, V., Ntormousi, E., Pettitt, A., Pinto, C., Samal, M. R., Schneider, N., and Zavagno, A. Age, size, and position of hregions in the galaxy - expansion of ionized gas in turbulent molecular clouds. *A&A*, 568:A4, 2014.

[135] Jordan A Turner, Daniel A Dale, Janice C Lee, Médéric Boquien, Rupali Chandar, Sinan Deger, Kirsten L Larson, Angus Mok, David A Thilker, Leonardo Ubeda, and et al. Phangs–hst: star cluster spectral energy distribution fitting with cigale. *Monthly Notices of the Royal Astronomical Society*, 502(1):1366–1385, Jan 2021.

[136] Gerardo A. Vázquez and Claus Leitherer. Optimization of Starburst99 for Intermediate-Age and Old Stellar Populations. *ApJ*, 621(2):695–717, March 2005.

[137] Wei Wei, E A Huerta, Bradley C Whitmore, Janice C Lee, Stephen Hannon, Rupali Chandar, Daniel A Dale, Kirsten L Larson, David A Thilker, Leonardo Ubeda, Médéric Boquien, Mélanie Chevance, J M Diederik Kruijssen, Andreas Schruba, Guillermo A Blanc, and Enrico Congiu. Deep transfer learning for star cluster classification: I. application to the PHANGS–HST survey. *Monthly Notices of the Royal Astronomical Society*, 493(3):3178–3193, 02 2020.

[138] Bradley C. Whitmore, Crystal Brogan, Rupali Chandar, Aaron Evans, John Hibbard, Kelsey Johnson, Adam Leroy, George Privon, Anthony Remijan, and Kartik Sheth. ALMA Observations of the Antennae Galaxies. I. A New Window on a Prototypical Merger. *ApJ*, 795(2):156, November 2014.

[139] Bradley C. Whitmore, Rupali Chandar, Hwihyun Kim, Catherine Kaleida, Max Mutchler, Matt Stankiewicz, Daniela Calzetti, Abhijit Saha, Robert O'Connell, Bruce Balick, Howard E. Bond, Marcella Carollo, Michael J. Disney, Michael A. Dopita, Jay A. Frogel, Donald N. B. Hall, Jon A. Holtzman, Randy A. Kimble, Patrick J. McCarthy, Francesco Paresce, Joseph I. Silk, John T. Trauger, Alistair R. Walker, Rogier A. Windhorst, and Erick T. Young. USING hα MORPHOLOGY AND SURFACE BRIGHTNESS FLUCTUATIONS TO AGE-DATE STAR CLUSTERS IN m83. *ApJ*, 729(2):78, feb 2011.

[140] Bradley C. Whitmore, Rupali Chandar, Janice Lee, Leonardo Ubeda, Angela Adamo, Alessandra Aloisi, Daniela Calzetti, Michele Cignoni, David Cook, Daniel Dale, and et al. Legus and h -legus observations of star clusters in ngc 4449: Improved ages and the fraction of light in clusters as a function of age. *The Astrophysical Journal*, 889(2):154, Feb 2020.

[141] Bradley C. Whitmore, Janice C. Lee, Rupali Chandar, David A. Thilker, Stephen Hannon, Wei Wei, E. A. Huerta, Frank Bigiel, Médéric Boquien, Mélanie Chevance, Daniel A. Dale, Sinan Deger, Kathryn Grasha, Ralf S. Klessen, J. M. Diederik Kruijssen, Kirsten L. Larson, Angus Mok, Erik Rosolowsky, Eva Schinnerer, Andreas Schruba, Leonardo Ubeda, Schuyler D. Van Dyk, Elizabeth Watkins, and Thomas Williams. Star cluster classification in the PHANGS-HST survey: Comparison between human and machine learning approaches. *MNRAS*, 506(4):5294–5317, October 2021.

[142] Bradley C. Whitmore and Francois Schweizer. Hubble Space Telescope Observations of Young Star Clusters in NGC 4038/4039, "The Antennae" Galaxies. *AJ*, 109:960, March 1995.

[143] Bradley C. Whitmore, Francois Schweizer, Claus Leitherer, Kirk Borne, and Carmelle Robert. Hubble Space Telescope Discovery of Candidate Young Globular Clusters in the Merger Remnant NGC 7252. *AJ*, 106:1354, October 1993.

[144] Bradley C. Whitmore and Qing Zhang. What Fraction of the Young Clusters in the Antennae Galaxies Are "Missing"? *AJ*, 124(3):1418–1434, September 2002.

[145] Bradley C. Whitmore, Qing Zhang, Claus Leitherer, S. Michael Fall, François Schweizer, and Bryan W. Miller. The Luminosity Function of Young Star Clusters in "the Antennae" Galaxies (NGC 4038-4039). *AJ*, 118(4):1551–1576, October 1999.

[146] J. P. Williams and C. F. McKee. The Galactic Distribution of OB Associations in Molecular Clouds. *ApJ*, 476:166–183, February 1997.

[147] A. Wofford, S. Charlot, G. Bruzual, J. J. Eldridge, D. Calzetti, A. Adamo, M. Cignoni, S. E. de Mink, D. A. Gouliermis, K. Grasha, E. K. Grebel, J. C. Lee, G. Östlin, L. J. Smith, L. Ubeda, and E. Zackrisson. A comprehensive comparative test of seven widely used spectral synthesis models against multi-band photometry of young massive-star clusters. *MNRAS*, 457(4):4296–4322, April 2016.

[148] E. Zackrisson, Bergvall, N., Olofsson, K., and Siebert, A. A model of spectral galaxy evolution including the effects of nebular emission. *A&A*, 375(3):814–826, 2001.

[149] Erik Zackrisson, Claes-Erik Rydberg, Daniel Schaerer, Göran Östlin, and Manan Tuli. THE SPECTRAL EVOLUTION OF THE FIRST GALAXIES. i.JAMES WEBB SPACE TELESCOPEDETECTION LIMITS AND COLOR CRITERIA FOR POPULATION III GALAXIES. *ApJ*, 740(1):13, sep 2011.

[150] Peter Zeidler, Elena Sabbi, Antonella Nota, Eva K. Grebel, Monica Tosi, Alceste Z. Bonanos, Anna Pasquali, Carol Christian, Selma E. de Mink, and Leonardo Ubeda. A HIGH-RESOLUTION MULTIBAND SURVEY OF WESTERLUND 2 WITH THEHUBBLE SPACE TELESCOPE. i. IS THE MASSIVE STAR CLUSTER DOUBLE? *AJ*, 150(3):78, aug 2015.

[151] Qingya Zhang, Todd Hunter, T. K. Sridharan, and Riccardo Cesaroni. Shock-heated nh3 in a molecular jet associated with a high-mass young star. *ApJ*, 527:L117–L120, 12 1999.

[152] B. Zuckerman and II Evans, N. J. Models of Massive Molecular Clouds. *ApJ*, 192:L149, September 1974.